INFORMATION TO USERS

This manuscript has been reproduced from the microfilm master. UMI films the text directly from the original or copy submitted. Thus, some thesis and dissertation copies are in typewriter face, while others may be from any type of computer printer.

The quality of this reproduction is dependent upon the quality of the copy submitted. Broken or indistinct print, colored or poor quality illustrations and photographs, print bleedthrough, substandard margins, and improper alignment can adversely affect reproduction.

In the unlikely event that the author did not send UMI a complete manuscript and there are missing pages, these will be noted. Also, if unauthorized copyright material had to be removed, a note will indicate the deletion.

Oversize materials (e.g., maps, drawings, charts) are reproduced by sectioning the original, beginning at the upper left-hand corner and continuing from left to right in equal sections with small overlaps.

Fatigue Resistance of High Performance Steel (HPS) Details

by

Huating Chen   ©

A thesis submitted to the Faculty of Graduate Studies and Research in partial fulfillment
of the requirements for the degree of Doctor of Philosophy

in

Structural Engineering

Department of Civil and Environmental Engineering

Edmonton, Alberta

Spring 2005

ABSTRACT

Because of its superior toughness and weldability, high performance steel (HPS) has gained increasing popularity for use in highway bridges. Its fatigue resistance, however, is not yet well characterized. Established analytical methods that can predict both fatigue crack initiation and propagation, coupled with a material-based testing program, provide a sound and cost effective approach to studying fatigue behavior of HPS.

In order to obtain the necessary material input parameters for the proposed methods, and to better understand the properties of high performance steel, material tests were conducted on ASTM A709 HPS 485W steel and on two conventional structural steels to characterize their monotonic and cyclic material properties. HPS 485W steel shows high strength and good ductility, resulting in high fracture toughness. Fatigue test results, however, indicate that HPS 485W steel exhibits a fatigue resistance comparable to that of lower strength and toughness structural steels but with significantly higher fatigue limit.

Fatigue life prediction analysis was performed on six common structural details of which test results are available in literature. The proposed methods predicted fatigue lives of all details well, comparing with the test results. HPS shows slightly higher fatigue resistance than conventional structural steels in the high cycle fatigue region for non-welded details. However, fatigue resistance of HPS welded details is similar to that of conventional structural steels welded details. The current fatigue design provisions are still applicable to HPS welded details.

ACKNOWLEDGEMENTS

Huating Chen

December 2004

Canada

TABLE OF CONTENTS

LIST OF TABLES

LIST OF FIGURES

LIST OF SYMBOLS

A fatigue life constant

A_i coefficients in 4th order polynomial description of stress field ($i = 0$ to 4)

A_{pl} area under the load vs. load-line displacement curve

a crack length (half distance between crack tips of a through-thickness crack); minor semi-axis length of an elliptical crack

a/W non-dimensional crack length

a_f final crack size

a_i initial crack size; coefficients in the correction factor for stress intensity factor ($i = 0$ to 14)

a_w web crack size in an I-girder

$a_{w,i}$ initial web crack size in an I-girder

B specimen thickness

b fatigue strength exponent

b_f flange width of an I-girder

b_i initial uncracked ligament

C constant in crack growth equation; compliance

$CMOD$ crack mouth opening displacement

CVN standard Charpy V-Notch energy at transition temperature

c fatigue ductility exponent; major semi-axis length of an elliptical crack

D damage parameter

$D/2$ hole radius for the plate with a circular hole detail

D_0 value of the damage parameter at the fatigue limit (when $N_f \rightarrow \infty$)

d depth of an I-girder

da/dN crack growth rate

d_w web depth of an I-girder

E Young's modulus of elasticity

e eccentricity of web crack in an I-girder

F	coefficient in damage parameter versus fatigue life curve, coefficient in total strain energy density versus fatigue life curve
F_p	coefficient in plastic strain energy density versus fatigue life curve
F_t	coefficient in plastic plus tensile elastic strain energy density versus fatigue life curve
f_L	correction factor for the stress intensity factor of the lower tip of a through thickness web crack in an I-girder
f_U	correction factor for the stress intensity factor of the upper tip of a through thickness web crack in an I-girder
H	specimen height
I_1^{max}	first invariant of stress tensor at maximum load
J	J-integral
J_{IC}	J-integral at the onset of stable crack extension
J_Q	conditional J-integral at the onset of stable crack extension
J_i	J-integral when instability occurs before the onset of stable crack extension
J_{el}	elastic component of J-integral
J_{pl}	plastic component of J-integral
J_u	J-integral when instability occurs after stable crack extension
K	stress intensity factor
K'	cyclic strength coefficient
K^*	strength coefficient of master curve
K_C	critical fracture toughness
K_{IC}	plane strain fracture toughness
K_Q	conditional plane strain fracture toughness
K_f	fatigue notch factor
K_{max}	maximum stress intensity factor
K_{min}	minimum stress intensity factor

K_t	elastic stress concentration factor
k	normalized stress range distribution
L	bridge span
m	slope of $\Delta\sigma - N$ curve; exponent in crack growth equation
N	number of cycles to failure
N_{ei}	the ith estimated fatigue life from regression line
N_t	number of cycles to failure in smooth fatigue specimens, fatigue life including crack initiation and crack propagation up to a crack about 1.0 mm long in larger detail
N_i	fatigue crack initiation life; the ith tested fatigue life
N_p	fatigue crack propagation life
n	number of points in regression analysis
n'	cyclic strain-hardening exponent
n^*	strain-hardening exponent of master curve
P	load
P_Q	conditional load
P_{max}	maximum load
R	stress ratio (minimum stress divided by maximum stress); load ratio
s	standard deviation
T	test temperature
t	plate thickness
t_f	flange thickness of an I-girder
t_w	web thickness of an I-girder
U	non-dimensional $CMOD$
W	plate dimension in the direction of crack size; specimen width
Z_L	lower crack tip position of a web crack in an I-girder
Z_U	upper crack tip position of a web crack in an I-girder

α	exponent in damage parameter versus fatigue life curve, exponent in total strain energy density versus fatigue life curve
α_p	exponent in plastic strain energy density versus fatigue life curve
α_t	exponent in plastic plus tensile elastic strain energy density versus fatigue life curve
β	geometry parameter in an I-girder; material constant in obtaining fatigue notch factor
β_E	crack front shape correction factor
β_G	stress gradient correction factor
β_S	free surface correction factor
β_W	finite width correction factor
Δa	amount of stable crack extension; increment of the minor crack tip of an elliptical crack
Δa_L	increment of the lower crack tip of a web crack in an I-girder
Δa_U	increment of the upper crack tip of a web crack in an I-girder
Δc	increment of the major crack tip of an elliptical crack
$\Delta \varepsilon$	strain range
$\Delta \varepsilon / 2$	strain amplitude
$\Delta \varepsilon^e / 2$	elastic strain amplitude, $\Delta \varepsilon^e / 2 = \Delta \sigma / 2E$
$\Delta \varepsilon^p$	plastic strain range
$\Delta \varepsilon^p / 2$	plastic strain amplitude, $\Delta \varepsilon^p / 2 = \Delta \varepsilon / 2 - \Delta \varepsilon^e / 2$
ΔK	stress intensity factor range
ΔK_a	stress intensity factor range at the minor crack tip of an elliptical crack
ΔK_c	stress intensity factor range at the major crack tip of an elliptical crack
ΔK_i	initial stress intensity factor range
ΔW	total strain energy density per cycle
ΔW^{el}	elastic strain energy density per cycle
ΔW^p	plastic strain energy density per cycle

$\Delta W'$	plastic plus tensile elastic strain energy density per cycle
ΔW_0	value of total strain energy density at the fatigue limit (when $N_f \to \infty$)
ΔW_0^p	value of plastic strain energy density at the fatigue limit (when $N_f \to \infty$)
$\Delta W_0'$	value of plastic plus tensile elastic strain energy density at the fatigue limit (when $N_f \to \infty$)
ΔW_M^p	plastic strain energy density per cycle corresponding to Masing behaviour
ΔW_N^p	plastic strain energy density per cycle due to non-Masing behaviour
$\Delta \sigma$	stress range (the algebraic difference between maximum and minimum stress)
$\Delta \sigma / 2$	stress amplitude (half of stress range)
$\Delta \sigma_x$	corrected nominal stress range for bolted shear splice
$\delta \sigma_0$	amount of shifting in order to get matching upper hysteresis loop branches (master curve), also an indication of change in proportional limit
ε	strain; normalized eccentricity of a two-tip through thickness web crack in an I-girder
ε_i	principal strain ($i = 1$ to 3), with $\varepsilon_1 < \varepsilon_2 < \varepsilon_3$
ε_{max}	maximum strain
ε_{min}	minimum strain
ε_f'	fatigue ductility coefficient
Φ_0	elliptical integral of the second kind
ϕ	angle with respect to major axis of elliptical crack
η	material mean stress sensitivity property
λ_w	normalized crack size of a two-tip through thickness web crack in an I-girder
ρ	multiaxial stress state severity indicator; notch root radius
σ	reference stress
σ_1	nominal stress at mid-bottom flange of an I-girder

σ_2	equivalent nominal stress at mid-bottom flange of an I-girder considering transverse stiffener
σ_Y	effective yield strength
σ_{YS}	0.2% offset yield strength at room temperature
$\sigma_{YS(T)}$	0.2% offset yield strength at testing temperature
σ_m	mean stress
$\dfrac{\sigma_m}{\Delta\sigma/2}$	mean stress to stress amplitude ratio
σ_{max}	maximum stress
σ_{min}	minimum stress
σ_u	material tensile strength
σ_x	normal stress in the x axis
σ_{eq}^{max}	equivalent stress at maximum load
σ_f'	fatigue strength coefficient
ν	effective Poisson's ratio
$(\Delta\sigma/2)_{-1}$	equivalent fully reversed stress amplitude

CHAPTER 1.

INTRODUCTION

1.1. Background

Compared to conventional structural grade steels, high performance steel (HPS) provides superior strength, improved weldability, greatly enhanced fracture toughness, high ductility, and weathering characteristics. The improved performance of HPS is achieved through lower levels of carbon, the addition of alloying elements, and advanced thermal-mechanical processing techniques, resulting in a low carbon, fine grain, martensitic microstructure.

Although the development of HPS in North America spans only the past decade, it is rapidly gaining popularity for use in highway bridges. It is estimated that there are more than 200 HPS bridges in various stages of design and construction in the United States (Wilson 2004). However, utilizing the full benefits of HPS with higher yield strengths (say, higher than 585 MPa) may not be possible under current design standards because the fatigue limit state is likely to control the design (Sause 1996). This observation is based on the assumption that the fatigue performance of details made of HPS is the same as for conventional structural steels. Research to date on HPS has mainly focused on design aspects related to strength, ductility, and stability of HPS members. Little attention has been paid to its fatigue properties.

1.2. Objectives and Scope

A comprehensive research program aimed at investigating the fatigue characteristics of HPS and methods of fatigue life prediction and their applicability to conventional details fabricated using HPS was initiated at the University of Alberta. The principal objectives of the study are to:

1. Answer the fundamental question of whether the high toughness of HPS provides any benefit in fatigue resistance.

1

2. Develop an experimental database from which the key HPS material properties related to fatigue can be established.

3. Develop a method to predict the fatigue life of components and structures from crack initiation to final fracture, considering the effects of multiaxial stress state and mean stress.

4. Study the fatigue resistance of conventional details made with HPS and compare with those made with conventional structural grade steels.

5. Make recommendations for fatigue design of HPS.

Although HPS have also been developed in Europe and Japan, the research project presented in the following has focussed on HPS developed in the United States and specified in ASTM A709 as grade HPS 485W, where W indicates that the steel is also a weathering steel. Other important issues in fatigue, such as effects of variable amplitude loading, multiple crack interaction and corrosion are not investigated in this study.

1.3. Methodology

Since fatigue testing of large scale details is time consuming and expensive, analytical techniques that have been developed to predict both the crack initiation and propagation stages of fatigue life from cyclic material tests are attractive alternatives to testing in investigating the fatigue resistance of HPS. Different approaches to fatigue life prediction are assessed by comparing predicted fatigue response to test results from specimens made of conventional structural steels and HPS. The validated approach and cyclic and fatigue material properties for HPS can be used to predict the fatigue life of HPS details and to develop fatigue design curves for HPS. A validation of various fatigue life prediction approaches through comparison with fatigue tests on conventional grade steels and HPS provides a useful tool to assess the fatigue performance of HPS details.

2

1.4. Thesis Organization

The *Literature Review* (Chapter 2) summarizes the background information about: (1) current fatigue design specifications and fatigue detail categories; (2) major fatigue life prediction techniques; (3) previous research on high performance steel; and (4) fatigue of high strength low alloy steel. In Chapter 3, *Fatigue Life Prediction*, analytical techniques and procedures that are used to predict the fatigue life of various structural details are described in detail. Based on the fatigue life prediction approaches, material fatigue tests were carried out to provide the input information for prediction of HPS fatigue performance and compare with those of more conventional structural steels. The details of the experimental program, including the test results and associated discussion, are presented in Chapter 4, *Experimental Investigation*. *Results of Analysis* (Chapter 5) presents the finite element analysis and fatigue life prediction results of six common structural details. Finally, *Summary, Conclusions and Recommendations* are proposed in the last chapter (Chapter 6) of this thesis.

3

CHAPTER 2.

LITERATURE REVIEW

2.1. Introduction

A review of four aspects related to fatigue of high performance steel is presented in this chapter. First, current fatigue design specifications and detail categories are briefly reviewed because of the frequent comparisons of test results and fatigue life predictions with existing fatigue design curves throughout the thesis. Following this, the main fatigue life prediction techniques are introduced, including a brief discussion of their development, application, advantages and limitations. Because high performance steel is a relatively new material, its properties and applications as well as available fatigue research are reviewed. Lastly, since high performance steel is essentially a high strength low alloy steel, fatigue of conventional high strength low alloy steel is mentioned.

2.2. Fatigue Design Standard and Detail Categories

2.2.1. Introduction

Widespread application of welding in the fabrication of steel structures since the 1950s triggered research into fatigue problems in civil engineering, as welding produced more severe fatigue details compared to riveted and bolted joints. At the same time, more traffic and heavier loads became prevalent on bridges (Fisher *et al.* 1998). Extensive investigations of the fatigue strength of steel beams under the National Cooperative Highway Research Program set the foundation for all subsequent fatigue research studies and for current design standards (Fisher *et al.* 1970; Fisher *et al.* 1974).

Fatigue tests on many different welded details have shown that the stress range, $\Delta\sigma$, is the most important stress-related parameter that describes the fatigue life of a structure (Fisher *et al.* 1970; Fisher *et al.* 1974). The stress range is defined as $\Delta\sigma = \sigma_{max} - \sigma_{min}$, where σ_{max} and σ_{min} are the maximum and minimum applied stresses, respectively.

4

For welded details, it has been found that other stress parameters such as stress ratio, $R = \sigma_{min} / \sigma_{max}$, and mean stress, $\sigma_m = (\sigma_{min} + \sigma_{max}) / 2$, have a negligible effect on fatigue resistance (Fisher et al. 1998). The dependence of fatigue life solely on stress range is largely a reflection of the presence of high tensile residual stresses, coupled with high stress concentrations, at some locations of welded details (Fisher et al. 1998). Since the residual stresses can be expected to be more moderate in rolled, riveted, and bolted connections than in welded details, the conclusion that the stress ratio does not influence the fatigue life of a non-welded detail is not necessarily correct.

For civil engineering structures, it is generally agreed that the strength and grade of steel have a negligible effect on fatigue resistance. The effect of the strength, hence grade of steel, have therefore been neglected in design standards. However, for non-welded details, the material characteristics, or more precisely the microstructure of steel, can have an influence on fatigue resistance; an increase in fatigue life with an increase in the yield strength of the steel has been observed in case of high cycle fatigue (Stephens et al. 2000).

Fatigue curves have traditionally been plotted as straight lines when stress range $\Delta\sigma$ and fatigue life N are expressed with log scales. The fatigue curve is represented by the equation $\log N = \log A - m \log \Delta\sigma$, where A is the fatigue life constant and m is the slope of the straight line.

2.2.2. Classification of Fatigue Details (Detail Categories)

It is standard practice in fatigue design of civil engineering structures to separate various structural details into categories in accordance to their fatigue resistance and nominal stress range. The classification of fatigue details is mainly based on the severity of the stress concentration in the various structural details. While many of these details have been tested in research programs, some were merely categorized using engineering judgement (Fisher et al. 1998).

5

Each category of weld details has an associated nominal stress range versus fatigue life curve, commonly referred to as a S–N curve. The fatigue curves adopted by the American Association of State Highway and Transportation Officials (AASHTO 1998) for components and details susceptible to load-induced fatigue cracking, which are also used in the Canadian highway bridge design standard CAN/CSA–S6 (CSA 2000), are illustrated in Figure 2-1. S–N curves are presented for eight categories of weld details, A through E', in order of decreasing fatigue strength. Each detail category consists of a straight line with a slope of 3 and a horizontal part, which represents the constant amplitude fatigue limit (CAFL). The slopes have been standardized at 3 because the slope of the regression line fit to the test data for welded details is typically in the range 2.9 to 3.1 (Fisher et al. 1998). The effect of the welds and other stress concentrations are reflected in the ordinate of the S–N curves for the various detail categories. The CAFL occurs at an increasing number of cycles for lower fatigue categories. The AASHTO specification and CSA standard include descriptions and illustrative examples for various fatigue design categories, as well as fatigue life constants, A, and CAFL for each detail category. Klippstein (1987) suggested that there is a need to establish the CAFL more accurately using statistical approaches.

As seen Figure 2-1, the highest allowable fatigue stress ranges are provided by fatigue Category A, which includes details with no stress concentration such as the base metal of plain rolled plates with flame-cut edges (with limitations on surface roughness) and rolled sections. Lower stress ranges are specified for details of increasing notch severity, such as: Category B for built-up members with continuous longitudinal fillet welds, or high-strength bolted connections; Category C' with welded transverse stiffeners; Category D for welded attachments longer than 50 mm or greater than 12 times the attached plate thickness, but less than or equal to 100 mm, or riveted connections. More details about detail categorization are given in the design code (CSA 2000).

2.2.3. Design Curve versus Mean Curve

The fatigue curves presented in North American design standards (Figure 2-1) are based on extensive experimental data and are generally represented by a line set at two standard

6

deviations below the mean regression line. For reasonably large numbers of test data, the corresponding confidence limit is estimated to be approximately 95%, with a 95% survival limit (Fisher *et al.* 1998).

The standard deviation of the results of tests specifically designed for the establishment of fatigue design curves and other comparative data in other relevant fatigue studies available in literature varied from 0.078 to 0.273, with an average of 0.25 (Klippstein 1987).

2.2.4. Fracture Toughness Requirement

Toughness considerations are included in the AASHTO Specification (1998) in the section on "Fatigue and Fracture Considerations". The Charpy V-Notch (CVN) impact requirements vary, depending on the type of steel, type of construction, whether welded or mechanically fastened, and the applicable minimum service temperature (three temperature zones were specified: Zones 1, 2, and 3 with decreasing service temperature). The fracture toughness requirement is necessary to avoid brittle fracture that prevents achievement of adequate fatigue resistance of a structure. Charpy V-Notch tests provide a useful means of screening out materials that would be susceptible to brittle fracture at small crack sizes.

2.3. Fatigue Life Prediction

2.3.1. Introduction

Fatigue design philosophy has evolved from fatigue limit and infinite life criteria to approaches based on finite life behaviour (Ellyin 1997). At present, there are two major numerical approaches to predict the fatigue life that a component or structure can sustain before failure: empirical correlation approach, and fracture mechanics approach (Ellyin 1997; Dowling 1999). The empirical correlation approach uses a damage parameter to correlate with fatigue test results, in which fatigue life calculation is generally performed with respect to final fracture or crack initiation. The application of fracture mechanics approach is widespread, especially for crack propagation life. In this section, general

7

descriptions, development and applications as well as advantages and disadvantages of the two major approaches are reviewed.

2.3.2. Empirical Correlation Approach

In order to predict the fatigue life under a specified condition, different empirical damage parameters, D, have been proposed to correlate with the fatigue life (number of cycles to failure, N_f). The damage parameter to fatigue life function generally takes the form of $D = F(N_f)^\alpha + D_0$, where $\alpha < 0$, $F > 0$ and as $N_f \to \infty, D \to D_0$ (D_0 is the corresponding value at the fatigue limit) (Ellyin 1997). The coefficient F and exponent α are evaluated by a best fit technique from experiment data. The above function is shown schematically in Figure 2-2. The empirical correlation approach is generally divided into three categories, i.e., stress-based method, strain-based method and energy-based method, when stress, strain or energy is used as the damage parameter, respectively.

2.3.2.1. Stress-based method

The stress-based method that underlies many fatigue specifications is the most widely used method. It proceeds from the nominal stresses in the critical cross section and compares them with the nominal stress $S-N$ curve, which comprises the influence of material, geometry and surface condition (Radaj and Sonsino 1998). The stress-based method emphasizes nominal stresses, rather than local stresses and strains, and normally employs elastic stress concentration factors and empirical modifications to account for the concentration effect of notches (Leis et al. 1973). Stress-based methods have been shown in some cases to predict fatigue lives that differ from test values by more than two orders of magnitude (Everett 1992). The stress-based method is most applicable to cases of high cycle fatigue where material response is mostly elastic. However, the accuracy of life prediction depends heavily on an accurate evaluation of the severity of stress concentrations at the fatigue detail.

8

2.3.2.2. Strain-based method

The strain-based method has found wide applications in fatigue analysis, especially for fatigue crack initiation life calculation. Initially developed in the late 1950s and early 1960s for ductile metals at relatively short lives, the method also applies where there is little plasticity at long lives. Now it is a comprehensive method that can be used in place of stress-based methods (Dowling 1999). In contrast to the stress-based method, the strain-based method considers the plastic deformation that may occur in localized regions where fatigue cracks initiate. The strain-based method assumes the material in highly strained areas, such as at a notch root, behaves similarly to material in a smooth specimen under cyclic strain controlled loading with the same strain (Morrow and Socie 1981). Thus, the evaluation of inelastic strain at the critical location is one of the key parts in fatigue life prediction. The method can account directly for the difference in stress concentrations among different fatigue details through an inelastic finite element evaluation of the strain distribution. Dowling (1982) has reported that the estimated life is not very sensitive to the calculated strain, thus making the use of the local strain method a useful tool for the prediction of crack initiation life.

The strain-based method uses a cyclic stress versus strain curve and a strain versus life curve instead of the *S–N* curve used in stress-based method. The coefficients and exponents that define these curves are treated as fatigue properties of the material. At the early developmental stages for the technique, there were insufficient fatigue data to quantify the fatigue properties of many engineering metals and various equations were proposed to correlate the fatigue properties to the tensile properties (Morrow and Socie 1981). The widespread adoption of closed-loop mechanical testing systems and the development of the strain-based method has largely eliminated the need for these empirical equations and there is an abundance of data defining the fatigue properties of numerous engineering metals (Rice *et al.* 1988).

For engineering materials at room temperature, cyclic hardening or softening is usually rapid at first and then approaches a stable condition. The stable cyclic stress versus strain curve is often defined using the Ramberg-Osgood equation (Dowling 1999). The curve

9

can be determined from several companion specimens cycled at various constant strain amplitudes or from a single specimen in conformity with the incremental step test method (Morrow and Socie 1981). The companion test approach is preferred because in certain steels the two methods may not lead to the same result because of the interaction between the different levels of strain amplitude (Hatanaka 1990). In the strain versus life curve, a linear log-log relation between elastic or plastic strain amplitude and fatigue life according to the Coffin-Manson equation is used (Dowling 1999). It should be noted that at long lives, the strain versus life curves tend to be very flat and may even be horizontal for steels exhibiting a fatigue limit. Life predictions made in this region can be expected to be only estimations within factor of ten or more (Morrow and Socie 1981). However, in fatigue testing, the scatter in fatigue life also increases with increasing life.

2.3.2.3. Energy-based method

Experimental observations have confirmed the significant role that plastic deformation plays in the fatigue damage process. As cyclic plastic deformation is related to slip along crystallographic planes and dislocation movement, cyclic stress is related to the resistance to such movement at the microscopic level and strain energy is dissipated during such irreversible deformations (Ellyin 1997). The energy-based method uses energy as a damage parameter to characterize fatigue, emphasizing the interrelation between stress, strain, and the fatigue damage process. It unifies high and low cycle fatigue, and has the potential to bridge fatigue data obtained in different laboratories using specimens of different geometry and size and tested under different controls (Chan and Miller 1982; Sarihan 1994). As a relatively new method (mainly developed in the last two decades), it has not been widely used but the method seems promising.

Commonly, the total absorbed energy to the point of fatigue failure is assumed to depend on the total number of cycles sustained and the fatigue damage during each cycle is assumed to relate directly to the area under the hysteresis loops of the stress versus strain curve obtained during cyclic loading (Ellyin 1997). Various measures of energy have been proposed depending on the stress level, namely, the plastic strain energy density per cycle (ΔW^p), the total strain energy density per cycle (ΔW), and the plastic plus tensile

10

elastic strain energy density per cycle ($\Delta W'$). The $\Delta W''$ criterion is more appropriate when the plastic strains are large, and ΔW is believed to be more suitable for small strain magnitude because during high cycle fatigue the plastic strain energy is very small and is difficult to measure accurately. The plastic plus elastic tensile strain energy density per cycle, $\Delta W'$, was proposed to predict the mean stress effect (Kujawski and Ellyin 1995) and is believed to be more suitable for deformation controlled situations.

2.3.3. Fracture Mechanics Approach

For many engineering structures, the major portion of fatigue life is expended in propagating a crack from an existing flaw, that is, only the fatigue crack propagation life needs to be determined (Jaske 1995). The use of fracture mechanics in fatigue propagation life prediction has become widespread since it was first applied to fatigue crack growth 40 years ago (Paris 1998).

The parameter describing the stress field around the advancing crack tip is an important component in the fracture mechanics approach. The stress intensity factor, K, is used in linear-elastic fracture mechanics (LEFM) when the nominal stress versus strain response is essentially elastic. When plasticity effects are considered, various parameters have been proposed, among which $CTOD$ (crack tip opening displacement) and J-integral are most commonly used in elastic-plastic fracture mechanics (EPFM). In highly ductile materials and where the crack tip plastic zone is large, EPFM may be more appropriate. However, for small-scale plasticity conditions, the K approach, corrected for the effect of the small plastic zone effect, offers the greatest advantages regarding the correlation of crack growth data (Nowack 1983).

Crack propagation life calculations are carried out from a specific initial crack size to a final crack size at failure, which may be determined from the material fracture toughness. However, a number of parameters are difficult to determine in practice, especially the initial crack size and shape. Brock (1989) suggested that initial weld defects such as porosity, undercut, lack of fusion, and lack of penetration can be identified, and the initial size can be determined on the basis of weld quality control criteria. To determine

11

fracture toughness, plane strain conditions are generally required in standard tests. However, most steels have insufficient thickness to maintain plane strain conditions under normal loading and service temperatures (Nowack 1983). Non-standard specimens can provide valuable information if parameters like the geometry factor for the specimen is known (Broek 1989).

2.4. High Performance Steel

2.4.1. Introduction

2.4.1.1. Material properties

Primarily due to the AISI/FHWA/USN (American Iron and Steel Institute/Federal Highway Administration/U.S. Navy) joint program starting in 1994, high performance steels (HPS) with unique properties, intended principally for highway bridge applications, have been successfully developed. Because of advanced chemical composition and processing practice, HPS possess improved weldability, toughness and corrosion resistance, as well as comparable strength and ductility (Krouse 1999). Grade HPS 485W, the first one developed and commercialized in the HPS program, was first fully integrated into the ASTM A709 standard in 1997 and the AASHTO specification in 1999. The latest specifications also include grade HPS 345W. Grade HPS 690W is expected to be included in the near future (Wilson 2004).

The low carbon content (0.11% max) and carbon equivalent (CE) place HPS in Zone I of the Graville weldability diagram shown in Figure 2-3, making it unsusceptible to heat affected zone (HAZ) hydrogen induced cracking, and thus having improved weldability. Only minimal precautions are necessary when welding steels with such low carbon content (Wilson 2004).

A 0.006% maximum sulphur level with calcium treatment for inclusion shape control is specified to provide HPS with improved toughness, as characterized by a targeted Charpy V-Notch energy absorption of 48 J at −23°C (ASTM 2002a). Wright *et al.* (1995) tested over 80 compact tension specimens of HPS 485W and demonstrated that HPS has much

12

higher toughness than the more conventional structural grade steel ASTM A572, and the material remains ductile at testing temperatures as low as −40°C. The toughness enhancement of HPS typically observed is far in excess of that required by design standards (Wright *et al.* 2001).

High performance steel also has weathering properties, i.e., it has the ability to perform under normal atmospheric conditions without corrosion protective coatings. An atmospheric corrosion resistance index can be used to indicate the resistance of a steel to long-term corrosion exposure; the higher the index, the more corrosion resistant the steel. The index can be calculated from the chemistry of the steel as follows (ASTM 2002b):

$$\text{Index} = 26.01\ (\%Cu) + 3.88\ (\%Ni) + 1.20\ (\%Cr) + 1.49\ (\%Si) + 17.28\ (\%P) -$$
$$7.29\ (\%Cu)(\%Ni) - 9.10\ (\%Ni)(\%P) - 33.39\ (\%Cu)^2 \tag{2-1}$$

HPS has a minimum weathering index of 6.0, which is the same as conventional weathering steels.

A tighter range of chemistry for HPS is specified so that the performance can be more reproducible from plate to plate and producing mill to producing mill. HPS 485W is produced by quenching and tempering (Q&T) or Thermo-Mechanical-Controlled Processing (TMCP). Because the Q&T process limits plate lengths to 15.2 m in North America, TMCP practices have been developed on the identical HPS 485W chemistry to produce plates up to 38 m long and 50 mm thick (Wilson 2000). The differences between Q&T and TMCP processing are shown schematically in Figure 2-4. TMCP includes controlled rolling below the austenite recrystallization temperature, and with or without accelerated cooling of water spray. HPS 345W, an HPS version of the more common 345W grade with improved weldability and toughness, is provided from the exact chemistry of HPS 485W but processed using conventional hot rolling or controlled rolling (Figure 2-4). Other requirements imposed on the manufacture of HPS are that they are made of killed steel, have low nitrogen level (0.015% max), have a fine grain structure, and are made using a low hydrogen practice (ASTM 2002a).

13

2.4.1.2. Applications

Since plates from the first mill heat of HPS 485W were produced in 1996 and HPS was first used in bridges in 1997, there has been steady growth in the use of HPS in bridges. It is estimated that there are more than 200 HPS bridges in various stages of design and construction (among which more than 100 were open to traffic in 2003) in the United States (Wilson 2004). Because of its greater strength, the use of HPS 485W generally leads to 5-10% project cost savings, while the best result to date is a 28% reduction in weight and 18% reduction in cost (Wilson 2004). Although some initial plate girder bridges were made entirely of HPS 485W, hybrid designs with HPS 485W in highly stressed flange locations and 345W in webs and other flange locations have become popular.

2.4.2. Research on HPS Components

Homma and Sause (1995) studied the potential cost reduction resulting from the use of HPS in bridge design. The reduction in weight of steel was used as a measure of potential cost reduction. The cross sections of two existing I-girder bridges, one simple-span and one continuous-span, both originally designed with 345 MPa yield strength steel, were redesigned using HPS with yield strengths of 485 MPa, 585 MPa, and 690 MPa. When the fatigue limit state was excluded from the redesign, weight reduction was often not observed at yield strengths greater than 485 MPa. This is because the AASHTO design specification of that time did not permit the criteria for compact sections to be used for steels with these higher yield strengths, a restriction which was based on the lower ductility capacity of conventional high strength steels. It should be noted that only the high strength of HPS was considered in the study; the potential gains from improved weldability, fracture toughness and other properties were not considered.

So far, the focus of many of the experimental and numerical studies on HPS has addressed limitations of design standards that prevent the full utilization of HPS in bridge designs, and primarily on HPS 485W steel (Azizinamini *et al.* 2004). Some of the most significant studies conducted to date include:

14

1. Flexural capacity and ductility of compact and non-compact I-shaped HPS plate girders in the negative moment region (Yakel et al. 1999; Barth et al. 2000; Sause and Fahnestock 2001) – The studies show that non-compact plate girders are able to develop a moment capacity in excess of their yield moment capacity and, in many situations, the plastic moment capacity. Compact plate girders are able to develop their plastic moment capacity but are not able to provide the required inelastic rotational ductility of 3. In order to achieve adequate ductility for compact sections, more stringent flange and web compactness and bracing criteria are proposed for HPS 485W I-shaped beams (Thomas and Earls 2003). The proposed changes include a maximum flange slenderness ratio of 5.5, a web slenderness ratio limit of 54, and an unbraced length limit equal to depth of the cross section.

2. Ductility of HPS 485W plates in tension (Dexter et al. 2002) – The ability of HPS plates, which have a relatively high yield to tensile strength ratio, to develop large tensile strains without fracture was investigated. Experimental and analytical research was conducted to determine the ductility performance of tension members and the tension flange of flexural members fabricated with HPS 485W steel. Wide plate tension members performed well in the experiments and the tensile ductility of HPS 485W was found to be well within the required range for structural steel. Although it is not clear what level of ductility is required, the researchers indicate that an elongation in the range of six to ten times the yield strain would be required. Three point bending tests of ten large scale girders also demonstrated good performance of the tension flange in flexure.

3. Shear capacity of hybrid HPS plate girders (Hash and Azizinamini 2001) – It has been shown that the best use of HPS in plate girders is in the hybrid form where flanges are made of 485 MPa steel and the web of 345 MPa steel (Horton et al. 2003), resulting in the most economical design. Results from extensive testing and refined finite element modeling suggest that tension field action contributes significantly to the shear capacity of non-compact hybrid sections. Interaction between shear and moment was found to be negligible.

15

4. Innovative HPS highway bridge girder concepts (Kulicki 2000) – Various options that include I-shaped girders with composite webs, corrugated webs, and tubular flanges have been investigated to take full advantage of HPS. Some of the advantages of these systems include the elimination of transverse and longitudinal stiffeners that are unfavourable for fatigue, a higher allowable web slenderness, and enhanced stability of compression flange.

5. Use of HPS in seismic applications (Dusicka *et al.* 2003) – Fully reversed low cycle fatigue tests at strain amplitudes between 1% to 7% and large scale shear link experiments were conducted. HPS 485W showed low cycle fatigue life and deformation capacity similar to conventional grade 345 steel. The HPS 485W shear link components demonstrated a similar ductile hysteretic response to those fabricated from grade 345 steel.

6. Live load deflection criteria for HPS bridges (Barth *et al.* 2003) – Because of the high strength of HPS, the L/800 live load deflection criterion was found to be the controlling limit state for some design situations, particularly in cases with high span-to-depth ratios. An average of approximately 20% more steel may be required to meet the deflection limit. The rationale behind the current limit was investigated and it was found that there is no relationship between either reported bridge damage or objectionable vibration characteristics and a direct check of live load deflections.

7. Strength and ductility of undermatched weldments (Kaufmann and Pense 2000) – Undermatched welding was investigated because the use of undermatched consumables can reduce the potential for hydrogen cracking and conventional consumables for Grade 345W are readily available. Test specimens consisting of HPS 485W steel plates and conventional weld metals for Grade 345W steel were fabricated with a full penetration groove weld at the centre of the specimens. Three wide plate tension test results showed that the overall yield and tensile strength consistent with the base metal were reached if the undermatching of the weld metal strength to the plate was no more than 18%. All undermatched weldments indicated

16

reduced but sufficient ductility with strains at fracture of 5 to 7%, which are well above the typical strain for bridge members under the most severe service conditions.

8. Fatigue and fracture resistance of HPS members considering the superior toughness of the material – Relevant research studies are discussed in detail in the following section.

2.4.3. Fatigue and Fracture Performance of HPS Components

2.4.3.1. Homma and Sause (1995)

Homma and Sause (1995) found that the fatigue limit state can control the design of HPS members. Weight reduction with increasing yield strength is not possible beyond a yield strength of 485 MPa when fatigue Category C' details (transverse stiffeners and diaphragm connection plates attached to the web and flange plates of I-section girders) are taken into account. The researchers thus suggested developing new fatigue resistant connection details to avoid these Category C' details. This conclusion is based on the assumption that the fatigue performance of details made of HPS is the same as that of those made with conventional steel. Fatigue therefore represents one of the barriers to effective use of HPS.

2.4.3.2. Takamori and Fisher (2000)

Three geometrically identical large scale HPS 485W plate girders with coverplate and transverse stiffener details were tested by Takamori and Fisher (2000) to evaluate the effect of ultrasonic peening on the fatigue strength of welded joints. Each girder was 6.7 m long and 0.9 m deep. The flanges and web were made of HPS 485W steel, whereas the coverplates and the stiffeners were made of ASTM A588 Grade 50 weathering steel. Ultrasonic peening was applied to the weld toe of transverse stiffeners welded to the web and flanges (Category C') and to the welds at the coverplate ends (Category E'). The girders contained both as-welded details and ultrasonic peening treated details. Altogether, 11 out of the 18 welded details on the specimens were treated

17

by ultrasonic peening, and the remaining seven were left untreated, including four stiffeners and three coverplate details.

The data from the as-welded details are consistent with previous research on similar details made of conventional structural steels. Ultrasonic peening was found to improve the fatigue strength of all welded details: the transverse stiffeners improved to Category B fatigue resistance and the coverplate details achieved Category C. Three ultrasonic peening treated details remained uncracked at the end of the fatigue tests which were terminated because fatigue cracks initiated in fabrication defects at the bottom flange in the constant moment region. Because of this failure mode, three data points at longitudinal web-to-flange welds were obtained, even though the girders were not initially designed to test fatigue Category B details. The AASHTO Category B fatigue resistance curve shows a lower bound to the test data.

2.4.3.3. Kaufmann and Pense (2000)

Four 6.7 m long and 0.9 m deep welded plate girders made of HPS 485W steel were tested to investigate the effect of weld undermatching on fatigue resistance (Kaufmann and Pense 2000). Two test specimens were fabricated with a flange thickness transition detail consisting of a full penetration groove weld performed with an undermatched electrode. The test results were consistent with AASHTO fatigue Category B. Two test data of the web-to-flange fillet welds fabricated with undermatched weld metal also indicated a fatigue resistance similar to Category B. It was thus concluded that there was no decrease in fatigue performance due to undermatching.

2.4.3.4. Wright (2003)

Wright (2003) investigated the fatigue and fracture performance of full size HPS I-girders, emphasizing the effect of high toughness of HPS on fracture resistance of the girders. The girders were tested under cyclic loads to develop fatigue cracks, chilled to a low temperature, and subjected to an overload stress to attempt to initiate fracture. If no failure occurred during the overload cycle, the fatigue cracks were grown larger and the overload test was repeated until eventual failure. The fracture tests were performed at

18

load rates and temperatures that simulated service conditions for AASHTO Zone 2 applications. Linear elastic, elastic-plastic, as well as limit load analyses were performed to determine how best to predict the behaviour of the girders. A total of four test girders were fabricated, two from each of the steel grades studied, HPS 485W and HPS 690W. All girders were about 1.0 m deep and more than 8.8 m long. For each grade of steel, one girder was fabricated with no welded attachments, representing a fatigue Category B, and a saw-cut notch on one of the flange tips was used to artificially initiate a fatigue crack at a small number of loading cycles. The other girder contained transverse stiffener attachments on the web, which represents a fatigue Category C', common in highway bridges. Each girder was doubly symmetric in an attempt to perform fracture tests on both flanges by turning the girder upside down. However, the replicate tests on Category C' detail girders were not successful because of difficulties encountered in repair.

The fatigue crack initiation lives for two test girders with Category C' stiffeners fall within the expected statistical scatter of data based on the literature. However, Wright (2003) asserts that it is not statistically conclusive because there are only two data points. One flange edge crack initiated unexpectedly from the flame-cut edge of the HPS 485W girder containing stiffeners, and the data point fell just below the fatigue Category B curve. The large scale I-girder fracture test results indicated that HPS is immune to brittle fracture down to a temperature of -34°C.

HPS 485W steel was found to be capable of reaching the yield limit state on the net section in bending, while the tested HPS 690W steel was not able to reach yield. Wright (2003) suggested that the overall impact of using high toughness steels in I-girders is to increase the crack tolerance, thus greatly increasing the probability of detecting fatigue cracks through visual inspection.

2.4.3.5. Summary

Although the enhanced toughness of HPS is utilized to simplify welding and eliminate special toughness requirements for fracture critical members (Mertz 1999), little work has

19

been done to investigate the fatigue resistance of HPS itself. As fatigue design requirements have been observed to limit the full utilization of the increased strength of HPS, an investigation is required to ascertain whether or not the toughness enhancement can be utilized to liberalize the fatigue provisions (Mertz 1999).

All four studies on fatigue of HPS components available in literature were conducted at Lehigh University and FHWA. The majority of them were experimental investigations on large-scale plate girders with welded attachments (four point bending and a stress ratio of about 0.1). Based on this research, Fisher and Wright (2001) concluded that the fatigue performance of HPS welded details is the same as for conventional steel welded details and, therefore, the existing AASHTO fatigue guidelines also apply to HPS bridge structures. They further suggested that fatigue susceptible welded details must be avoided through innovative cross-section designs or by weld improvement treatments.

2.5. Fatigue of High Strength Low Alloy (HSLA) Steel

HPS is indeed a high strength low alloy steel. Fatigue research on conventional HSLA steels that are widely used in ships and offshore structures is relatively abundant (Boyer 1986), especially for the highly tough HSLA-80 steel. With very high toughness, the critical crack size may be increased considerably. However, it was found that fatigue properties do not significantly improve with increasing toughness (Thomas 1996).

Fatigue testing has been conducted on over 100 large scale HSLA-80 steel I-shaped beams, featuring details of longitudinal web-to-flange fillet welds and transverse groove welds (Dexter et al. 1993), and on 78 large scale HSLA-80 I-shaped beams with various types of one-sided and two-sided longitudinal welded joints for the web-to-flange connections (Dexter et al. 1995). The lower confidence limits for the S-N curves of the HSLA-80 weld details were not significantly different from those of similar weld details fabricated from plain carbon–manganese steel. The researchers concluded that fatigue strength of this steel is no better than that of ordinary structural steel, in spite of the fact that the sections showed ductile crack extension and no brittle fracture (Dexter et al. 1995).

20

2.6. Summary

From the literature review, it can be concluded that the most appropriate manner to predict the fatigue life of a structural fatigue detail is to combine an empirical correlation approach together with a fracture mechanics approach, the former for crack initiation life and the latter for crack propagation life. Both the strain-based and energy-based methods seem promising for the former because the damage parameter can be physically related with the fatigue damage process. However, the necessary fatigue properties of HPS for these methods need to be obtained, ideally from companion specimens. Because of the small stresses generally present in fatigue problems, the plastic zone at the tip of cracks is limited and LEFM is therefore a useful tool for fatigue crack propagation life prediction.

A number of experimental investigations on large scale plate girders made of HPS and conventional HSLA steels with welded attachments indicate that, in spite of their high strength and fracture toughness, the fatigue resistance of welded details in these steels was not significantly different from that of similar details in conventional steels.

21
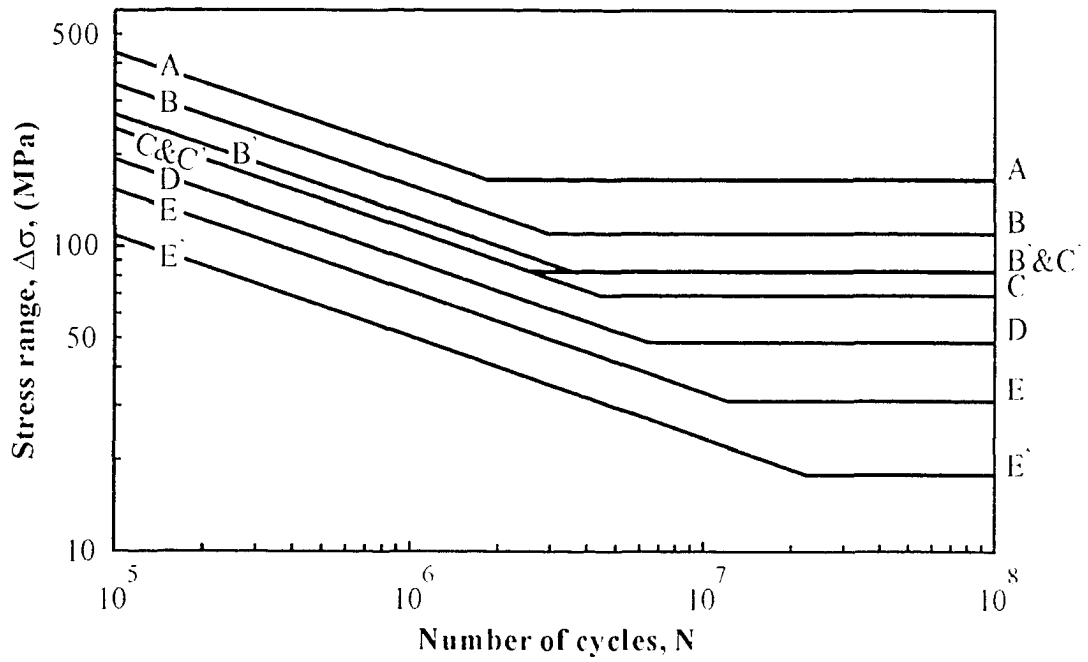
Figure 2-1 *S–N* Curves according to AASHTO (1998)
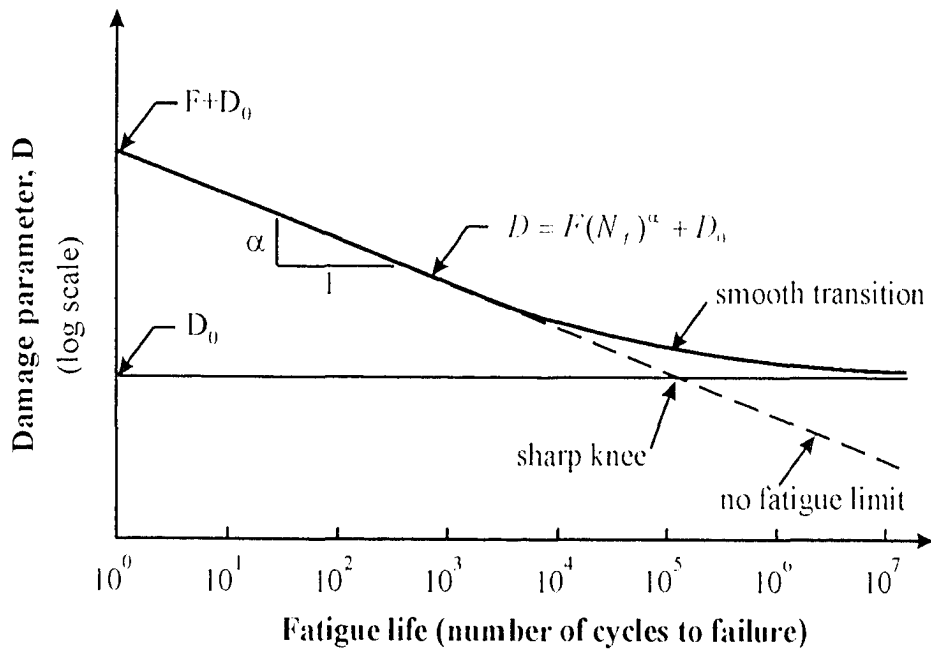
Figure 2-2 Schematic Plot of Damage Parameter versus Fatigue Life Curve (Ellyin 1997)

22
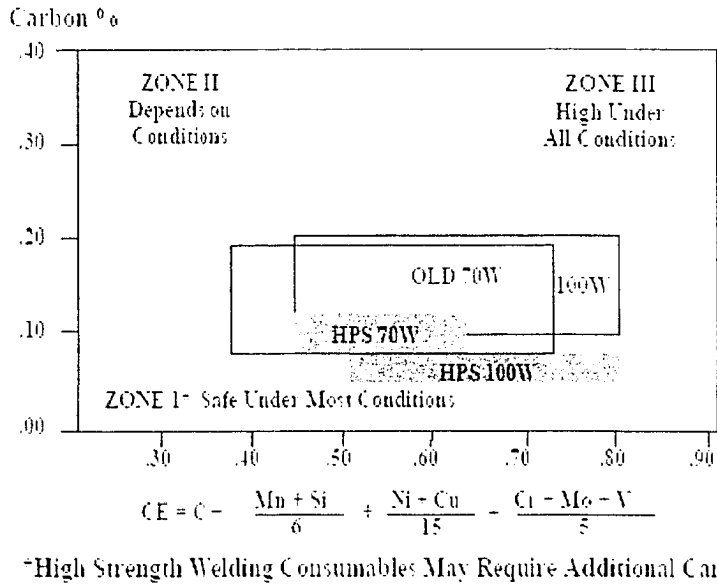
Figure 2-3 Susceptibility of HPS to HAZ Cracking — Graville Weldability Diagram

(Wilson 2004)
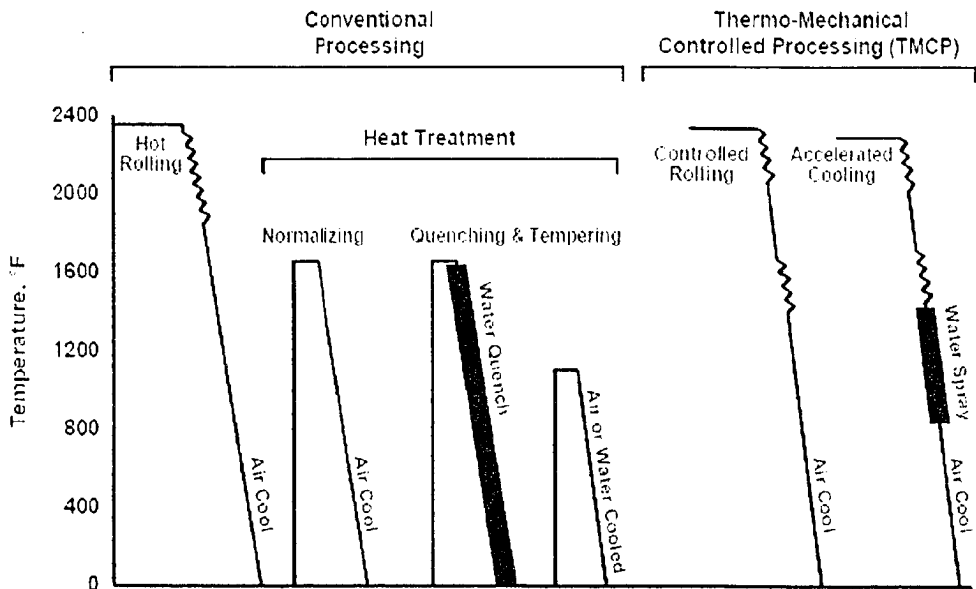
Figure 2-4 Processes for Producing Steel Plates (Wilson 2000)

23

CHAPTER 3.
FATIGUE LIFE PREDICTION

3.1. Introduction

Because of the high cost of large scale fatigue testing, reliable analytical techniques to predict both the crack initiation and the crack propagation stages of fatigue life are desirable to investigate the fatigue resistance of high performance steel details. The fatigue life prediction approaches investigated in this research include stress-based, strain-based, and energy-based methods for fatigue crack initiation and the early stage of crack propagation, and linear elastic fracture mechanics for the crack propagation stage. As some of these methods have not been used in conventional civil engineering applications, a general review of these analytical techniques is first presented.

3.2. Description of the Analysis Methods

3.2.1. General Procedure

The general fatigue process comprises microstructural phenomena, including moving dislocations, microcrack initiation on slip bands and further crack growth by local slip mechanisms at the crack tip (Ellyin 1997). For engineering applications, the process can be described approximately by the initiation and propagation of a crack, as shown in Figure 3-1. Thus, the crack initiation phase actually includes the physical crack initiation and part of the stable physical crack propagation phases. The number of cycles required to initiate and to propagate a crack to a certain length, e.g., of the order of one millimetre, is taken to represent the fatigue life of a smooth specimen (N_f), and is referred to as the crack initiation life (N_i) in the case of large components.

The fatigue material properties coupled with an inelastic finite element analysis can be used to predict the fatigue life of details under various load conditions. This procedure requires the cyclic stress versus strain curve obtained from stabilized hysteresis loops so that the finite element analysis results of monotonic loading represent the stabilized

24

condition after material cyclic hardening or softening. The stresses and strains calculated at the critical location (the "hot spot") using an inelastic finite element model are used with the material strain–life, stress–life, or energy–life curves to calculate the crack initiation and early crack propagation stages of the fatigue life. The fatigue crack propagation life can be calculated from a linear elastic fracture mechanics approach, applied from an initial crack length to the critical crack size. The general fatigue life prediction procedure is illustrated in Figure 3-2.

The above procedure can be used to derive mean S–N curves for various fatigue details. As is commonly done, a suitable design curve could then be obtained by subtracting two standard deviations on the stress axis from the mean predicted fatigue life curve to account for variability. The standard deviation observed from previous fatigue tests on similar details can be used for this purpose.

The finite element program ABAQUS, Version 6.3 (2003), is used in this work to quantify the critical stresses, strains, and/or energies needed for the fatigue life calculations. A metal plasticity model with isotropic hardening was specified by giving stress and plastic strain pairs in accordance to the mean material cyclic stress versus strain curve. Static nonlinear analysis can then be carried out with general analysis steps for various loading cases. For each loading case, the stress, strain, and/or energy response according to maximum load and load amplitude can be obtained directly from finite element analysis. The response of a material cycled between ε_{min} and ε_{max} is illustrated in Figure 3-3, where ABA represents the stable hysteresis loop response for subsequent cycles. If the unloading and loading branches of the hysteresis loop are assumed to be geometrically similar, it follows that both the maximum stress response and the stress amplitude response can be obtained from the cyclic stress versus strain curve.

25

3.2.2. Fatigue Crack Initiation Life

3.2.2.1. Uniaxial fatigue under fully-reversed condition

Stress-based method

Stress has been used for a long time as a damage parameter to correlate with the fatigue life. Similar to $S-N$ curves, the relation between stress amplitude $\Delta\sigma/2$ and the number of cycles to failure, N_f, can be approximated by a straight line when the stress amplitude and the fatigue life are both expressed on a log scale, thus resulting in:

$$\Delta\sigma/2 = \sigma_f^{'} (N_f)^b \tag{3-1}$$

where $\sigma_f^{'}$ is the fatigue strength coefficient, and b is the fatigue strength exponent. Both parameters can be obtained experimentally.

Strain-based method

From Equation (3-1), the elastic component of strain amplitude, $\Delta\varepsilon^e/2$, can be obtained as follows:

$$\Delta\varepsilon^e/2 = \frac{\sigma_f^{'}}{E}(N_f)^b \tag{3-2}$$

where E is the modulus of elasticity. The plastic strain amplitude $\Delta\varepsilon^p/2$ versus fatigue life can also be linearized on a logarithmic scale for low cycle fatigue. The relationship between the plastic strain amplitude and fatigue crack initiation life can be expressed in the following form:

$$\Delta\varepsilon^p/2 = \varepsilon_f^{'}(N_f)^c \tag{3-3}$$

26

where ε_f' is the fatigue ductility coefficient, and c is the fatigue ductility exponent, both determined experimentally.

By adding the elastic and plastic components of strain amplitude, Equations (3-2) and (3-3) respectively, the relationship between the total strain amplitude, $\Delta\varepsilon/2$, and fatigue life can be expressed as:

$$\Delta\varepsilon/2 = \Delta\varepsilon^e/2 + \Delta\varepsilon^p/2 = \frac{\sigma_f'}{E}(N_f)^b + \varepsilon_f'(N_f)^c \tag{3-4}$$

The cyclic stress versus strain curve can be modeled by the Ramberg-Osgood equation as follows:

$$\Delta\varepsilon/2 = \frac{\Delta\sigma/2}{E} + (\frac{\Delta\sigma/2}{K'})^{1/n'} \tag{3-5}$$

where K' is the cyclic strength coefficient and n' is the cyclic strain-hardening exponent.

Energy-based method

Energy approaches are based on the assumption that fatigue damage is directly related to the area under the hysteresis loops created during cyclic loading. The area under the hysteresis loops is related to the plastic deformation taking place during a load cycle, which relates to the 'fatigue damage' sustained during one load cycle.

Three measures of energy are illustrated in Figure 3-4, namely, the plastic strain energy density, ΔW^p, the total strain energy density, ΔW, and the plastic plus tensile elastic strain energy density, ΔW^t. They are related as:

$$\Delta W = \frac{\Delta W^p}{2} + \frac{\Delta\sigma\Delta\varepsilon}{2} \tag{3-6}$$

and

27

$$\Delta W^t = \Delta W^p + \frac{\sigma_{max}^2}{2E}$$ (3-7)

Methods to obtain the plastic strain energy density per cycle, ΔW^p, corresponding to the area under a hysteresis loop with a stabilized stress range of $\Delta \sigma$ and plastic strain range of $\Delta \varepsilon^p$, are presented in Appendix A.

The energy versus crack initiation life curves that relate the various measures of energy as fatigue damage parameter with fatigue life are expressed as:

$$\Delta W^p = F_p(N_i)^{\alpha_p} + \Delta W_0^p$$ (3-8)

$$\Delta W = F(N_i)^{\alpha} + \Delta W_0$$ (3-9)

$$\Delta W^t = F_t(N_i)^{\alpha_t} + \Delta W_0^t$$ (3-10)

The coefficients F_p, F, F_t, the exponents α_p, α, α_t, and the corresponding measures of energy at the fatigue limit ΔW_0^p, ΔW_0, ΔW_0^t are material properties determined experimentally. The plastic strain energy approach, expressed by Equation (3-8), is more appropriate when the plastic strains are large, while the total strain energy approach, expressed by Equation (3-9), is believed to be more suitable for small strain magnitudes. The plastic plus tensile elastic strain energy approach expressed by Equation (3-10) is believed to be more appropriate to predict mean stress effect (Kujawski and Ellyin 1995).

3.2.2.2. Mean stress effect

For many loading cases, the mean stress is not zero. Although the mean stress effect is often neglected in fatigue life calculations for welded details, the high residual stresses in such details tend to obliterate any possible effect of applied mean stress. However, in non-welded details, the effect of mean stress must be accounted for in the fatigue life calculations. Models to account for the effect of mean stress with the stress-based, strain-

28

based and energy-based methods have been proposed. These models are presented in the following.

Stress-based method

Morrow (Dowling 1999) proposed a correction to account for the mean stress effect as follows:

$$\Delta\sigma/2 = (\sigma_f' - \sigma_m)(N_f)^b \tag{3-11}$$

where σ_m is the mean stress and the other variables are the same as for Equation (3-1). The effect of the tensile mean stress is thus equivalent to a reduction of the fatigue strength coefficient. The model assumes that a given combination of stress amplitude $\Delta\sigma/2$ and mean stress σ_m is expected to have the same fatigue life as a fully reversed stress amplitude of $(\Delta\sigma/2)_{-1}$, where $(\Delta\sigma/2)_{-1} = \dfrac{\Delta\sigma/2}{1 - \sigma_m/\sigma_f'}$. The Morrow correction for stress-based method was found to work reasonably well for structural grades of steels (Dowling 1999).

Strain-based method

For the strain-based method, the mean stress effect can be corrected by the Smith, Watson, and Topper (SWT) model. The model appears to give good results for a wide range of materials and is a good choice for general use (Dowling 1999). The SWT model assumes that the fatigue life for any level of mean stress is a function of the product of the maximum stress and the strain amplitude, $\sigma_{max}\Delta\varepsilon/2$. The model can be expressed as:

$$\sigma_{max}\Delta\varepsilon/2 = \frac{(\sigma_f')^2}{E}(N_f)^{2b} + \sigma_f'\varepsilon_f'(N_f)^{b+c} \tag{3-12}$$

where the various parameters are as defined earlier.

29

Energy-based method

The $\Delta W'$ criterion expressed by Equation (3-10) takes the mean stress effect into account without modification, as mean stress is implicit in the $\Delta W'$ calculation. Ellyin (1997) developed a more general expression that explicitly includes the mean stress in the formulation as follows:

$$D = \Delta W^p + f(\frac{\sigma_m}{\Delta\sigma/2})\frac{(\Delta\sigma/2)^2}{2E} = K_t(N_f)^{\alpha_t} + \Delta W_0' \tag{3-13}$$

$$f(\frac{\sigma_m}{\Delta\sigma/2}) = 1 + \eta \times (\frac{\sigma_m}{\Delta\sigma/2}) \tag{3-14}$$

where the coefficient η is a material property varying from 0 to 1 and characterizes the material sensitivity to mean stress. It can be evaluated from a few fatigue tests conducted at different mean stress levels in the high cycle region.

3.2.2.3. Energy-based criterion for multiaxial stress state

Multiaxial stress states are encountered in the majority of structural components. Equivalent-stress, equivalent-strain, and energy-based criteria that relate the multiaxial fatigue life with uniaxial conditions have been proposed (Ellyin 1997). However, it is generally agreed that the equivalent stress and strain are insensitive to hydrostatic pressure (mean stress) and fail to account for the path dependency of the cyclic plastic deformation. The essential interaction between stress and plastic strain is inherently included in the energy-based method. Moreover, the calculated energy for a state of stress and strain is a scalar, independent of coordinate system.

The $\Delta W'$ measure of energy was expanded as a multiaxial fatigue failure criterion under proportional loading by Ellyin (1997):

$$\frac{\Delta W^p}{\rho} + \Delta W^{e+} = K_t(N_f)^{\alpha_t} + \Delta W_0' \tag{3-15}$$

where all the data on the right hand side of the equation are uniaxial material properties, and the multiaxial constraint factor ρ is an indication of the severity of multiaxial stress state and is defined as follows:

$$\rho = (1 + \upsilon)\frac{\varepsilon_3}{\varepsilon_3 - \varepsilon_1} \tag{3-16}$$

where υ is the effective Poisson's ratio and is obtained from (Ellyin 1997):

$$\upsilon = \frac{\upsilon^p(1 - \upsilon^e)(\varepsilon_2 + \varepsilon_3) + (\upsilon^e - \upsilon^p)(\varepsilon_2^e + \varepsilon_3^e)}{(1 - \upsilon^e)(\varepsilon_2 + \varepsilon_3) + (\upsilon^e - \upsilon^p)(\varepsilon_2^e + \varepsilon_3^e)}, \varepsilon_2 \neq -\varepsilon_3 \tag{3-17}$$

In the above equations, ε_1, ε_2, and ε_3 are principal logarithmic (true) strains with $\varepsilon_1 < \varepsilon_2 < \varepsilon_3$. Superscripts e and p refer to the elastic and plastic values, respectively. For structural grade steels, $\upsilon^e = 0.3$ and υ^p can be taken as 0.5.

Both ΔW^p and ΔW^{e+} can be obtained from the results of a finite element analysis. Alternatively, equations are available to calculate the energy directly. For example:

$$\Delta W^{e+} = \frac{1 + \upsilon^e}{3E}(\sigma_{eq}^{max})^2 + \frac{1 - 2\upsilon^e}{6E}(I_1^{max})^2 \tag{3-18}$$

where σ_{eq}^{max} is the von Mises equivalent stress at maximum load and I_1^{max} is the first invariant of the stress tensor at maximum load. ΔW^p can be calculated in the same manner as in Equation (A-7), except using equivalent stresses and strains.

3.2.3. Fatigue Crack Propagation Life

3.2.3.1. Basic procedure

Fatigue crack propagation life can be predicted using linear elastic fracture mechanics (LEFM). Using the well known Paris crack growth model, the crack growth rate da/dN

31

and the stress intensity factor range ΔK follow a straight line relationship on a log-log scale, i.e.,

$$da/dN = C(\Delta K)^m \tag{3-19}$$

where the constant C and exponent m are material properties obtained from experimental data. Integration of Equation (3-19) gives the following expression for the fatigue life:

$$N_p = \int_{a_i}^{a_f} \frac{da}{C(\Delta K)^m} \tag{3-20}$$

where a_i is the initial crack size, and a_f is the final crack size.

The stress intensity factor range ΔK is normally defined as the algebraic difference between the stress intensity factors corresponding to the maximum and the minimum stress, i.e., $K_{max} - K_{min}$. However, ASTM E647 (ASTM 2000c) allows for another operational definition of $\Delta K = K_{max}$ for the cases where load ratio $R < 0$, which essentially means that only the tension portion of the stress cycle is considered in the fatigue life calculation. Caution should therefore be exercised to make sure that a ΔK definition is consistently used in both the fatigue crack propagation life calculation and the material data da/dN versus ΔK.

The determination of the initial crack size, a_i, and the final crack size, a_f, are discussed further in the following two sections. Section 3.2.3.4 to Section 3.2.3.6 present a summary of the stress intensity factor equations available in the literature that best apply to fatigue prediction of common structural details.

3.2.3.2. Initial crack size a_i

The demarcation between crack initiation and propagation stages is not easily defined. The approximate value of initial crack size a_i is normally taken as an engineering size

32

crack that is easily visible with the naked eye, approximately 1~5mm. The rationale is that if the initial crack size is chosen to be too small, small crack effects may need to be considered and LEFM may not apply (Ellyin 1997). However, a non-arbitrary definition of the initial crack size as the boundary between the initiation and propagation phases is desirable.

The results of fatigue testing up to a defined crack initiation are considered for this purpose. However, the crack size a itself cannot be treated directly as such a criterion, as a 1 mm crack in a smooth fatigue coupon does not necessarily behave the same way as a 1 mm crack in a structural component, such as a large girder, for example. Moreover, it was noticed from the test program presented in Chapter 4 that a fatigue crack is normally unstable at the end of a smooth specimen fatigue test, which is defined as a 50% drop of tensile load capacity.

From an engineering point of view, the start of the crack propagation phase should be when the crack growth becomes stable. Stable crack propagation can be considered to start at a point of an initial stress intensity factor range ΔK_i (shown in Figure 3-2) above which LEFM applies. This corresponds to the range where the logarithm of crack growth rate da/dN shows straight-line relation with the logarithm of the stress intensity factor range ΔK. From this ΔK_i, the corresponding initial crack size a_i in fatigue details can be calculated, which should vary in size depending on geometry and loading condition of the detail. The British standard BS 7910 (BSI 1999) recommends a more precise two-stage law for fatigue crack growth rate properties, shown in Figure 3-5, along with the simplified law. The transition of the mean fatigue properties between Stage A and Stage B occurs at ΔK of 196 $MPa\sqrt{mm}$ (6.2 $MPa\sqrt{m}$) for steels in air with load ratios $R \geq 0.5$. Lindstrom et al. (2000) studied fatigue crack growth threshold in structural materials in air. For the four types of steel investigated, which included a low alloy steel, it was demonstrated that the log da/dN versus log ΔK curves became linear at about ΔK of 6 $MPa\sqrt{m}$. It is therefore believed that ΔK_i of 6.2 $MPa\sqrt{m}$ can be used to determine the initial crack size a_i.

33

3.2.3.3. Final crack size a_f

The final crack size a_f is determined from the following two modes of failure: fracture, or yielding due to overload on the remaining net section. When information on the plane strain fracture toughness K_{IC}, or the critical fracture toughness K_C that is most applicable to the actual application of the structural components is not available, empirical equations can be used to estimate K_{IC}. The fracture toughness, K_{IC}, used for the critical crack size calculation, for example, can be conservatively estimated from the following empirical correlation (Barsom and Rolfe 1999):

$$\frac{K_{IC}^2}{E} = 6.4 \times 10^{-4} (CVN) \tag{3-21}$$

where CVN is the standard Charpy V-Notch energy at the transition temperature in Joules, for E in MPa and K_{IC} in $MPa\sqrt{m}$.

3.2.3.4. General expression of stress intensity factor

A general expression for the stress intensity factor, K, can be defined as follows (Anderson 1995):

$$K = \beta_E \beta_S \beta_W \beta_G \sigma \sqrt{\pi a} \tag{3-22}$$

where σ is the reference stress and a is the crack size. The expression is applicable to the analysis of all test specimens presented in Chapter 5, except the large scale plate girders tested by Wright, because more suitable expressions for the girders are available as presented in Section 3.2.3.5 and 3.2.3.6.

The crack front shape correction factor, β_E, at the minor semi-axis tip of a part-through elliptical crack is:

34

$$\beta_E \approx \frac{1}{\frac{3\pi}{8} + \frac{\pi}{8}(a/c)^2} \qquad (3\text{-}23)$$

where a/c is the aspect ratio of the elliptical crack. The crack front shape correction crack β_E for a straight through thickness crack is 1.0.

The free surface correction factor, β_S, for an edge crack can be taken as a constant of 1.12 (Anderson 1995).

The finite width correction factor, β_W, is calculated using one of the following two equations:

$$\beta_W = \sqrt{\sec\frac{\pi a}{W}} \qquad (3\text{-}24a)$$

$$\beta_W = \sqrt{\frac{W}{\pi a}\tan\frac{\pi a}{W}} \qquad (3\text{-}24b)$$

where W is the plate dimension in the direction of crack size. Equation (3-24a) is used for a straight through thickness crack, while Equation (3-24b) is used for a three-dimensional crack as the net ligament around a part-through crack is believed to provide more crack opening restraint (Albrecht and Yamada 1977).

By integration of Green's functions (Anderson 1995), the stress gradient correction factor, β_G, is obtained as:

$$\beta_G = A_0 + \frac{2A_1}{\pi}a + \frac{A_2}{2}a^2 + \frac{4A_3}{3\pi}a^3 + \frac{3A_4}{8}a^4 \qquad (3\text{-}25)$$

where the A coefficients are the constants in a fourth order polynomial fitted through the normalized stress distribution in the uncracked structure at the location of the fatigue crack. In a three-dimensional crack problem in some structural components, the stress distribution is symmetric about the centreline of plate thickness and normally only half of

35

the plate thickness is modelled. By simple mathematical manipulation, β_G is found to be a symmetric function about the centreline of plate thickness as well. Thus, Equation (3-25) can be used to calculate β_G for a crack size $a \le t/2$, where t is the plate thickness. For a crack size $a \ge t/2$, $\beta_G(a) = \beta_G(t-a)$, where $\beta_G(t-a)$ can be obtained from Equation (3-25) directly.

3.2.3.5. Thumbnail web crack

Newman and Raju (1984) developed a general solution for a semi-elliptical surface crack in a finite thickness plate subjected to a uniform stress as shown in Figure 3-6. The expression is applicable to analysis of a thumbnail web crack at the transverse stiffener details of plate girders, as presented in Chapter 5. The parameter t in Figure 3-6 is the web plate thickness, and W is the distance in the web depth direction between the crack centre and the top surface of the bottom flange. The proposed stress intensity factor takes the following form:

$$K = \sigma \sqrt{\frac{\pi a}{Q}}(F)$$

(3-26a)

where,

$$Q = 1 + 1.464(a/c)^{1.65}$$

(3-26b)

$$F = [M_1 + M_2(a/t)^2 + M_3(a/t)^4] f_\phi f_w g$$

(3-26c)

$$M_1 = 1.13 - 0.09(a/c)$$

(3-26d)

$$M_2 = -0.54 + \frac{0.89}{0.2 + (a/c)}$$

(3-26e)

$$M_3 = 0.5 - \frac{1.0}{0.65 + (a/c)} + 14[1.0 - (a/c)]^{24}$$

(3-26f)

36

$$f_\phi = [(a/c)^2 \cos^2\phi + \sin^2\phi]^{0.25} \tag{3-26g}$$

$$f_w = \sqrt{\sec[(\frac{\pi c}{W}) \cdot \sqrt{a/t}]} \tag{3-26h}$$

$$g = 1 + [0.1 + 0.35(a/t)^2](1 - \sin\phi)^2 \tag{3-26i}$$

3.2.3.6. Two-tip through thickness web crack in I-girders

In the analysis presented in Chapter 5 of a two-tip through thickness web crack at the transverse stiffener detail of plate girders, the solution of such a crack in an I-girder proposed by Feng (1996) is used. The crack and girder geometry and terminology are presented in Figure 3-7. The solution was developed by fitting an equation to the results of a finite element parametric study that calculated the stress intensity factor K for a practical range of I-girder geometry. The solution accounts for the geometric constraint added by the tension flange to the web crack. The U and L subscripts correspond to the upper and lower crack tips, respectively:

$$K_{(U,L)} = f_{(U,L)}\sigma\sqrt{\pi a_w} \tag{3-27a}$$

$$
\begin{aligned}
f_{(U,L)} = {} & a_0 + a_1\varepsilon + a_2\beta\varepsilon + a_3\varepsilon^2 + a_4\lambda_w + a_5\beta\lambda_w + a_6\varepsilon\lambda_w + a_7\lambda_w^2 + a_8\beta\varepsilon\lambda_w + \\
& a_9\beta^2\varepsilon + a_{10}\beta\varepsilon^2 + a_{11}\lambda_w\beta^2 + a_{12}\lambda_w\varepsilon^2 + a_{13}\beta\lambda_w^2 + a_{14}\varepsilon\lambda_w^2
\end{aligned} \tag{3-27b}
$$

$$\varepsilon = \frac{e}{(d - t_f)/2} \tag{3-27c}$$

$$\lambda_w = \frac{a_w}{(d - t_f)/2 - e} \tag{3-27d}$$

$$\beta = \frac{2b_f t_f}{d_w t_w} \tag{3-27e}$$

The coefficients a_0 to a_{14} are listed in Table 3-1 for the upper and lower crack tips.

37

3.2.4. Evaluation of Prediction Methods

Fatigue life prediction models can only be used effectively if the prediction results are verified by experimental data. For assessing fatigue life prediction methods, the scatter of the "actual life/predicted life" ratio obtained from a large number of predictions can be a good criterion. Heuler and Schuetz (1986) claimed that a fatigue life prediction method should be considered adequate if the ratios for all predictions lie within the range of 0.5 to 2.0. Alternatively, if 90% of the prediction ratios fall into a range of 1.0 to 2.0, the method is considered suitable and conservative. However, the above criteria are overly strict and are almost impossible to meet for test results with large variations. For example, for specimens tested under the same stress conditions in the high cycle fatigue region, the difference between the longest and the shortest fatigue life might be one order of magnitude. It is therefore felt that the mean regression line and the scatter band of the test results could be used as a more realistic criterion to evaluate the fatigue life prediction methods. As long as the predicted fatigue life falls within a 95% confidence interval, the prediction model is considered accurate.

3.2.5. Design Curve

The predicted fatigue life versus nominal stress range should be treated as a mean fatigue life curve because they are obtained using nominal load, nominal geometry, average material properties and average crack information. For design purposes, a larger probability of survival is required. By assigning this mean curve as the 50% confidence limit, other curves with any specified constant confidence limits could be obtained, for example, those corresponding to upper and lower 95% confidence limits.

For design purposes, a fatigue curve is usually obtained from test results at two standard deviations on the stress axis below the mean curve. The design curve obtained this way represents approximately a 95 % probability of survival for a large number of test results (Klippstein 1987). The standard deviation s can be calculated as

$$s = \sqrt{\frac{\sum (\log N_i - \log N_{ci})^2}{n-2}}$$, where N_i and N_{ci} are the ith tested fatigue life and the ith

38

estimate from the regression line, respectively. The constant n is the number of data points used for the regression analysis.

The variation observed in fatigue test results is not observed when the fatigue life is calculated using the analytical procedures outlined above. It is therefore not possible to obtain a representative standard deviation s for the analytically predicted curve. In fact, the standard deviation in predicted fatigue life is strictly governed by the variations in the smooth specimen fatigue test results, the crack growth rate test results, the sizes and shape of fatigue cracks. There are also other parameters not included in the material tests, such as residual stresses and size effects (if similar details are found in components of different sizes), that create variability in the fatigue resistance of structural details. Since detailed information about the variability of these parameters is not always available, a standard deviation observed from previous fatigue tests can be used as a reasonable value for this purpose. In the absence of a standard deviation for a particular set of test results, s of 0.25, expressed in log of load cycles, can be used to derive a design curve, as this value was observed from fatigue tests on a large number of details and has been recommended for all the fatigue curves in design standards (Klippstein 1987).

3.3. Considerations for Welded Details

3.3.1. Potential Problems with Welded Details

Since the 1950s, welding has become a common method of joining steel elements in fabrication and welded details have been the most common locations for fatigue cracking. However, fatigue prediction of welded details is still considered particularly complicated because of the following uncertainties (Radaj and Sonsino 1998):

1. Welding defects and imperfections: No weld is completely perfect. The welding defects could include cracks, porosity, slag inclusions, incomplete fusion or penetration, and imperfect shape etc. The shape, location, size, and distribution of

39

imperfections are all random variables that are also affected by welding methods and workmanship.

2. Inhomogeneous materials – Variations in material properties do exist in regions of varying microstructure such as the weld metal, heat affected zone (HAZ), and the base metal.

3. Welding residual stresses – Due to the nature of the welding process, welding residual stresses exist and vary through the weld, HAZ, and base metal.

4. Weld geometry – Weldments usually cause geometrical discontinuities and weld profiles are usually irregular.

5. Possible multiple crack interaction – Fatigue cracks at welds can either be single part-through cracks, or they can initiate at multiple adjacent points and eventually join to form a long and shallow crack. Unfortunately, the number and location of flaws that serve as crack initiation points are unpredictable.

3.3.2. Simplifying Assumptions

For engineering applications, it is undoubtedly too complex to take into account all the above-mentioned characteristics of welded structures. The following simplifying assumptions were made in this research to facilitate the fatigue life prediction of welded details. Assumptions were made regarding welding defects and imperfections, inhomogeneous materials, welding residual stresses, weld geometric parameters and possible multiple crack interaction.

3.3.2.1. Fatigue crack initiation and propagations stages

It is generally accepted that cracks are the most harmful weld defects, particularly when located at the surface. Therefore, welding codes do not allow the presence of a crack in a welded joint. For example, both the Structural Welding Code (AWS 2002) and Bridge Welding Code (AASHTO and AWS 1995) specify visual inspections, during which no

40

crack or lack of fusion is allowed. The acceptable weld profile, size of undercut and density of porosity are also specified in welding codes. In addition, the use of radiography, magnetic particle, ultrasound and/or liquid penetrants is recommended to identify potential imperfections. The International Institute of Welding divides welded joints into low, medium, and high quality classes that mainly reflect the quality of workmanship and are intended to be used for quality control (Raj *et al.* 2000). The limits of the numbers, sizes and locations of the weld defects are specified in the quality classes. Again, cracks and lack of fusion are not permitted in any case, and incomplete penetration and elongated cavities are not permitted except in low quality class welded joints.

In summary, no code allows the most harmful defects, such as detectable cracks in welded structures. Welding indeed causes frequent imperfections, but microcracks in the order of the grain size can exist and remain undetected even in smooth fatigue coupons and plain materials. Therefore, although crack initiation life of welded details can be conservatively neglected in fatigue life predictions, it is felt that this part of the fatigue life — that includes the initiation of microcracks and the growth to a technical crack — should be included in the analysis of welded details to provide more accurate results. Besides the criteria outlined in Section 3.2.3.2, the initial crack size a_i could be taken as either the size of initial weld defects such as porosity, undercut, and lack of penetration identified by non-destructive flaw inspection, or conservatively as the initial size determined on the basis of weld quality control criteria (Radaj and Sonsino 1998). There is increasing evidence that the initiation and early growth of fatigue cracks becomes the controlling portion of the fatigue life at long lives (Everett 1992).

3.3.2.2. Fatigue material properties of base metal, weld metal and HAZ

Research on the variations of fatigue properties among base metal, HAZ and weld metal are neither extensive nor conclusive. Available research seems to indicate that although there is variation in fatigue material properties, this variation is rather small and may be practically overlooked.

41

Lee et al. (2000) studied the variations of crack initiation and propagation properties in a butt-welded joint of AH36 steel, a Korean steel used mainly in the ship-building industry with a yield strength of 334 MPa, produced in a thermo-mechanically-controlled process (TMCP). Single edge notched specimens were made from the welded plate at varying distances from the fusion line. The resistance to crack initiation and growth was found to increase from the base metal towards the weld metal as the contents of fine acicular ferrite became larger. However, both the variation of fatigue crack initiation life in the weldment and the ratio of the crack growth rate of the base metal to the weld metal at a fixed ΔK are mostly within a factor of 2. The difference may be disregarded in practical applications.

For a comparison of fatigue crack initiation properties, Radaj and Sonsino (1998) obtained smooth specimens from a fillet-welded detail made of one weld metal and two base metals of fine-grained steels. The cyclic stress versus strain, strain versus life, and energy versus life curves for the three materials were found to be very similar. In fact, in the long life range (life longer than 10^6 cycles), the weld metal even had slightly better properties than the base metal, although the difference was negligible. In a similar study on a T-shaped welded tubular joint made from a normalized C-Mn steel (Radaj and Sonsino 1998), the cyclic stress versus strain curves of the HAZ and the weld metal were found to be similar. The strain versus life curve of the HAZ was only slightly lower than that of the base metal in the high cycle fatigue region (longer than 10^5 cycles), and the resulting energy versus life curves were quite similar between HAZ and base metal, with HAZ offering slightly better performance.

Maddox (1974) compiled fatigue crack growth rate data on various weldments including structural C-Mn steels. The fatigue crack growth rate in the weld metal and in the HAZ was found to be equal to or less than that in the base metal. It was suggested that the upper bound of the scatter band established by testing the base metal at room temperature may be used as a conservative estimate of fatigue properties of the weld metal and the HAZ.

42

Therefore, it seems possible to use base material properties for the weld metal and HAZ. One may argue that the difference between the materials is negligible because weld metal and base metal have comparable hardness values, whereas the hardness peak in the HAZ is only restricted to a relatively small volume.

3.3.2.3. Residual stresses

Welded structural components usually contain residual stresses of yield stress magnitude (Gurney 1968) that cause early local material yielding when external loads are applied. The influence of welding residual stresses, however, is reduced by cyclic loading if the ductility of the material is sufficiently high and the cyclic loading sufficiently severe, that is, with amplitudes higher than the endurance limit (Radaj and Sonsino 1998). In the fatigue crack initiation life predictions, mean stresses caused by cyclic loading are considered explicitly and the effect of neglecting the residual stresses may not be significant.

Fatigue cracks in regions of tensile residual stresses propagate under high stress ratios. The high stress ratios affect the magnitude of the threshold stress intensity factor range and the unstable fracture region, but have only a small effect on the fatigue crack growth rate in the stable crack growth region (Barsom and Rolfe 1999). Moreover, a residual stress field does not change the stress intensity factor range needed for fatigue crack propagation life prediction using LEFM.

3.3.2.4. Weld profile

The weld geometry parameters such as radius of curvature at weld toe or weld root, slope of weld contour near weld toe, or amount of weld reinforcement, are normally variables that show large scatter and are seldom reported. Thus, for simplicity, only the stress concentration due to a perfect fillet weld geometry profile (with a 45° slope and equal leg sizes) will be considered in this work.

43

3.3.2.5. Crack configuration

When a single long crack is considered in LEFM, coalescence among several small cracks has already happened (Radaj and Sonsino 1998). In general, fatigue cracks in most common structural details are semi-elliptical, have initiated at the weld toe and their aspect ratio remains approximately constant during propagation (BSI 1999; Brock 1989; Fisher *et al.* 1974).

3.4. Stress Intensity Factor at Transverse Stiffener Detail in Plate Girders

3.4.1. ABAQUS Contour Integral Evaluation

The stress intensity factors used in the LEFM approach for cracks in homogeneous, linear elastic materials can be obtained from ABAQUS contour integral evaluations. Several contour integral evaluations are possible at each location along the crack front. Each contour consists of a ring of elements completely surrounding the crack tip or crack front from one crack face to the opposite crack face. Stress intensity factor estimates from different contours may vary because of the approximate nature of the finite element solution; the estimate from the first ring of elements abutting the crack front normally does not provide an accurate result. However, sufficiently accurate contour integral estimates from ABAQUS can usually be obtained even with quite coarse meshes.

The infinitesimal strain assumption is usually made to model sharp cracks and refined focused meshes around the crack tips are normally provided. Second order elements must be used with a collapsed face to create singular stress fields at the crack tip. Figure 3-8 shows the collapsed 20 node brick element. Square root singularity, which is most suitable for linear elastic materials, can be obtained by constraining the nodes on the collapsed face of the edge planes to move together and moving the adjacent mid-side nodes to the ¼ points (ABAQUS 2003), as depicted in the figure.

44

3.4.2. Stress Intensity Factor for One Crack Size

Stress intensity factor expressions for a two-tip through thickness web crack at a common structural fatigue detail, the transverse stiffener detail in plate girders, are not available in the literature. Expressions for the stress intensity factor specifically applicable to the girder HPS-485W-C1 tested by Wright (2003), which will be analyzed in detail in Section 5.7, were obtained from a finite element analysis. The global model of girder HPS-485W-C1 and the submodel in the vicinity of a transverse stiffener are shown in Figure 3-9 and Figure 3-10, respectively.

Second order solid elements were used to model the transverse stiffener region: element C3D15 for the stiffener-to-web weld and web-to-flange weld and element C3D20R for the rest of the model. The mesh sizes along the web depth were approximately equal so that calculations of stress intensity factor for cracks of various lengths could be performed easily. The largest element size in the z direction (direction of the depth of the girder) is 3.4 mm. Symmetry about a vertical plane at the web centreline was exploited by modelling the girder on one side of this plane only. Figure 3-10 shows part of the finite element model with a two-tip through thickness web crack. To expose the crack, only one side of the model is shown. The crack size is 6.4 mm and the lower crack tip is located just above the end point of stiffener-to-web weld. The through thickness crack was represented by two sets of separate nodes along the crack length.

The stress intensity factor for the upper crack tip was requested as an output from the analysis. Table 3-2 shows the calculated mode I stress intensity factor range at the upper crack tip of the crack shown in Figure 3-11. The reference stress range $\Delta\sigma$, taken as the nominal stress range at mid-bottom flange, is 108.7 MPa. At any crack front location, the ΔK values are very stable from contours 2 to 8, indicating the path independency was obtained and the mesh was sufficiently refined for stress intensity factor calculations. Because contour 1 yielded a different stress intensity factor range value than contours 2 to 8, it was omitted from the average ΔK value calculation. Figure 3-12 shows the average ΔK estimates at different positions along the upper and lower crack fronts. The

45

figure indicates a variation of ΔK through the web thickness. The ΔK at the web surface (contour J0) is expected to have the largest value because the stress is the largest at that location (Figure 5-31). However, finite element results indicate that the largest ΔK was obtained from contour J2. It is believed that insufficient accuracy of the results at the submodel boundary is the cause for this inconsistency. Therefore, a curve was fitted from the calculated average ΔK at positions J2 to J10 and the curve was extrapolated to the web surface J0. The extrapolated value of ΔK at the web surface was used for the crack. The stress intensity factor range ΔK from the finite element analysis is 11.1 $MPa\sqrt{m}$ and 11.7 $MPa\sqrt{m}$ for the upper crack tip and lower crack tip, respectively. Both values are about 62% of those calculated using Equations (3-27), which ignores the existence of the stiffener (18.3 $MPa\sqrt{m}$ for upper crack tip and 18.6 $MPa\sqrt{m}$ for lower crack tip).

3.4.3. Stress Intensity Factor Expressions for Various Crack Sizes and Positions

To be able to calculate the crack propagation life, the value of the stress intensity factors for various crack lengths and positions are required. Ideally, the stress intensity factor should be expressed as a function of these factors so that numerical integration could be carried out easily. It is expected that a two-parameter function similar to the one proposed by Feng (1996) should be able to simulate the stress intensity factor at the two crack tips for the particular geometry of the girder studied. The function $f_{(\varepsilon,\lambda)}$ takes the following form:

$$f_{(\varepsilon,\lambda)} = a_0 + a_1\varepsilon + a_2\varepsilon^2 + a_3\lambda_w + a_4\lambda_w^2 + a_5\varepsilon\lambda_w + a_6\varepsilon\lambda_w^2 + a_7\varepsilon^2\lambda_w \tag{3-28}$$

where the parameter ε is related to the crack position, the parameter λ_w represents the crack size, and they are defined the same as those in Equations (3-27), with some of their constituent parameters defined in Figure 3-7. The $d - t_f$ term for the geometry of the girder HPS-485W-C1 is 965.7 mm (Wright 2003).

46

For girder HPS-485W-C1, the experimental observations indicated that the values of ε and λ_w are 0.8542 and 0.1048, respectively, for the initial crack. For the final crack, $\varepsilon = 0.8218$ and $\lambda_w = 0.5799$. Therefore, for fatigue crack propagation life calculation of girder HPS-485W-C1, ε is assumed to vary from 0.8 to 0.9 at an increment of 0.01 or 0.02 (i.e., 0.80, 0.82, 0.84, 0.85, 0.86, 0.88, 0.90), and λ_w is taken to vary from 0.1 to 0.6 at an increment of 0.1. For any combination of ε and λ_w, the amount of eccentricity e and the crack size a_w can be calculated from Equations (3-27c) and (3-27d). The upper and lower crack tip position (measured vertically from the middle of the bottom flange) can then be determined as $Z_U = 965.7/2 - e + a_w$ and $Z_L = 965.7/2 - e - a_w$, respectively. The nodes in the finite element model with the closest position were selected and ε, λ_w, e, and a_w were then calculated again based on the actual positions of the crack tips. A total of 34 cases of two-tip web crack with varying position and size were studied; the combinations of ε, λ_w, e, and a_w are listed in Table 3-3.

Table 3-3 shows the calculated stress intensity factor ranges at the upper and lower crack tips for various crack lengths located at various positions along the potential crack plane. A software was used to fit Equation (3-28) to the obtained finite element results. The resulting coefficients a_0 to a_7 are presented in Table 3-4. Figure 3-13 and Figure 3-14 present a 3D view of the function f and the finite element results for the upper crack tip and the lower crack tip, respectively. The function shows good agreement with the finite element results.

47

Table 3-1 Coefficients for Two-Tip Web Crack in I-Girders (Feng 1996)

Coefficient	Upper Crack Tip (U)	Lower Crack Tip (L)
a_0	0	0
a_1	1.02395	1.02052
a_2	-0.02824	-0.03142
a_3	-0.02660	-0.02841
a_4	-0.51095	0.48403
a_5	-0.00309	-0.02169
a_6	0.66587	-0.19538
a_7	0.02106	0.10116
a_8	-0.03243	-0.02670
a_9	0.00337	0.00206
a_{10}	0.02660	0.03282
a_{11}	0.00483	0.01704
a_{12}	-0.14302	-0.20652
a_{13}	-0.01281	-0.06069
a_{14}	-0.04610	-0.28079

Table 3-2 Finite Element ΔK Estimates at Upper Tip of a 6.4 mm Two-Tip Web Crack

Crack Front Location	ΔK Value ($MPa\sqrt{mm}$) at Contour								Average Value, Contours 2-8	
	1	2	3	4	5	6	7	8	($MPa\sqrt{mm}$)	($MPa\sqrt{m}$)
J0	323.2	319.4	319.8	319.6	319.6	319.6	319.4	319.4	319.54	10.10
J1	337.6	333.6	333.8	333.8	333.8	333.8	333.6	333.6	333.71	10.55
J2	343.8	340.0	340.4	340.2	340.2	340.2	340.0	340.0	340.14	10.76
J3	335.6	331.2	331.6	331.6	331.4	331.4	331.4	331.2	331.40	10.48
J4	328.4	324.8	325.2	325.0	325.0	325.0	324.8	324.8	324.94	10.28
J5	315.8	311.8	312.2	312.2	312.0	312.0	312.0	311.8	312.00	9.87
J6	302.4	299.2	299.4	299.4	299.4	299.2	299.2	299.2	299.29	9.46
J7	288.8	285.2	285.4	285.4	285.4	285.2	285.2	285.2	285.29	9.02
J8	274.2	271.0	271.4	271.4	271.2	271.2	271.2	271.0	271.20	8.58
J9	267.6	264.2	264.4	264.4	264.4	264.4	264.2	264.2	264.31	8.36
J10	260.8	257.8	258.0	258.0	258.0	258.0	257.8	257.8	257.91	8.16

Extrapolated Value: 11.12

48

Table 3-3 Finite Element ΔK Estimates for Various Crack Sizes and Locations

Case No.	ε	λ_u	e^* (mm)	a_u^* (mm)	Upper Crack Tip ΔK ($MPa\sqrt{m}$)	f	Lower Crack Tip ΔK ($MPa\sqrt{m}$)	f
1	0.80	0.10	387.50	9.60	12.14	0.6432	12.10	0.6411
2	0.80	0.20	387.50	19.20	15.70	0.5882	15.16	0.5680
3	0.80	0.30	387.50	28.80	17.50	0.5353	18.08	0.5531
4	0.80	0.40	387.43	38.33	18.32	0.4858	17.42	0.4619
5	0.80	0.50	387.45	47.95	18.50	0.4386	18.84	0.4466
6	0.80	0.61	387.75	57.85	18.12	0.3911	19.16	0.4135
7	0.82	0.09	395.50	8.00	11.42	0.6628	11.28	0.6547
8	0.82	0.20	395.50	17.60	15.08	0.5901	15.66	0.6128
9	0.82	0.31	395.46	27.16	17.08	0.5380	16.60	0.5229
10	0.82	0.41	396.95	35.05	17.94	0.4974	18.04	0.5002
11	0.82	0.50	395.55	43.25	18.46	0.4608	19.02	0.4748
12	0.82	0.61	395.85	53.15	18.58	0.4184	17.44	0.3927
13	0.84	0.10	405.10	8.00	11.52	0.6686	12.26	0.7116
14	0.84	0.19	405.10	14.40	14.12	0.6108	15.16	0.6558
15	0.84	0.31	404.99	23.89	16.32	0.5482	16.64	0.5589
16	0.84	0.39	405.05	30.35	17.22	0.5131	18.20	0.5423
17	0.84	0.51	406.95	38.65	17.94	0.4737	18.92	0.4996
18	0.85	0.09	409.90	6.40	11.12	0.7216	11.70	0.7592
19	0.85	0.20	411.43	14.33	14.30	0.6202	14.42	0.6254
20	0.85	0.30	409.75	22.25	16.02	0.5575	16.86	0.5868
21	0.85	0.40	409.95	28.85	16.96	0.5183	18.34	0.5605
22	0.85	0.49	410.15	35.45	17.62	0.4858	18.80	0.5183
23	0.86	0.10	416.26	6.36	11.56	0.7523	10.62	0.6912
24	0.86	0.21	414.59	14.29	14.62	0.6349	14.66	0.6367
25	0.86	0.30	414.65	20.75	15.86	0.5716	17.08	0.6155
26	0.86	0.40	414.85	27.35	16.78	0.5267	18.34	0.5757
27	0.86	0.50	415.05	33.95	17.38	0.4897	17.02	0.4795
28	0.88	0.11	425.75	6.25	10.76	0.7065	11.06	0.7262
29	0.88	0.19	424.25	11.15	14.20	0.6981	14.12	0.6942
30	0.88	0.30	424.45	17.75	16.54	0.6445	16.70	0.6507
31	0.88	0.42	424.65	24.35	17.14	0.5702	16.20	0.5389
32	0.90	0.10	433.84	4.96	9.90	0.7295	10.54	0.7767
33	0.90	0.21	435.68	9.93	12.80	0.6670	13.66	0.7118
34	0.90	0.30	434.25	14.75	14.94	0.6386	14.10	0.6027

* Refer to Figure 3-7 for a definition of e and a_w.

49

Table3-4 Coefficients for Two-Tip Web Crack in Girder HPS-485W-C1

Coefficient	Upper Crack Tip (U)	Lower Crack Tip (L)
a_0	-10.3259	1.2661
a_1	24.9116	-2.4416
a_2	50.5324	-28.3964
a_3	-13.9281	2.1759
a_4	-5.4562	5.1666
a_5	-118.5782	64.1329
a_6	68.3391	-36.9293
a_7	7.0767	-6.0144
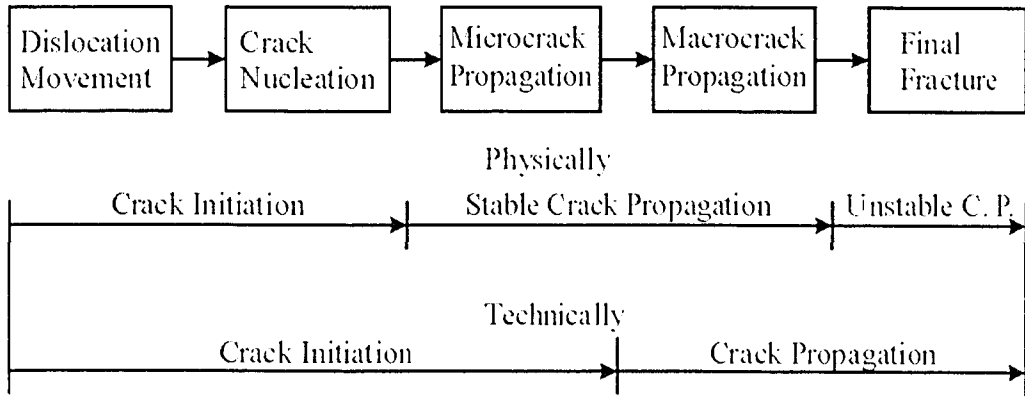
Figure 3-1 Initiation and Propagation Phases in Fatigue of Materials

Total fatigue life $N = N_i + N_p$
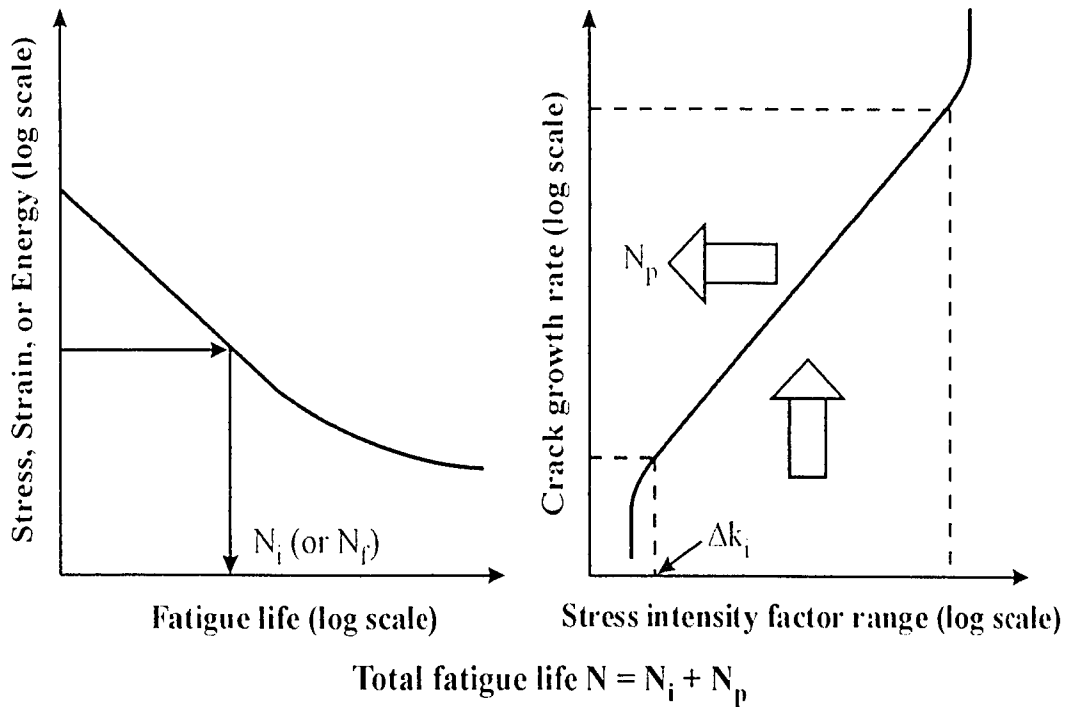
Figure 3-2 Illustration of Fatigue Life Prediction Procedure

51
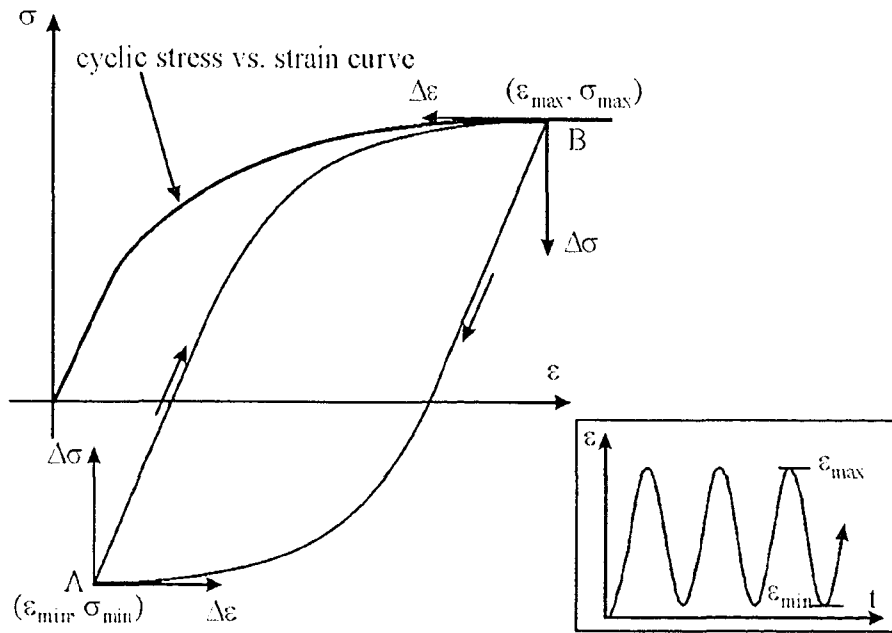
Figure 3-3 Illustration of Cyclic Loading and Unloading Behaviour

52
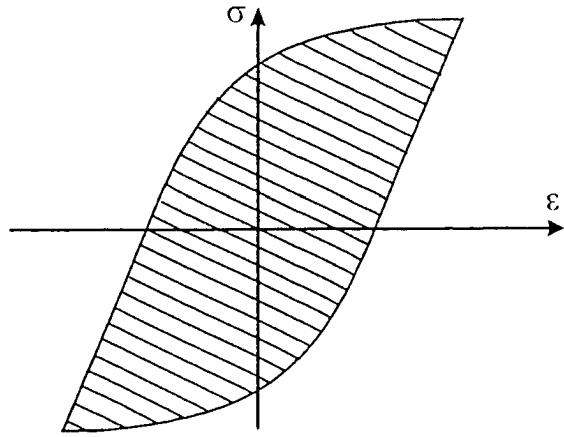
(a) Plastic Strain Energy, ΔW^p
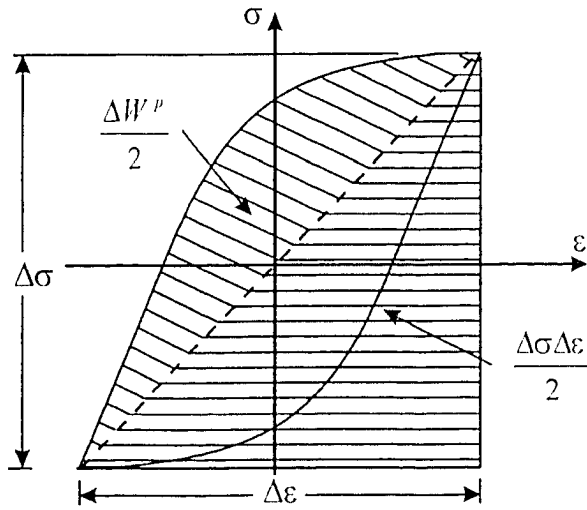
(b) Total Strain Energy, ΔW
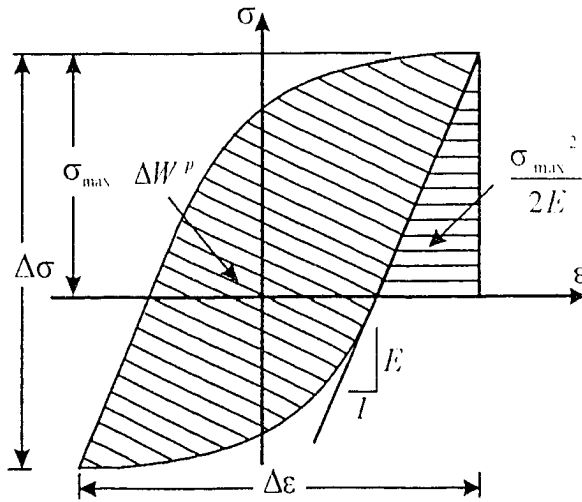
(c) Plastic plus Tensile Elastic Strain Energy, ΔW^t

Figure 3-4 Illustration of Various Measures of Energy

53
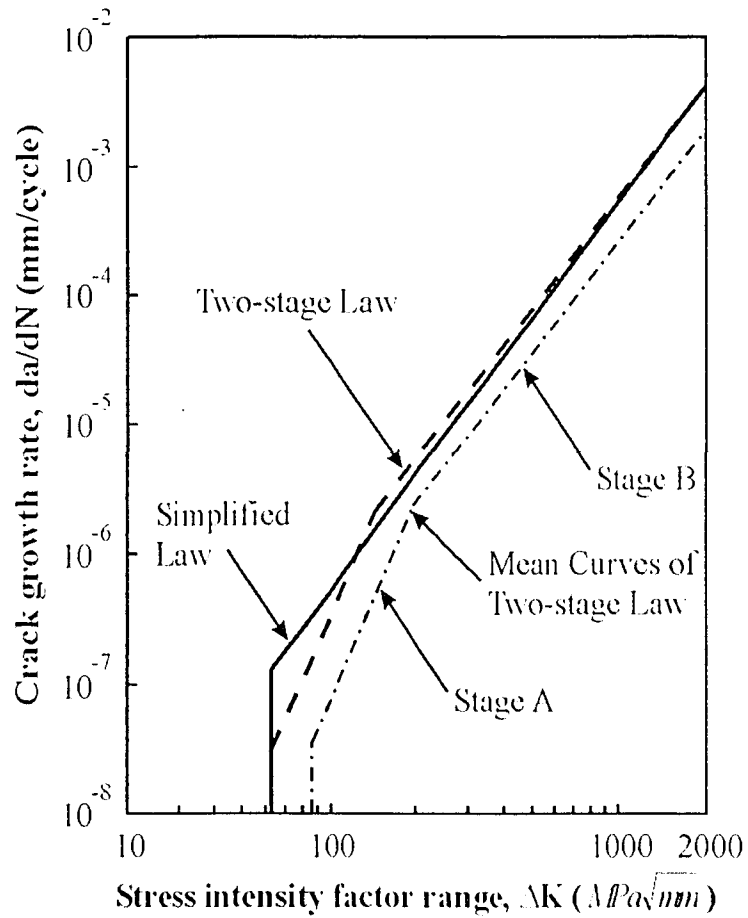
Figure 3-5 Two-stage Fatigue Crack Growth Rate Law in BS 7910 Code (1999)

Section A-A
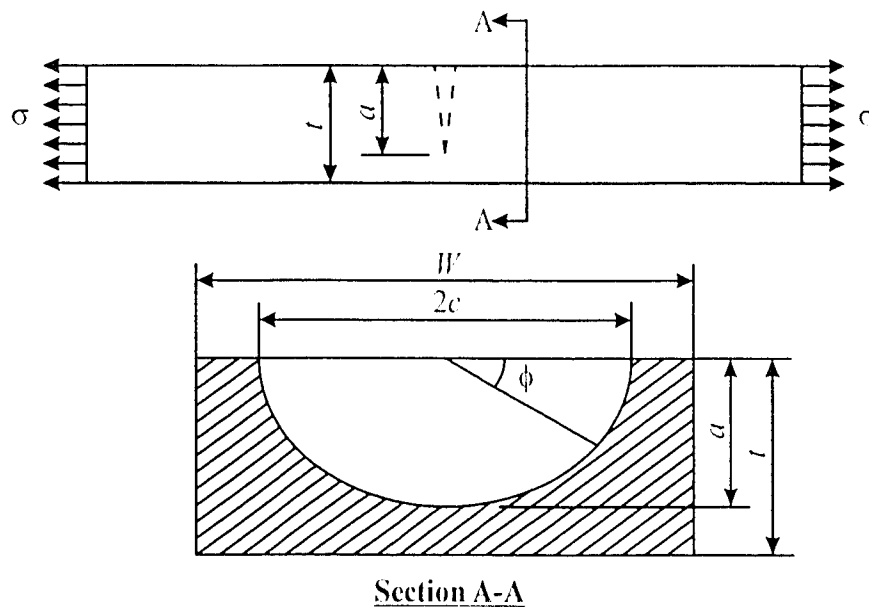
Figure 3-6 Semi-Elliptical Surface Crack in a Plate under Uniform Tension

54
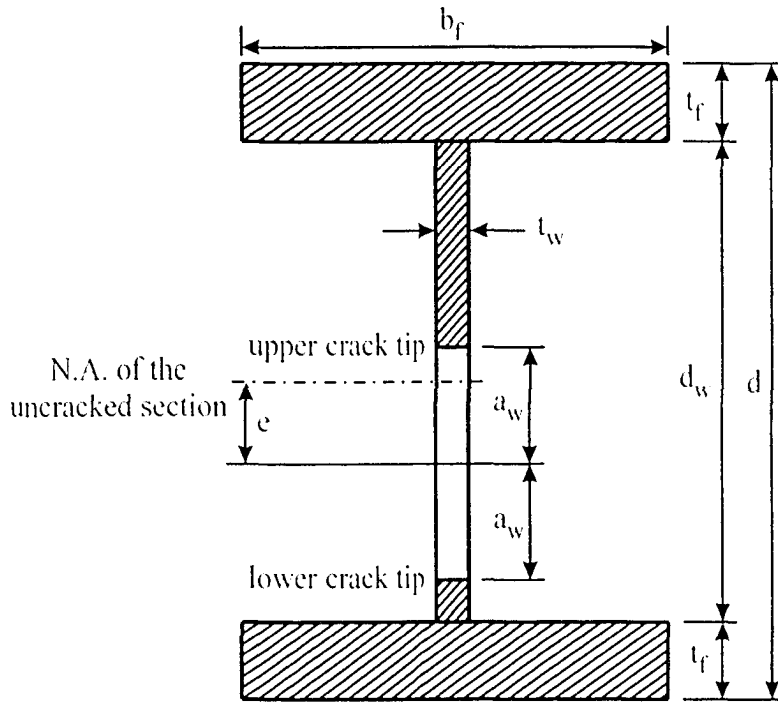
Figure 3-7 Through-Thickness Web Crack in an I-Girder
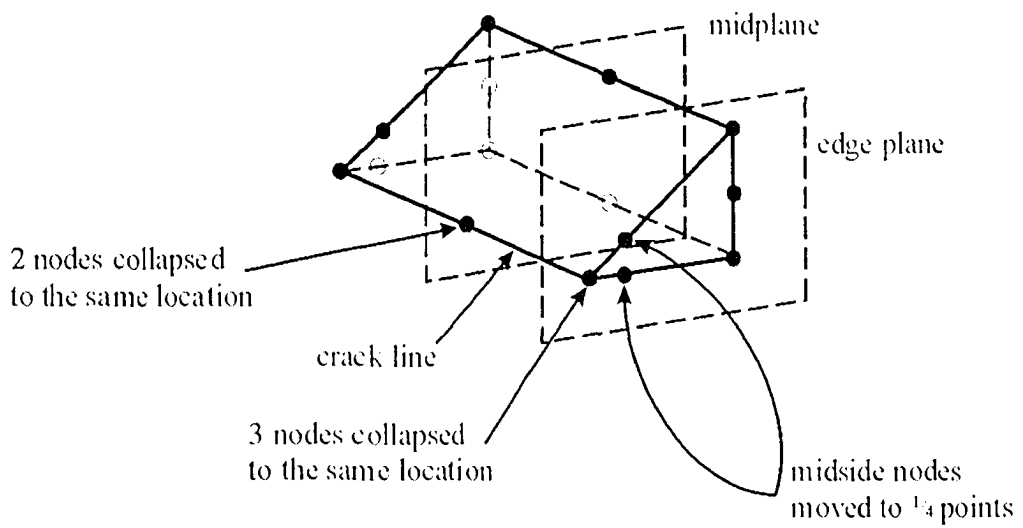
Figure 3-8 Collapsed 20 Node Brick Element from ABAQUS

55
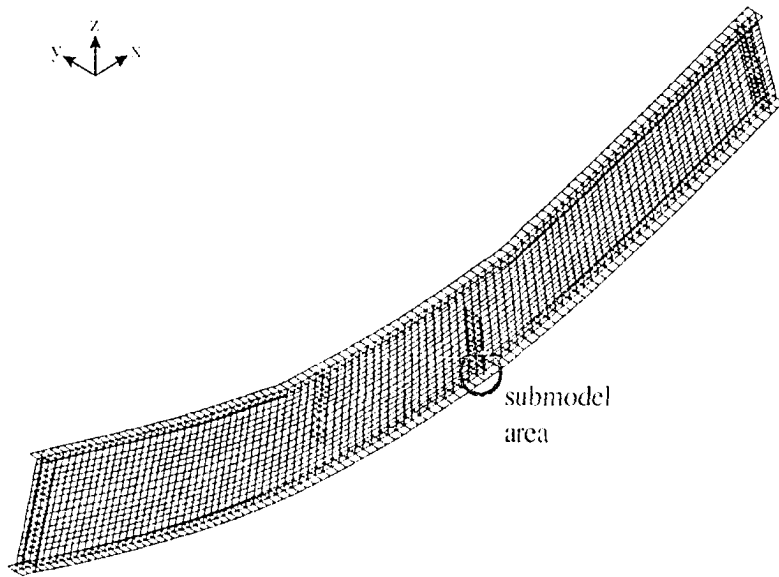
Figure 3-9 Global Model of Girder HPS-485W-C1

the cracked area is shown in Figure 3-11
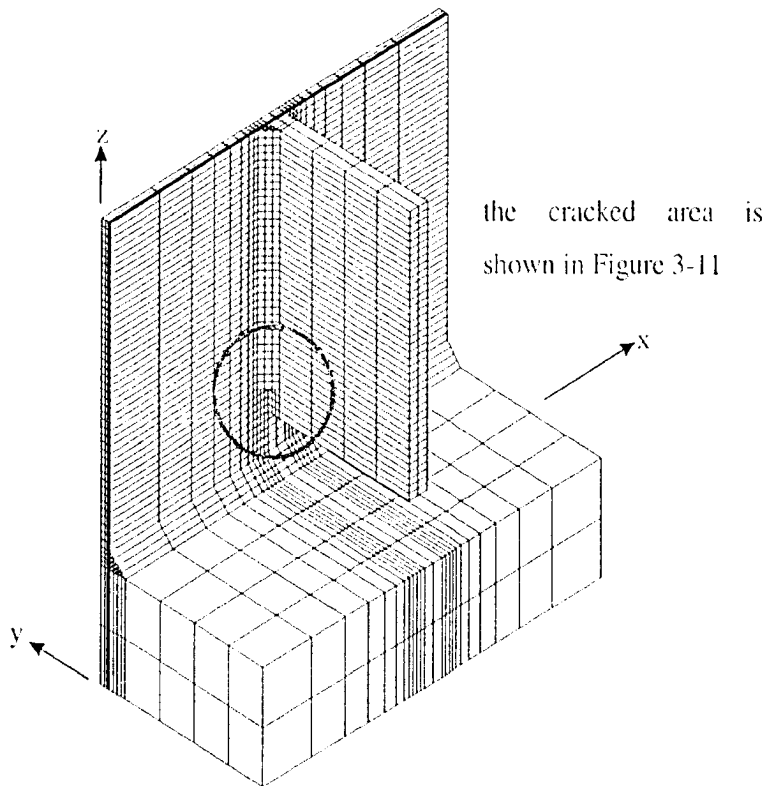
Figure 3-10 Submodel in the Vicinity of Transverse Stiffener Detail

56
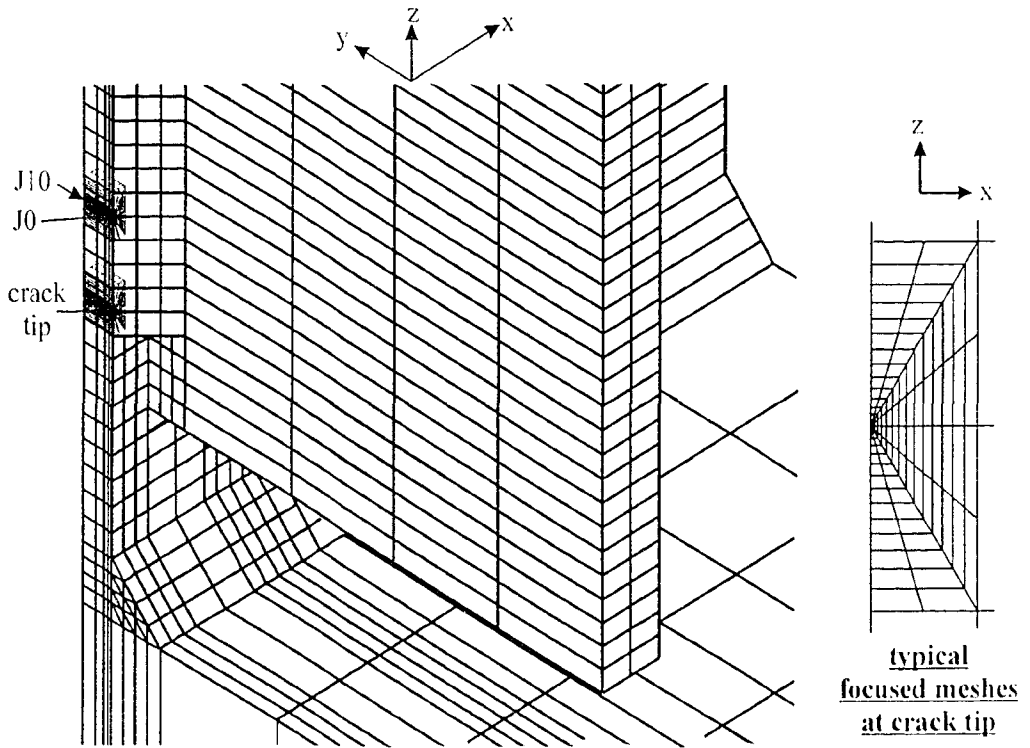
Figure 3-11 Close-up View of a Two-Tip Through Thickness Web Crack
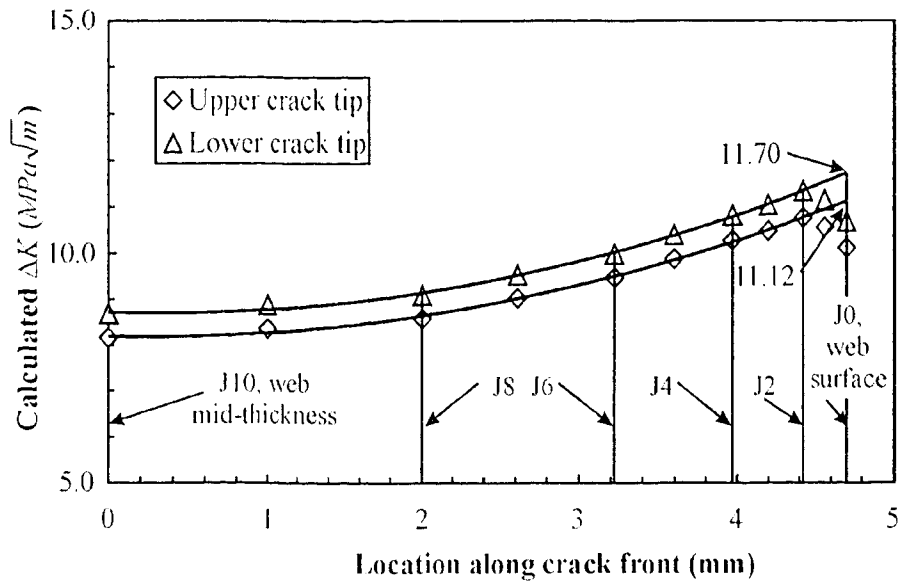
Figure 3-12 Calculated ΔK at Various Locations of the Upper Crack Front of a 6.4 mm
Two-Tip Web Crack in Girder HPS-485W-C1

57
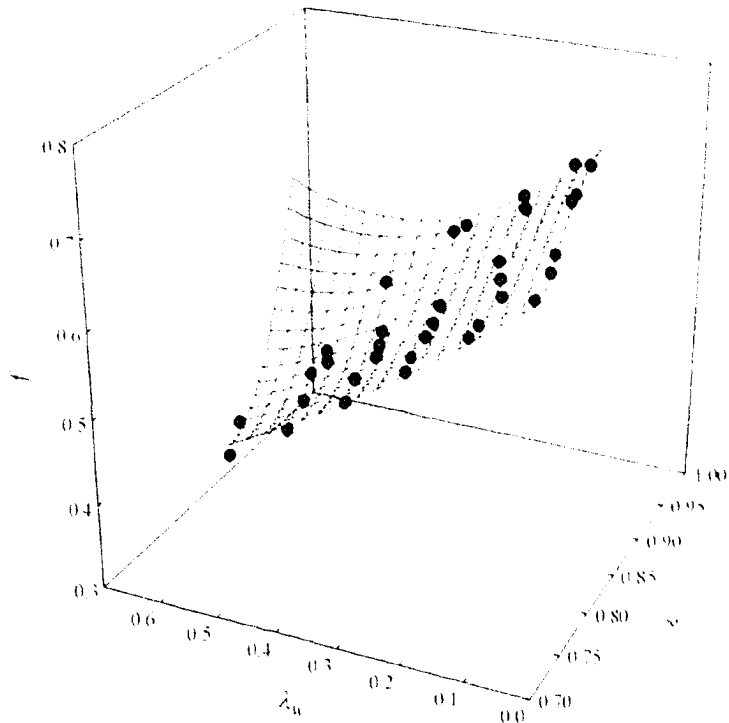
Figure 3-13 Correction Factor for the Stress Intensity Factor at the Upper Crack Tip
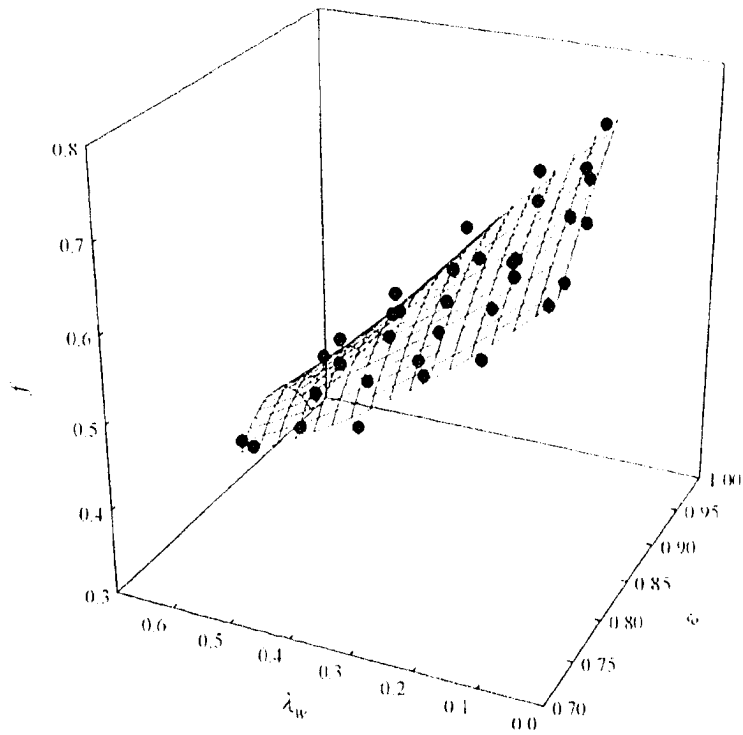
Figure 3-14 Correction Factor for the Stress Intensity Factor at the Lower Crack Tip

58

CHAPTER 4.

EXPERIMENTAL INVESTIGATION

4.1. Introduction

Chapter 3 outlined analytical techniques used to predict the fatigue life (crack initiation and propagation up to fracture) of various details. The use of these techniques requires both cyclic and monotonic material properties. Experimental work was therefore conducted to characterize the monotonic, cyclic, and fatigue properties of high performance steel. The material test results obtained from HPS and conventional structural steel grades are presented and compared. Chemical analyses, Charpy V-Notch tests, and tension coupon tests were used to characterize the chemical and monotonic mechanical properties. Fatigue tests on smooth specimens were conducted to characterize the fatigue crack initiation and early stage crack propagation properties under both fully reversed stress and positive mean stress conditions. The fatigue endurance limit was also determined from tests on smooth specimens. The results of the fully reversed tests were used to obtain cyclic stress versus strain curves and stress amplitude, strain amplitude, and energy per cycle versus crack initiation life curves. The effect of mean stress on fatigue crack initiation resistance was evaluated. Crack growth rate tests were conducted to determine the stable crack growth characteristics. Finally, the fracture resistance of the steels used in this program was defined from fracture toughness tests. Table 4-1 presents the test matrix used in this test program to characterize four different steels.

ASTM A709 Grade HPS 485W steel (ASTM 2002a), the steel currently being used in HPS bridge projects in the United States, was used in the test program. Since an important aspect of the research program was to provide a comparison between the performance of HPS and other structural steel grades, tests were conducted on ASTM A7 steel (ASTM 1965), which represents steel commonly encountered in older structures, and G40.21 350WT steel (CSA 1998), which represents modern steels with a specified low temperature toughness requirement.

59

The experimental investigation presented in this chapter also includes fatigue tests on a plate with a central circular hole to compare the fatigue performance of a simple fatigue detail made of HPS with the performance of the same detail made of conventional structural steel. Test results from the HPS detail is used for a partial validation of the methods adopted in the analytical investigation outlined in Chapter 3.

4.2. Test Program

4.2.1. Ancillary Tests

4.2.1.1. Chemical analysis and microstructure examination

Chemical analyses were conducted to confirm the chemical compositions of the steels used in the test program. The analyses were conducted at a commercial metallurgical laboratory, where various analysis methods were used depending on the alloying elements and levels. The results of the analyses were reported to within 2% accuracy.

Steel samples of approximately 10 mm square were obtained from each plate specimen for metallographic examinations. The samples were polished and etched with a 2% nital solution.

4.2.1.2. Charpy V-Notch impact tests

Strictly speaking, Charpy V-Notch (CVN) impact tests do not provide a good measure of fracture toughness (Barsom and Rolfe 1999). Nevertheless, they are commonly used by industry for quality control. Charpy tests were therefore conducted on the steels used in the test program. The minimum Charpy impact energy level for HPS 485W is specified to be 48 J at –23°C (ASTM 2002a), which is significantly higher than more commonly used structural steel grades.

Standard Charpy V-Notch specimens were obtained from three HPS 485W plates of different thickness (6.4 mm, 19 mm and 51 mm). The specimens from the 6.4 mm plate were half-size (5 mm x 10 mm), while the specimens from the 19 mm and 51 mm plates

60

were full-size (10 mm x 10 mm). Three Charpy specimens from the 51 mm plate were obtained at the locations illustrated in Figure 4-1. Standard half-size specimens were also obtained from a 6.4 mm thick A7 steel plate and full-size specimens from a 38 mm thick G40.21 350WT steel plate. All specimens were oriented in the rolling direction and the notch root was oriented in the thickness direction. Test temperatures varied from -75°C to +25°C. All tests were conducted in a commercial laboratory in accordance with ASTM A370 (ASTM 2000a).

4.2.1.3. Tension coupon tests

Both the Charpy impact tests and tension coupon tests were conducted to confirm the steel grades used in the test program. Standard sheet-type tension coupons were obtained from the 6.4 mm HPS 485W steel plate in both the longitudinal (rolling) and transverse directions, and from the 6.4 mm A7 steel plate in the transverse direction only. Standard plate-type tension coupons were made from the 51 mm HPS 485W steel plate and the 38 mm G40.21 350WT steel plate in longitudinal direction. All tension coupon tests were conducted in accordance with ASTM A370 standard (ASTM 2000a). The sheet-type coupons were machined as 50 mm gauge length coupons and tested in a MTS 1000 universal testing machine at an average testing strain rate of about 10 $\mu\varepsilon$/sec in the elastic range and 50 $\mu\varepsilon$/sec after strain hardening. The plate-type coupons were machined as 200 mm gauge length coupons and tested in a MTS 6000 universal testing machine at strain rates similar to those used for the 50 mm gauge length coupons.

4.2.2. Smooth Specimen Fatigue Tests

Fatigue tests were conducted on smooth specimens to study the fatigue crack initiation properties of HPS 485W steel under a fully reversed condition (FR series) and at levels of mean stress varying from 226 MPa to 483 MPa (MS series). All specimens were designed and tested in accordance with ASTM standard E606 (2000b).

61

4.2.2.1. Test matrix

FR series – fully reversed series

The cyclic stress versus strain curve and the stress amplitude, strain amplitude, or energy per cycle versus fatigue life curves were obtained from the uniaxial fatigue tests conducted under a fully reversed stress or strain condition. The majority of the specimens (33 out of 44) were tested under a strain control condition. A strain-controlled test is believed to be a fair representation of the condition typically experienced by the material in yielded zones because at highly stressed regions, plastic deformation is controlled by the surrounding elastic matrix (Ellyin 1997). Specimens were fatigue tested under strain amplitudes varying from 0.1% to 0.625%. The cyclic waveform was sinusoidal and applied at frequencies ranging from 2 Hz at 0.625% strain amplitude to 10 Hz at 0.1% strain amplitude, with the frequency held constant for all specimens at the same strain amplitude. The average strain rate was therefore held constant at about 0.05/sec for all specimens at all strain amplitude levels. All tests were started in tension.

Tests were also conducted to obtain the fatigue endurance limit under fully reversed stress cycling. As stress control is equivalent to strain control in the high cycle fatigue region, eleven tests were conducted under stress control for the HPS 485W steel, six on the 6.4 mm plate, and five on the 51 mm plate. All stress-controlled tests were conducted at 10 Hz. Considering the large variations in fatigue life at stress levels near the fatigue limit, a statistical approach is more appropriate to determine the fatigue limit. The well-known Probit method requires that a minimum of 30 specimens be used to establish the fatigue limit (Little and Jebe 1975). The large number of test specimens and long testing duration required made it unfeasible for this research project. An alternative approach to determine the fatigue limit is the up-and-down (or staircase) method, which tends to home in on the fatigue limit fairly rapidly with fewer tests. The approximate level of the fatigue limit was thus estimated with the up-an-down method, whereby the test stress range is adjusted based on each successive test result in an attempt to converge to the

62

endurance limit (Little and Jebe 1975). The stress spacing used in the up-and-down method was approximately 1% to 3% of the tensile strength of the material.

MS series – mean stress effect series

It is generally agreed that a tensile mean stress is usually detrimental to the fatigue resistance of metals in both high cycle fatigue and low cycle fatigue regimes (Stephens *et al.* 2000). When the effect of mean stress is investigated, tests are generally run in one of two modes: strain-controlled cycling with constant mean strain or stress-controlled cycling with constant mean stress. In low cycle fatigue, mean stress relaxation is known to occur in strain-controlled mode and the mean strain does not appreciably affect fatigue life. On the other hand, additional damage is caused by accumulated cyclic creep strain when tests are conducted in the stress-controlled mode (Ellyin 1997). The mean stress effect was investigated in this test program under stress control in the high cycle region where the two types of tests are equivalent. The cyclic creep strain effect was minimized by conducting tests at small stress amplitude levels. The effect of mean stress was evaluated for HPS 485W steel at two tensile mean stress levels.

4.2.2.2. Test specimens

Smooth specimens were machined from the 6.4 mm and the 51 mm HPS plates and the 6.4 mm A7 steel plate. The reduced section of the smooth fatigue test specimens was 8.3 mm wide by 6.0 mm thick. The smooth fatigue test specimen dimensions are shown in Figure 4-2. Flat sheet-type specimens were used because the more common circular cylindrical specimens could not be obtained from the 6.4 mm thick steel plates. For the 51 mm HPS plate, three specimens were obtained through the plate thickness direction, in a similar way as illustrated in Figure 4-1 for the CVN specimens. After machining, all specimens were polished with fine emery paper to a maximum surface roughness of 0.2 μm. In order to relieve the machining residual stresses, the specimens were stress relieved at 593°C for 2 hours and then left to cool slowly in the furnace.

63

4.2.2.3. Test set-up and instrumentation

All smooth specimen fatigue tests were conducted at room temperature in a MTS 1000 closed-loop servo-controlled universal testing machine. Figure 4-3 shows a typical test specimen in the testing machine. Load was measured with a load cell and a 10 mm gauge length extensometer with full scale range of 20,000 $\mu\epsilon$ was used to measure the total axial strain in the reduced section. Cyclic signals with the desired amplitude and frequency were produced by the micro-profiler that was controlled with the program LabView[TM]. Load and strain readings were sampled at a rate of 250 Hz and real time stress versus time, strain versus time, and stress versus strain curves were displayed to facilitate monitoring of tests. The data, as well as peak values, were recorded at preset intervals during the tests.

The tests were terminated when the maximum tensile load had dropped to 50% of its measured initial value. This allowed the crack to propagate approximately 50% to 60% through the cross section of the specimen (ASTM 2000b). Tests that did not lead to failure of the test specimen were stopped at 10^7 cycles, which is defined herein as a run-out.

4.2.2.4. Trial tests

Several trial tests were conducted to ensure that the specimens could be aligned in the testing machine without creating secondary bending strains greater than 5% of the mean normal strain (i.e., 50 $\mu\epsilon$ bending strain is allowed for a test conducted with 0.1% strain amplitude). Four strain gauges were mounted on the reduced section and load was applied monotonically up to a stress of 300 MPa and average strain of 0.15%. The strain gauges mounted on opposite sides of the specimen were found to be in good agreement (less than 3% difference between opposite gauges), which indicated negligible bending strain. The difference between the extensometer and mean strain gauge readings was also negligible.

64

4.2.2.5. Test procedure

The smooth specimens fatigue tests were conducted as follows:

1. Preparation of test specimen – The cross-section dimensions were measured to an accuracy of 0.001 mm at three locations along the reduced section. The minimum area was used to calculate stress from the measured loads. Two stiffening plates (25 mm x 25 mm x 100 mm) were placed at each gripping end of the test specimens tested under fully reversed loading at a strain amplitude larger than 0.4%. These plates were used to prevent buckling of the test specimens in the compression excursions.

2. Installation of test specimen – The specimens were aligned carefully in the hydraulic grips to prevent loading of the test specimens during gripping. To ensure that no load was applied during gripping, the lower grip pressure was turned on slowly to allow the necessary time for adjusting the displacement set point. A 10 mm gauge length extensometer was then mounted to the test specimen. In order to avoid creating pressure points at the extensometer knife edges, small patches of epoxy were placed on the test specimens where the knife edges were to be mounted. These prevented direct contact of the knife edges with the surface of the test specimens.

3. Testing – As explained above, tests were conducted under either load or strain control. The maximum and minimum stress limits were set electronically to stop the test when the failure criterion was met. Load and displacement upper and lower limits were also set to protect the extensometer against any unexpected events. After failure of the specimens, the fracture location, the appearance of the fracture surface and any unusual features were recorded.

4.2.3. Crack Growth Rate Tests

Crack growth rate tests were conducted on the 6.4 mm HPS 485W steel and on G40.21 350WT steel to obtain the steady state crack propagation properties.

65

4.2.3.1. Test specimens

The middle tension M(T) specimen was chosen over the more commonly used compact tension C(T) specimen because M(T) allows the use of hydraulic grips and tension-compression loading. The specimens from HPS 485W steel were 100 mm wide, 300 mm long and 6 mm thick. The straight through notch in the centre of each specimen was 20 mm long and 2 mm wide and was made by electrical-discharging machining (EDM). The specimens were prepared in accordance to ASTM E647 standard (ASTM 2000c). All specimens were stress relieved using the same procedure as for the smooth fatigue specimens. Figure 4-4 shows the geometry of the M(T) specimens and the notch detail.

The ASTM standard (2000c) requires that the two cracks emanating from the machined notch shall not differ by more than 2.5 mm (2.5% of specimen width), and the crack length measurements on the front and back surfaces shall not differ by more than 1.5 mm (25% of specimen thickness). The front/back crack length requirement was easily satisfied for the M(T) specimen configuration. However, the first three trial tests failed to satisfy the two cracks length symmetry requirement, although the specimens were aligned in the testing machine with great care. After the cracks had propagated through about half of the specimen width, the two crack lengths started to differ significantly (i.e., the crack was no longer centered). The difficulty in keeping the crack centered during the fatigue test makes the M(T) specimen difficult to use for crack growth rate testing.

On the other hand, single-edge tension SE(T) specimens offer two distinct advantages over the M(T) specimens: (1) only one crack tip needs to be monitored; (2) the crack symmetry requirement is no longer an issue. Two SE(T) specimens were therefore cut from one M(T), as shown in Figure 4-4. The newly exposed edges were then milled. The finished specimens were about 48 mm wide. Although the SE(T) crack growth rate test specimen is not part of the ASTM E647 standard specimen geometries, Blatt *et al.* (1994) demonstrated that the SE(T) specimen can be used successfully for fatigue crack growth testing of monolithic and composite materials. Blatt *et al.* (1994) demonstrated that the crack growth rate versus stress intensity factor range data obtained from the

66

SE(T) specimen correlates well with data obtained from standard compact tension C(T) specimens. A comparison of the crack growth behaviour obtained from one M(T) specimen and one SE(T) specimen for HPS 485W steel also indicated that the crack growth rate obtained from the SE(T) specimen is in good agreement with that obtained from the standard M(T) specimen. The SE(T) specimen was therefore adopted for this test program.

The geometry and notch details for specimens obtained from G40.21 350WT steel are similar to those SE(T) specimens from HPS 485W, except the specimen thickness, width and length were 12 mm, 75 mm and 400 mm, respectively. As the 350WT steel plate was 38 mm thick, three specimens were obtained through the thickness: one specimen at the middle plane and two specimens near the surfaces. A total of twelve specimens were made from 350WT steel.

4.2.3.2. Pre-cracking and testing

All crack growth rate tests were conducted using a closed-loop servo-hydraulic controlled universal testing machine. Figure 4-5 shows a typical test specimen in the testing machine. The tests were conducted at room temperature at a frequency of 10 Hz. The grip length at both ends of the specimens was about 50 mm, which made the specimen length to width ratio H/W about 4. The specimens were divided into various groups, tested under different load ratio, R (minimum load/maximum load). Three specimens each were tested at R of -1 (fully reversed), 0, and 0.5 for HPS 485W steel. Six and two specimens of G40.21 350WT steel were tested at a load ratio, R, of 0.1 and 0.5, respectively. The load ratio was kept constant for both pre-cracking and testing.

Each specimen was pre-cracked and tested under constant load conditions in accordance to the ASTM specified procedures. The minimum and maximum loads were maintained within ±2% throughout more than 95% of the test duration. In order to initiate a fatigue crack from the notch with minimal plastic damage at the crack tip, while making the pre-cracking within a reasonably short time, a cyclic load with the maximum load about 8% larger than that used during testing was normally used to initiate and grow the crack up to

67

2 mm. The load was then dropped and the crack was further propagated to about 4 mm by the time the initial crack satisfied the code requirement for starting the test. A complete test matrix of the specimen number, specimen location, load ratio, and maximum testing load is presented in Table 4-2 for both HPS 485W and 350WT steels.

4.2.3.3. Crack length measurement

An electronic imaging system was employed to visually monitor the crack length on the front surface, part of which is depicted on the photograph of the test setup presented in Figure 4-5. The imaging system consisted of a high resolution and high magnification digital camera with close focus zoom lens, a fibre optic illuminator and LabView program, which was used to monitor the number of load cycles and collect photographs of the crack tip at preset load cycles. The interval at which photographs of the crack tip were collected varied from 6000 cycles to 500 000 cycles, depending on the crack length and the expected crack growth rate. When the preset cycle was reached, the cycle count, the minimum and maximum loads, and the minimum and maximum strains were recorded. The strain data were obtained from a 10 mm gauge length extensometer mounted to the SE(T) specimen on the edge of the notch opening. The crack length on the specimen back surface was monitored at regular intervals with a self-illuminated reticle microscope. During the initial stage of the testing program, the microscope was also used to measure the crack length on the front surface to compare with the digital camera and the readings were found to be in good agreement.

The crack tip was identified clearly when the digital camera was used at a magnification of about 50X. At this high magnification, only an area 7.8 mm x 6 mm could be monitored with the camera, thus requiring the camera to be regularly re-adjusted in order to observe the crack tip. A scale with resolution of 0.5 mm was placed on the specimen to determine the actual length of crack. To facilitate the detection of the crack tip, a thin coat of white wash was applied with the brush strokes perpendicular to the expected crack plane. The crack length could be read directly from the photographs. A sample photograph is shown in Figure 4-6. Microsoft Photo Editor[TM] was used to help determine

68

the crack length since it can show the position of individual pixels on the photograph. The slight misalignment between the graduated scale and the edge of the specimen was taken into account by considering the offset between the notch edge and the 10 mm scale line (see Figure 4-6).

The recorded load and strain data were also used to calculate the crack length from the compliance method as outlined in the ASTM standard. The compliance method assumes that the crack length can be related to the crack mouth opening displacement (CMOD) that could be converted from strain readings. The relation between the non-dimensionalized crack length, a/W (W is the width of the SE(T) specimen) and the non-dimensionalized CMOD, U, for specimens with a length to width ratio H/W of 4, was given by Blatt et al. (1994) as follows:

$$a/W = 1.2928 + 2.3435U - 46.9715U^2 + 160.9788U^3 - 236.7674U^4 + 131.4813U^5 \quad (4-1)$$

where $U = \dfrac{1}{\sqrt{EBC}+1}$, E is the modulus of elasticity, B is the specimen thickness, and C is the compliance, taken as the slope of the upper linear part of the load-displacement curve, $CMOD/P$. The equation is valid in the range $0.1 \le a/W \le 0.95$.

4.2.4. Fracture Toughness Tests

Fracture toughness of HPS was determined in accordance with the recently developed ASTM E1820 standard (2000d). The test method is particularly useful when material response cannot be anticipated prior to testing. By using the resistance curve procedure outlined in the standard, a resistance curve can be obtained from a single test specimen by unload-reload sequences that produce crack extension. Depending on the specimen behaviour, the fracture toughness parameter K or J can be obtained from the tests.

The fracture toughness test specimens were made from the 51 mm thick HPS plate, which was the thickest plate available for this test program. Standard single-edge bend SE(B) specimens, shown in Figure 4-7, were used for the material toughness tests. Three specimens were machined from the steel plate along the rolling direction and stress

69

relieved. A 45 mm long straight through notch was machined at the edge of the test specimens at mid-length. In order to obtain a conservative lower bound of fracture toughness, specimens were tested at a temperature as low as -51°C, which corresponds to the lowest anticipated service temperature for AASHTO Zone 3 (1998). Four similar specimens were obtained from the 38 mm G40.21 350WT steel plate. The machined edge notch for these specimens was 35 mm long. The specimen thickness and test temperature for each specimen are listed in Table 4-3.

4.2.4.1. Test procedure

The fracture toughness tests were performed in a 1000 kN servo-hydraulic load frame. Fatigue pre-cracking to form the edge crack was performed under constant amplitude load control in a 3-point bending setup until a fatigue crack initiated from the machined notch and propagated to about 4 mm long. The pre-cracking procedure was monitored with the same high magnification digital camera that was used in the crack growth rate tests. The fracture toughness tests were performed on the pre-cracked test specimens under displacement control.

A typical test specimen in the test fixture is shown in Figure 4-8. A 4.5 mm range clip gauge was installed on knife edges to measure the $CMOD$ at the notched edge during testing. Another set of knife edges was installed at about 4 mm closer to each other and was used after the clip gauge had reached its limit in the first set of knife edges, thus giving the clip gauge a total range of 8.5 mm. A LVDT was installed to measure the load-line displacement. Unfortunately, the resolution and stability of the LVDT at low temperature was later found to be inadequate to measure the displacement accurately. The displacement from the machine actuator was therefore used to approximate the load-line displacement. This displacement includes the elastic compression of the test fixture, indentation of the specimen at the loading points, and the deformation of the testing machine. However, these additional deformations are believed to be insignificant.

In order to conduct the fracture toughness tests at low temperature, the test specimen and test setup were both enclosed in a specially designed environmental chamber made of

70

high density polyurethane foam. Figure 4-9 shows a picture of the low temperature test setup. Dry ice was placed in the chamber and three electric fans were used to circulate air through the dry ice to bring the temperature of the specimen to the desired test temperature. The temperature of the test specimens was measured using two thermistors, one on the front surface and the other on the back surface, within 20 mm from the expected crack trajectory. The temperature was controlled by adjusting the speed of three fans in the chamber. The specimens were exposed to the test temperature for at least 1 hour prior to testing to allow through thickness temperature stabilization and the temperature variations during testing was controlled within $\pm 3\,^{\circ}C$.

Periodic 15 to 20 kN unloadings were performed to measure the specimen compliance and calculate the amount of crack extension occurring during the test. A linear regression analysis was used to determine the slope of the unloading part of load versus crack mouth opening displacement curve. The crack length was calculated using the compliance equation for SE(B) specimen geometry given in ASTM E1820 as follows:

$$a/W = 0.999748 - 3.9504U + 2.9821U^2 - 3.21408U^3 + 51.51564U^4 - 113.031U^5 \quad (4-2)$$

where $U = \dfrac{1}{\sqrt{EBC}+1}$, E is the modulus of elasticity, B is the specimen thickness, and C is the compliance obtained at an unloading/reloading sequence.

The test was terminated either at fracture of the test specimen or when the clip gauge limit was reached under stable crack extension. Depending on behaviour, different parameters are calculated from the data to provide measures of fracture resistance as described in the following sections (ASTM 2000d).

4.2.4.2. Plane-strain instability

Plane-strain fracture toughness (K_{IC}) is obtained when instability occurs without significant crack tip plastic deformation. A conditional load (P_Q) is determined from the load versus CMOD data based on 95% secant line and K_Q is calculated as follows:

71

$$K_Q = \frac{P_Q S}{B W^{3/2}} f(a/W)$$ (4-3)

where $f(a/W)$ is a geometry function of the SE(B) specimen given as:

$$f(a/W) = \frac{3(a/W)^{1/2}[1.99 - (a/W)(1 - a/W)(2.15 - 3.93(a/W) + 2.7(a/W)^2)]}{2(1 + 2a/W)(1 - a/W)^{3/2}}$$ (4-4)

The following two requirements must be met for K_Q to be the size independent parameter (K_{IC}):

$$P_{max}/P_Q \leq 1.10$$ (4-5)

$$B \geq 2.5(K_Q/\sigma_{YS(T)})^2$$ (4-6)

where P_{max} is the maximum load the specimen was able to sustain, and $\sigma_{YS(T)}$ is the 0.2% offset yield strength at testing temperature.

4.2.4.3. Elastic-plastic instability

Instability preceded by a significant amount of crack tip plasticity is analyzed by using the J-integral approach. The calculated J is the summation of the elastic and plastic components of the strain energy density around the crack tip:

$$J = J_{el} + J_{pl}$$ (4-7)

The elastic component J_{el} is a function of K (calculated from Equation (4-3) ignoring the Q subscripts and setting a equal to initial crack size a_i) as follows:

$$J_{el} = \frac{K^2(1 - v^2)}{E}$$ (4-8)

72

The plastic component J_{pl} is calculated from the area under the load versus load-line displacement curve (A_{pl}) as follows:

$$J_{pl} = \frac{2A_{pl}}{Bb_i}$$ (4-9)

where b_i is the initial uncracked ligament ($b_i = W - a_i$). For small plastic deformations, J_{el} dominates and J can be directly related to K.

When instability occurs during a test, single point J values can be calculated to quantify toughness at the point of instability. If instability occurs before the onset of stable crack extension, the toughness is defined as J_c. If instability occurs after stable crack extension, the term J_u is used.

4.2.4.4. Stable crack extension

When cracks extend by stable tearing, a J-R resistance curve can be constructed, showing how J changes as a function of crack extension. ASTM E 1820 provides an incremental algorithm for applying Equations (4-7) to (4-9) to calculate J as plastic strain increases during testing. Crack length is periodically calculated during testing using the unloading compliance method. If the data meet certain requirements, J_{IC} can be calculated as the point where stable crack extension begins during the test. Similar to the K_{IC} calculation procedure, a provisional J_Q is calculated from the power law regression line of the qualifying data in the form of:

$$\ln J = \ln C_1 + C_2 \ln(\Delta a)$$ (4-10)

where Δa is the crack extension. If J_Q meets a series of qualification criteria, $J_Q = J_{IC}$. A spreadsheet was set up to process the raw data obtained from fracture toughness tests and implement the ASTM E 1820 calculation procedure.

73

4.2.4.5. Effect of temperature on yield strength

The effect of temperature on yield strength must be considered in analyzing fracture toughness data. Procedures for qualifying K_{IC} and J_{IC} require knowledge of the yield and tensile strength at the test temperature. Wright (2003) demonstrated that the effect of temperature on yield strength of steels with $\sigma_{ys} \leq 485$ MPa, tested at a slow load rate as specified in ASTM A307, can be accounted for using the following equation:

$$\sigma_{ys(T)} = \sigma_{ys} + \frac{666500}{(9.55 + \log \sigma_{ys(T)})(T + 273)} - 188.9 \qquad (4\text{-}11)$$

where $\sigma_{ys(T)}$ is the yield strength at temperature T (°C) and σ_{ys} is the room temperature 0.2% offset yield strength. As the shape of the stress versus strain curve for temperature $T \geq -80$ °C is similar to that at room temperature (Wright 2003), a constant yield to tensile strength ratio can be assumed. The effective yield strength σ_y, defined as the average of yield and ultimate tensile strength, can also be obtained.

4.3. Test Results

4.3.1. Ancillary Tests

4.3.1.1. Chemical composition and microstructure

As the changes in chemical composition requirements from old to modern structural steels are minimal (ASTM 1965; CSA 1998), chemical analysis was not conducted on G40.21 350WT steel. The chemical compositions of the HPS 485W and A7 steels investigated in this program are presented in Table 4-4 (a). Table 4-4 (b) lists the chemical requirements for the two steels as specified in the associated material standards (ASTM 2002a; ASTM 1965). The chemical analysis of each steel reveals that they both fall within the specified limits. It is noted that, as expected, the HPS has a significantly lower carbon and sulphur content than A7 steel, and higher contents of alloy elements such as copper, nickel, chromium, and aluminum. For this particular HPS, the total alloy

74

content (excluding carbon, manganese, phosphorus, and sulphur) is approximately 1.5%, and the weathering index is 6.6 as obtained from Equation (2-1).

Figure 4-10 shows the microstructures of (a) G40.21 350WT steel, and (b) HPS 485W steel, under an optical microscope. The 350WT steel shows a typical ferrite-pearlite microstructure. However, the HPS 485W steel has a more or less uniform microstructure of tempered martensite. The recrystallized structure consists of fine ferrite with small spheroidal cementite particles at the grain boundaries and within the grains. Fine carbide particles precipitated during the tempering treatment of the quenched steel offer "obstacles" to advancing cracks (Smith 1993); therefore, toughness of the steel is improved. Figure 4-10 also shows a finer grain size for the HPS 485W steel than for the G40.21 350W steel.

4.3.1.2. Charpy V-Notch impact toughness properties

Results from the Charpy V-Notch impact tests conducted at varying temperatures are presented in Table 4-5 and Table 4-6, for half-size specimens and full-size specimens, respectively. The test results are also presented in graphical form in Figure 4-11 and Figure 4-12. The equivalent energy absorption values of full-size specimens from the test results on the half-size specimens were obtained by multiplying the absorbed energy by a half size specimen by 2.0 in accordance to ASTM A370 (2000a).

Comparison between HPS 485W and A7 steel

The Charpy V-Notch energy versus temperature curves shown in Figure 4-11 for half-size HPS 485W and A7 steel impact specimens are remarkably different. Although there is no significant difference in upper and lower shelf energy between the two steels, the ductile to brittle transition temperature, taken at half of the upper shelf energy, is significantly lower for HPS 485W than for A7 steel (−50°C for HPS 485W compared to +12°C for A7).

75

Charpy impact tests conducted on specimens obtained from HPS of three different plate thicknesses (51, 19, and 6.4 mm), also corresponding to different heats of steel, are presented in Figure 4-12. There is a large difference in toughness between the different plate thicknesses of HPS and the 6.4 mm plate seems to have the lowest toughness, while the 51 mm plate has the highest value. Charpy tests on the 19 mm plate, which has the intermediate toughness, were conducted only at room temperature. The 6.4 mm plate, 19 mm plate, and 51 mm plate are thus identified hereafter as HPS(LT), HPS(MT), and HPS(HT), respectively. The suffix represents the relatively low, medium, and high toughness character of the three HPS plates.

The energy absorption of the HPS(HT) plate is larger than that of the HPS(LT) plate. As the rolling process itself causes some material variations in the plate thickness direction due to reasons such as residual stress and carburization, the variations in CVN energy might have been caused by the way the specimens were prepared (for example, there is not much material removed from the surface for the half-size specimens; and three specimens were made in the plate thickness direction for the 51 mm plate as indicated in Figure 4-1). However, a closer look at the CVN test results from the 51 mm plate does not indicate any noticeably different trend between the middle specimens and the side specimens, as shown in Figure 4-13.

Although the exact reason for the large variation in energy absorption between the different HPS plates is not known, such variations are likely caused by the fact that all three heats were early HPS heats produced with the thermo-mechanically controlled process (TMCP). However, as shown in Figure 4-12, even the HPS plate with the lowest energy absorption, with an average of 85 J at $-24°C$, easily met the requirement for HPS 485W steel, which is 48 J at $-23°C$.

Test results of full-size Charpy specimens of 350WT steel at a temperature of –45°C are shown in Figure 4-12 as well, along with all the results for HPS 485W steel. The average energy absorption from the three 350WT specimens was 139 J at –45°C, which satisfies the toughness requirement (40 J minimum) for Grade 350WT steel of Category 4. It is apparent that the 350WT steel has energy absorption capability comparable to that of the 51 mm HPS steel plate.

Examination of fracture surfaces

Figure 4-14 shows the appearance of the fracture surface of typical CVN specimens of HPS(LT) steel plate at various temperatures. The light areas on the fracture surfaces in Figure 4-14 indicate areas of brittle fracture, whereas the darker and dull areas represent the ductile fracture surface. It is apparent that the percentage of ductile fracture area increases as temperature increases. A selected sample was examined in a scanning electron microscope to identify the fracture mechanism. Typical photographs of fracture surfaces at +25°C, –75°C, and –45°C are shown in Figure 4-15, Figure 4-16, and Figure 4-17, respectively. Figure 4-15 shows a typical ductile fracture characterized by microvoid coalescence. The microvoids are extremely elongated, indicating almost pure shear fracture. At low temperature (–75°C), the fracture surface shows a typical brittle fracture mode, characterized by cleavage facets. Also typical of brittle fracture is the river pattern observed in Figure 4-16. Within the transition range (–45°C), the fracture surface presents a mixture of ductile fracture regions and brittle fracture regions, as shown in Figure 4-17.

4.3.1.3. Tensile properties

A summary of the static tensile properties of the HPS 485W, A7, and G40.21 350WT steels used in the test program is presented in Table 4-7. Figure 4-18 shows typical stress versus strain curves of the steels.

77

HPS(LT) is the only steel of the four steels tested in this program that does not display a yield plateau. The yield strength, defined by 0.2% offset method, is 8% to 13% lower than the specified 485 MPa. This is consistent with Focht and Manganello's (1996) observation on stress versus strain behaviour of some earlier heats of HPS 485W steel. Compared to HPS(LT), HPS(HT) shows a slightly higher yield strength but 20% lower tensile strength: 518 MPa for HPS(HT) and 653 MPa for HPS(LT). The tensile strength of HPS(HT) is also 11% lower than the specified minimum of 585 MPa for HPS 485W steel. The large differences in material strength between the HPS 485W and A7 steels are evident from Figure 4-18. The measured tensile strength of the A7 steel just reaches the specified minimum requirement of 380 MPa. The tensile strength in the longitudinal direction is expected to be slightly higher. The mean static yield strength of the 350WT steel was measured at approximately 365 MPa, which satisfies the requirement for this grade of steel.

Although the ductility of HPS 485W is not as high as that of A7 steel, it is considered to be very good with at least 23% elongation at rupture, measured on a 50 mm gauge length. and a 44% reduction of area. The ASTM A709 (2002a) requires a minimum elongation of 19% over a 50 mm gauge length; however, the minimum elongation over a 200 mm gauge length is not specified. Both HPS plates satisfy the standard requirements. HPS(HT) shows better ductility than HPS(LT). The apparent elongation of the two steels is about the same, but the gauge length for HPS(HT) is 200 mm, while it is only 50 mm for HPS(LT). A larger value of elongation can be expected for HPS(HT) if the gauge length were 50 mm. The typical stress versus strain curves in Figure 4-18 for HPS(HT) and 350WT end at an elongation of about 16% because the LVDTs that were used to measure the strains in the tests were out of range.

All longitudinal coupons were observed to fracture at the centre of the gauge length. whereas all the transverse coupons fractured very close to the gauge marks, within the gauge length. All coupons displayed typical ductile cup and cone fracture surfaces, except for HPS(HT) steel, which displayed an irregular fracture pattern as shown in Figure 4-19. Besides the major fracture surface perpendicular to the axis of specimen,

78

large secondary cracks formed that were oriented parallel to the applied load. The reason for such a crack pattern is unknown, although it probably relates to the triaxial tensile stress state around the necking area.

4.3.2. Fatigue Crack Initiation Properties

A total of 44 fatigue tests on smooth specimens of HPS(LT), HPS(HT), and A7 steels were conducted in the fully reversed (FR) series. The fatigue material specimens were oriented both in the longitudinal and in the transverse directions. The fatigue tests were conducted with strain ranges varying from 0.2% to 1.25% under strain control, or with stress ranges varying from 480 MPa to 610 MPa under stress control. The test results are presented in Table 4-8 where the total strain amplitude, stress amplitude, fatigue life, elastic and plastic components of the strain amplitude, and plastic strain energy density per cycle are shown. Table 4-9 presents the fatigue test results from the mean stress (MS) effect series. The mean stress, stress amplitude, total strain amplitude, fatigue life and plastic strain energy are tabulated in the table. A total of 13 specimens oriented in the longitudinal direction were tested at a mean stress to stress amplitude ratio, $\dfrac{\sigma_m}{\Delta\sigma/2}$, of 1 or 3, of which nine were obtained from HPS(LT) steel and four from HPS(HT). All stress and strain amplitude values were obtained from stable hysteresis loops (at approximately half-life) as explained in the following section. The plastic strain energy, ΔW^p, was also measured directly from these recorded stable hysteresis loops.

4.3.2.1. FR series – fully reversed series

The test results with fatigue life around and longer than 10^5 cycles were used to determine the fatigue limit of HPS 485W steel. The cyclic stress versus strain curves, the stress, strain, and energy versus life curves were obtained from a regression analysis of test results at various strain amplitudes. The test run-outs, indicated in subsequent figures by an arrow attached to the test result symbol, were excluded from the regression analysis. In addition, the specimens with zero plastic strain (taken as less than 5 $\mu\varepsilon$) were excluded from the regression analyses on plastic strain, and the specimens with negligible

79

plastic strain energy (less than 0.10 MJ/m^3) were excluded from the regression analyses on plastic strain energy.

Cyclic response

It was observed that material response varies with number of cycles during the early stage of a fatigue test. For strain-controlled tests, if the uncontrolled stress decreases with increasing number of cycles, the phenomenon is called strain softening while the opposite is called strain hardening. The stress versus strain response (hysteresis loops) are illustrated in Figure 4-20 (a) for strain softening, and Figure 4-20 (b) for strain hardening.

In the current test program, both cyclic responses were observed in the early stage of fatigue testing — strain softening in A7 and HPS(HT) steels and strain hardening in HPS(LT) steel. However, material response stabilized after approximately 500 cycles, thus a stable stress versus strain behaviour was reached after 1% to 25% of the total fatigue life. In order to ensure that a stable condition was used, the hysteresis loops at about half of the fatigue life were used to obtain material fatigue limit, cyclic stress versus strain curves and the associated stress/strain/energy versus life curves.

Fatigue limit

The fatigue limit is defined as the stress amplitude level below which no fatigue failure takes place (i.e., the fatigue life is infinite). The results obtained from the stress controlled tests are presented in Figure 4-21 for HPS 485W steel. The figure also includes some data from the strain controlled tests.

These combined results, as shown in Figure 4-21, can be used to evaluate the fatigue limit. For HPS(LT), the fatigue limit is found to lie between 265 MPa (largest stress amplitude with no failures) and 321 MPa (smallest stress amplitude with no run-outs). Two run-outs and one failure at 7.4x10^6 cycles were observed at a stress amplitude of 298 MPa, which indicates that the fatigue limit is likely close to 300 MPa. On the other hand, the fatigue limit for HPS(HT) lies below 285 MPa, with two failures at less than

80

1 million cycles at a stress amplitude of about 285 MPa. The fatigue limit can be reasonably estimated to be approximately 270 MPa, with one run-out and one specimen HPS(HT)-FR-10 that failed at 4.3 million cycles near the lower grip.

The difference between the fatigue limits of the two HPS steels can be attributed to the difference in tensile strength between the two steels (Table 4-7). Fatigue research has indicated that the fatigue limit is closely related to the tensile strength level (Breen and Wene 1979). While the yield strength for the two steels are approximately the same, HPS(HT) has a much lower tensile strength than HPS(LT) (518 MPa for HPS(HT) compared to 653 MPa for HPS(LT) for coupons oriented in the longitudinal direction).

The fatigue limit has also been shown to be a function of surface roughness (Boyer 1986). Since the fatigue tests were conducted on polished specimens, the fatigue limit for fatigue Category A details (hot rolled smooth details within 0.025 mm surface smoothness (CSA 2000)) can be obtained by multiplying the observed fatigue limit by a surface roughness correction factor of 0.67 for HPS(LT) and 0.75 for HPS(HT) (Boyer 1986). The correction factors are different for the two grades of HPS because the surface roughness effect has been found to be a function of material strength (Boyer 1986). Applying these correction factors brings the Category A fatigue limits, expressed in term of stress amplitude under full reversal, for both HPS plates to approximately 200 MPa, whereas the corresponding value in the current bridge design standard is 82.5 MPa (165 MPa if expressed as a stress range) (CSA 2000). This indicates that HPS has the potential to provide a distinct advantage over conventional structural steels in the high cycle fatigue region.

Cyclic stress versus strain curve

An illustration of the procedure used to obtain the cyclic stress versus strain curve by joining the tips of the stable hysteresis loops at various strain amplitude levels is shown in Figure 4-22. The cyclic strength coefficient K' and the cyclic strain-hardening exponent n', defined in Equation (3-5), are obtained by using a least square regression analysis to fit a line through the stress amplitude versus plastic strain amplitude data

81

according to Equation (3-5), where the modulus of elasticity E is obtained from tension coupon tests and the mean value of which is presented in Table 4-7. The values of the material constants K' and n' are presented in Table 4-10.

The cyclic stress versus strain curves for the two heats of HPS 485W steel in both the longitudinal (rolling) and transverse directions and A7 steel in the transverse direction are shown in Figure 4-23, along with the typical monotonic stress versus strain curves for HPS(LT) in the longitudinal direction and A7 steel in transverse direction. A comparison of the monotonic and cyclic stress versus strain properties of HPS 485W and A7 steels presented in Figure 4-23 indicates different strain response. At small strain ranges A7 steel cyclically softens, whereas HPS(LT) cyclically hardens slightly, which increases the maximum stress it can sustain during high cycle fatigue. The test results indicate that HPS 485W has some benefit for high cycle fatigue conditions in terms of strength.

Stress versus life curve

Plots of stabilized stress amplitude, $\Delta\sigma/2$, obtained at half of the fatigue life of the smooth specimens, versus number of cycles to failure, N_f, are presented in Figure 4-24 for two heats of HPS 485W steel in the longitudinal and transverse directions and for A7 steel in the transverse direction. A comparison between the transverse and longitudinal test specimens from HPS(LT) indicates that the material coupon orientation has no significant effect on the stress amplitude versus fatigue life data. However, there is a significant difference in fatigue life between the HPS and the A7 steel, which is caused by the large difference in strength between the two steels.

The stress amplitude, $\Delta\sigma/2$, versus fatigue life, N_f, (stress–life) curve in Figure 4-24 is expressed mathematically by Equation (3-1), where the fatigue strength coefficient σ_f' is the stress amplitude corresponding to the stress–life curve intercept at one cycle, and the fatigue strength exponent b represents the slope of the stress–life curve. The constants

82

σ'_f and b, obtained from a regression analysis of the stress amplitude versus life data, are presented in Table 4-10.

Strain versus life curve

The fatigue test data, expressed in terms of total strain amplitude, $\Delta\varepsilon/2$, versus fatigue life, N_f, are presented in Figure 4-25 for the HPS in the rolling and transverse directions and A7 steel in the transverse direction. The difference between the transverse and longitudinal fatigue properties for HPS(LT) is insignificant. There is also no apparent difference between the fatigue resistance of two HPS steels and A7 steel.

The strain amplitude versus fatigue life (strain–life) curve in Figure 4-25 is expressed mathematically by Equation (3-4), where the fatigue ductility coefficient ε'_f is the strain amplitude corresponding to the plastic strain line intercept at one cycle, and the fatigue ductility exponent c represents the slope of the plastic strain line.

Figure 4-26 illustrates the regression analysis for HPS(LT) steel in the rolling direction. The elastic and plastic components of the strain amplitude, $\Delta\varepsilon^e/2$ and $\Delta\varepsilon^p/2$, respectively, are plotted separately and a regression analysis of this data (shown as dashed lines in Figure 4-26) was used to determine the coefficients and exponents used in Equation (3-4). Although fatigue life is conventionally plotted on the x-axis in fatigue data presentation, it was taken as the dependent variable in all regression analyses.

Table 4-10 presents the parameters used in Equation (3-4) for the steels tested in this program. Although Figure 4-25 shows no significant difference between the different steels, Table 4-10 presents the strain–life constants obtained from a regression analysis on the individual steel samples.

The exponents of the cyclic stress versus strain, stress versus life, and strain versus life curves presented in Table 4-10 fall generally within the expected range for the majority of steels. The expected range for the cyclic strain-hardening exponent n' is from 0.05 to

83

0.25. The range for the fatigue strength exponent b is –0.05 to –0.15 with an average value of –0.085, and the fatigue ductility exponent c can vary from –0.4 to –0.8 with a mean value of about –0.6 (Ellyin 1997).

Energy versus life curve

The fatigue test results for HPS 485W and A7 steels are presented in Figure 4-27, Figure 4-28, and Figure 4-29 as fatigue life as a function of the plastic strain energy density per cycle, ΔW^p, the total strain energy density per cycle, ΔW, and the plastic plus tensile elastic strain energy density per cycle, ΔW^t, respectively. The three measures of energy were described in Figure 3-4. The three figures show no significant difference between the different steels and the different orientations. The plastic strain energy damage parameter, ΔW^p, for the HPS(HT) specimens presented in Figure 4-27 does not seem to correlate well with the test results at fatigue lives longer than 10^5 cycles. This is because ΔW^p is very small in the high cycle fatigue region and is therefore difficult to measure accurately.

The energy density per cycle, ΔW^p, ΔW, and ΔW^t, versus fatigue life, N_f, (energy–life) curves presented in Figure 4-27 to Figure 4-29 can be expressed mathematically by Equations (3-8) to (3-10). The coefficients F_p, F, F_t and the exponents α_p, α, α_t are obtained from a regression analysis of the experimental data (ΔW^p, ΔW, and ΔW^t versus fatigue life). The limiting value of ΔW^p, i.e. the value of ΔW^p as the fatigue life approaches infinity, for most steels is in the range of 10^{-4} to 5×10^{-2} MJ/m^3, with a mean of about 1.5×10^{-2} MJ/m^3 (Ellyin 1997). This represents only a very small percentage of ΔW^p for cases where the plastic strains are large enough for the plastic strain energy approach to be considered appropriate and is therefore normally neglected (i.e., $\Delta W_0^p = 0$). The limiting value of ΔW, ΔW_0, can be approximated as

$$(\frac{\Delta\sigma\Delta\varepsilon}{2})_{N_f \to \infty} = \{\frac{2(\Delta\sigma/2)^2}{E}\}_{N_f \to \infty} ; \text{ similarly, } \Delta W_0^t \approx (\frac{\sigma_{max}^2}{2E})_{N_f \to \infty} = \{\frac{(\Delta\sigma/2)^2}{2E}\}_{N_f \to \infty} . \text{ The}$$

stress amplitude $\Delta\sigma/2$ for a fatigue life approaching infinity was obtained by

84

extrapolating the material stress versus life curve to 10^7 cycles. The coefficients, exponents and limiting values for Equations (3-8) to (3-10) are presented in Table 4-11.

4.3.2.2. MS series – mean stress series

A total of 13 specimens were tested to evaluate the effect of mean stress on fatigue life and to evaluate if available life prediction models are suitable for HPS. The models considered for correcting for the mean stress effect include Morrow's model (Equation (3-11)), the Smith, Watson, and Topper (SWT) model (Equation (3-12)), and Ellyin's models (Equations (3-13) and (3-14)). The parameters used in this series of tests are summarized in Table 4-9. The stress amplitude was varied from 143 MPa to 288 MPa, and the ratio of mean stress to stress amplitude, $\dfrac{\sigma_m}{\Delta\sigma/2}$, was set at 1 for 10 tests and 3 for the remaining tests.

Figure 4-30 shows the test results in terms of stress amplitude versus fatigue life and the stress–life curves obtained from fully reversed tests for HPS(LT) and HPS(HT) steel. The horizontal part of the lines is the fatigue limit obtained from the test program. The tests with mean stresses other than zero all fall below the fully reversed fatigue curves indicating that mean tensile stress reduces the fatigue life. The reduction in fatigue life varied from a factor of 2 to a factor of 10, which increased with an increase in the mean stress ratio, $\dfrac{\sigma_m}{\Delta\sigma/2}$. Considerable variation in fatigue life was observed for the HPS(LT) specimens with $\dfrac{\sigma_m}{\Delta\sigma/2}$ of 3, all tested at similar stress level, with two run-outs and one specimen failing very early. The stress amplitude was about 150 MPa, which is probably close to the fatigue limit for this mean stress ratio. At this stress ratio, the maximum stress of 600 MPa was very close to the tensile strength of the material (653 MPa). Tensile plasticity was a likely competitive failure mechanism. The mean stress ratio of 3 is the upper bound that could be experimentally investigated for the steel. The equivalent fully reversed stress amplitude $(\Delta\sigma/2)_{-1}$, as defined in Section 3.2.2.2 for Morrow's mean stress correction, is plotted in Figure 4-31 for the test results from the MS series

85

and compared with the fully reversed stress-life curves. The corrected test results are found to fall very close to the stress-life curves indicating that Morrow's mean stress correction is a suitable parameter to account for mean stress effect in HPS.

Figure 4-32 shows the test results from the MS series tests in terms of strain amplitude versus fatigue life. A comparison of the test results with the regression lines for the fully reversed strain test results indicate once again that the mean stress effect is significant. The Smith, Watson and Topper (SWT) model can be applied to account for the mean stress effect. A plot of the SWT parameter, i.e. the maximum stress times the strain amplitude (see Equation (3-12)), versus fatigue life is shown in Figure 4-33. The close proximity of the test results to the regression lines from the fully reversed stress results indicates that the correction proposed by Smith, Watson and Topper provides a good approximation of the mean stress effect.

Figure 4-34 shows the test results compared with the total strain energy versus fatigue life curves. The test results fall well above the energy-life curves, by a factor of at least 2 on the life scale, indicating that the ΔW^t parameter is overly conservative. Ellyin (1997) indicated that the parameter would generally overestimate the mean stress effect if the magnitude of mean stress is large and suggested that the use of the total strain energy be restricted to small values of mean stress to stress amplitude ratio ($\frac{\sigma_m}{\Delta\sigma/2} < 0.1$). The more general total strain energy parameter D in Equation (3-13), with η in Equation (3-14) is taken as 1.0, was considered. The 13 test data and the revised energy-life curves are shown in Figure 4-35. However, the regression line of HPS(LT) steel does not seem in good agreement with the test results, and unconservative predictions are likely to result from this correction model.

4.3.2.3. Examination of smooth fatigue specimens

All the test specimens that failed during the fatigue tests, except specimen HPS(HT)-FR-10 that failed near the lower grip end, failed by fracture in the reduced area. The fracture surface was within a few degrees of perpendicular to the longitudinal axis of the

86

specimen. From a visual examination of the fracture surfaces, it was observed that more than 93% of the cracks had an elliptical crack front, of which more than 82% of the crack initiation occurred at the corner of the rectangular cross section. Although the aspect ratio of the fatigue cracks spans from 0.6 to 1.6, more than 70% of cracks have an aspect ratio of approximately 1, resulting in a more or less circular corner fatigue crack. The crack size, measured on the surface of the material specimen at the end of the tests, varied from 3.2 mm to 6 mm, with a mean value of 4.5 mm. The larger cracks were observed to occur in those specimens tested with smaller maximum stresses. Figure 4-36 shows a typical fractured specimen and a fracture surface showing a circular corner crack.

A select number of fracture surface samples from typical specimens and specimens that had shown a much lower fatigue life than the other replicates, were further investigated by examining the fracture surface in a scanning electron microscope. The objectives of these examinations were to determine the origin of the fatigue fracture and to assess whether there were any unusual features on the fracture surfaces. A typical fracture surface is shown in Figure 4-37 where fatigue striations can be detected. The flat parts are damaged fracture surface, which was typical for the specimens tested under the fully reversed condition and mechanical damage imparted during the compression cycle. An inclusion, about 5 μm in diameter, as shown in Figure 4-38, was found near the corner where the fatigue crack initiated in specimen HPS(LT)-FR-7. This was one of the fatigue test specimen that displayed a shorter fatigue life (5.7×10^3 cycles compared to an average of 7.7×10^3 for six specimens tested at a similar strain condition). An X-Ray diffraction analysis indicated that the inclusion is a manganese sulphide (MnS) inclusion. The examination under a scanning electron microscope did not reveal any other irregularities in the microstructure or the chemical composition of the surfaces.

4.3.3. Crack Growth Rate Tests

4.3.3.1. Validation of measurement technique

Accurate crack size measurement is an important aspect of the crack growth rate evaluation. In order to assess the ability of the imaging equipment to measure crack size

87

accurately, tests were conducted to compare the crack size determined with the imaging system with the actual crack size. A trial specimen was fatigued to produce a small crack of about 4 mm, which corresponds to the initial crack size in typical crack propagation tests. The surface crack size was measured using the camera and the test specimen was then broken by tensile overload. The crack size was then measured directly on the fracture surface. This measurement confirmed that the crack measurement made with the imaging system before fracture was accurate. The crack length measured with the imaging system was also compared to the crack length estimated using the compliance method and measurements made using an optical micrometer. The comparison between the three methods is shown in Figure 4-39 for specimen HPS(LT)-CGR-8. The figure indicates that all three methods effectively yield the same results.

A comparison between the crack length measured on the front surface and on the back surface of test specimen HPS(LT)-CGR-5 is shown in Figure 4-40. The figure indicates that the front and back surface crack lengths are almost identical. Figure 4-41 shows a photo of the fractured specimen showing a straight crack front. This was observed for all the crack growth rate test specimens except for specimen HPS(LT)-CGR-6, where the two surface crack lengths differed by 1 to 2 mm before the crack reached 27 mm. Figure 4-42 shows the measured crack length versus number of cycles for this specimen. The figure also shows the crack length calculated using the compliance method, which was found to lie just between the measured crack lengths. The crack length obtained from the compliance method can therefore be treated as an average crack length because both the load and measured crack mouth opening displacement are the average value for the specimen. Figure 4-40 and Figure 4-42 demonstrate that, despite the underlying assumption of the compliance method, it still could be used successfully if a well-calibrated compliance equation is available.

Since the different crack length measurement methods give almost identical results and the front/back surface cracks are almost identical for the majority of the test specimens, the crack length measured using the camera alone could be used to compute the crack growth rate, da/dN, and the stress intensity factor range, ΔK. The crack growth rate

88

was calculated by seven points incremental polynomial method as recommended by the standard (ASTM 2000c). The stress intensity factor for the SE(T) specimen used in this test program was calculated by numerical integration as outlined in Blatt *et al.* (1994).

It is desirable to compare the results from crack growth rate tests conducted with the SE(T) specimen with the results obtained with a standard M(T) specimen for HPS 485W steel. However, a direct comparison between the SE(T) test specimen and the M(T) test specimen was difficult. By the time the crack length in the M(T) specimen had reached about 25 mm, it no longer satisfied the symmetry requirement. At this point, the maximum stress intensity factor range, ΔK, for the M(T) specimen was only about 14 $MPa\sqrt{m}$. This corresponds to only the early crack propagation stage of the SE(T) specimens. Fortunately, solutions for the stress intensity factor at both tips of an unsymmetrical crack in a finite width plate subject to uniform tension are available in the literature (Tada *et al.* 2000). A comparison of the stress intensity factor calculated using the simplified approach (neglecting the eccentricity of the crack) with the solution provided in Tada *et al.* (2000) indicated that the simplified approach underestimated the value of the stress intensity factor by 15% for the longer crack and overestimated the stress intensity factor for the short crack tip by 6%. A comparison of the test results obtained from a M(T) specimen (including results from both crack tips) with the results obtained from a SE(T) specimen of the same material is shown in Figure 4-43. The figure shows that the test results from the SE(T) and M(T) specimens are similar. The single edge (SE(T)) crack test specimens were therefore adopted for the crack growth rate tests.

4.3.3.2. Results and discussions

The crack growth rate test results for HPS(LT) steel are presented in Figure 4-44, Figure 4-45, and Figure 4-46 for load ratios, R, of –1, 0, and 0.5, respectively. The variation in test results for the three specimens presented in the figures is very small. The test results presented in Figure 4-44 are expressed in two ways: for one case, the stress intensity factor range is taken as the difference between the maximum and minimum stress

89

intensity factor, and for the other case, only the tension portion of the stress cycle is considered, i.e. $\Delta K = K_{max} - 0$. The ASTM standard suggests the operational definition of ΔK as $K_{max} - 0$, which assumes that crack closes as soon as the applied load goes to zero and does not include local crack tip effects such as crack closure, residual stress, and blunting (ASTM 2000c). On the other hand, the whole compressive branch is assumed effective, if ΔK is defined as the algebraic difference between K_{max} and K_{min}. In reality, however, the effective stress intensity factor range is somewhere between the two cases presented in Figure 4-44. Although the exact value beyond which the compressive branch portion remains effective in closing the crack is uncertain, it should be a function of the applied K_{max}. Test results with alternating loading are still useful as long as the R is the same, and the definition for ΔK is consistent in the applications and the original source.

All the test results from HPS 485W steel are presented in Figure 4-47, from which the effect of stress ratio can be observed. The mean regression lines are essentially parallel to each other, but for a given ΔK, an increase in stress ratio, R, results in an increase in the crack growth rate. As R increases from 0 to 0.5, the growth rate increases by approximately 80%. However, this increase is considered to be only secondary because the variability in test results from nominally identical tests for other steels is typically within a factor of two (ASTM 2000c). The test results for $R = -1$ are very close to those for $R = 0$ if ΔK is defined as $K_{max} - 0$. The results of tests on G40.21 350WT steel for $R = 0.1$ and 0.5 are also shown in Figure 4-47. The $R = 0.1$ test results include all six specimens because the specimen location did not seem to have any noticeable effect on the crack growth behaviour of 350WT steel. A comparison between the two steels indicates that the difference in the crack growth properties between this particular HPS and 350WT steel might be insignificant.

Since the most frequently reported crack growth behaviour usually refers to a stress ratio, R, of 0, the results from HPS(LT) at $R = 0$ are compared with test results reported in the literature for other steels in Figure 4-48. The results from HPS 485W steel are well

90

within the general scatter band of steels. In fact, the scatter band for HPS 485W steel is very close to the scatter band for ferrite-pearlite steels. The crack propagation properties of this particular HPS do not seem to be different from those of conventional grades of structural steel in the stable crack propagation region.

The crack growth rate can be expressed in the following form:

$$da / dN = C(\Delta K)^m \qquad (4-12)$$

where C and m are crack growth rate constants presented in Table 4-12 for HPS 485W steel and 350WT steel. Table 4-12 also presents the crack growth rate constants obtained using a definition of ΔK as $K_{max} - 0$ for the fully reversed stress condition.

4.3.4. Fracture Toughness Tests

Three fracture toughness tests were performed on HPS 485W steel and four tests on G40.21 350WT steel. Table 4-3 shows the test matrices as well as the test results in terms of fracture behaviour and applicable fracture toughness parameters.

4.3.4.1. HPS 485W steel

Figure 4-49 shows the load versus crack mouth opening displacement curves for three tests on the 51 mm HPS 485W steel plate (HPS(HT)). Although all three specimens failed by instability, there is a significant difference in the amount of deformation occurring before failure. Specimen HPS(HT)-FT-1 showed markedly higher toughness than the other two specimens. Some of this difference may be explained by the difference in testing temperature, since specimen HPS(HT)-FT-1 was tested at –43°C while the other two specimens were tested at about –51°C. However, the behaviours of the two tests at around –51°C, specimen HPS(HT)-FT-2 and specimen HPS(HT)-FT-3, are very similar. Valid K_{Ic} results were obtained from the two specimens, although both of them only marginally met the qualification criteria expressed by Equation (4-5) and Equation (4-6), indicating that a plane strain condition was achieved at the test

91

temperature for the plate thickness. Both tests failed by instability after little stable crack extension was measured.

Figure 4-50 shows the resulting J-R curves for the three fracture toughness test specimens. A valid J_{IC} value was determined for specimen HPS(HT)-FT-1, indicating the point where stable crack extension begins. While both specimen HPS(HT)-FT-2 and HPS(HT)-FT-3 show an apparent R curve, a valid J_{IC} cannot be obtained from specimen HPS(HT)-FT-2 because of the small number of data points. For reference, the dashed lines show the specimens measurement capacity limits, which are defined in ASTM E1820 standard as follows:

$$(J)_{max} = B\sigma_{YS(T)} / 20 \qquad\qquad (4\text{-}13)$$

$$(a/W)_{max} = b_i / 4 + a_i = (1 + 3a_i) / 4 \qquad\qquad (4\text{-}14)$$

where the symbols are as defined earlier. All specimens failed well below these limits.

4.3.4.2. 350WT steel

Figure 4-51 shows the load versus crack mouth opening displacement plots for four tests performed on 350WT steel. Specimen 350WT-FT-1 was tested at room temperature and other three specimens were tested at temperatures close to −50°C. No instability was observed in the 350WT-FT-1 test; the end of the load versus displacement plot indicates where the test was stopped. The clip gauge used to measure the CMOD was repositioned at approximately 3 mm and the test was stopped when the gauge ran out of range for the second time. The specimen underwent a small amount of stable crack extension. The test results for the three specimens tested at low temperature are almost identical. The nonlinear portion of the load versus displacement curve indicates some crack tip blunting (plasticity) before fracture, but still before the onset of stable crack extension because the slope of the unloading lines is still almost constant. However, the tests do not satisfy the

92

requirements for plane strain K_{IC} behaviour for the test temperature and specimen thickness selected.

Figure 4-52 shows the J-R curves for all 350WT specimens. Specimen 350WT-FT-1 reached the specimen measurement capacity limit, which is typical in ductile materials. Again, the J-R curves of the three specimens tested at $-50°C$ are very close to each other. All three specimens showed little plasticity and negligible crack extension before crack instability.

4.3.4.3. Comparison between HPS 485W and 350WT steel behaviours

Comparing Figure 4-49 and Figure 4-51, HPS 485W steel shows two peculiarities in the load versus displacement behaviour compared to 350WT steel. For all three HPS specimens, their respective load carrying capacity is almost constant throughout the fracture test, while 350WT steel tested at room temperature shows apparent strain hardening as plastic strain accumulates. Although the shape of the uniaxial stress versus strain curves of the two materials is similar, it is not known why HPS(HT) steel shows no strain hardening in the fracture toughness tests. Moreover, all three HPS steel specimens showed an unusual unloading behaviour. Figure 4-53 illustrates the difference in unloading between the 350WT steel and HPS(HT) steel. The 350WT steel behaved as expected and the load versus displacement curve started on the elastic unloading curve as soon as the load was reduced. On the other hand, HPS(HT) steel first followed the original loading path (part 1 in Figure 4-53) and then followed a line that is approximately straight and parallel to the original elastic curve (segment 2 in Figure 4-53). The cause of this peculiar behaviour observed in the fracture toughness tests is not known.

Figure 4-54 shows the summary of J for all fracture tests performed on HPS 485W and 350WT steels. The shading of the symbols indicates the failure mode as follows: (1) Open symbols indicate instability occurring before stable crack extension (J_i); (2) Grey symbols indicate instability occurring after some amount of stable crack extension (J_u);

93

and (3) Black symbols indicate no instability occurs before the end of the test (J_{max}). J is plotted in terms of the non-dimensional ratio $J / B\sigma_y$ to reduce the effect of material yield strength and specimen size. Although there is not enough information to fit a complete J versus temperature curve, the expected trend that J increases as temperature increases is observed. At a temperature of –50°C, the 350WT steel indicates a lower shelf behaviour as instability occurs before stable crack extension. HPS 485W steel consistently shows higher toughness at this temperature, although the difference is very small.

4.3.4.4. Fracture surfaces examination

The typical fractured test specimens are shown in Figure 4-55. Specimen 350WT-FT-1 (Figure 4-55 (a)) shows large plastic deformation at room temperature, whereas specimen 350WT-FT-4 (Figure 4-55 (b)) shows no plastic deformation when tested at –50°C. In contrast, a significant amount of plastic deformation is apparent in specimen HPS(HT)-FT-3 (Figure 4-55 (c)) tested at the same low temperature, which can also be seen on the fracture surfaces shown in Figure 4-56. Figure 4-57 and Figure 4-58 show the fracture surface appearances, as observed in a scanning electron microscope, for specimens 350WT-FT-4 and HPS(HT)-FT-3, respectively. The fracture surface of the 350WT steel tested at –50°C shows extensive cleavage facets with only very small areas of microvoid coalescence. The mode of failure for HPS 485W steel can be best classified as quasi-cleavage where more ductile dimples are surrounded by the cleavage facets that are still dominant.

4.4. Testing of HPS Fatigue Detail (Plate with a Central Circular Hole)

Eight test plates with a central circular hole detail were made from the 6.4 mm thick HPS(LT) plate. The test specimens were 264 × 50 × 6.4 mm steel plates with a 7.6 mm diameter hole at the centre. The dimensions of a typical test specimen are shown in Figure 4-59. The gripping length was 82 mm at both ends. Specimens were saw cut from the 6.4 mm plate and the edges were milled smooth but the mill scale remained

94

intact. A 7.6 mm circular hole was drilled at the centre of the specimen after a 3.2 mm pilot hole was drilled initially. The specimen dimensions were obtained with a calliper after the holes were drilled. The measurements indicated that the average hole offset in a set of eight specimens was 0.19 mm and the maximum value was 0.28 mm. All eight specimens were tested under load control at a frequency of 10 Hz with a fully reversed condition for four stress amplitude levels. The failure criterion used to terminate the tests was that the maximum load would drop to half of the initial value and the run-out limit was set at 10 million cycles. The geometry of the specimens, testing conditions and failure criterion were designed to be as close as possible to those used by Sehitoglu (1983) in order to make a direct comparison with ASTM A36 steel.

In seven out of eight specimens, a through-thickness crack was observed to start at one side of the circular hole, generally the side with the smaller edge distance. By the time the crack had almost reached the edge, another smaller crack had usually initiated on the other side of the hole. The fatigue life of the specimens varied from 1.5×10^5 to 10 million cycles (run-out).

The fatigue test results are summarized in Table 4-13 and presented graphically in Figure 4-60. It is apparent from the figure that there is quite a lot of variation among the test results, as is expected in the high cycle fatigue region. The test results for A36 steel obtained by Sehitoglu (1983) are also shown for comparison. In the high cycle fatigue region, HPS(LT) steel seems to perform slightly better than A36 steel in the nominal stress range region between 230 MPa and 350 MPa.

4.5. Summary

An experimental program was conducted to investigate the fatigue performance of high performance steel and to compare its performance with that of conventional structural steels. Monotonic and cyclic material properties of two heats of HPS 485W steel, ASTM A7 steel and G40.21 350WT steel were obtained from material tension tests, Charpy V-Notch tests, and smooth specimen fatigue tests, to provide the input parameters for stress-based, strain-based and energy-based approaches. Crack growth rate tests and

95

fracture toughness tests were also conducted on HPS 485W steel and G40.21 350WT steel. The following summarizes the findings of the test program.

1. The ductility of HPS 485W steel, determined from tension coupon tests, is comparable to the ductility of conventional structural steel.

2. Of three heats of high performance steel, one shows similar upper shelf energy absorption as A7 steel, but has a transition temperature 60°C lower than that of A7 steel. The other two have better performances.

3. A difference of 200 J in the upper shelf energy and 15°C in transition temperature was observed between two different heats of HPS.

4. The HPS 485W steel tested provides a fatigue limit 2.4 times that of conventional structural steels based on smooth specimen fatigue tests.

5. The fatigue crack initiation properties of a higher toughness HPS 485W steel (HPS(HT)) are similar to those for a lower toughness HPS(LT) steel.

6. Crack initiation properties of HPS are similar to conventional structural steels in terms of strain and energy, but very different in terms of stress due to the higher tensile strength of HPS.

7. The effect of mean stress on fatigue life of HPS was found to be significant. The effect of mean stress can be accounted for reliably by the Morrow and SWT models.

8. The crack propagation properties of HPS and 350WT steel are similar.

9. HPS(HT) steel shows slightly higher fracture toughness at low temperature than the conventional notch tough 350WT.

10. Plates with a circular hole detail made from HPS(LT) steel performed slightly better in the high cycle fatigue region than similar plates made of ASTM A36 steel.

96

Table 4-1 Complete Matrix of Material Properties Characterization Test Program

Material*	Chemical Analysis	Charpy V-Notch Test	Tension Coupon Test	Smooth Specimen Fatigue Test		Crack Growth Rate Test	Fracture Toughness Test
				FR Series	MS Series		
HPS(LT)	1	25 (L)**	3 (L)	22 (L)	9 (L)	9 (L)	
			3 (T)**	5 (T)			
HPS(HT)		24 (L)	3 (L)	11 (L)	4 (L)		3 (L)
A7	1	25 (T)	4 (T)	6 (T)			
350WT		3 (L)	3 (L)			8 (L)	4 (L)

* HPS(LT) and HPS(HT) are two heats of HPS 485W steel with remarkably different toughness, where LT and HT represent the relatively low and high toughness character of the plates. 4 Charpy V-Notch tests were also conducted on a HPS plate with medium toughness that is designated as HPS(MT).

L** Longitudinal, specimens oriented in the rolling direction of plate.

T** Transverse, specimens oriented in the transverse direction of plate.

Table 4-2 Summary of Crack Growth Rate Test Conditions

Material	Load Ratio R P_{min}/P_{max}	Specimen Designation	Specimen Location	Maximum Testing Load P_{max} (kN)
HPS(LT)	-1	HPS(LT)-CGR-1	Full thickness	15.0
		HPS(LT)-CGR-2	Full thickness	12.0
		HPS(LT)-CGR-3	Full thickness	12.0
	0	HPS(LT)-CGR-4	Full thickness	15.0
		HPS(LT)-CGR-5	Full thickness	16.0
		HPS(LT)-CGR-6	Full thickness	14.0
	0.5	HPS(LT)-CGR-7	Full thickness	28.0
		HPS(LT)-CGR-8	Full thickness	26.0
		HPS(LT)-CGR-9	Full thickness	26.0
350WT	0.1	350WT-CGR-1	Surface	50.0
		350WT-CGR-2	Surface	50.0
		350WT-CGR-3	Surface	50.0
		350WT-CGR-4	Surface	60.0
		350WT-CGR-5	Middle	50.0
		350WT-CGR-6	Middle	50.0
	0.5	350WT-CGR-7	Surface	60.0
		350WT-CGR-8	Surface	60.0

97

Table 4-3 Summary of Fracture Toughness Tests

Material	Thickness (mm)	Specimen Designation	Test Temperature (°C)	Fracture Behaviour*	K_Q ($MPa\sqrt{m}$)	J_c, J_u, J_{max} (kJ/m³)	J_{ic} (kJ/m³)
HPS(HT)	50	HPS(HT)-FT-1	-43	II	79	799	103
		HPS(HT)-FT-2	-52	II	68[a]	107	N.A.[b]
		HPS(HT)-FT-3	-50	II	72[a]	167	58
350WT	38	350WT-FT-1	+20	III	72	852	685
		350WT-FT-2	-50	I	62	61	
		350WT-FT-3	-50	I	65	42	
		350WT-FT-4	-50	I	66	51	

* Fracture behaviour I, instability before stable crack extension.

 Fracture behaviour II, instability after some stable crack extension.

 Fracture behaviour III, no instability by the end of test.

[a] Valid K_{ic}.

[b] Not available because of too few data points.

Table 4-4 Chemical Analyses of HPS 485W and A7 Steels (% Weight)

(a). Chemical Analysis Results of HPS 485W and A7 steels

Material	C	Mn	P	S	Si	Cu	Ni	Cr	Mo	V	Al	N
HPS 485W*	0.102	1.15	0.010	0.005	0.33	0.299	0.311	0.53	0.047	0.051	0.026	0.008
A7	0.216	0.737	0.005	0.017	<0.01	0.013	0.014	0.013	0.006			

* Sample was taken from the 6.4 mm HPS plate HPS(LT). The chemistry was found to be very close to that from mill report. The report also showed that the difference between the chemical composition of the three HPS 485W steel plates of different thicknesses (from three different heats) is negligible.

(b). Chemical Composition Requirements for HPS 485W and A7 steels

Material	C	Mn	P	S	Si	Cu	Ni	Cr	Mo	V	Al	N
HPS 485W	0.11 max	1.10-1.35	0.020 max	0.006 max	0.30-0.50	0.25-0.40	0.25-0.40	0.45-0.70	0.02-0.08	0.04-0.08	0.010-0.040	0.015 max
A7			0.04 max	0.05 max								

98

Table 4-5 Charpy V-Notch Impact Tests Results — Half-size Specimens

HPS 485W (6.4 mm plate)

Temperature (°C)	Specimen Designation	CVN Energy (J)
-75	HPS(LT)-CVN-1	19
	HPS(LT)-CVN-2	27
	HPS(LT)-CVN-3	22
-60	HPS(LT)-CVN-4	35
	HPS(LT)-CVN-5	43
	HPS(LT)-CVN-6	49
-45	HPS(LT)-CVN-7	73
	HPS(LT)-CVN-8	49
	HPS(LT)-CVN-9	43
	HPS(LT)-CVN-10	49
	HPS(LT)-CVN-11	68
-35	HPS(LT)-CVN-12	76
	HPS(LT)-CVN-13	81
	HPS(LT)-CVN-14	43
	HPS(LT)-CVN-15	84
	HPS(LT)-CVN-16	52
-24	HPS(LT)-CVN-17	81
	HPS(LT)-CVN-18	84
	HPS(LT)-CVN-19	87
0	HPS(LT)-CVN-20	95
	HPS(LT)-CVN-21	98
	HPS(LT)-CVN-22	87
+25	HPS(LT)-CVN-23	92
	HPS(LT)-CVN-24	103
	HPS(LT)-CVN-25	106

A7 (6.4 mm plate)

Temperature (°C)	Specimen Designation	CVN Energy (J)
-75	A7-CVN-1	3
	A7-CVN-2	3
	A7-CVN-3	3
-60	A7-CVN-4	3
	A7-CVN-5	3
	A7-CVN-6	5
-45	A7-CVN-7	3
	A7-CVN-8	3
	A7-CVN-9	3
-35	A7-CVN-10	3
	A7-CVN-11	3
	A7-CVN-12	3
-24	A7-CVN-13	5
	A7-CVN-14	5
	A7-CVN-15	5
0	A7-CVN-16	16
	A7-CVN-17	19
	A7-CVN-18	19
+12	A7-CVN-19	76
	A7-CVN-20	57
	A7-CVN-21	84
	A7-CVN-22	54
+25	A7-CVN-23	92
	A7-CVN-24	100
	A7-CVN-25	108

99

Table 4-6 Charpy V-Notch Impact Tests Results — Full-size Specimens

HPS 485W (19 mm plate)

Temperature (°C)	Specimen Designation	CVN Energy (J)
+25	HPS(MT)-CVN-1	255
	HPS(MT)-CVN-2	229
	HPS(MT)-CVN-3	231
	HPS(MT)-CVN-4	228

HPS 485W (51 mm plate)

Temperature (°C)	Specimen Designation	Specimen Location	CVN Energy (J)
-75	HPS(HT)-CVN-1	Side	163
	HPS(HT)-CVN-2	Middle	7
	HPS(HT)-CVN-3	Side	56
	HPS(HT)-CVN-4	Middle	159
	HPS(HT)-CVN-5	Side	148
-60	HPS(HT)-CVN-6	Side	163
	HPS(HT)-CVN-7	Middle	9
	HPS(HT)-CVN-8	Side	165
-45	HPS(HT)-CVN-9	Side	176
	HPS(HT)-CVN-10	Middle	201
	HPS(HT)-CVN-11	Side	15
-35	HPS(HT)-CVN-12	Side	195
	HPS(HT)-CVN-13	Middle	119
	HPS(HT)-CVN-14	Side	172
	HPS(HT)-CVN-15	Side	186
-24	HPS(HT)-CVN-16	Side	194
	HPS(HT)-CVN-17	Middle	199
	HPS(HT)-CVN-18	Side	209
0	HPS(HT)-CVN-19	Side	216
	HPS(HT)-CVN-20	Middle	262
	HPS(HT)-CVN-21	Side	239
+25	HPS(HT)-CVN-22	Side	269
	HPS(HT)-CVN-23	Middle	369
	HPS(HT)-CVN-24	Side	328

350WT (38 mm plate)

Temperature (°C)	Specimen Designation	CVN Energy (J)
-45	350WT-CVN-1	170
	350WT-CVN-2	141
	350WT-CVN-3	106

100

Table 4-7 Tension Coupon Tests Results

Material	Orientation	Specimen Designation	Young's Modulus (MPa)	Static Yield Strength[a] (MPa)	Static Tensile Strength (MPa)	Elongation[b] (%)	Reduction in Area (%)
HPS(LT)	Longitudinal	HPS(LT)-TC-1	200 500	447	660	26	61
		HPS(LT)-TC-2	194 900	424	641	27	41
		HPS(LT)-TC-3	195 800	443	657	25	49
		Average	197 100	438	653	26	50
	Transverse	HPS(LT)-TC-4	202 600	442	649	23	38
		HPS(LT)-TC-5	199 200	447	639	20	49
		HPS(LT)-TC-6	201 900	448	636	25	45
		Average	201 200	446	641	23	44
HPS(HT)	Longitudinal	HPS(HT)-TC-1	205 600	438	505	29	68
		HPS(HT)-TC-2	194 500	459	518	27	60
		HPS(HT)-TC-3	191 000	461	532	25	63
		Average	197 000	453	518	27	64
A7	Transverse	A7-TC-1	203 200	275	389	31	56
		A7-TC-2	200 400	256	370	31	58
		A7-TC-3	198 000	252	371	30	61
		A7-TC-4	203 900	250	375	34	61
		Average	201 400	258	376	32	59
350WT	Longitudinal	350WT-TC-1	187 100	360	472	N.A.*	N.A.
		350WT-TC-2	198 700	365	441	N.A.	N.A.
		350WT-TC-3	188 700	369	471	N.A.	N.A.
		Average	191 500	365	461		

[a] Yield strength was obtained using the 0.2% offset method.

[b] Gauge length is 50 mm for HPS(LT) and A7 coupons, and is 200 mm for HPS(HT) and 350WT coupons.

* Not available.

101

Table 4-8 FR Series Smooth Specimen Fatigue Test Results

Material	Orientation	Control	Specimen Designation	Total Strain Amplitude $\Delta\varepsilon/2$ (%)	Stress Amplitude $\Delta\sigma/2$ (MPa)	No. of Cycles to Failure N_f (×1000)	Elastic Strain Amplitude $\Delta\varepsilon^e/2$ (%)	Plastic Strain Amplitude $\Delta\varepsilon^p/2$ (%)	Plastic Strain Energy ΔW^p (MJ/m³)
HPS(LT)	Longitudinal	Strain	HPS(LT)-FR-1	0.67	522	0.8	0.265	0.407	6.88
			HPS(LT)-FR-2	0.63	499	2	0.253	0.380	6.04
			HPS(LT)-FR-3	0.63	503	2	0.255	0.373	5.81
			HPS(LT)-FR-4	0.44	449	11	0.228	0.211	2.41
			HPS(LT)-FR-5	0.40	471	6	0.239	0.161	2.40
			HPS(LT)-FR-6	0.40	454	10	0.230	0.169	2.24
			HPS(LT)-FR-7	0.40	453	6	0.230	0.166	2.12
			HPS(LT)-FR-8	0.40	466	6	0.236	0.159	2.18
			HPS(LT)-FR-9	0.31	433	18	0.220	0.088	0.98
			HPS(LT)-FR-10	0.29	443	21	0.225	0.070	0.93
			HPS(LT)-FR-11	0.29	443	17	0.225	0.069	0.79
			HPS(LT)-FR-12	0.17	321	354	0.163	0.010	0.04
			HPS(LT)-FR-13	0.16	355	510	0.158	0.000	0.03
			HPS(LT)-FR-14	0.12	226	10 000*	0.115	0.001	0.00
			HPS(LT)-FR-15	0.11	179	10 000*	0.091	0.017	0.01
			HPS(LT)-FR-16	0.10	192	10 000*	0.095	0.000	0.00
		Stress	HPS(LT)-FR-17	0.15	298	10 000*	0.151	0.001	0.00
			HPS(LT)-FR-18	0.15	298	10 000*	0.149	0.000	0.00
			HPS(LT)-FR-19	0.14	298	7 427	0.139	0.000	0.00
			HPS(LT)-FR-20	0.14	265	10 000*	0.134	0.007	0.00
			HPS(LT)-FR-21	0.14	252	10 000*	0.128	0.011	0.00
			HPS(LT)-FR-22	0.11	238	10 000*	0.110	0.000	0.00
	Transverse	Strain	HPS(LT)-FR-23	0.63	492	2	0.245	0.382	5.81
			HPS(LT)-FR-24	0.63	507	2	0.252	0.374	6.26
			HPS(LT)-FR-25	0.27	434	24	0.216	0.053	0.61
			HPS(LT)-FR-26	0.27	450	21	0.224	0.043	0.58
			HPS(LT)-FR-27	0.10	236	10 000*	0.099	0.000	0.00

102

Table 4-8 FR Series Smooth Specimen Fatigue Test Results (Cont'd)

Material	Orientation	Control	Specimen Designation	Total Strain Amplitude	Stress Amplitude	No. of Cycles to Failure	Elastic Strain Amplitude	Plastic Strain Amplitude	Plastic Strain Energy
				$\Delta\varepsilon/2$ (%)	$\Delta\sigma/2$ (MPa)	N_f (×1000)	$\Delta\varepsilon^e/2$ (%)	$\Delta\varepsilon^p/2$ (%)	ΔW^p (MJ/m³)
HPS(HT)	Longitudinal	Strain	HPS(HT)-FR-1	0.63	448	2	0.227	0.399	5.79
			HPS(HT)-FR-2	0.40	401	8	0.204	0.196	2.38
			HPS(HT)-FR-3	0.28	399	14	0.202	0.074	0.91
			HPS(HT)-FR-4	0.19	335	92	0.170	0.025	0.19
			HPS(HT)-FR-5	0.18	334	125	0.170	0.006	0.05
			HPS(HT)-FR-6	0.16	306	400	0.155	0.003	0.01
		Stress	HPS(HT)-FR-7	0.16	304	312	0.154	0.004	0.02
			HPS(HT)-FR-8	0.14	287	354	0.142	0.000	0.00
			HPS(HT)-FR-9	0.14	284	719	0.143	0.000	0.01
			HPS(HT)-FR-10	0.13	271	4 271[a]	0.126	0.000	0.00
			HPS(HT)-FR-11	0.13	269	10 000*	0.129	0.000	0.00
A7	Transverse	Strain	A7-FR-1	0.63	296	2	0.147	0.478	4.45
			A7-FR-2	0.62	308	2	0.153	0.471	4.69
			A7-FR-3	0.28	228	22	0.113	0.170	1.12
			A7-FR-4	0.28	235	17	0.117	0.166	1.15
			A7-FR-5	0.28	235	16	0.117	0.165	1.14
			A7-FR-6	0.10	198	10 000*	0.097	0.000	0.00

* Run-out.

[a] Specimen failed near lower grip.

103

Table 4-9 MS Series Smooth Specimen Fatigue Test Results

Material	Mean Stress Ratio $\frac{\sigma_m}{\Delta\sigma/2}$	Specimen Designation	Mean Stress σ_m (MPa)	Stress Amplitude $\Delta\sigma/2$ (MPa)	Total Strain Amplitude $\Delta\varepsilon/2$ (%)	No. of Cycles to Failure N_f (×1000)	Plastic Strain Energy ΔW^p (MJ/m³)
HPS(LT)	1	HPS(LT)-MS-1	291	288	0.15	88	0.09
		HPS(LT)-MS-2	269	270	0.13	119	0.05
		HPS(LT)-MS-3	248	256	0.12	97	0.05
		HPS(LT)-MS-4	251	243	0.15	8 447	0.00
		HPS(LT)-MS-5	226	227	0.11	10 000*	0.03
		HPS(LT)-MS-6	228	214	0.11	5 354	0.00
	3	HPS(LT)-MS-7	483	153	0.09	97	0.01
		HPS(LT)-MS-8	471	152	0.09	10 000*	0.00
		HPS(LT)-MS-9	458	143	0.08	10 000*	0.00
HPS(HT)	1	HPS(HT)-MS-1	246	240	0.13	130	0.07
		HPS(HT)-MS-2	234	233	0.12	308	0.06
		HPS(HT)-MS-3	227	232	0.11	293	0.04
		HPS(HT)-MS-4	232	225	0.11	10 000*	0.05

* Run-out.

Table 4-10 Cyclic Material Properties of HPS 485W and A7 Steels

Material	Orientation	K' (MPa)	n'	σ_f' (MPa)	b	ε_f'	c
HPS(LT)	Longitudinal	956	0.113	851	-0.069	0.775	-0.701
HPS(LT)	Transverse	690	0.058	741	-0.052	1.917	-0.830
HPS(HT)	Longitudinal	666	0.076	776	-0.073	6.207	-0.940
A7	Transverse	1139	0.248	760	-0.121	0.196	-0.486

Table 4-11 Energy-Life Curves of HPS 485W and A7 Steels

Material	Orientation	F_p (MJ/m³)	α_p	F (MJ/m³)	α	ΔW_0 (MJ/m³)	F_t (MJ/m³)	α_t	$\Delta W_0'$ (MJ/m³)
HPS(LT)	Longitudinal	2163	-0.784	705	-0.585	0.79	1463	-0.721	0.20
HPS(LT)	Transverse	6064	-0.922	1012	-0.642	1.02	2855	-0.814	0.25
HPS(HT)	Longitudinal	4523	-0.880	577	-0.578	0.58	1497	-0.741	0.14
A7	Transverse	622	-0.642	431	-0.560	0.12	551	-0.621	0.03

104

Table 4-12 Crack Propagation Properties of HPS 485W and 350WT Steels

Material	Load Ratio R P_{min}/P_{max}	C	m	Condition
HPS(LT)	-1	2.27×10^{-10}	3.26	$\Delta K = K_{max} - K_{min}$
	-1	2.18×10^{-9}	3.26	$\Delta K = K_{max} - 0$
	0	3.06×10^{-9}	3.12	
	0.5	5.48×10^{-9}	3.14	
350WT	0.1	8.88×10^{-9}	3.03	
	0.5	2.89×10^{-9}	3.59	

Note: ΔK in MPa$\sqrt{m}$ and da/dN in mm/cycle, based on test results for
$5 \times 10^{-6} \leq da/dN \leq 10^{-3}$ mm/cycle.

Table 4-13 Fatigue Test Results from Plates Made with HPS(LT) Steel

Specimen Designation	Nominal Stress Range (MPa)	No. of Cycles to Failure ($\times 1000$)
HPS-D-1	230	1 142
HPS-D-2	231	1 046
HPS-D-3	234	10 000*
HPS-D-4	246	1 189
HPS-D-5	252	1 016
HPS-D-6	262	1 277
HPS-D-7	262	637
HPS-D-8	347	151[a]

* Run-out.

[a] Test was continued on run-out specimen HPS-D-3 at higher stress range.

105

Notes:
- Shaded areas were discarded
- All dimensions are in mm
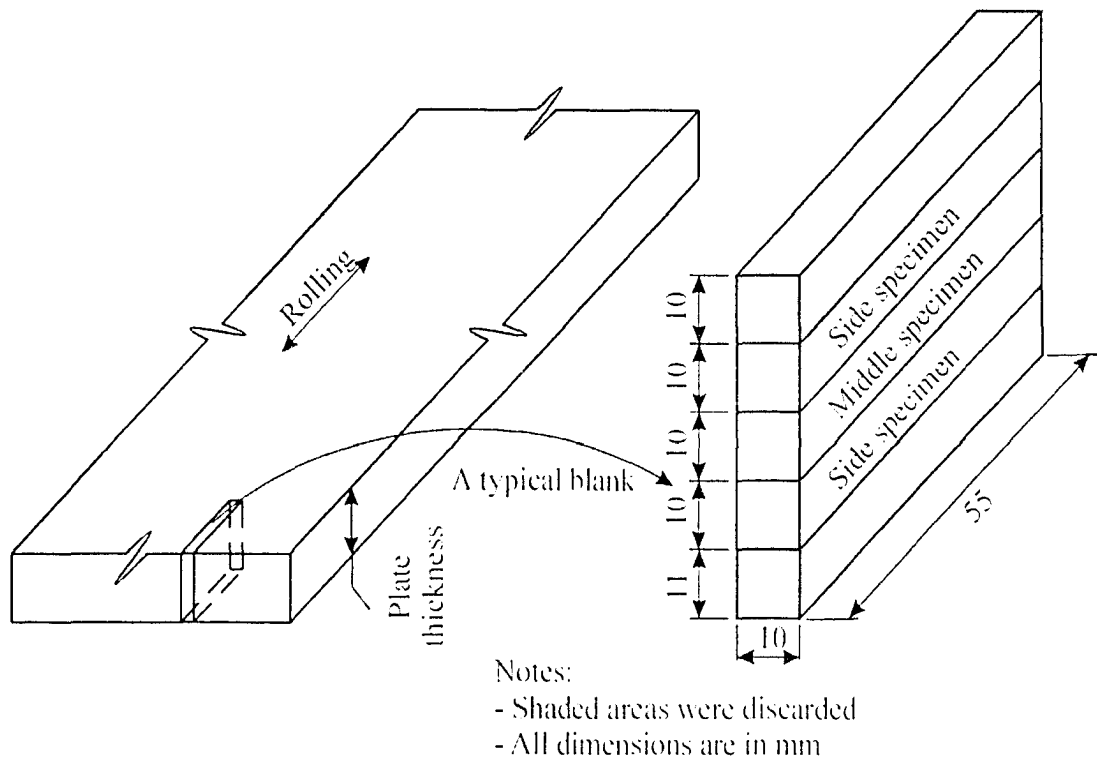
Figure 4-1 CVN Specimen Locations in 51 mm thick HPS 485W Steel Plate
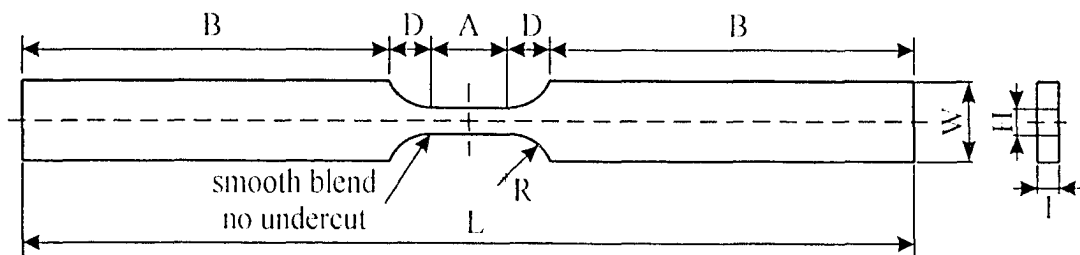
Reduced section length	A	21.5 mm
Reduced section width	H	8.3 mm
Gripping length	B	105.0 mm
Gripping width	W	25.4 mm
Radius	R	12.7 mm
Transition length	D	12.0 mm
Overall length	L	255.5 mm
Thickness	I	6.0 mm

Figure 4-2 Flat Sheet Smooth Fatigue Specimen with Rectangular Cross Section

106
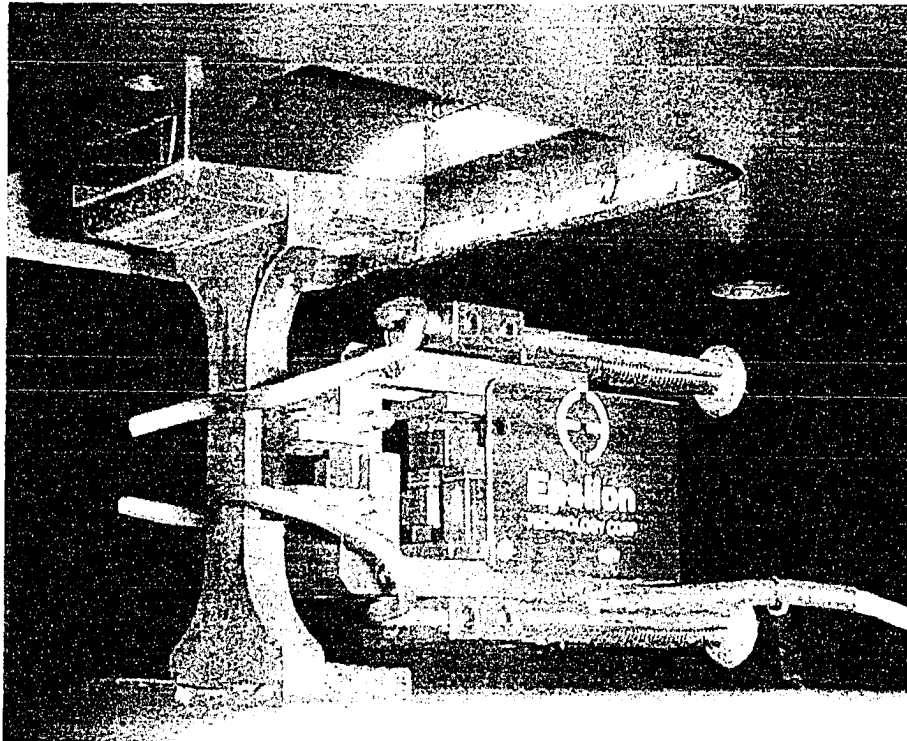
Figure 4-3 Smooth Specimen Fatigue Test Set-up
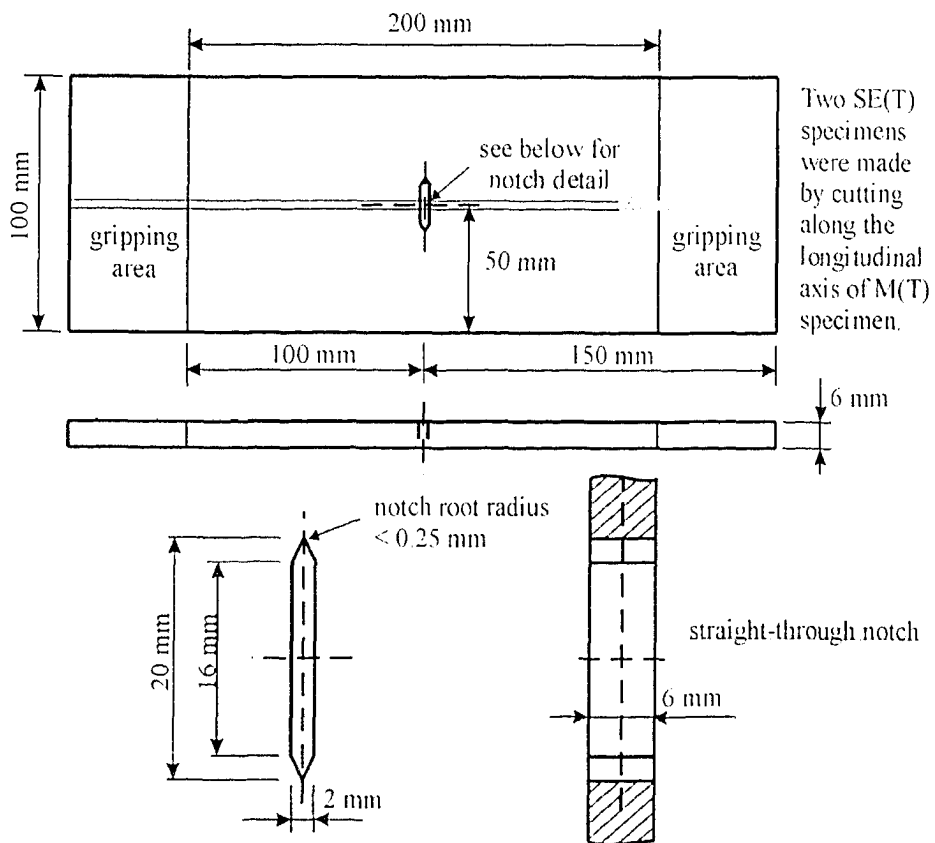
Figure 4-4 Geometry and Notch Detail of Crack Growth Rate Specimen

107
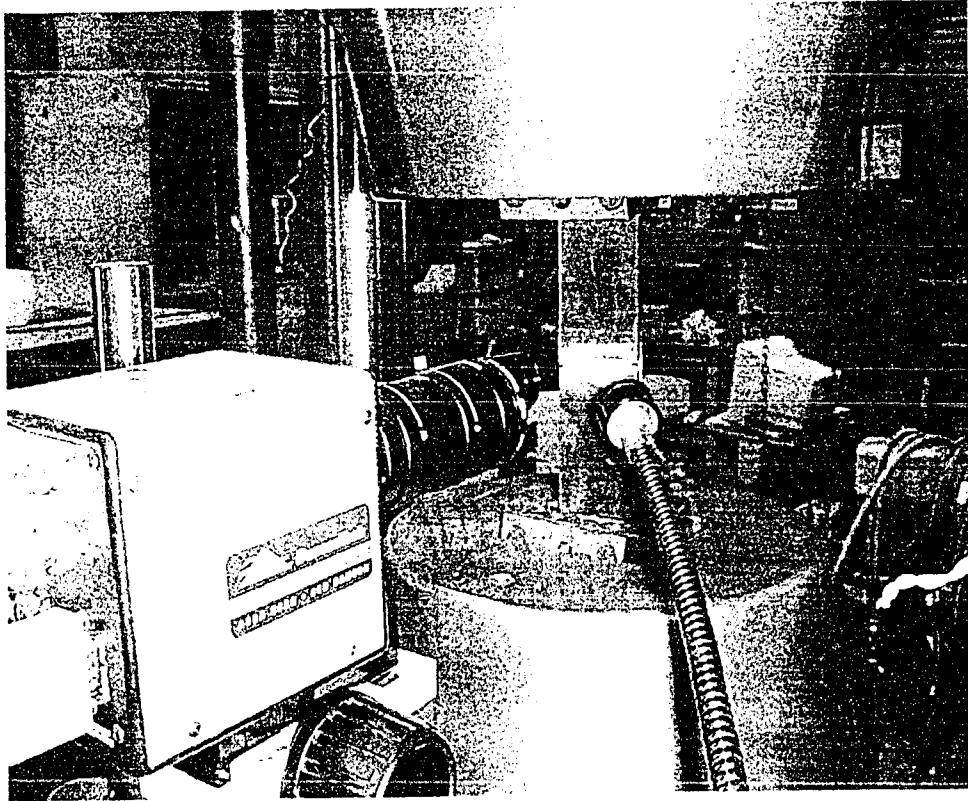
Figure 4-5 Crack Growth Rate Test Set-up
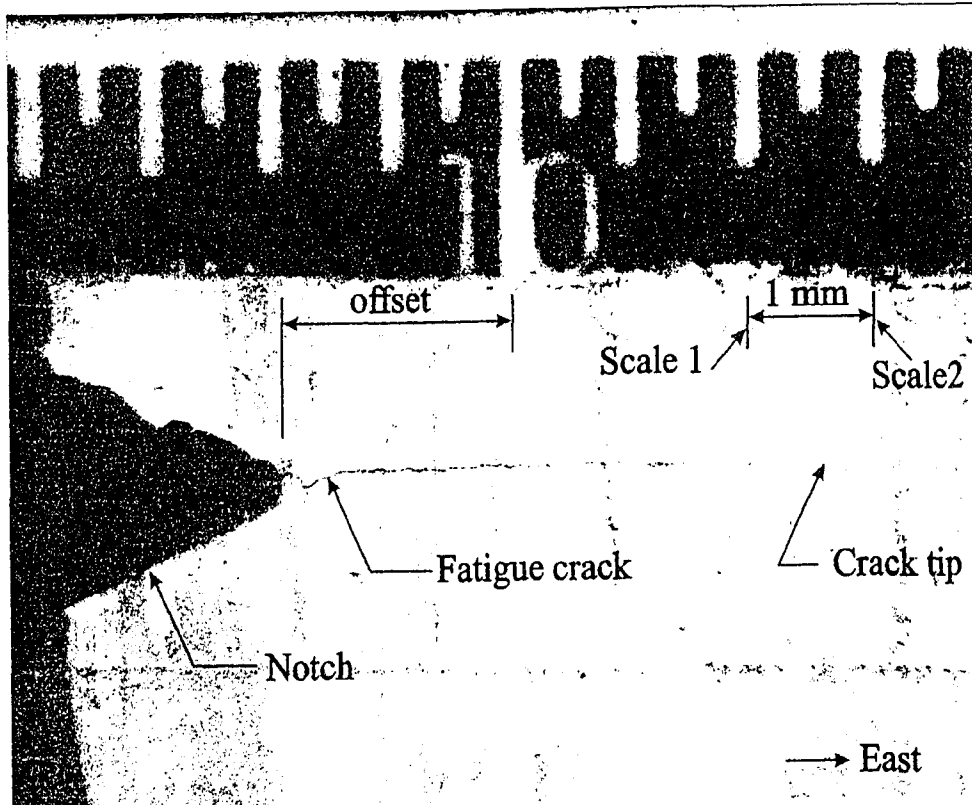
Figure 4-6 Illustration of Crack Length Measurement

108

Load Line

4 mm

45 mm

S=4W

2.25W | 2.25W

W

B
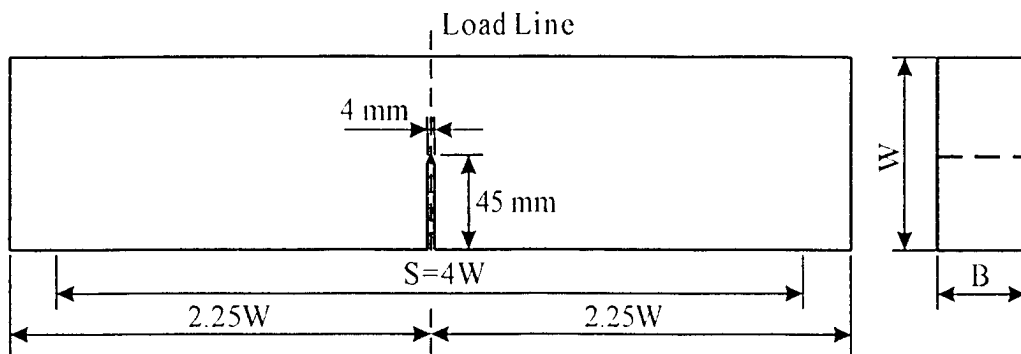
Figure 4-7 Fracture Toughness Specimen SE(B)
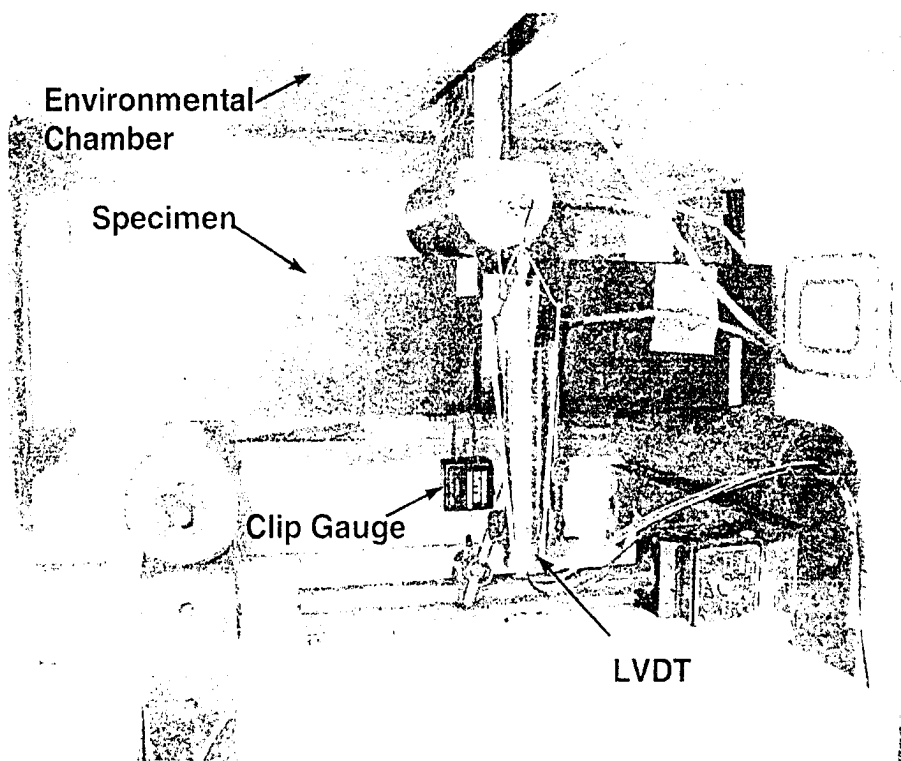
Figure 4-8 Fracture Toughness Test Fixture

109
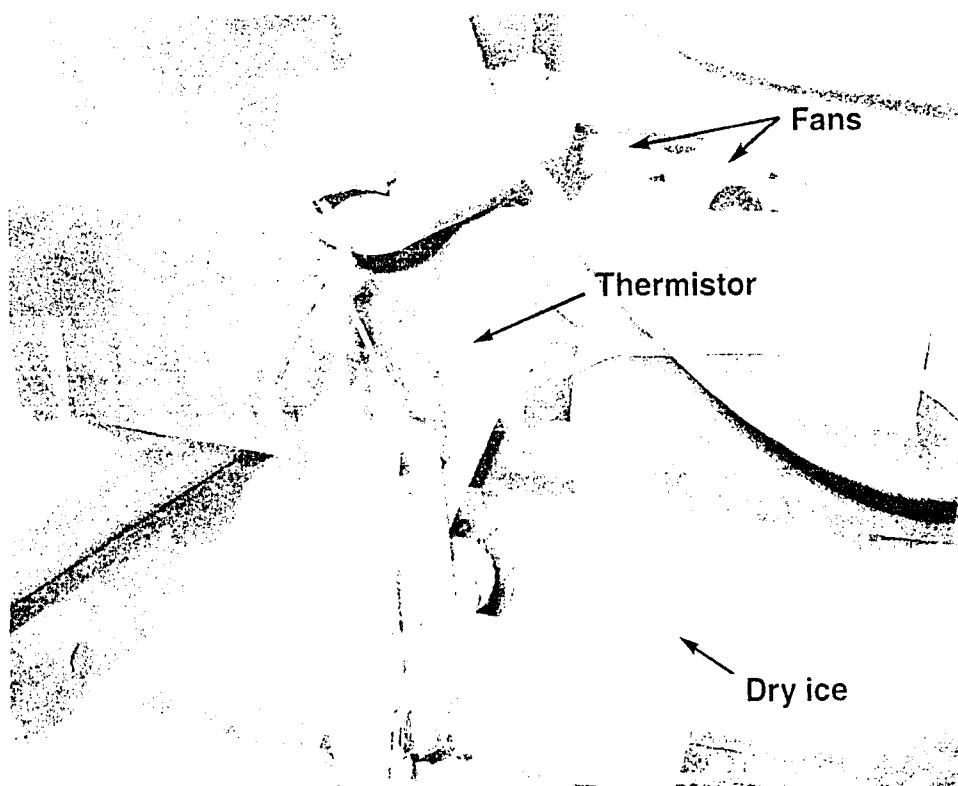
Figure 4-9 Low Temperature Fracture Toughness Test Set-up
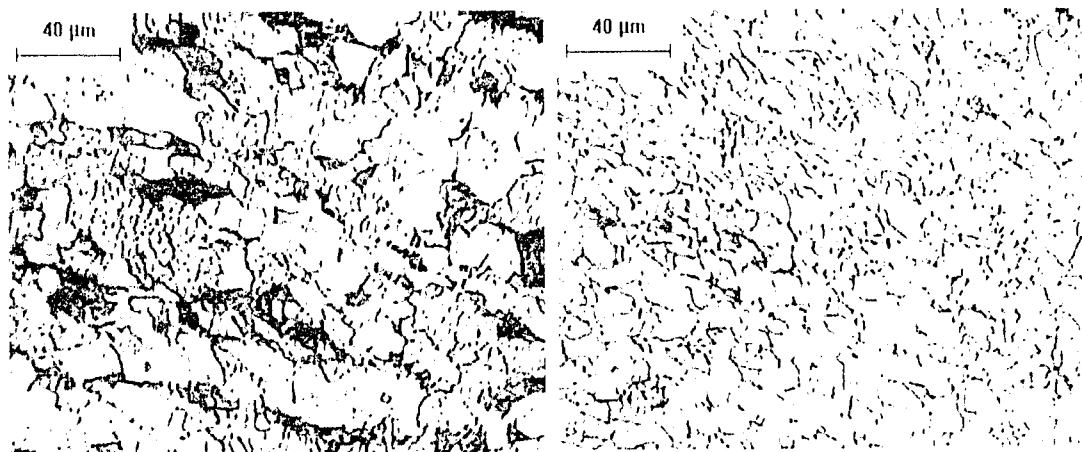
(a) 350WT Steel   (b) HPS 485W Steel

Figure 4-10 Microstructure of HPS 485W and 350WT Steels

110
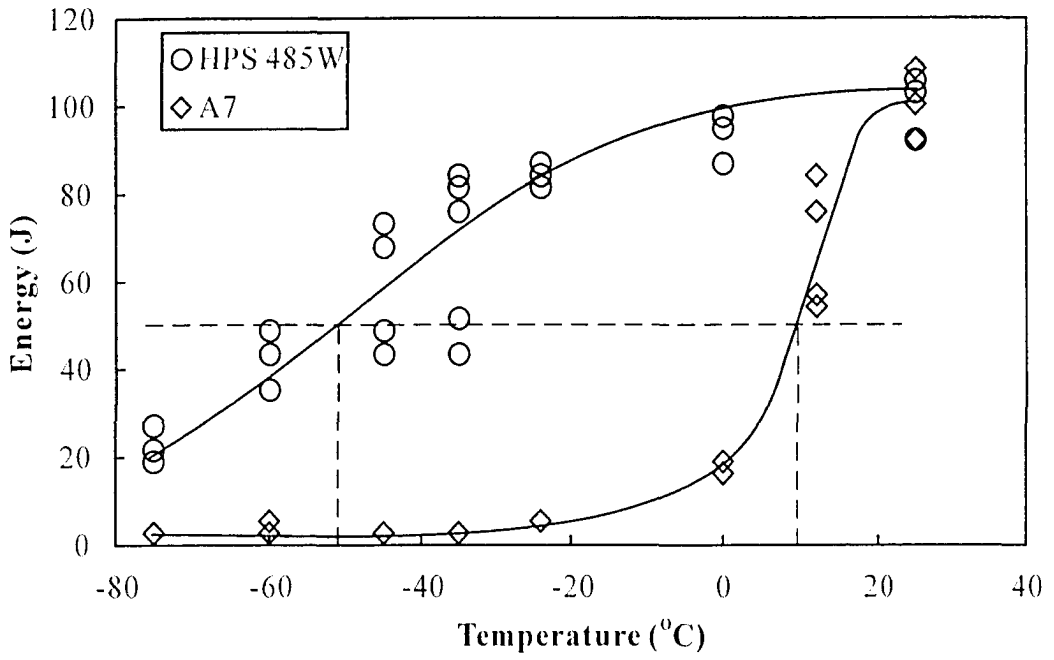
Figure 4-11 Charpy V-Notch Energy versus Temperature for HPS 485W and A7 Steels

(both from 6.4 mm thick plate)
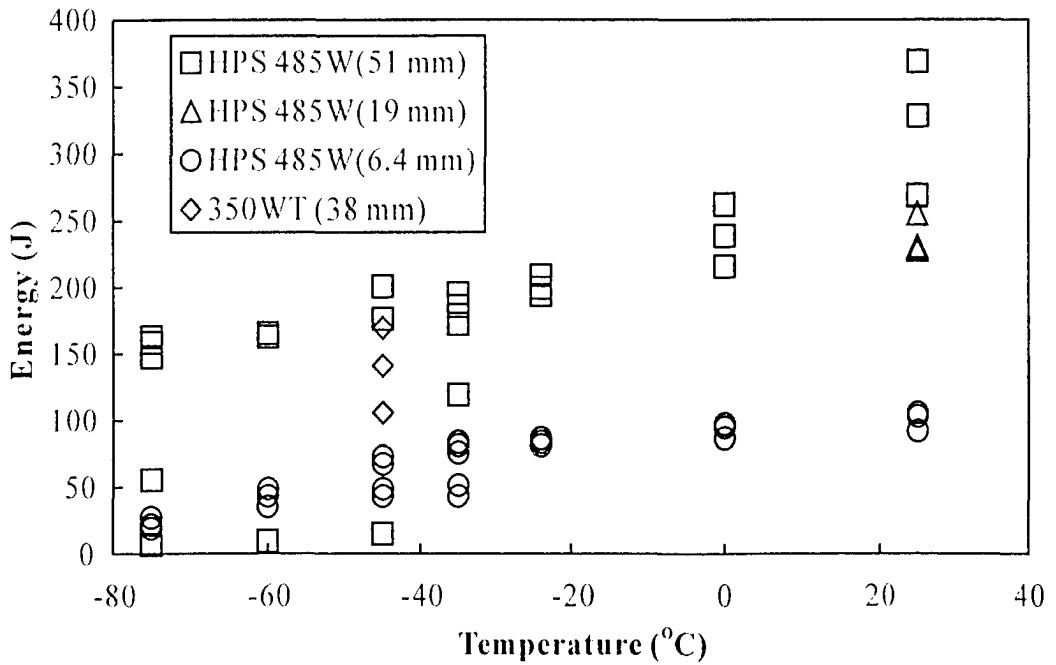
Figure 4-12 Charpy V-Notch Energy versus Temperature for

HPS 485W and 350WT Steels

111
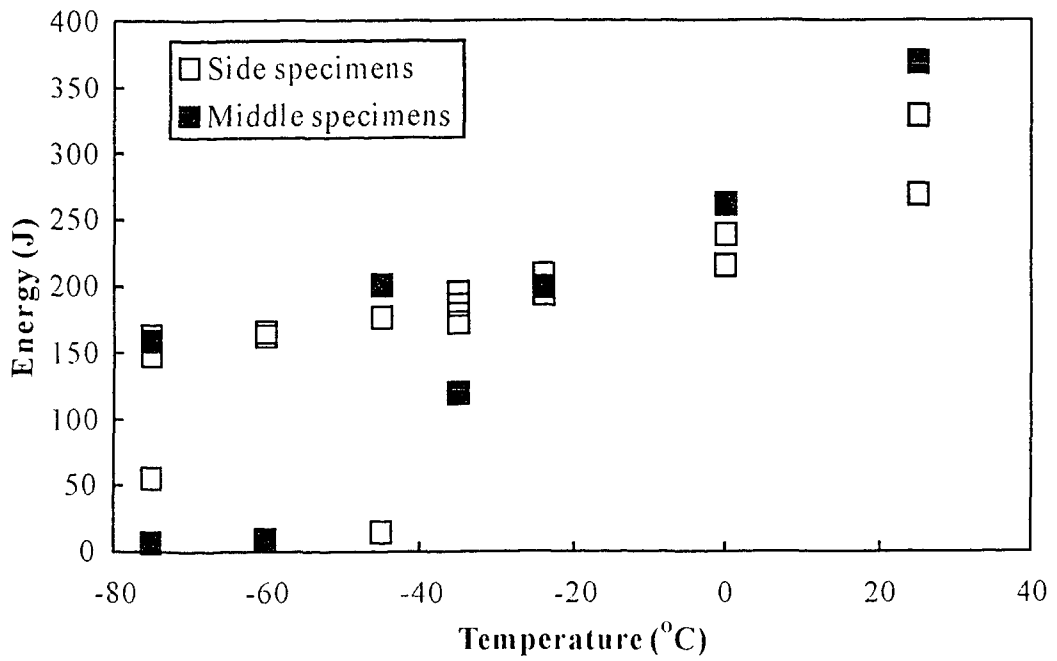
Figure 4-13 Comparison of Charpy V-Notch Energy versus Temperature between Side Specimens and Middle Specimens from the 51 mm HPS 485W Steel Plate
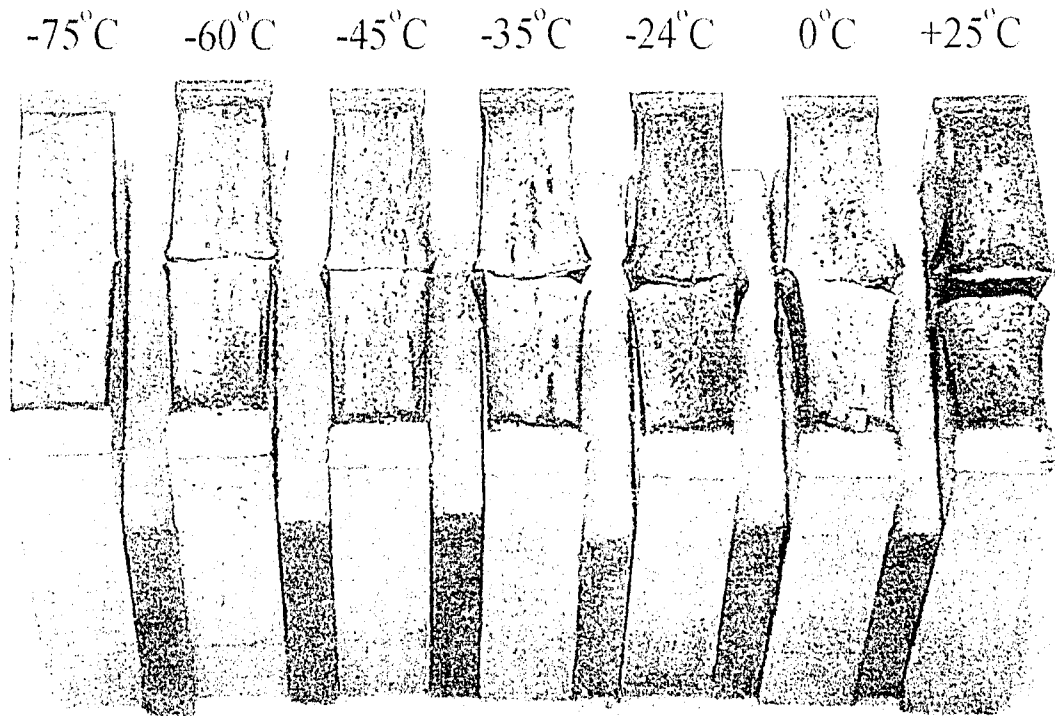
Figure 4-14 Fracture Surfaces at Various Temperatures of Typical Charpy V-Notch Half-Size Specimens from 6.4 mm HPS 485W Steel Plate

112
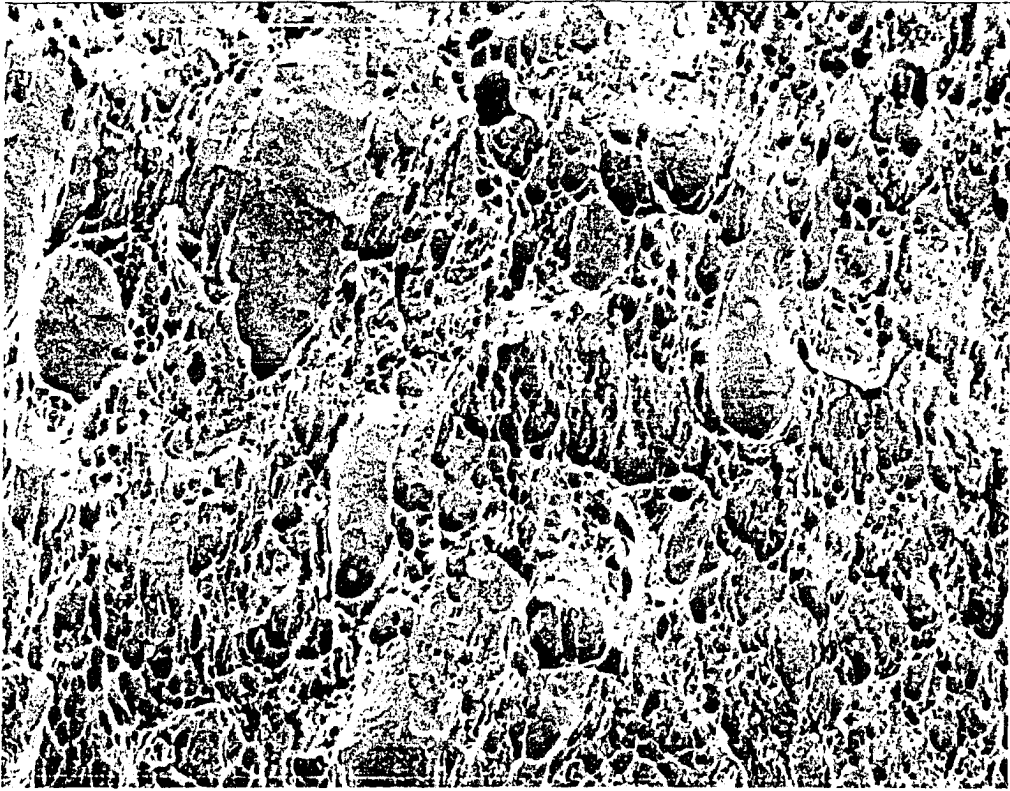
Figure 4-15 Ductile Fracture of HPS(LT) Steel at Room Temperature (+25°C)
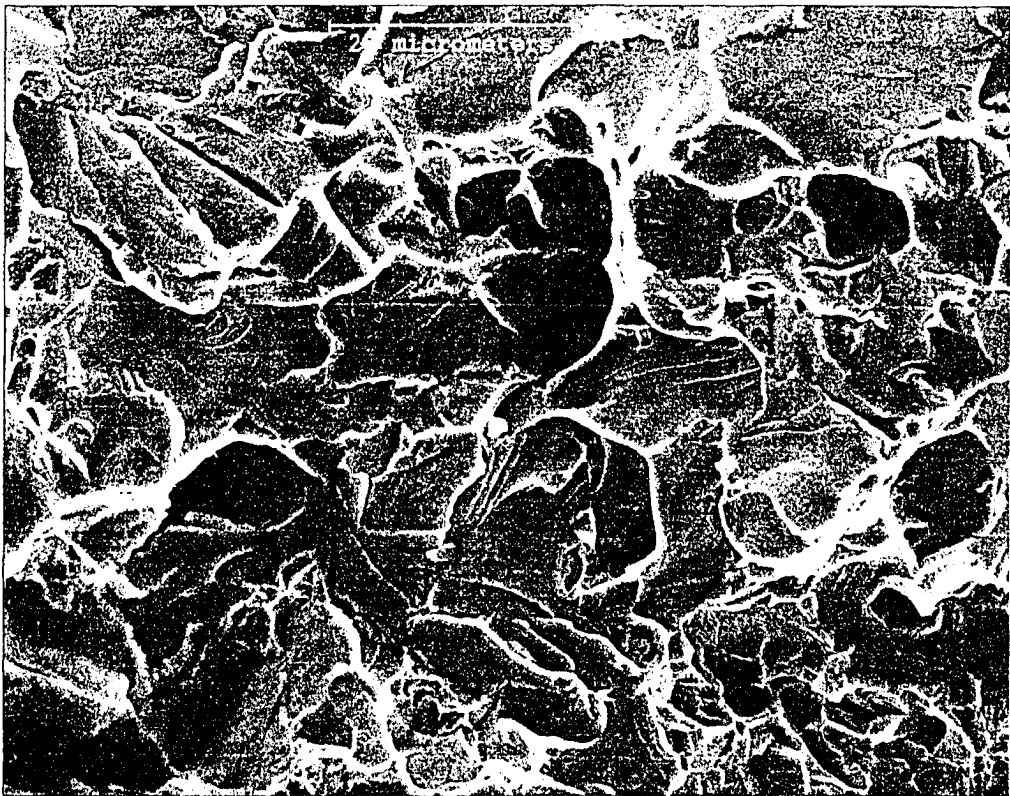
Figure 4-16 Brittle Fracture of HPS(LT) Steel at Low Temperature (–75°C)

113
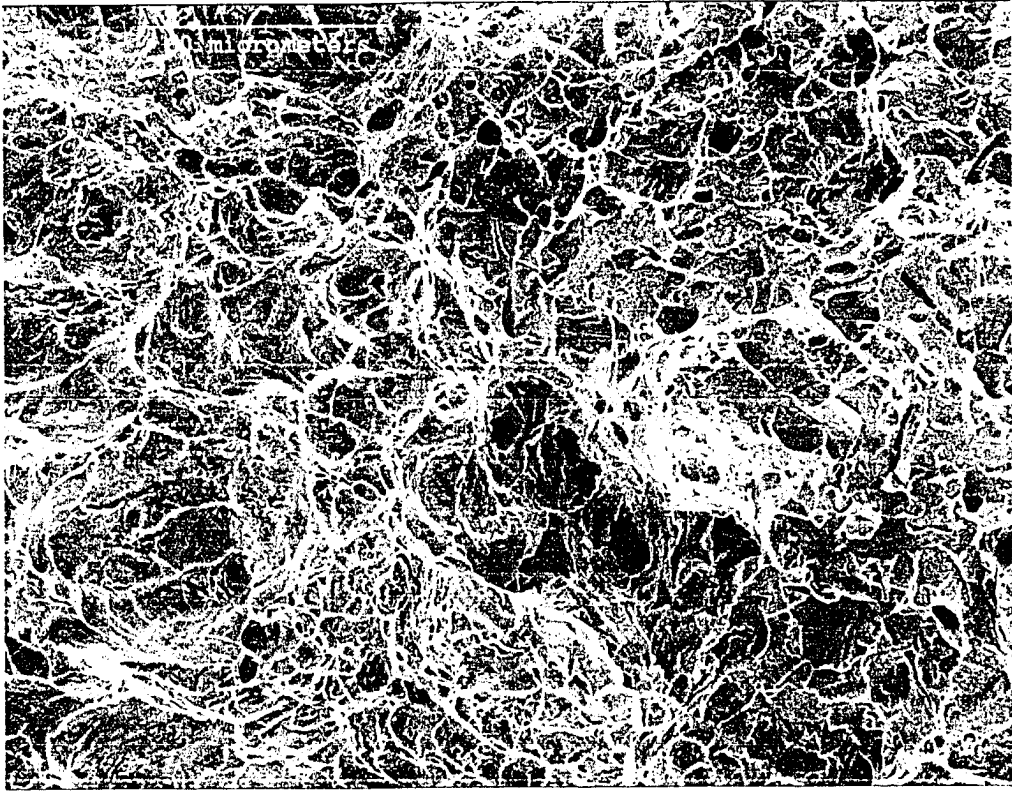
Figure 4-17 Mixed Fracture HPS(LT) Steel at Transition Temperature (–45°C)
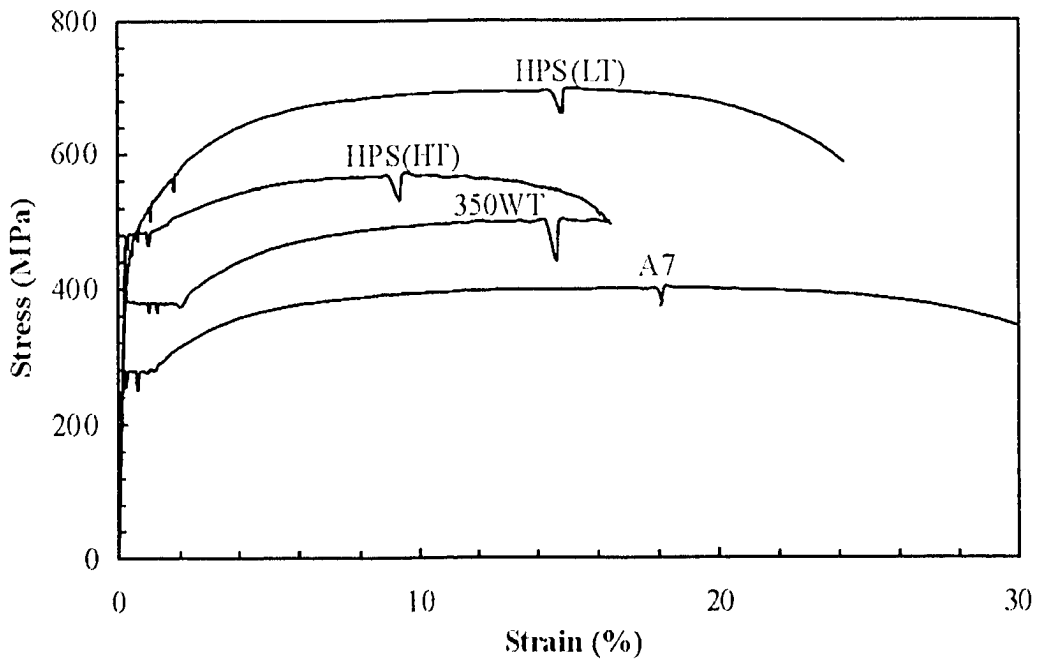
Figure 4-18 Typical Stress versus Strain Curves for HPS 485W, A7, and 350WT Steels

114

Figure 4-19 Fracture of HPS(HT) Steel Tension Coupons
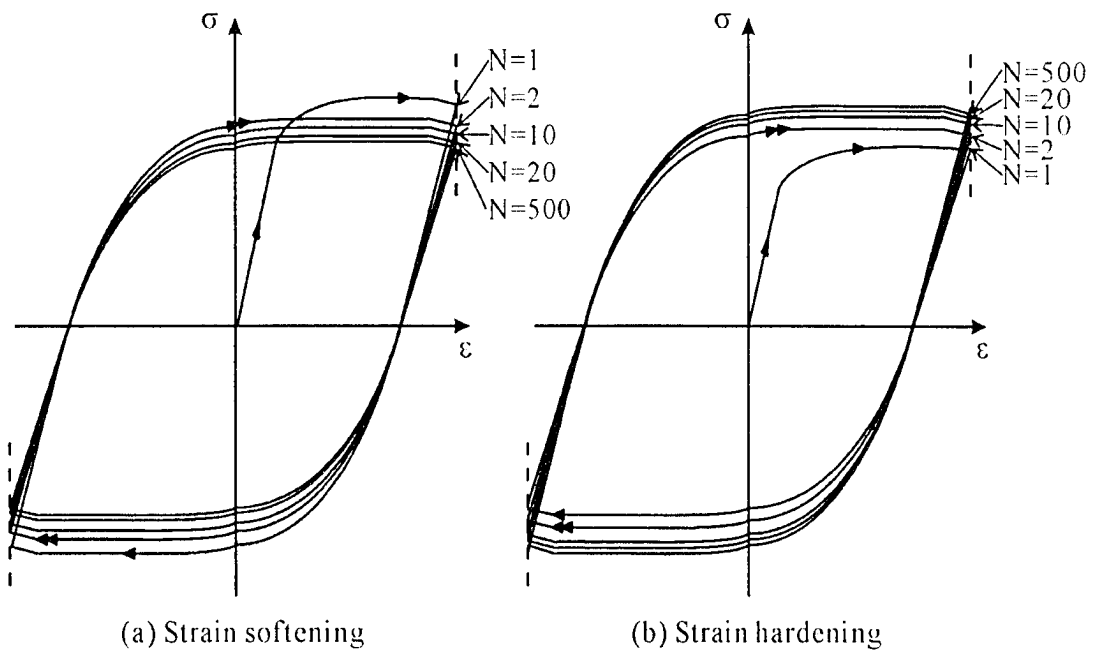
(a) Strain softening

(b) Strain hardening

Figure 4-20 Illustration of Stabilized Hysteresis Loops

115
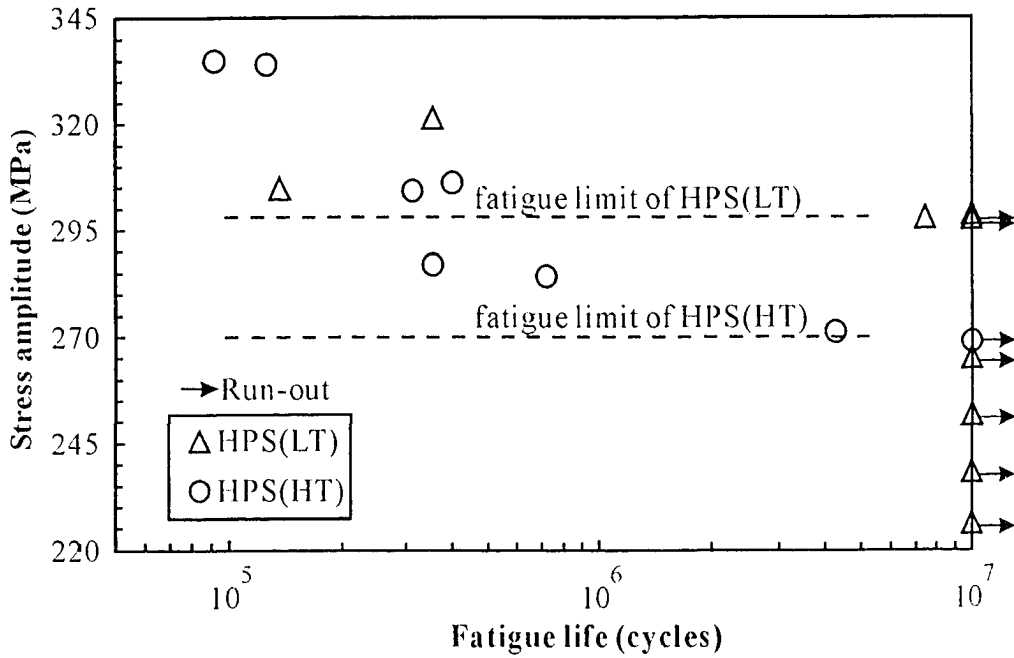
Figure 4-21 Smooth Specimen Fatigue Limit Test Results
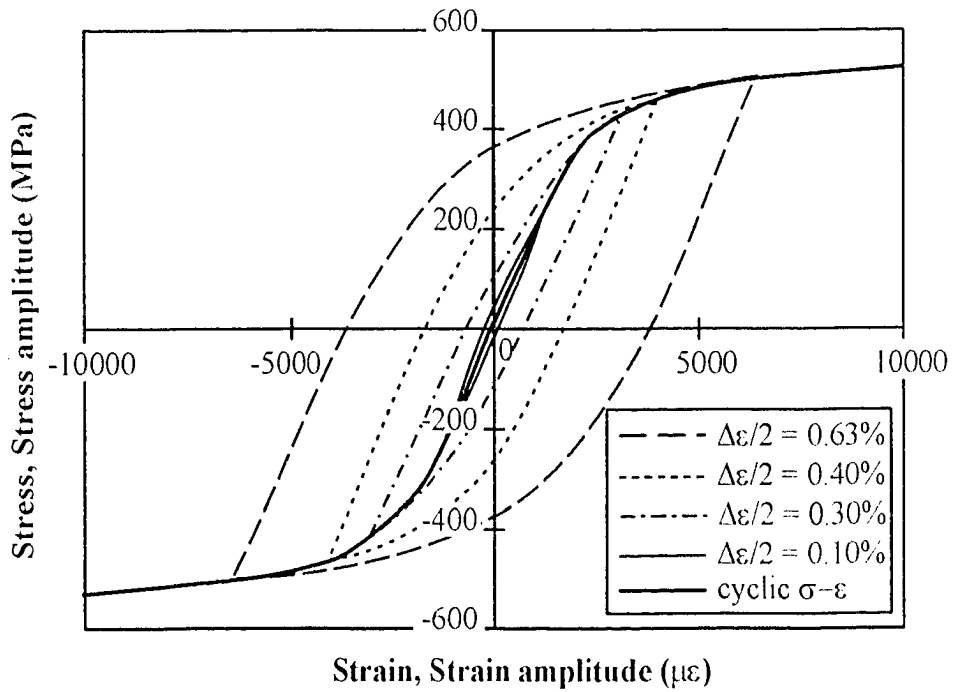
Figure 4-22 Method for Obtaining a Cyclic Stress versus Strain Curve

for HPS(LT) in Longitudinal Direction

116
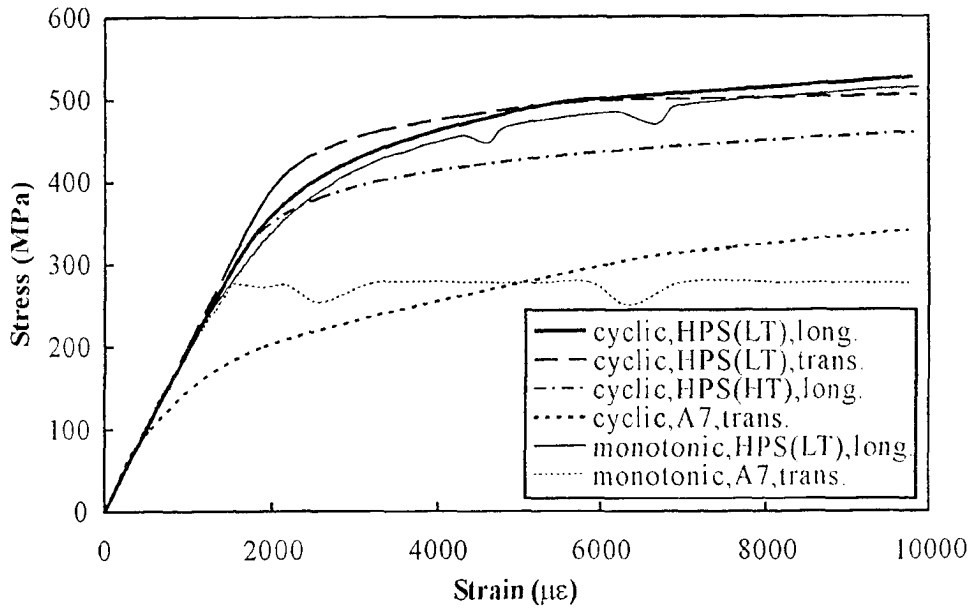
Figure 4-23 Cyclic and Monotonic Stress versus Strain Curves

for HPS 485W and A7 Steels
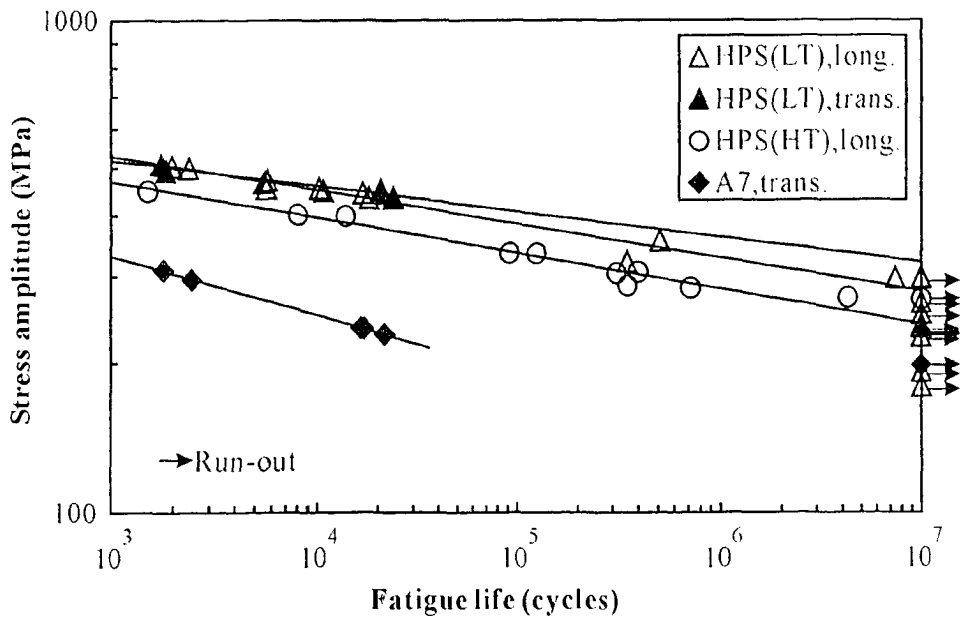
Figure 4-24 Stress Amplitude versus Fatigue Life Data

117
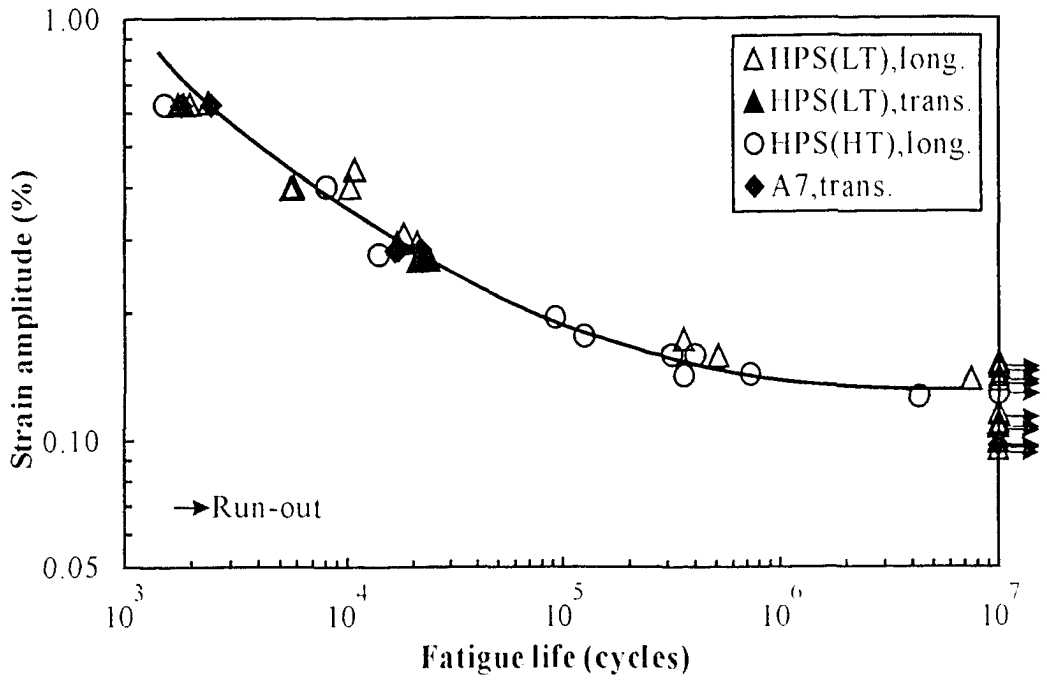
Figure 4-25 Strain Amplitude versus Fatigue Life Data
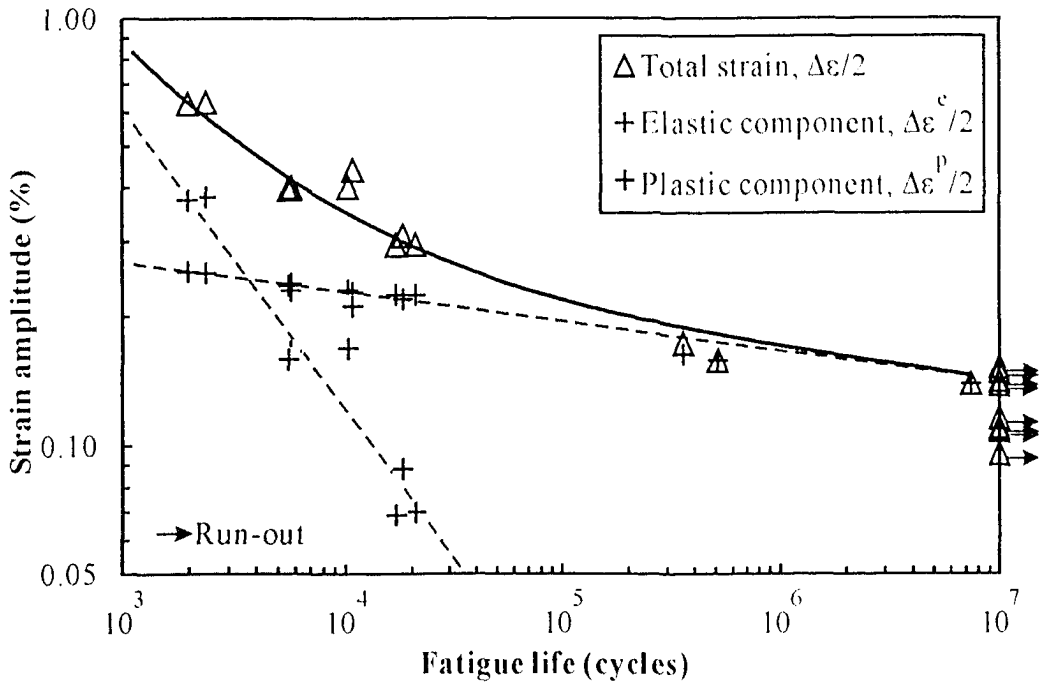
Figure 4-26 Illustration of Regression Analysis in Obtaining Strain versus Life Curve,

for HPS(LT) in Longitudinal Direction

118
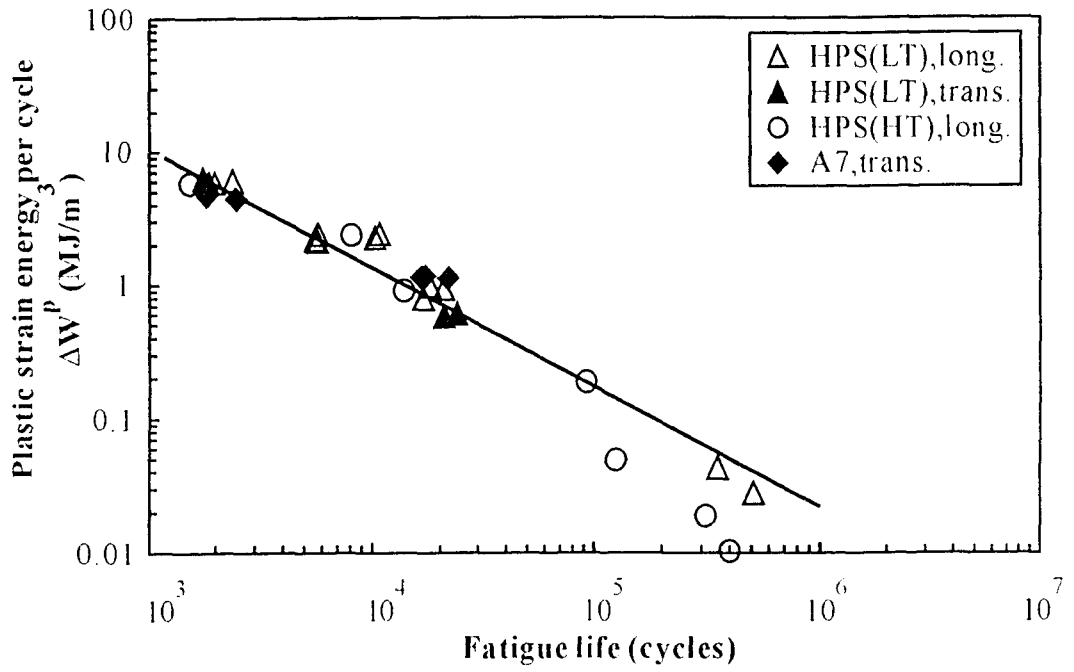
Figure 4-27 Plastic Strain Energy per Cycle (ΔW^p) versus Fatigue Life Data
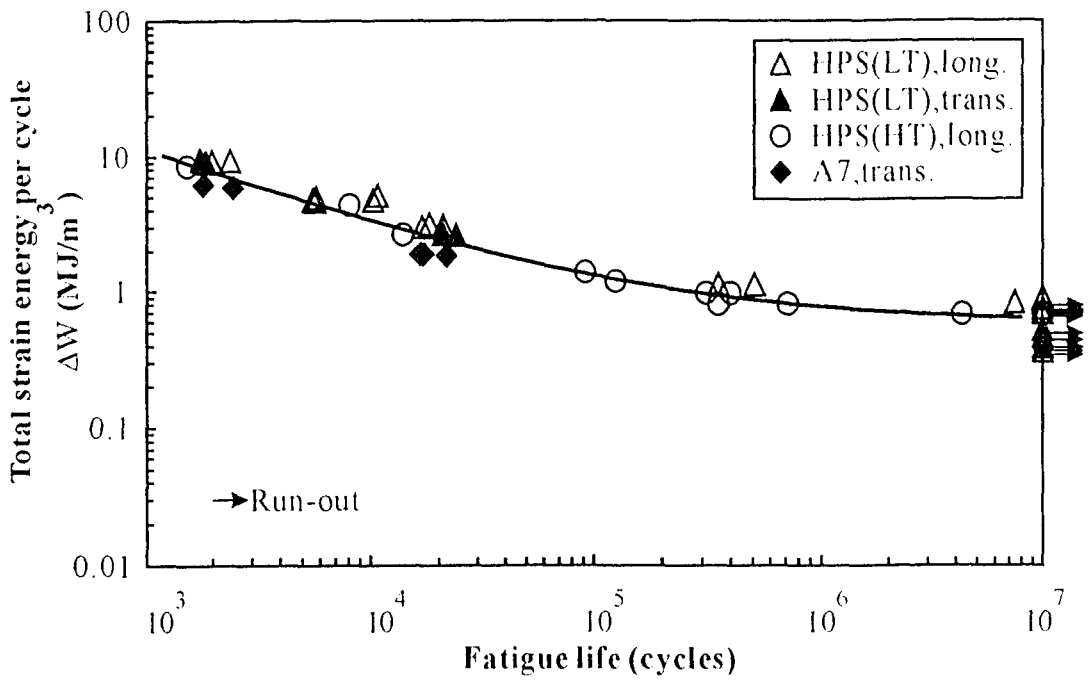
Figure 4-28 Total Strain Energy per Cycle (ΔW) versus Fatigue Life Data

119
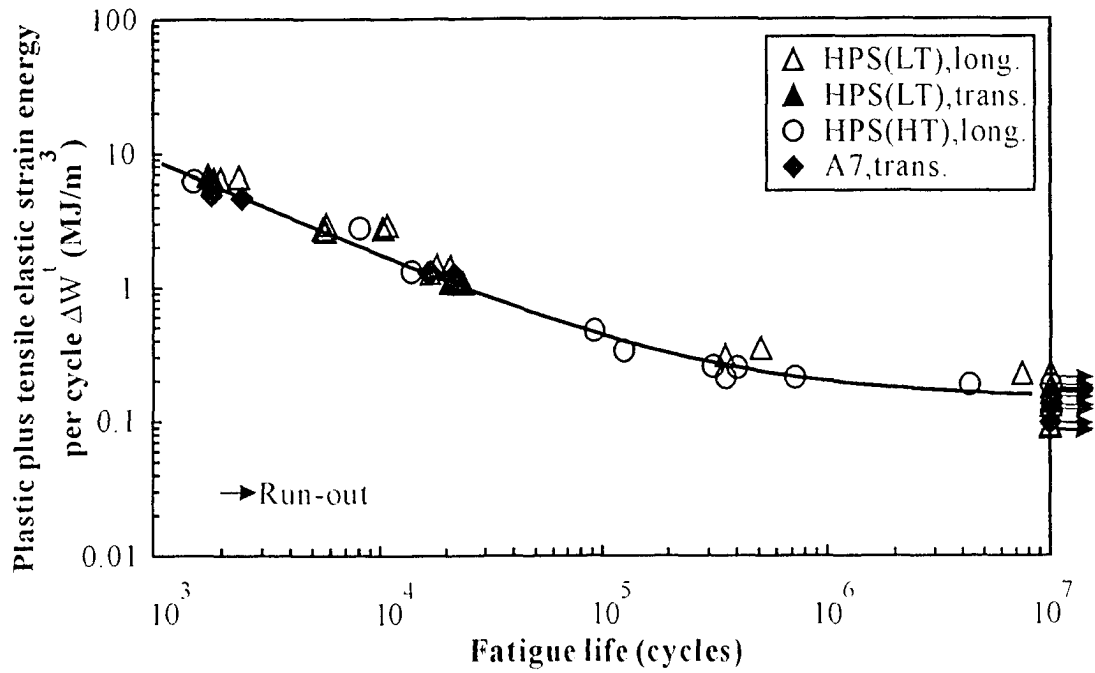
Figure 4-29 Plastic Plus Tensile Elastic Strain Energy per Cycle (ΔW^t) versus Fatigue Life Data
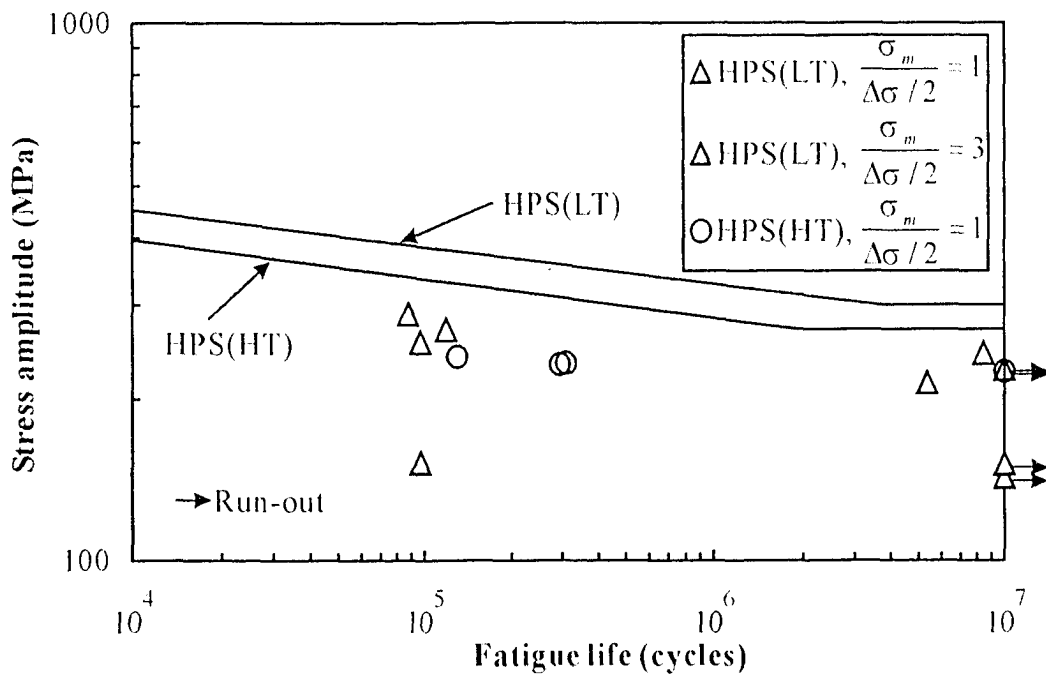
Figure 4-30 MS Series Test Results — Stress versus Life Data

120
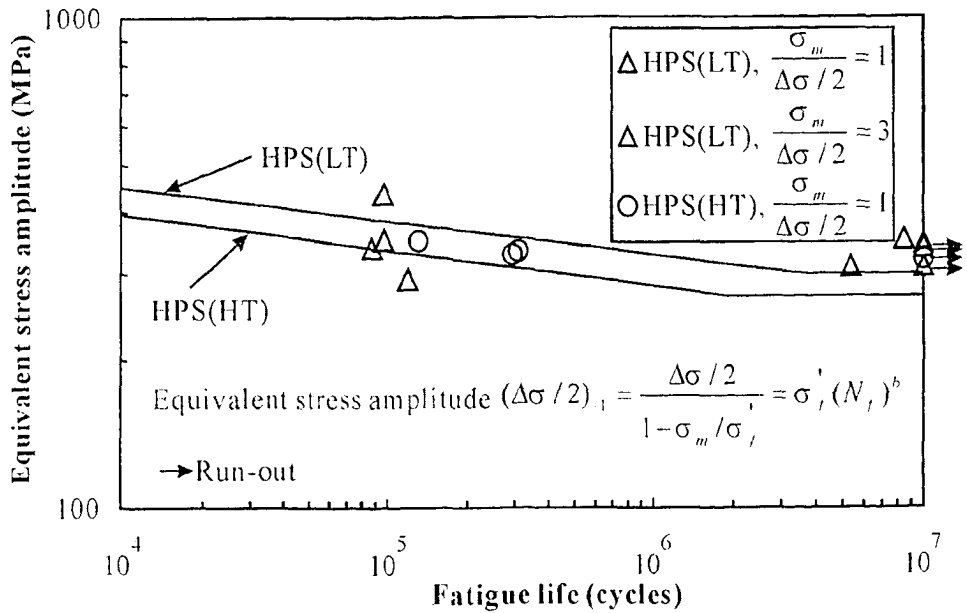
Figure 4-31 Fatigue Data from the MS Series Plotted in Terms of Equivalent Stress
Amplitude According to Morrow's Model
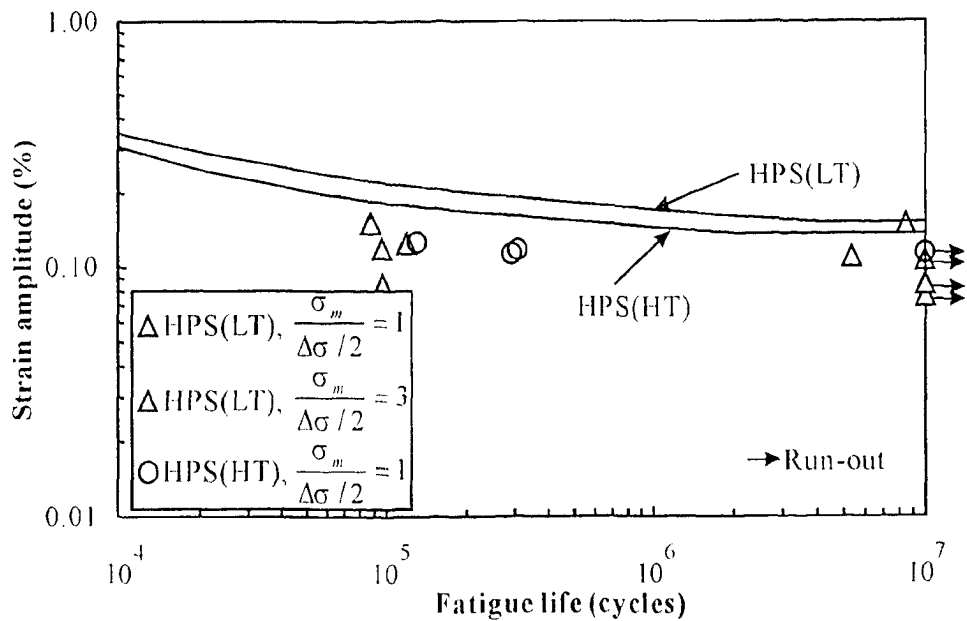
Figure 4-32 MS Series Test Results — Strain versus Life Data

121
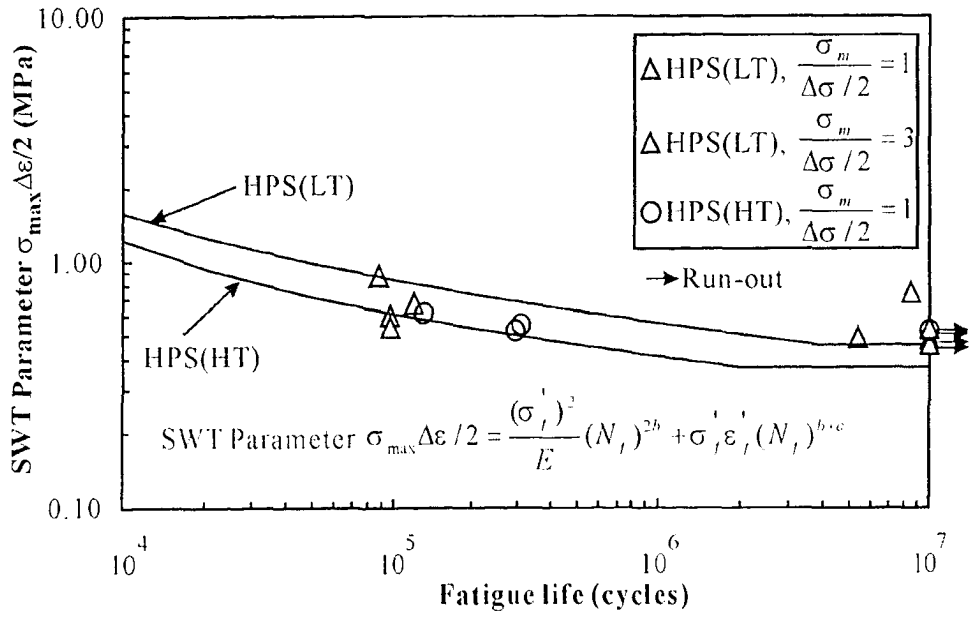
Figure 4-33 Fatigue Data from the MS Series Plotted in Terms of SWT Parameter

The figure shows a plot with axes:
- Y-axis: SWT Parameter $\sigma_{max}\Delta\varepsilon/2$ (MPa), from 0.10 to 10.00
- X-axis: Fatigue life (cycles), from 10^4 to 10^7

Legend:
$\triangle$ HPS(LT), $\frac{\sigma_m}{\Delta\sigma/2} = 1$
$\triangle$ HPS(LT), $\frac{\sigma_m}{\Delta\sigma/2} = 3$
$\bigcirc$ HPS(HT), $\frac{\sigma_m}{\Delta\sigma/2} = 1$
→Run-out

$$\text{SWT Parameter } \sigma_{max}\Delta\varepsilon/2 = \frac{(\sigma_f')^2}{E}(N_f)^{2b} + \sigma_f'\varepsilon_f'(N_f)^{b+c}$$
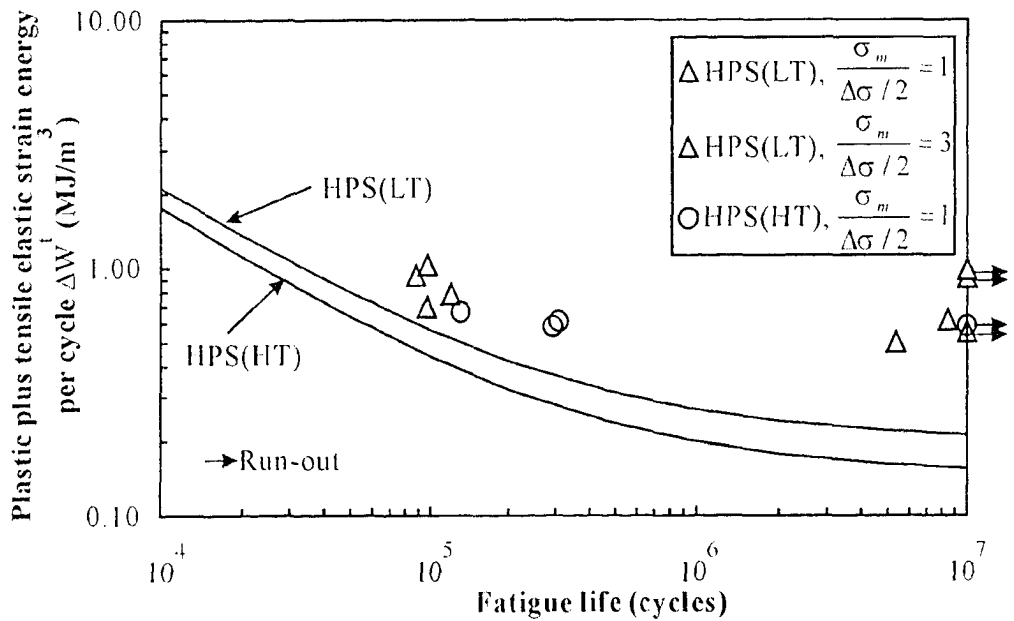
Figure 4-34 MS Series Test Results — Plastic Plus Tensile Elastic Strain Energy per Cycle (ΔW^t) versus Life Data

The figure shows a plot with axes:
- Y-axis: Plastic plus tensile elastic strain energy per cycle ΔW^t (MJ/m³), from 0.10 to 10.00
- X-axis: Fatigue life (cycles), from 10^4 to 10^7

Legend:
$\triangle$ HPS(LT), $\frac{\sigma_m}{\Delta\sigma/2} = 1$
$\triangle$ HPS(LT), $\frac{\sigma_m}{\Delta\sigma/2} = 3$
$\bigcirc$ HPS(HT), $\frac{\sigma_m}{\Delta\sigma/2} = 1$
→Run-out

122

Generalized total strain energy

$$D = \Delta W^p + (1 + \frac{\sigma_m}{\Delta\sigma/2})\frac{(\Delta\sigma/2)^2}{2E}$$

$$= K_t (N_f)^{\alpha_t} + \Delta W_0^t$$

△ HPS(LT), $\frac{\sigma_m}{\Delta\sigma/2} = 1$	
△ HPS(LT), $\frac{\sigma_m}{\Delta\sigma/2} = 3$	
○ HPS(HT), $\frac{\sigma_m}{\Delta\sigma/2} = 1$	

→ Run-out
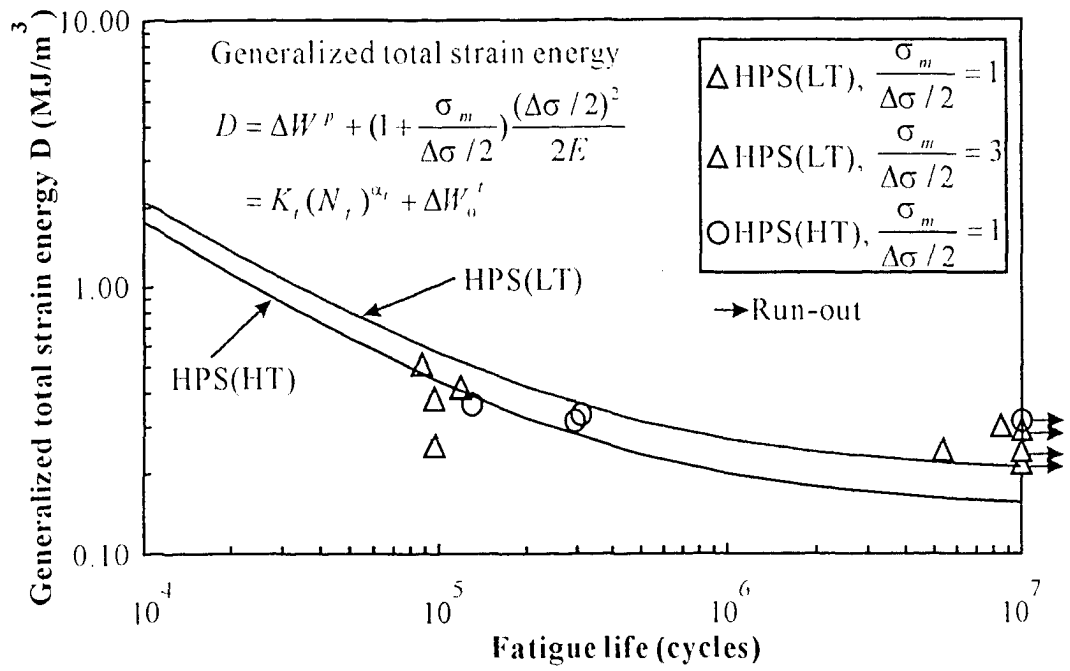
Figure 4-35 Fatigue Data from the MS Series Plotted in Terms of Generalized Total Strain Energy Parameter According to Ellyin's Model
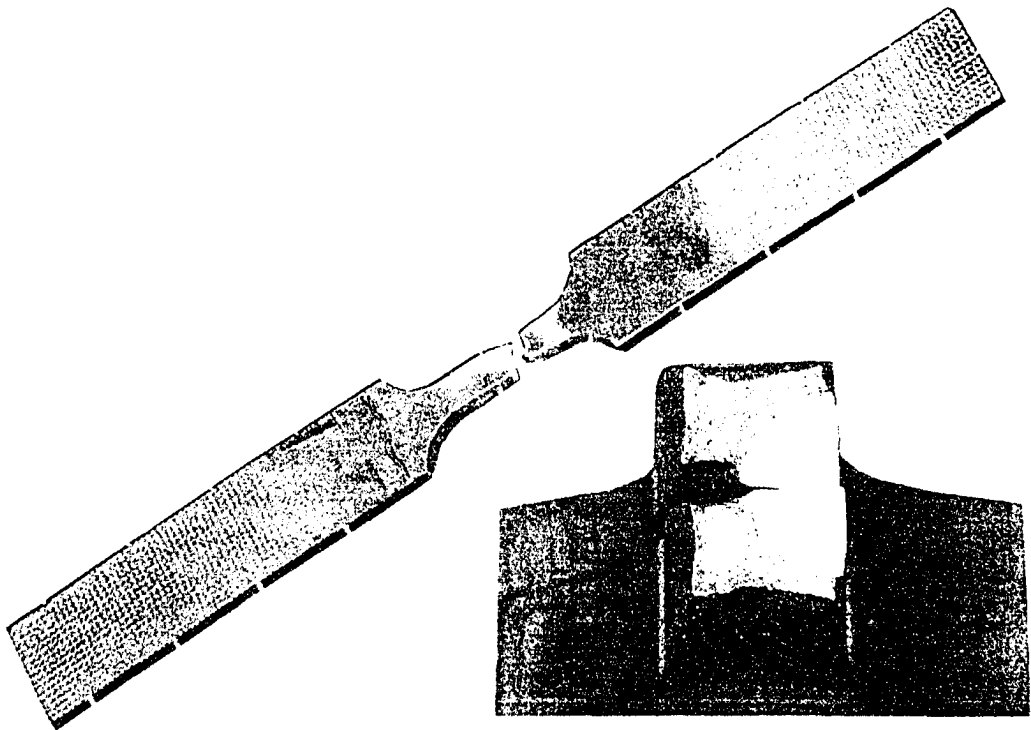
Figure 4-36 Typical Fractured Smooth Fatigue Specimen

123

Figure 4-37 Typical Fracture Surface of a Smooth Fatigue Specimen
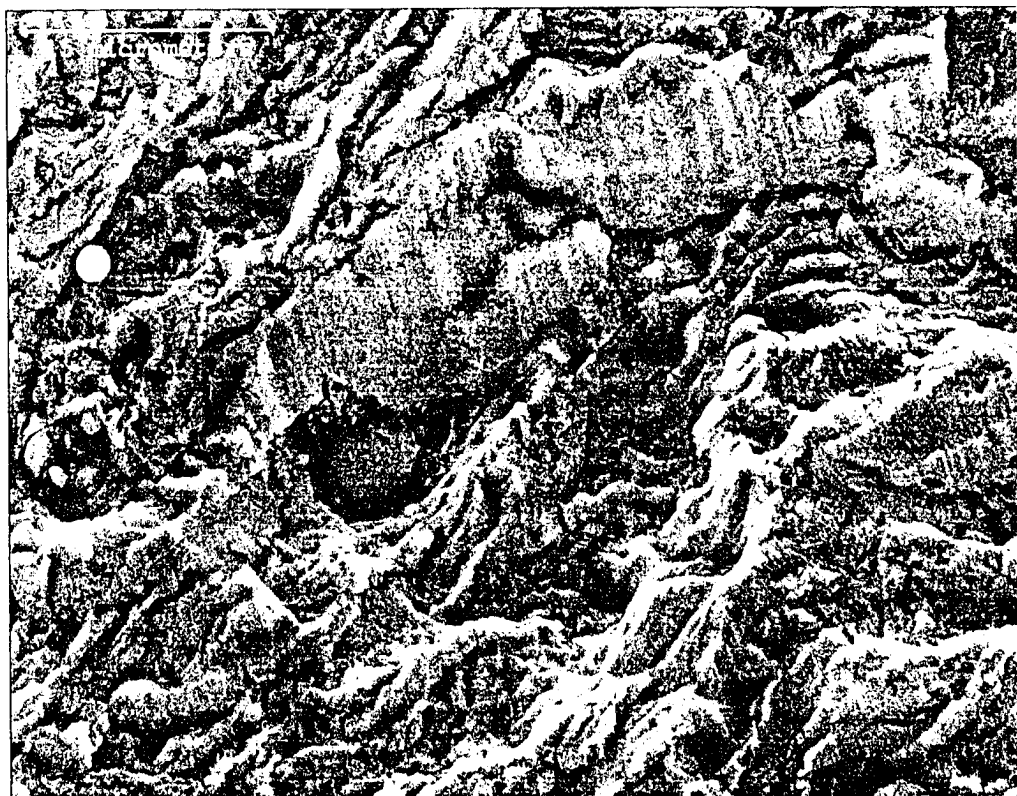
Figure 4-38 Fracture Surface of Specimen HPS(LT)-FR-7

124
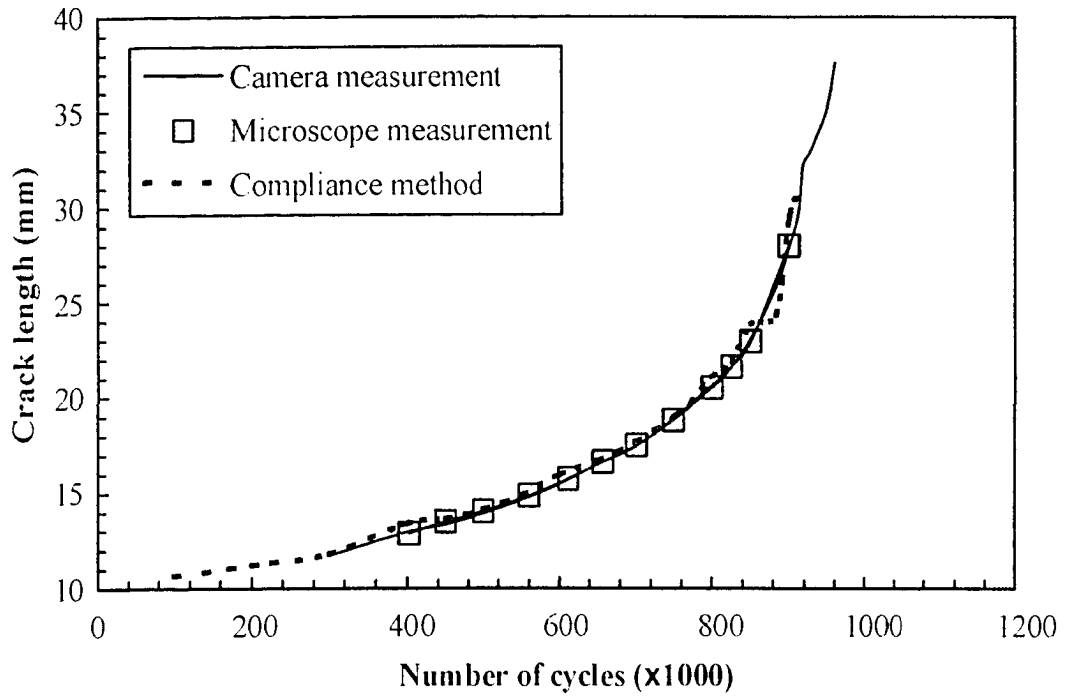
Figure 4-39 Comparison of Crack Length Measurements on HPS(LT)-CGR-8
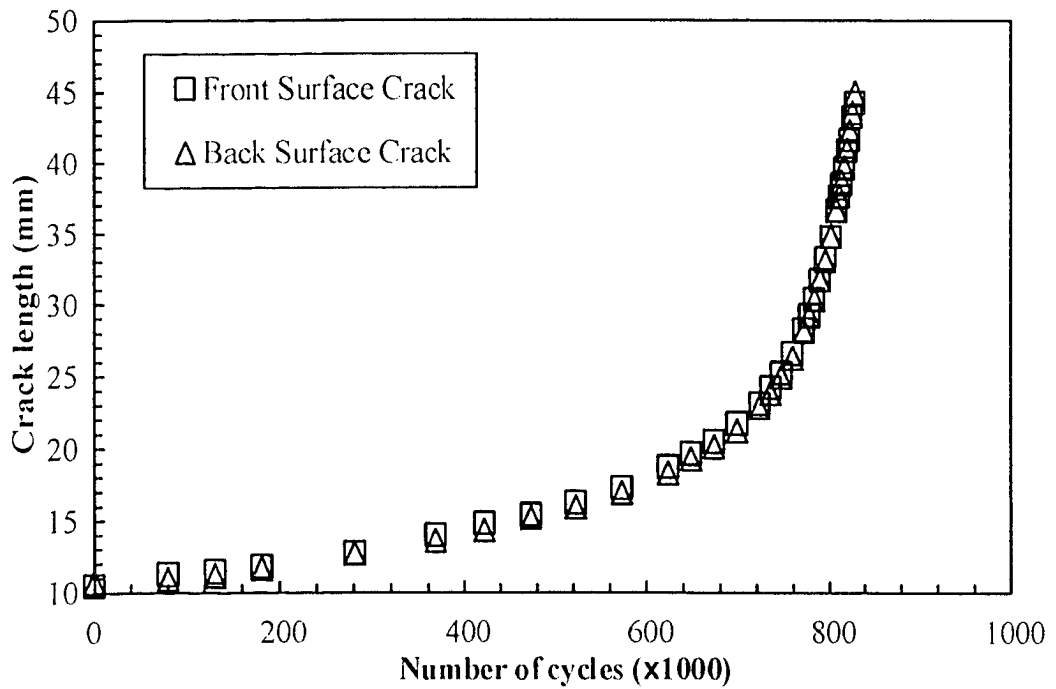
Figure 4-40 Comparison of Front and Back Surface Crack Length for Specimen
HPS(LT)-CGR-5

125
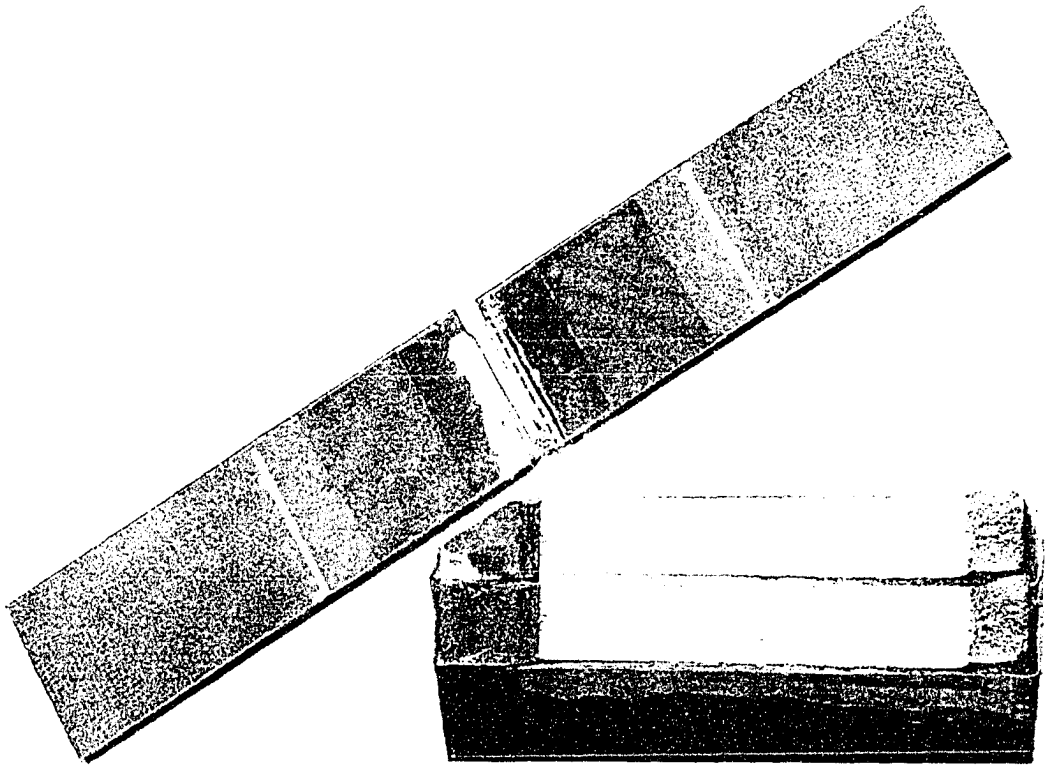
Figure 4-41 Typical Fractured Crack Growth Rate Specimen
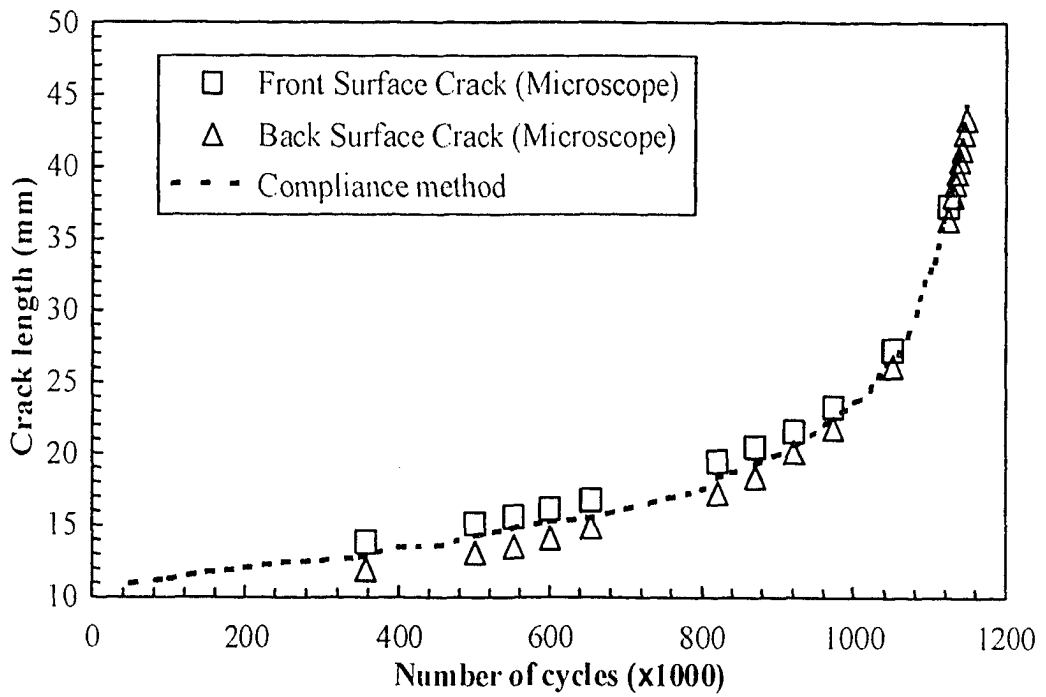
Figure 4-42 Comparison of Front and Back Surface Crack size for Specimen

HPS(LT)-CGR-6

126
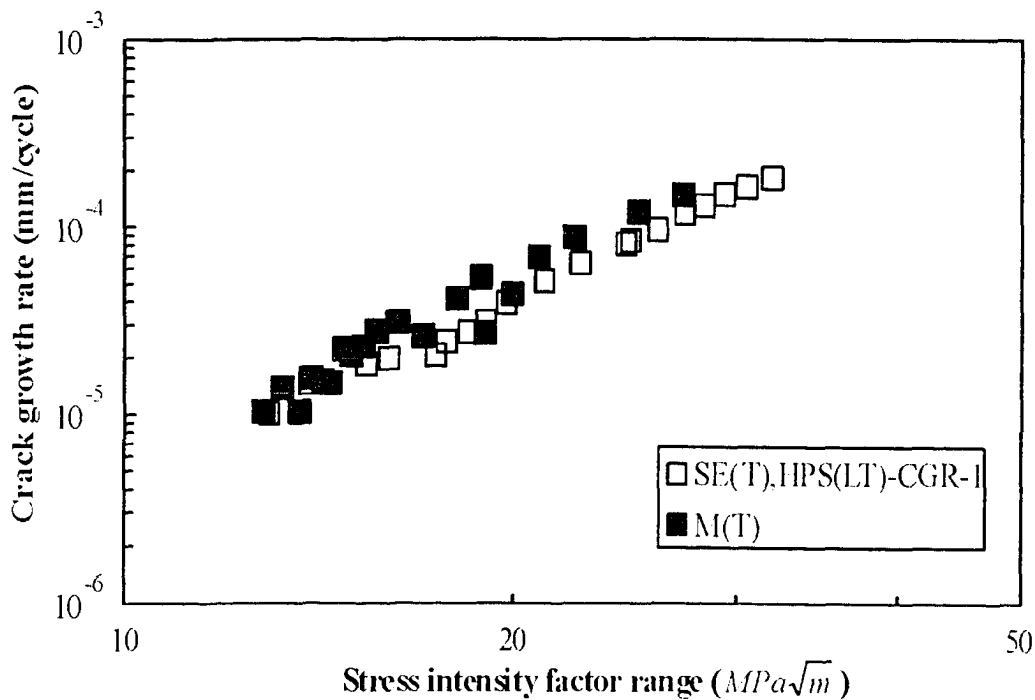
Figure 4-43 Comparison between M(T) and SE(T) Test Results
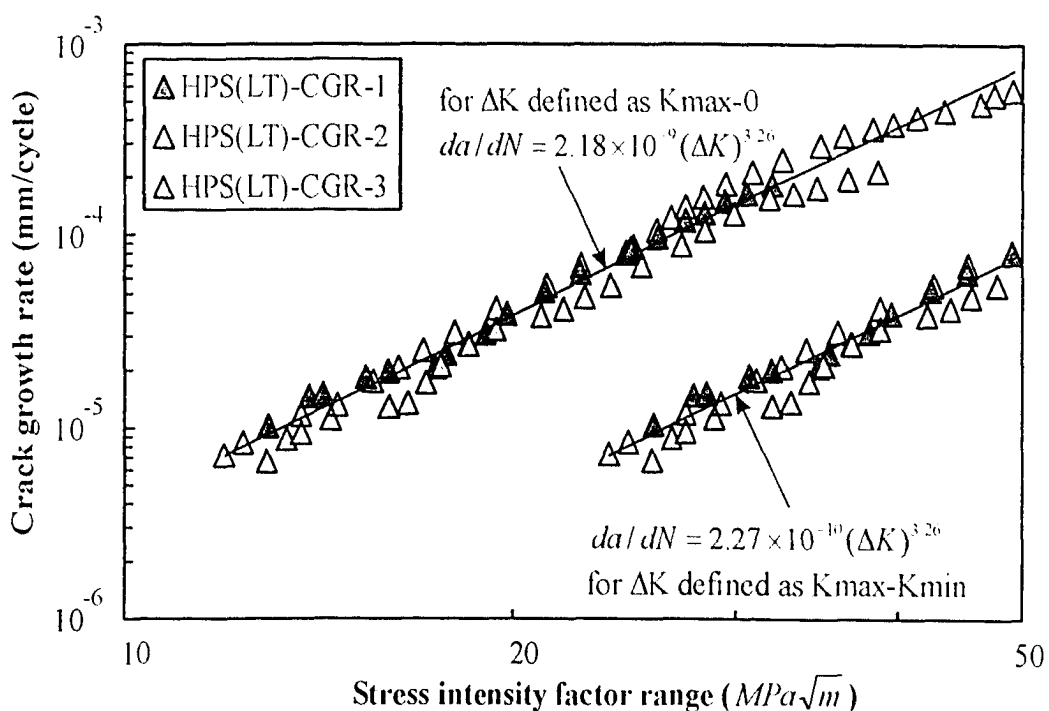
Figure 4-44 HPS 485W Steel Fatigue Crack Growth Rate Test Results ($R = -1$)

127
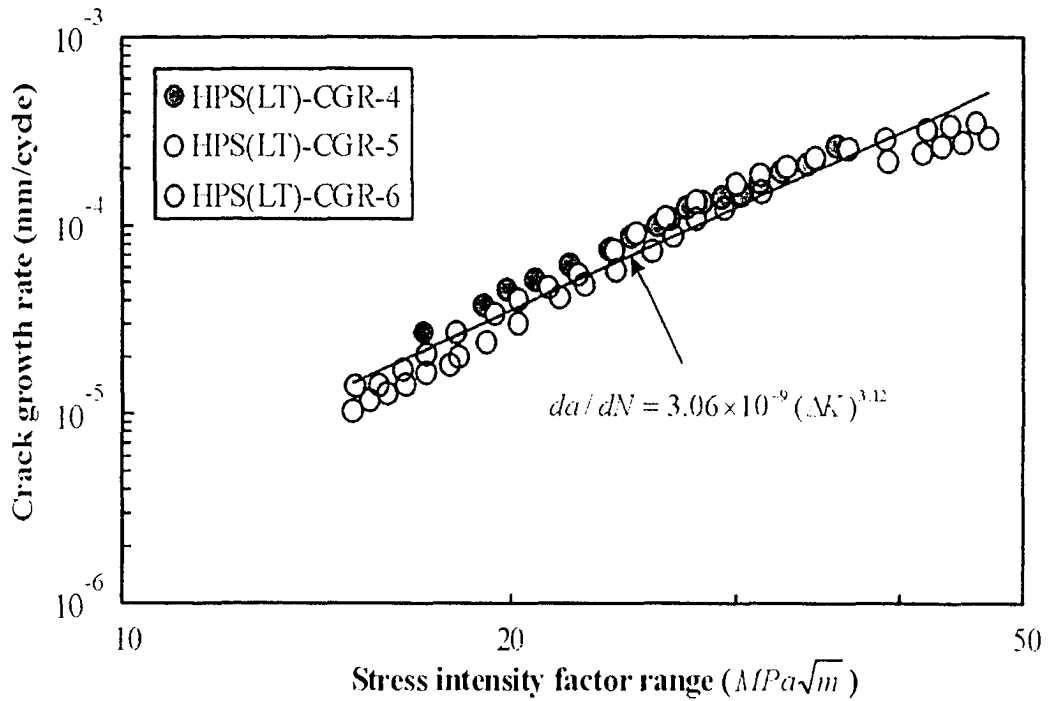
Figure 4-45 HPS 485W Steel Fatigue Crack Growth Rate Test Results ($R = 0$)
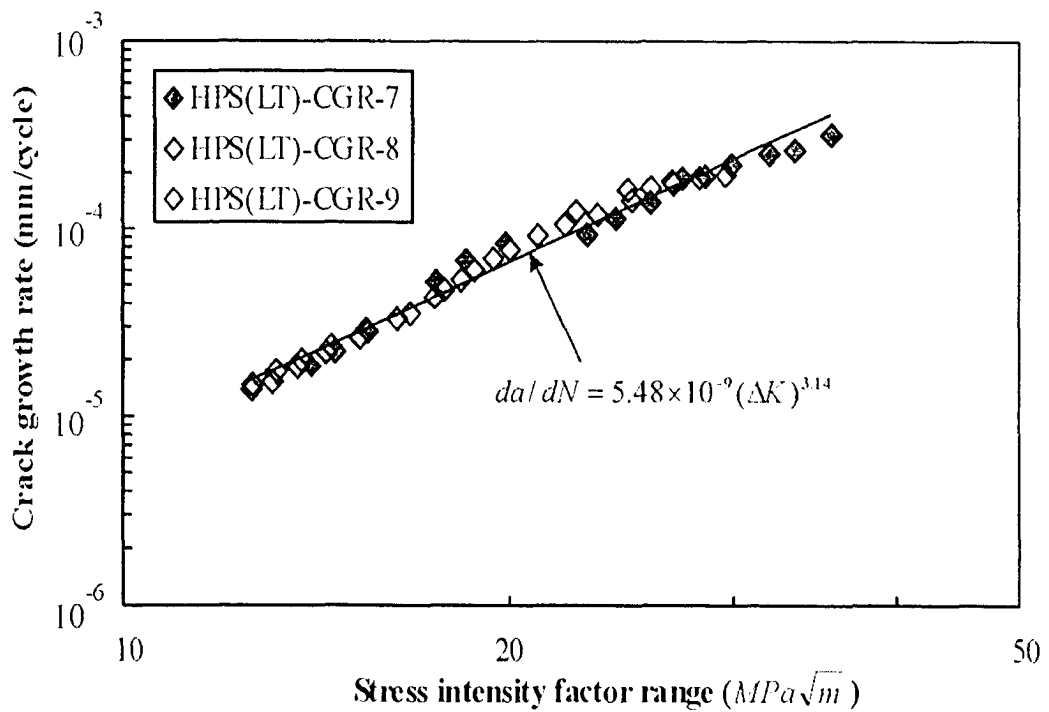
Figure 4-46 HPS 485W Steel Fatigue Crack Growth Rate Test Results ($R = 0.5$)

128
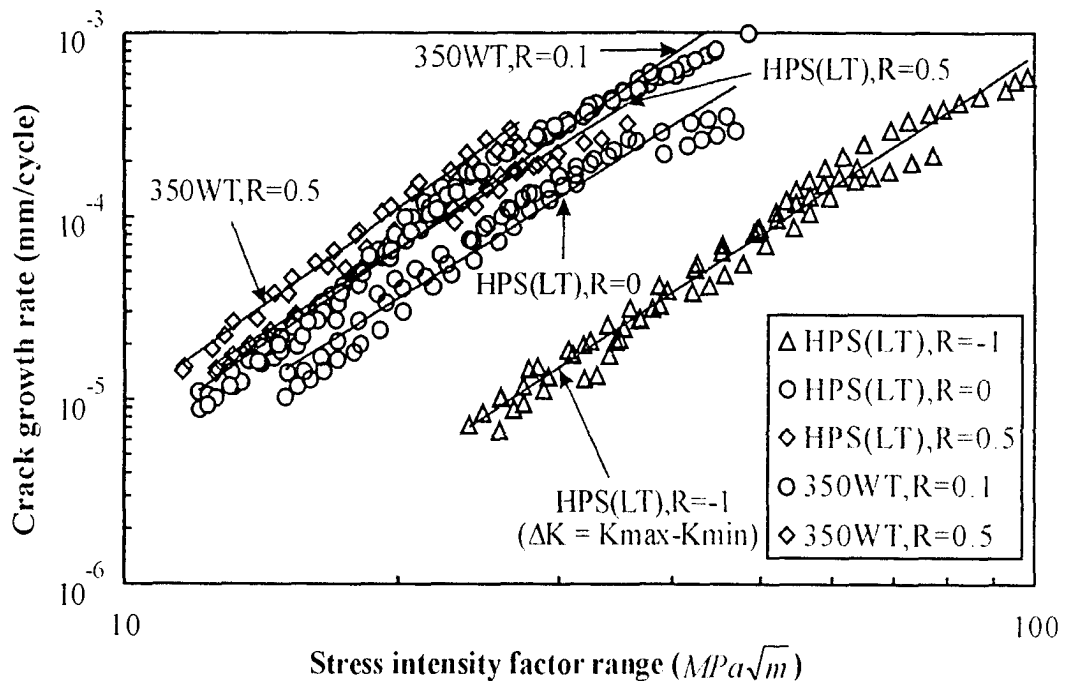
Figure 4-47 Summary of Fatigue Crack Growth Rate Test Results

for HPS 485W and 350WT Steels
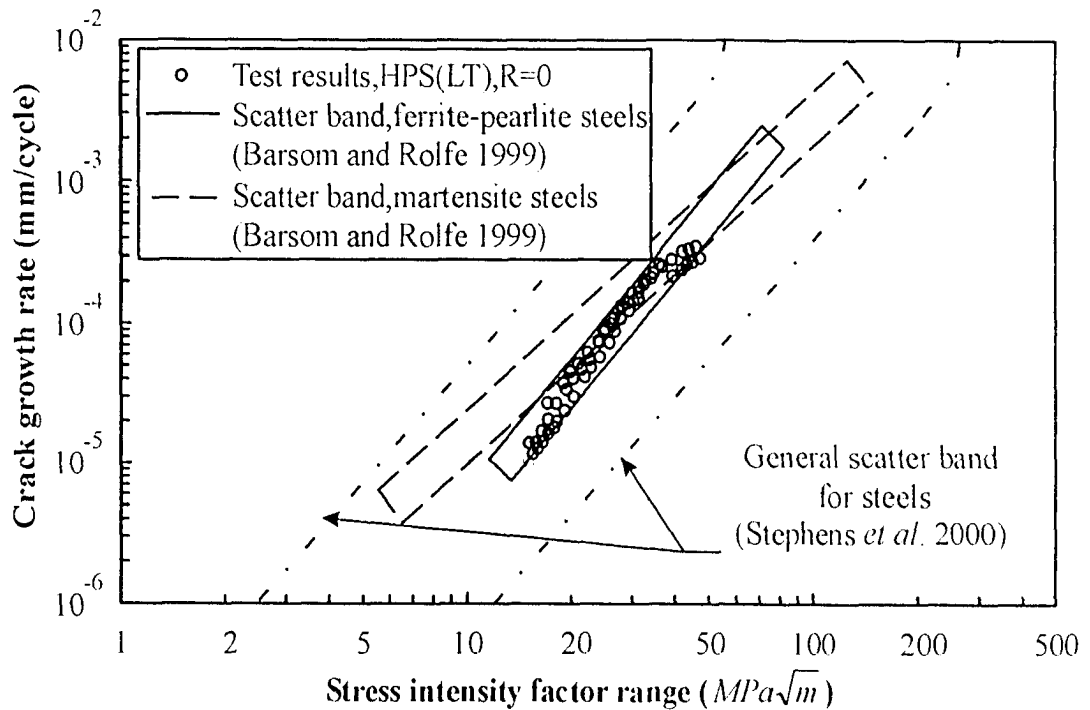
Figure 4-48 Comparison of HPS 485W Steel Test Results with Literature ($R = 0$)

129
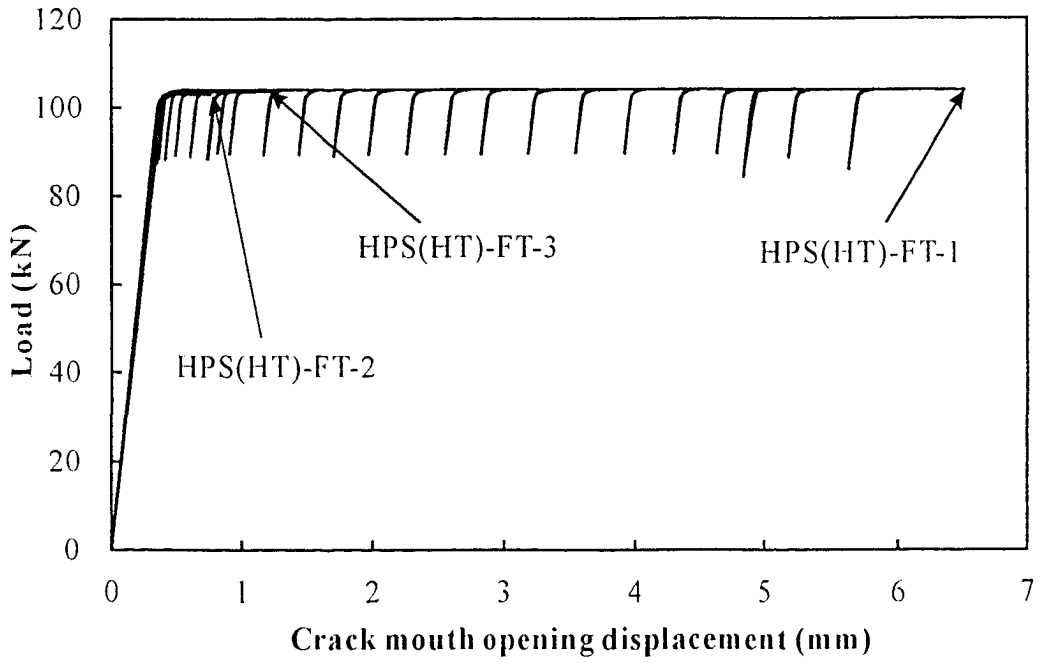
Figure 4-49 Fracture Toughness Test Results for HPS 485W Steel
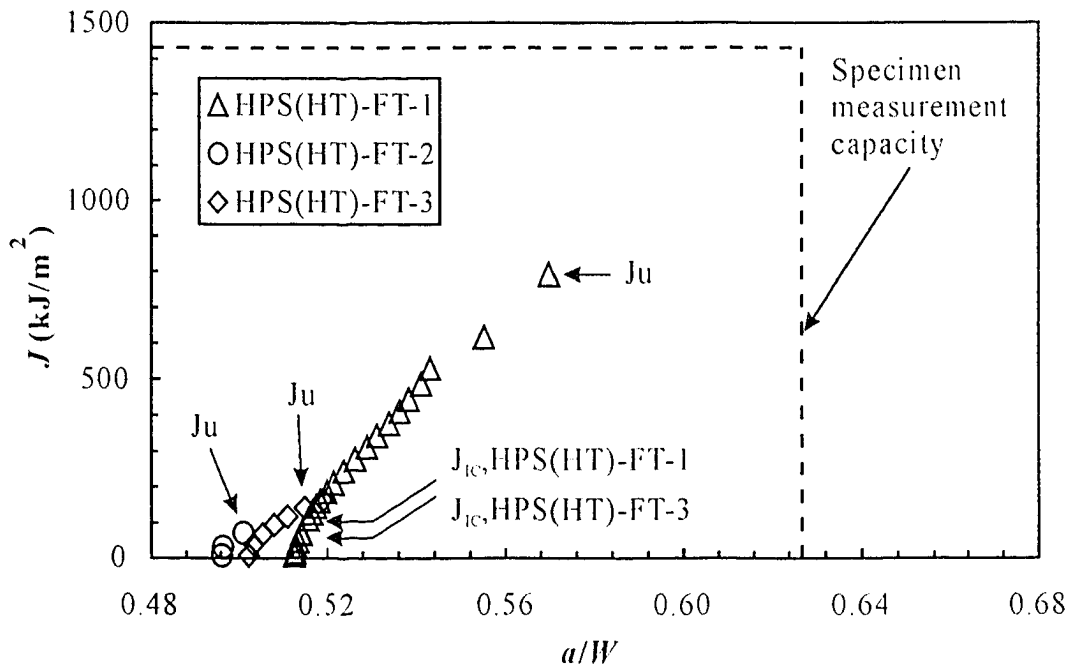
Figure 4-50 *J-R* Curves for HPS 485W Steel Fracture Toughness Tests

130
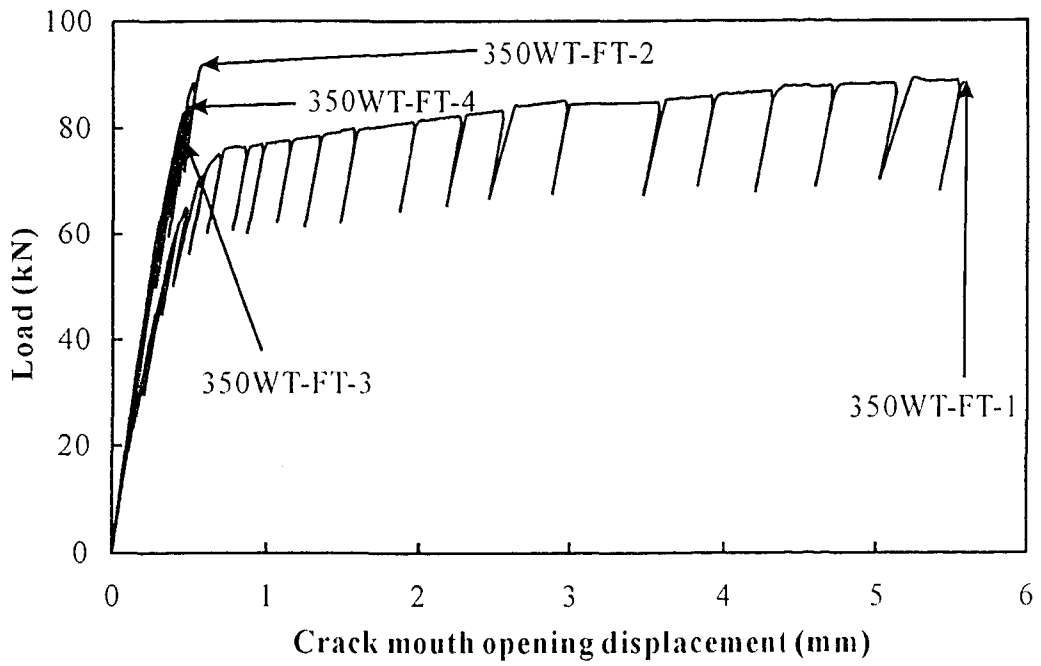
Figure 4-51 Fracture Toughness Test Results for 350WT Steel
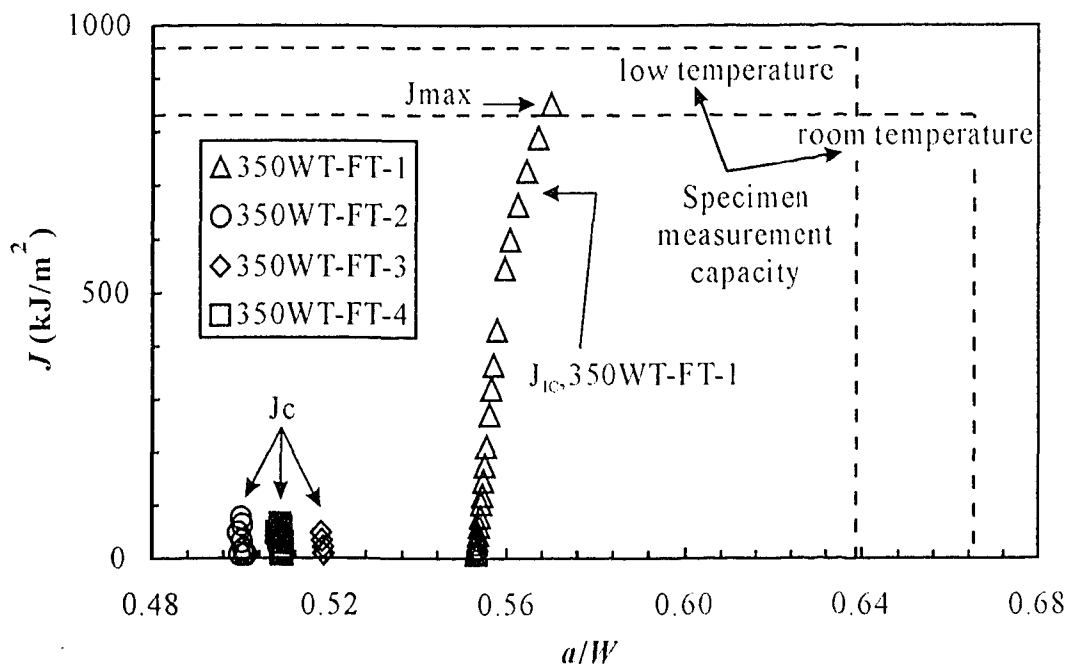
Figure 4-52 *J-R* Curves for 350WT Steel Fracture Toughness Tests

131
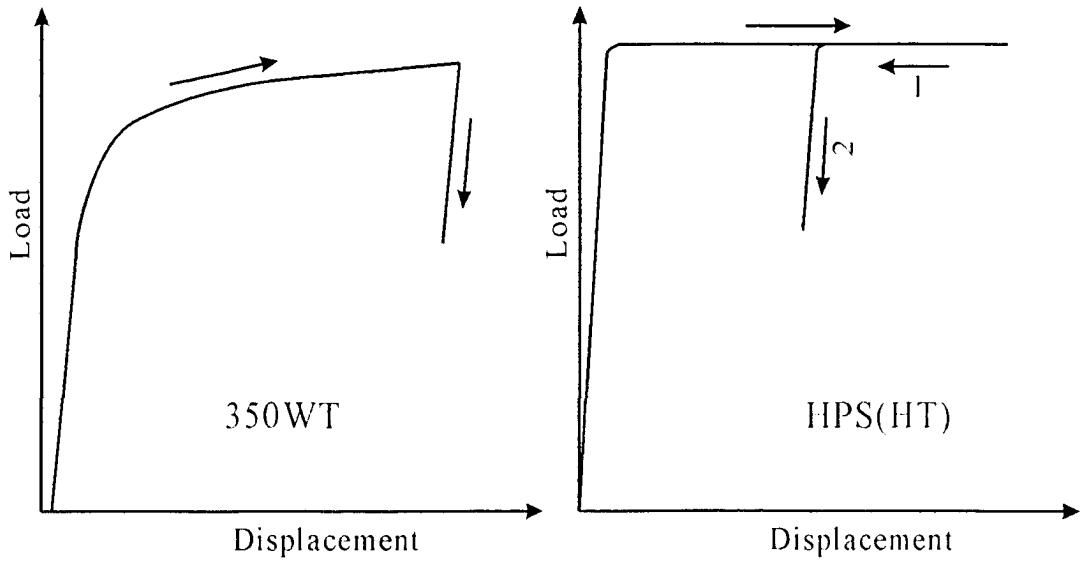
Figure 4-53 Illustration of Unloading Behaviour for
HPS 485W and 350WT Steels
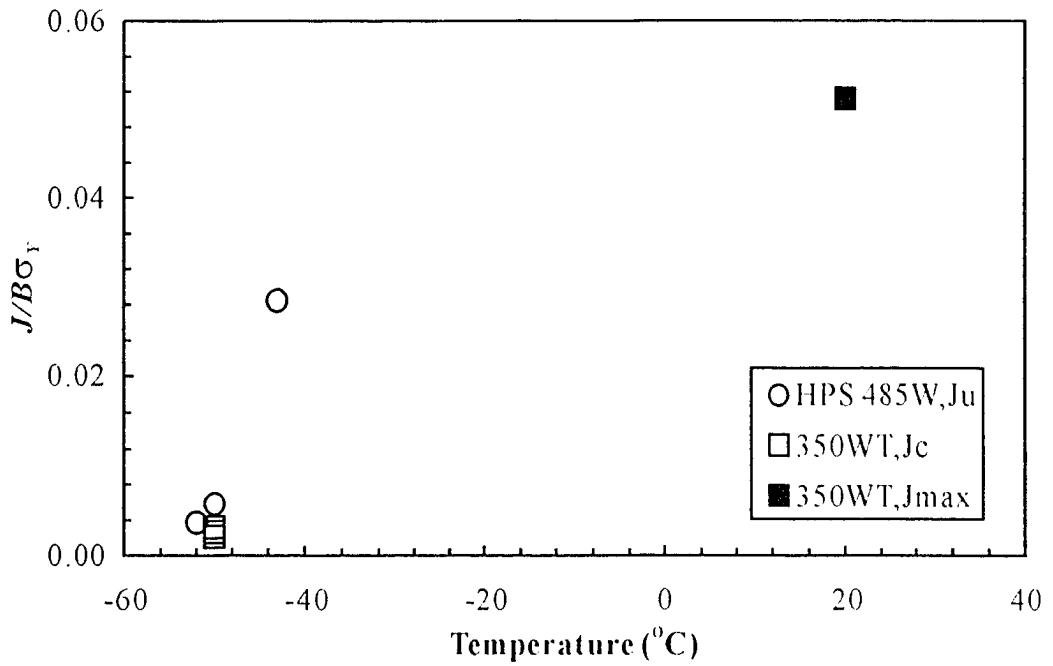
Figure 4-54 Summary of Fracture Toughness Test Results

132

(a) 350WT-FT-1,
plastic tearing at room temperature (+20°C)

(b) 350WT-FT-4,
unstable fracture at low temperature (-50°C)

(c) HPS(HT)-FT-3,
plastic tearing at low temperature (-50°C)
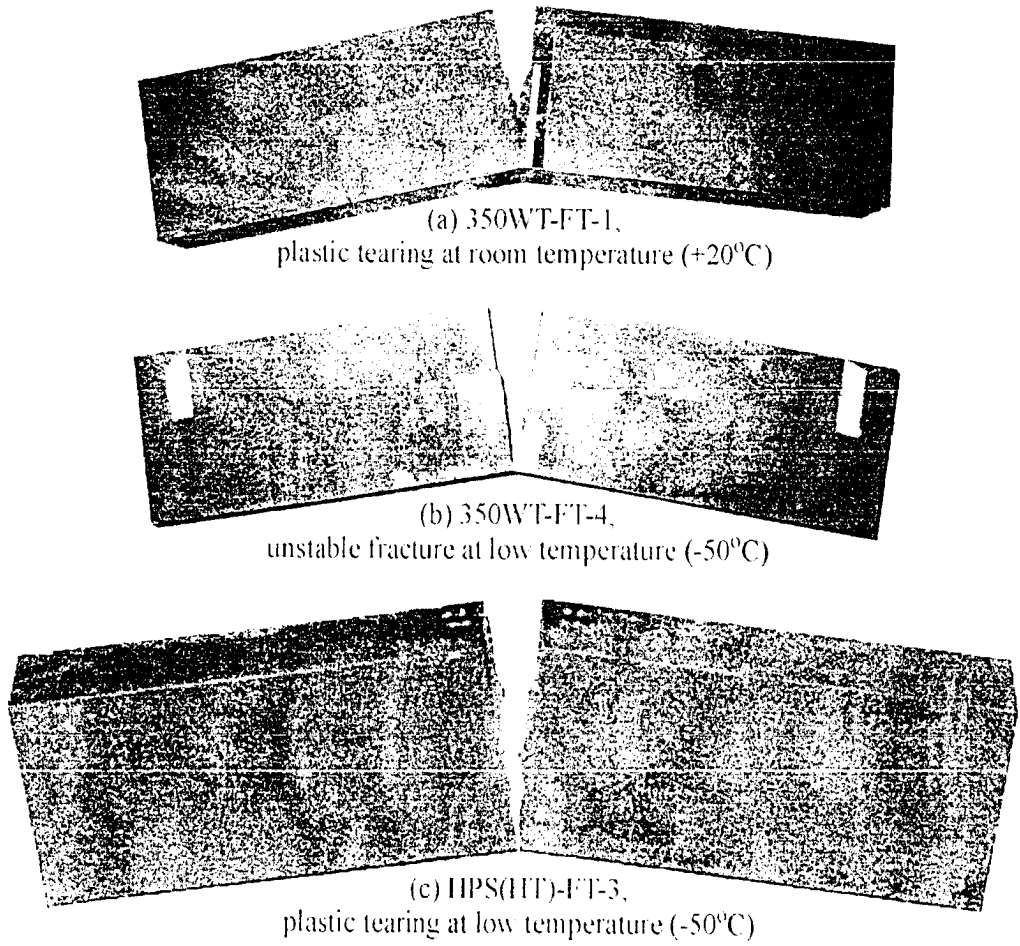
Figure 4-55 Typical Failure Modes of Fracture Toughness Specimens
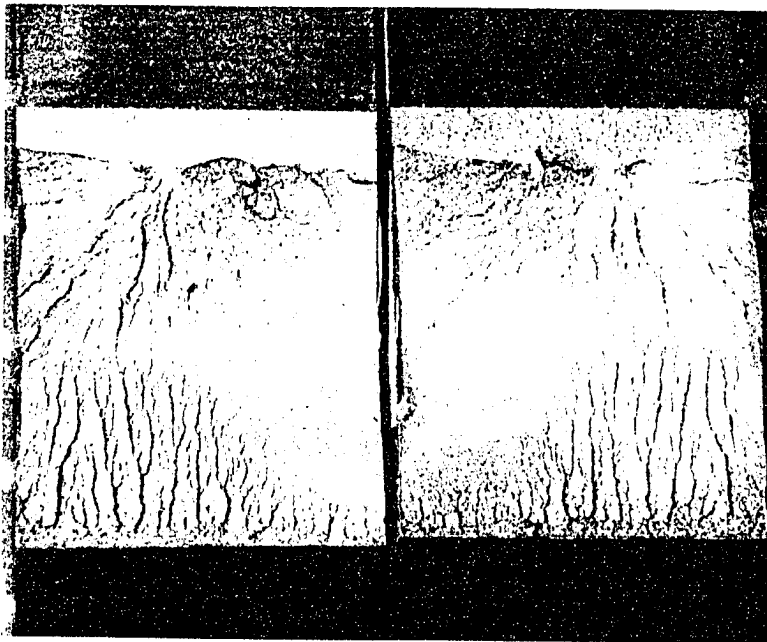
Figure 4-56 Fracture Surface of Specimen HPS(HT)-FT-3

133
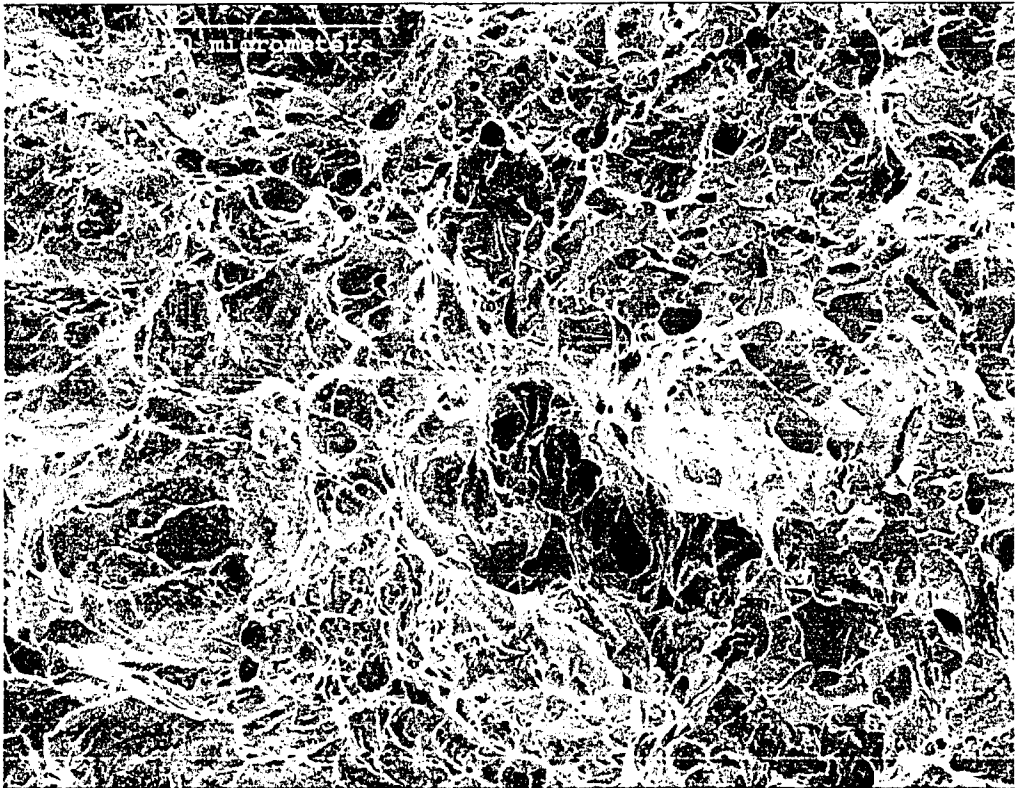
Figure 4-57 Fracture Surface of Specimen 350WT-FT-4 (Scanning Electron Micrograph)
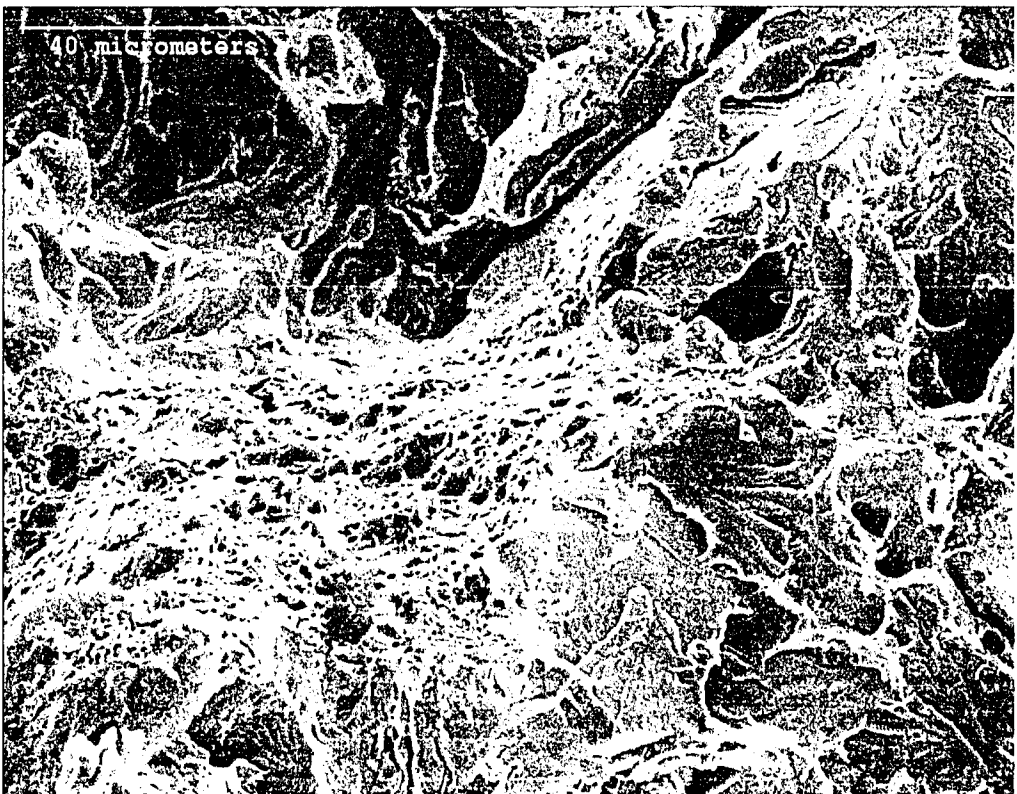
Figure 4-58 Fracture Surface of Specimen HPS(HT)-FT-3 (Scanning Electron Micrograph)

134
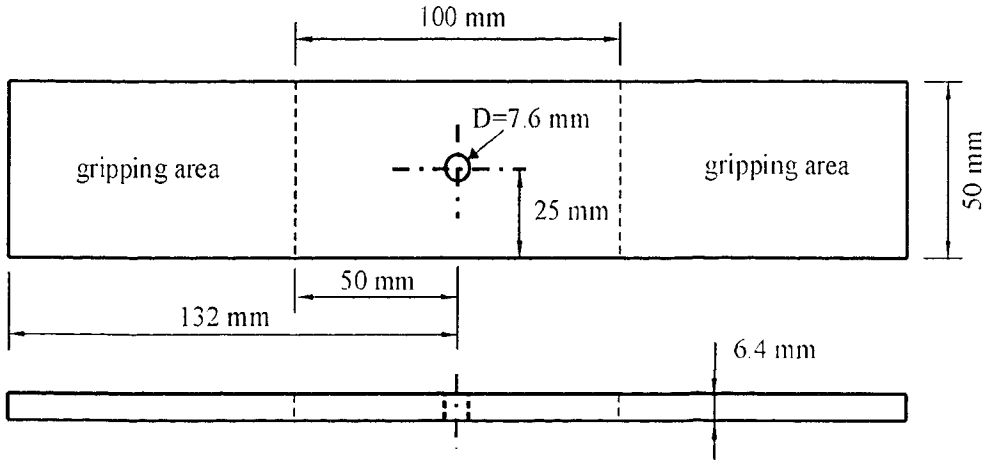
Figure 4-59 HPS Detail Test Specimen
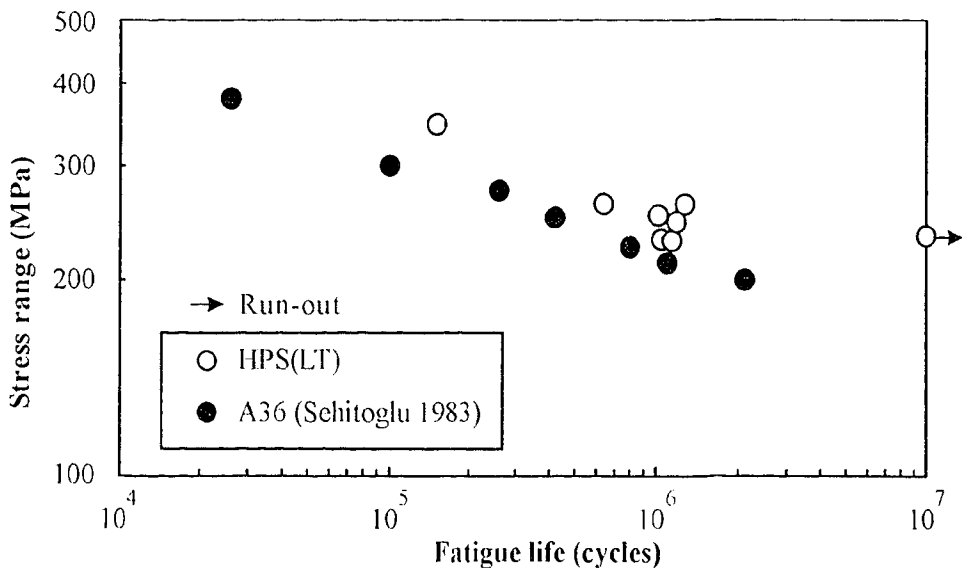
Figure 4-60 HPS Detail (Plate with a Circular Hole) Test Results

135

CHAPTER 5.

RESULTS OF ANALYSIS

5.1. Introduction

Using the analytical techniques and procedures described in Chapter 3 and the fatigue material properties presented in Chapter 4, fatigue analyses of six different details were carried out to predict their fatigue lives (including both crack initiation and crack propagation). The predicted fatigue performance of these details are compared with fatigue test results. The details investigated analytically are: plates with a circular hole tested by Sehitoglu (1983), bearing-type bolted shear splices tested by Josi et al. (1999), large scale beams tested by Baker and Kulak (1985), welded cruciforms tested by Friedland et al. (1982), welded cover plate joints tested by Friedland et al. (1982), and large scale welded plate girders tested by Wright (2003). This chapter presents a description of these test results and a detailed description of the finite element models and fatigue life prediction for each type of fatigue details. For some of the details that are made of conventional steel, predicted fatigue life of similar details made of high performance steel are also presented for comparison with conventional steel.

5.2. Plate with a Circular Hole (Sehitoglu 1983)

5.2.1. Test Description

Fatigue test results from hot rolled ASTM A36 steel plates with a circular hole subjected to uniform tension were first chosen to validate the proposed analysis approach (Sehitoglu 1983). Since the stress concentration factor and the stress intensity factor for this detail are well established, a comparison with existing literature can easily be made. Furthermore, the cyclic stress versus strain and fatigue properties necessary for stress-based and strain-based prediction methods have been reported by Sehitoglu (1983) as

$E = 200\,000$ MPa, $K' = 1336$ MPa, $n' = 0.226$, $\sigma_f' = 1036$ MPa, $b = -0.11$, $\varepsilon_f' = 0.242$, and $c = -0.48$ (refer to Equation (3-1), Equation (3-4), and Equation (3-5)).

136

Figure 5-1 shows the dimensions of a typical specimen tested by Sehitoglu (1983). The test specimens consisted of 280 x 50 x 5.7mm steel plates (with 90 mm grip lengths at each ends) with a 7.6 mm diameter hole at the centre. The method used to make the hole was not reported. The specimens were fatigue tested under load control and fully reversed condition. The nominal stress amplitudes, calculated at the net section, varied from 118 MPa to 271 MPa and the associated measured fatigue lives varied from 1.2×10^6 to 2 800 cycles.

5.2.2. Finite Element Model

Only the middle 100 mm portion was considered in the analysis. Because of the double symmetry of the test specimens, only one quarter of the test area needed to be modelled. The finite element mesh of a test specimen and the mesh around the centre hole are shown in Figure 5-2. Stress and strain components in the y-direction for the elements along x-axis were used for the analysis. Element 1, shown in Figure 5-2 (b) as the critical element, is the most highly stressed element where a localized plastic zone may be produced by high stress concentration fields around the hole.

The boundary conditions along the axes of symmetry consist of fully restrained nodes in the y-direction along the x-axis and free in the x-direction (Figure 5-2), while the nodes along the y-axis are fully restrained in x-direction and free to move in the y-direction. All the nodes in the model were restrained in the z-direction (perpendicular to the plane of the plate). Work equivalent node loads for a uniformly distributed tension load were applied to the top edge of the model. The four-node quadrilateral shell element S4R from the ABAQUS finite element library was used. The full model consists of 1344 elements and 1425 nodes.

An elastic, isotropic hardening material model was used to define the cyclic stress versus strain curve given by Sehitoglu (1983) as follows:

$$\Delta\varepsilon/2 = \frac{\Delta\sigma/2}{200000} + \left(\frac{\Delta\sigma/2}{1336}\right)^{1/0.226} \tag{5-1}$$

137

where $\Delta\varepsilon$ and $\Delta\sigma$ are the strain range and stress range, respectively. The stress versus strain curve defined by Equation (5-1) is shown in Figure 5-3 along with the input used to define this curve in the finite element analysis. A modulus of elasticity, E, of 200 000 MPa and Poisson's ratio, υ, of 0.3 were used to define the linear elastic portion of the stress versus strain curve. Stress and strain pairs in increasing order were then used to define the stress versus plastic strain curve. The first data pair corresponds to the onset of yielding, i.e., the stress value is the approximate proportional limit of 200 MPa and the plastic strain value is zero. The stress value of 540 MPa in the last data point corresponds with the tensile strength reported by Sehitoglu (1983). ABAQUS interpolates linearly for values between those given and the stress is assumed to be constant outside the given range. The modulus of elasticity, Poisson's ratio, and stress and plastic strain pairs used to define the cyclic stress versus strain curve are presented in Table 5-1 for all materials used in the analytical investigation.

Static nonlinear finite element analyses of the modelled specimens were carried out at various load levels, expressed in terms of nominal stress amplitudes. The analysis was conducted at the eight stress amplitude levels shown in Table 5-2, varying from 118 MPa to 271 MPa on the net area. Under the fully reversed loading condition, the maximum load is the same as the load amplitude. The inelastic finite element analysis results of the test specimens are shown in Table 5-2. As the nominal stress levels increased from 118 MPa to 271 MPa, the peak stresses at the edge of the hole increased from 233 MPa to 414 MPa and the corresponding peak strains increased from 0.161% to 0.768%. The stress concentration factor (with respect to gross section stress) obtained from the analysis therefore ranges from 2.33 to 1.80, with 2.33 approaching the fatigue notch factor at long fatigue lives.

138

5.2.3. Fatigue Life Prediction

5.2.3.1. Fatigue crack initiation life

For the stress-based method, the fatigue crack initiation life, N_i, can be obtained from Equation (3-1), with the stresses σ_{max} presented in Table 5-2, taken as the stress amplitude, $\Delta\sigma/2$, with $\sigma'_f = 1036$ MPa and $b = -0.11$. Using the inelastic finite element analysis results, the crack initiation life predicted for each stress amplitude from the test program of Sehitoglu (1983) are presented in the fifth column of Table 5-2.

The conventional stress-based method uses a fatigue notch factor, K_f, to correct the nominal stress for the stress concentration effect at the stress raiser. The fatigue notch factor can be calculated as (Dowling 1999):

$$K_f = 1 + \frac{K_t - 1}{1 + \sqrt{\beta/\rho}} \tag{5-2}$$

where K_t is the elastic stress concentration factor defined as the ratio of peak stress, obtained from an elastic analysis, to the gross section stress, assuming a linear-elastic response, ρ is the notch root radius (radius of the hole for the case examined here), and β is a material constant defined as:

$$\log\beta = -\frac{\sigma_u - 134}{586} \tag{5-3}$$

where σ_u is the tensile strength of the material in MPa. For a plate with a hole diameter to plate width ratio of 0.15, the elastic stress concentration factor K_t is 2.92 (Frocht 1936). For $\sigma_u = 540$ MPa and $\rho = 3.8$ mm (see Figure 5-1), K_f is calculated as 2.56. The peak stress at the edge of the hole is then obtained by multiplying the gross section stress by K_f. The crack initiation life can now be obtained from Equation (3-1). The predicted values are listed in the sixth column of Table 5-2.

139

The crack initiation life, N_f, can be obtained from the strain-based method using Equation (3-4) where the strain amplitude, $\Delta\varepsilon/2$, is taken as the maximum strain, ε_{max}, listed in the fourth column of Table 5-2 with $\sigma_f' = 1036$ MPa, $b = -0.11$, $\varepsilon_f' = 0.242$, and $c = -0.48$. The calculated crack initiation life is presented in the seventh column of Table 5-2.

Since Sehitoglu (1983) did not report the material properties necessary to use energy-based methods for fatigue life prediction, the material properties determined from tests on A7 steel were used to compare the strain-based method to the energy-based methods. Because the cyclic stress versus strain curve for A7 steel is significantly different from that of A36 steel, the analysis of the plate with a hole had to be repeated with the material properties for A7 steel. Table 5-3 presents the maximum stress and strain for each nominal stress amplitude level. A comparison of Table 5-3 with Table 5-2 indicates, as expected, that the maximum stress for the plates with a centre hole is significantly lower than that obtained for A36 steel, whereas the strains are higher for the lower grade steel. The crack initiation life predicted with the strain-based method was also re-calculated for A7 steel as shown in Table 5-3. Once again, a comparison of the results presented in Table 5-3 with those presented in Table 5-2 indicates a reduced fatigue crack initiation life for A7 steel compared to the predictions for A36 steel.

The plastic strain energy per cycle ΔW^p was obtained from Equation (A-7) with $K^* = 587$ MPa and $n^* = 0.143$ which were obtained from the material test program. The total strain energy per cycle ΔW and ΔW^t were calculated using Equations (3-6) and (3-7), respectively. The crack initiation life was then calculated using the three measures of energy presented above from Equations (3-8) to (3-10). For A7 steel, the parameters obtained from the material test program presented in Chapter 4 are: $F_p = 622$ MJ/m^3, $\alpha_p = -0.642$, $\Delta W_0^p = 0$; $F = 431$ MJ/m^3, $\alpha = -0.560$, $\Delta W_0 = 0.12$ MJ/m^3; and $F_t = 551$ MJ/m^3, $\alpha_t = -0.621$, $\Delta W_0^t = 0.03$ MJ/m^3. The cyclic and fatigue material properties of A7 steel are shown in Table 4-10. Fatigue material properties for all steels used in

140

fatigue life prediction in this chapter are also presented in Appendix B. The predicted crack initiation life from each of the measures of energy is presented in Table 5-3.

5.2.3.2. Fatigue crack propagation life

The fatigue crack propagation life was predicted for every specimen tested by Sehitoglu (1983). A single through-thickness edge crack was assumed to emanate from the edge of the circular hole in each of the test specimens. The stress intensity factor was calculated in accordance with Equation (3-22). For the geometry and load condition considered, the crack front shape correction factor, β_F, is 1.0, the free surface correction factor, β_S, is 1.12, and the finite width correction factor, β_W, is calculated from Equation (3-24a) where W is the distance from the hole edge to the plate edge, which is 21.2 mm for these test specimens. The stress gradient correction factor, β_G, is calculated from Equation (3-25). The normalized stress distribution along the x-axis of symmetry for a nominal stress amplitude of 271 MPa is shown in Figure 5-4, where k is a normalized stress range expressed as a fourth order polynomial fitted through the nodal stress distribution obtained from the finite element analysis; the constants A_0 through A_4 at each stress amplitude level are also presented in Figure 5-4. The normalized stress range was calculated as the stress range from the finite element analysis divided by the nominal applied stress range. The stress at a node was obtained by extrapolating element stresses to the node for all elements connected to the node. The average of these stresses was taken as the nodal stress. The crack propagation material properties for ferrite-pearlite steels were used to predict the crack propagation life: constant $C = 6.9 \times 10^{-9}$, exponent m = 3, for crack length a in mm and ΔK in $MPa\sqrt{m}$ (Barsom and Rolfe 1999). The initial fatigue crack size was taken as either an engineering crack size of 1 mm, or that determined from an initial stress intensity factor range of 6.2 $MPa\sqrt{m}$ (see section 3.2.3.2), whichever is larger. The fracture toughness was conservatively assumed to be 50 $MPa\sqrt{m}$. Fatigue crack propagation lives at each load level were then calculated

141

through numerical integration of Equation (3-20) and the results are presented in Table 5-2. The calculation at a nominal stress of 118 MPa is shown in Table 5-5 as an example.

For the plate with a circular hole detail, other empirical equations of stress intensity factor are available. For example, $\Delta K = 1.12(A_0\Delta\sigma)\sqrt{\pi a}$ was considered correct for a small crack size and $\Delta K = \Delta\sigma\sqrt{\pi(D/2 + a)}$ can be used when the crack size a is larger than the hole radius $D/2$ (Barsom and Rolfe 1999). The calculated fatigue crack propagation lives are listed in Table 5-2 as the empirical crack propagation life. These empirical stress intensity factor expressions are found to give fatigue crack propagation life predictions that are almost identical to the general expression of stress intensity factor presented in Section 3.2.3.4 for the geometry and load considered.

5.2.3.3. Comparison with test results

The comparison between the test results and the fatigue life predicted by the various methods presented in Tables 5-2 and 5-3 is illustrated in Figure 5-5. All seven crack initiation life curves and one total life curve, taken as the sum of the crack initiation life predicted using the inelastic stress-based method and the crack propagation life, are compared with Sehitoglu's test results. The predicted fatigue crack propagation life is relatively short, generally representing less than 10% of the total life, except at the two highest load levels, where 38% and 20% of the total life was spent propagating the crack.

Figure 5-5 indicates that the strain-based approach (using A36 material properties) predicts well the fatigue life of the test specimens. The stress-based approach predicts poorly the fatigue test results when the material properties are assumed linear elastic. The linear elastic approach overpredicts the peak stress at the hole by 10% to 42%. However, when inelastic material properties are used in the finite element model to determine the peak stress, the stress-based approach produces excellent predictions of the test results. The improved quality of the fatigue life prediction from the elastic stress-based approach to the inelastic stress-based approach is expected since high stress ranges

142

were used in the test program, thus causing localized yielding that cannot be accounted for by an elastic stress-based approach.

The four fatigue curves derived using experimentally determined cyclic material properties for A7 steel are also presented in Figure 5-5: three curves obtained using different energy methods and one curve using the strain-based method. These four curves demonstrate that the energy-based and the strain-based methods give almost identical results. However, there is a significant difference in fatigue resistance between the two steels used in this study. The comparisons presented in Figure 5-5 indicate that both strain-based and energy-based methods can be used for accurate prediction of fatigue life. The significant impact of material properties is also evident.

In order to compare the fatigue resistance of a fatigue detail of A36 steel with that of HPS 485W steel, the strain-based method was used to develop a mean S–N curve for a plate with centre hole for both A36 steel (tests from Sehitoglu) and HPS 485W steel (tests presented in Section 4.4). The mean S–N curve was determined from a regression analysis on the prediction results where fatigue life was taken as the dependent variable. For A36 steel, the predicted fatigue life N (including both crack initiation life and propagation life) in terms of the nominal stress range, $\Delta\sigma$, can be expressed as:

$$\log N = 19.9 - 6\log\Delta\sigma \tag{5-4}$$

This S–N curve is shown in Figure 5-6 with the test results from Sehitoglu. The figure also shows the test results from specimens of similar geometry to those of Sehitoglu, but made of 6.4 mm HPS 485W steel as outlined in Section 4.4. The predicted fatigue life for the HPS(LT) detail, obtained using the strain-based approach and linear elastic fracture mechanics, is presented in Table 5-4 and plotted in Figure 5-6. The sloping part of the fatigue curve is expressed as $\log N = 23.6 - 7\log\Delta\sigma$, determined from regression analysis. The horizontal part was determined by equating the maximum stress near the hole, obtained from an inelastic finite element analysis, to the fatigue limit for HPS(LT) steel obtained from the experimental program (300 MPa), giving a fatigue limit in terms of net section stress of 236 MPa as shown in Figure 5-6. Although the circular hole was

143

slightly off-center, this was not considered in the analysis. It is apparent from Figure 5-6 that the predictions captured the trend of the HPS(LT) test results very well. Consistent with the experimental observations, the predicted S–N curves indicate that the 6.4 mm HPS plate performed slightly better than the A36 steel plate.

5.2.3.4. Design curve

The analytical fatigue curves presented above were derived using average material properties, thus representing mean fatigue curves. Fatigue design curves, however, are usually set at two standard deviations below the mean curve. A standard deviation of 0.25 (i.e., log N = 0.25) was used to derive a design curve, as this value was observed from a large number of fatigue tests and was recommended for all the fatigue curves in code specifications (Klippstein 1987). Subtraction of two standard deviations from the mean fatigue curve thus provides the design curve for plates with a hole as:

$$\log N = 19.4 - 6\log\Delta\sigma \qquad\qquad (5\text{-}5)$$

This design curve is shown in Figure 5-7 with the test results from which it was derived. The design curve for the 6.4 mm HPS 485W steel was derived in a similar manner and is shown in Figure 5-7 as well, along with test results on HPS(LT) steel. The figure also shows fatigue Category B and C curves used in North American standards (CSA 2000). Although the predicted fatigue curves for the fatigue detail made of A36 steel or HPS fit the test results very well, neither curves are close to the curves for fatigue Categories B and C. The slopes of the proposed design curves are significantly different from the standardized slope of 3 used in fatigue design standards, which is applicable if the crack initiation life is short or non-existent (Fisher 1998). The design curve for HPS seems to be very close to the mean test results on A36 steel, which indicates that the difference between the two steels is about two standard deviations. For this particular detail, the design curve of HPS is better than that of A36 steel by one fatigue category.

144

5.3. Bearing-type Bolted Shear Splices (Josi *et al.* 1999)

5.3.1. Test Description

Fatigue tests on bolted bearing-type shear splices with staggered holes were conducted by Josi *et al.* (1999). The test program was designed to investigate the effect of bolt hole stagger on fatigue resistance of bearing-type connections. It included six series of double lap splice test specimens, for a total of 31 specimens with various bolt hole layouts and loading parameters. The specimens were made of CSA G40.21 300W steel (CSA 1998) and were tested in a universal testing machine under load control and a stress ratio of 0.3. A typical specimen is shown in Figure 5-8 where the stagger, s, varied from 0 to 76.2 mm in increments of 25.4 mm and the gauge distance, g, was either 45 mm or 61 mm. The 20 mm diameter bolt holes were match drilled for 19 mm bolts, which were installed to a snug tight condition. Even though the bolts were installed as snug tight only, the high strength bolts were tightened with a calibrated wrench in a similar manner for all the specimens so that the amount of bolt pretension was kept small and constant between specimens. The plate surfaces were left undisturbed, i.e., the mill scale was not removed.

Cracking was observed to initiate from a critical bolt hole (critical holes are the holes closest to the center of the splice plates) in more than 70% of the test specimens and 86% of the tests failed because of cracks starting at the outside of a hole. Most of the shear splices showed single cracks at the time of failure. The fatigue life of the test specimens varied from 3×10^5 to 9×10^6 cycles depending on the geometry and the applied load level of the bolted connection.

The geometries, test load levels and fatigue test results for the bearing-type shear splice plates are listed in Table 5-6. The corrected nominal stress range, $\Delta\sigma_{nc}$, was obtained by multiplying the gross section stress range by the ratio of the stress concentration factor (determined from a linear elastic finite element analysis) for the staggered bolt hole pattern to the stress concentration factor for the same connection with no stagger (S0 series). This procedure of correcting the gross section stress range was suggested by Josi *et al.* (1999) so that test data with different bolt layouts (with and without stagger) can be

145

compared to a common fatigue curve. The mean regression line for the test results, expressed in terms of the corrected stress range, is ($\log N = 20.1 - 7 \log \Delta \sigma_u$), with a standard deviation of 0.255. More details about the test specimens and the testing procedure can be found elsewhere (Josi *et al.* 1999).

5.3.2. Finite Element Model

Because the splice plates and main plates were match drilled and the bolts were only snug tight at the beginning of the test, it is assumed that the splice plates share the load equally and negligible friction develops on the faying surfaces. The test specimens were designed so that fatigue failure would take place in the splice plates rather than in the main plates. Therefore, it was necessary to model only one splice plate. Since cyclic and fatigue properties are not available for 300W steel, the material properties presented by Schitoglu (1983) for A36 steel are used for the finite element analysis and the fatigue life predictions.

Since the deformations were small and the out-of-plane effects were negligible, the four-node quadrilateral membrane element M3D4 from ABAQUS was used for the analysis. All nodes were restrained in the out-of-plane direction and the centre node of the mesh was restrained in other orthogonal directions in the plane of the plate. A typical converged mesh, determined from a mesh refinement study, is shown in Figure 5-9, where a 32 mm square outside the circular hole cut-out is divided into 16 parts on each edge with radial link of 6 and bias of 1. A mesh of about half of this density, built with nine-node quadrilateral membrane elements, M3D9, was shown to have converged to the exact solution (Josi *et al.* 1999). The load was assumed to be shared equally by all the bolts and transferred only by bearing. At each bolt hole, fifteen equal node loads were applied. The loaded nodes are identified in Figure 5-9 as black dots. The mid-loading points were restrained from displacement in the y direction.

Because the specimens were not tested under a fully reversed condition, finite element analysis was conducted at both the maximum load and the load amplitude used in the tests. Table 5-7 shows the analysis results for the test specimens. The table presents

146

stress amplitude, strain amplitude, and maximum stress, maximum strain at the edge of the critical bolt hole location and the coefficients of a 4th order polynomial equation that describes the normalized stress range (with respect to gross section stress range) along the potential crack path.

5.3.3. Fatigue Life Prediction

5.3.3.1. Fatigue crack initiation life

Because of the loading condition used in the tests, the mean stress is not zero and the mean stress effect must be accounted for in the fatigue life calculations. Both the Morrow model for the stress-based method and the SWT model for the strain-based method, as described in Section 3.2.2.2, were used to predict the fatigue crack initiation life and early stage of crack propagation of the shear splices. The Morrow correction for the stress-based method is expressed by Equation (3-11) using the stress amplitude and mean stress ($\sigma_m = \sigma_{max} - \Delta\sigma/2$) obtained from the data presented in Table 5-7. Using the maximum stress and the strain amplitude presented in Table 5-7, the fatigue life N_i predicted by the SWT model for strain-based method can be obtained from Equation (3-12). The fatigue life was also predicted using Equations (3-1) and (3-4), which do not contain a mean stress correction. The fatigue life was predicted using the various methods outlined above for the six series of tested shear splices at eleven load range levels. The results are presented in Table 5-8.

5.3.3.2. Fatigue crack propagation life

The fatigue crack propagation life was calculated in a similar manner as for the plate with a circular hole detail, using the general expression of stress intensity factor and numerical integration. The fracture mechanics calculations were carried out for a single crack initiating at the critical bolt hole, on the side of the hole with the maximum stress concentration factor. The finite width correction factor, $'\beta_w$, was obtained from Equation (3-24a) using the clear distance between the edge of the bolt hole and the edge

147

of the splice plate as the finite width, W. The stress gradient correction factor, β_G, is calculated from Equation (3-25) and the coefficients A_0 to A_4 presented in Table 5-7. The crack propagation material properties for ferrite-pearlite steels (Barsom and Rolfe 1999) were adopted for these calculations.

The calculated fatigue crack propagation life for the bearing-type shear splice specimens is shown in Table 5-8. The fatigue crack propagation life for this detail varies from 7.2×10^3 to 4.4×10^4 cycles, representing less than 5% of the total fatigue life. The effect of the mean stress was not considered in fatigue crack propagation analysis because it is generally accepted that the effect of mean stress on crack growth rate is small (Dowling 1999). Since the crack propagation life represents only a short portion of the total life, any error introduced by ignoring the effect of mean stress on crack propagation is expected to be small.

5.3.3.3. Comparison with test results

The predicted fatigue life and the test results reported by Josi et al. (1999) are presented in Figure 5-10. The figure presents the mean regression line and the upper and lower bounds from the test results. The stress range plotted in the figure is the corrected nominal stress range, $\Delta\sigma_{nc}$. A comparison of the mean regression line of the test data with the predicted fatigue curves indicates that mean stress effect is important. The stress-based method with the mean stress correction proposed by Morrow and the strain-based method with the SWT correction predict the fatigue test results very well. Both models predict the mean fatigue life and the slope of the experimental fatigue curve very well.

5.3.3.4. Design curve

The combination of the strain-based method with the SWT mean stress effect correction and the linear elastic fracture mechanics approach was used to derive a design curve for this detail, as shown in Figure 5-11. The design curve can be expressed as follows:

148

$$\log N = 17.2 - 6 \log \Delta \sigma_{xc}$$ (5-6)

where $\Delta \sigma_{xc}$ is the corrected nominal stress range proposed by Josi et al. (1999).

Bolted connections are commonly designed using the fatigue Category B curve (CSA 2000), which is shown in Figure 5-11 for comparison. The slope of the theoretical fatigue curve is 6, as opposed to 3 for all the fatigue category curves used in North American design standards. The design curves in the current standards are mostly based on fatigue test results on welded details (Fisher et al. 1970, Fisher et al. 1974). Both the experimental observations (Josi et al. 1999) and the analysis performed in the current study indicate that the current fatigue design curve for fatigue Category B is not appropriate for bearing-type bolted shear splices.

Fatigue life prediction was conducted in a similar manner for the shear splices using HPS(LT) steel properties obtained from the test program; the results of inelastic finite element analysis and fatigue life prediction are presented in Table 5-9. A design curve for HPS(LT) steel was similarly derived and is shown in Figure 5-11. The figure indicates that the 6.4 mm plate HPS performs slightly better than the A36 steel for bearing-type bolted shear splices. The difference between the two steels becomes larger than two standard deviations at a fatigue life of 5×10^5 cycles.

5.4. Large Scale Beam with Unfilled Holes (Baker and Kulak 1985)

5.4.1. Test Description

Baker and Kulak (1985) tested three beams containing punched holes in the tension flange. The specimens were used to simulate connections with completely loose rivets (rivets with zero clamping force) and members in which misplaced holes might be present. The fatigue tests were intended to represent a lower bound of fatigue strength of riveted connections in existing structures (Baker and Kulak 1985). The specimens consisted of W200x36 beams of CSA G40.21 300W steel (CSA 1998) with eight 21 mm diameter holes punched in the tension flange as shown in Figure 5-12.

149

Each simply supported beam was 3.2 m long and was tested on a 3.06 m span. The test sections, those with open holes, were contained within a constant moment region 910 mm long. Lateral bracings were provided at the loading points. All three beams were tested at a stress range of 216.1 MPa with a minimum stress of 27.6 MPa. The stress range was established using four strain gauges mounted on the underside of the bottom flange as shown in Figure 5-12. The failure criterion was an increase in midspan deflection of 0.5 mm. At this stage a fatigue crack had propagated through 25% to 50% of the flange cross section.

In all of the specimens tested, cracking started at the extremity of one of the end holes and propagated out towards the flange tip. Because of the large stress range used for the testing, the average fatigue life of the three tested beams was only 5.2×10^4 cycles, with all the tests within a range of 1.3×10^4 cycles.

5.4.2. Finite Element Model

Because the cyclic and fatigue material properties of G40.21 300W steel are not available, the properties presented by Sehitoglu (1983) for A36 steel were used for the finite element analysis. Because of symmetry, only one half of a test specimen was modelled. The four-node quadrilateral shell element S4R from ABAQUS was used. The model, shown in Figure 5-13, consists of 8576 elements and 8915 nodes. All the nodes at midspan were restrained from displacement in the x-direction and rotation about y-axis. A close up view of centre part of the beam where holes are present is shown in the top right corner of Figure 5-13. A finer mesh is provided in the critical region around the hole and general multi-point constraints are applied for changes in mesh density.

Because the load that was applied in the tests was not reported, an analysis was run to determine the loads that produce the same strains at the gauge position as measured in the tests. This consisted of a maximum stress of 243.7 MPa and stress range of 216.1 MPa at the strain gauge locations. A maximum load of 81.85 kN and a load range of 69.4 kN were determined. The maximum load and load amplitude were used in the same model

150

to determine the maximum stress or strain and the stress amplitude or strain amplitude at the critical element.

A contour plot of the normal longitudinal stress, σ_x, which is identified as S11 in ABAQUS, in the test section is shown in Figure 5-14. The critical region, which contains the largest stress concentration, is located between the flange tip and the edge of a hole as indicated in the figure. This is also the region observed in tests where crack initiation and propagation took place and where failure of the specimens occurred. The stress and strain conditions at the critical section were found to be: stress amplitude $\Delta\sigma/2 = 257.0$ MPa, strain amplitude $\Delta\varepsilon/2 = 0.196\%$, maximum stress $\sigma_{max} = 461.8$ MPa, and maximum strain $\varepsilon_{max} = 1.129\%$. The fourth order polynomial of the normalized stress range distribution with respect to the nominal gross section stress range of 216.1 MPa can be expressed as $k = 2.390225 - 0.173053x + 0.005263x^2 + 0.000169x^3 - 0.000009x^4$, where x is measured from the edge of the critical hole towards the edge of the flange, along the expected crack path. The shape of the normalized stress distribution k along the expected crack path is illustrated in Figure 5-14.

5.4.3. Fatigue Life Prediction

5.4.3.1. Fatigue crack initiation life

The stress and strain conditions at the critical element were used in the fatigue crack initiation calculations. As for the bolted shear splices detail (Josi et al. 1999), Morrow's model for the stress-based method and the SWT model for the strain-based method were used to account for the effect of mean stress on the predicted fatigue crack initiation life and early stage of crack propagation of the test beams. The fatigue life is calculated as 5.1×10^4 cycles and 5.2×10^4 cycles for the stress-based method and strain-based method, respectively.

151

5.4.3.2. Fatigue crack propagation life

The fatigue crack propagation life was calculated in the same manner as for the bearing-type bolted shear splices tested by Josi *et al.* (1999). The stress gradient correction factor β_G is obtained in accordance to Equation (3-25) based on the normalized stress, fourth order polynomial distribution with A_0 = 2.390225, A_1 = - 0.173053, A_2 = 0.005263, A_3 = 0.000169, and A_4 = - 0.000009. The calculated fatigue crack propagation life is 3.4×10^3 cycles at the normal stress range of 216.1 MPa.

5.4.3.3. Comparison with test results

The predicted fatigue life and the results of three beam tests are shown in Figure 5-15 where the vertical axis shows the nominal bending stress range at the net cross section. The fatigue Category D curve (CSA 2000), which is used for the net section nominal stress at a riveted connection, is also shown in the figure. The fatigue life obtained from the tests was shorter than indicated by fatigue Category D curve, which is two standard deviations below the mean curve. On the other hand, the total predicted fatigue life (using the strain-based method with the SWT mean stress effect correction for fatigue crack initiation life) is in excellent agreement with the test results.

The fatigue life for the detail tested by Baker and Kulak (1985) was also predicted using material properties obtained HPS(LT) steel as shown in Figure 5-15. The figure indicates that the same detail made of high performance steel would perform slightly better than the detail made of A36 steel at this particular stress range level. The predicted fatigue life for HPS is more that twice that for A36 steel, indicating the difference in fatigue life is log N = 0.31. This difference is larger than 0.25, the value of standard deviation that has been used to establish a design curve from the mean predicted life. As the tests were conducted at only one stress range level, no attempt was made to obtain a design curve from analysis for the beam with unfilled holes.

152

5.5. Welded Cruciform Detail (Friedland *et al.* 1982)

5.5.1. Test Description

Friedland, Albrecht, and Irwin (1982) reported results of fatigue tests of non-load-carrying cruciform specimens. A typical cruciform specimen is shown in Figure 5-16. The main plate was 330 x 25 x 10 mm to which two 50 x 25 x 7 mm transverse plates were attached with 5 mm fillet welds on each side using the shielded metal arc welding process. The specimens were made of ASTM A588 steel (high strength low alloy structural steel with weathering characteristics). Individual specimens were saw cut from a larger welded plate assembly into 25 mm widths.

Twenty non-weathered control specimens were tested at four levels of stress range (90, 138, 207, and 290 MPa), with five replicate specimens at each level. The minimum stress level was set at 3 MPa in all tests. Axial fatigue loading was applied to the main plate of the cruciform specimen only.

All semi-elliptical fatigue cracks initiated in the main plate at one or more points along the toe of the stiffener-to-main plate weld. They propagated through the thickness of the main plate until the net ligament ruptured at an average net section stress nearly equal to the tensile strength. The fatigue test results of these specimens are presented in Table 5-10. The observed fatigue life varied from 8.5×10^4 to 10^7 cycles, depending on the test stress range. The run out level was set as 10^7 cycles. The mean regression line of the test results was reported as $\log N = 12.5 - 3 \log \Delta\sigma$, with a standard deviation of 0.123.

5.5.2. Finite Element Model

A two-dimensional finite element model of a plane strain strip was used to analyze a typical cruciform specimen. Because the test specimens were doubly symmetric, only one quarter of the specimen was modelled. The quadrilateral linear plain strain continuum element CPE4R was used for the plates and triangular plain strain continuum element CPE3 was used for the fillet weld region. A model approximately 20 mm long

153

in both directions was found to be adequate to represent the whole specimen. The converged finite element mesh for a strip of unit width is shown in Figure 5-17. The circled mesh region represents the critical region where fatigue cracking is expected to take place. The potential crack plane is located as section A-A.

Table 5-11 presents the results of the inelastic finite element analysis in the critical region, including principal stress ($\sigma_1 < \sigma_2 < \sigma_3$), von Mises equivalent stress, principal strain ($\varepsilon_1 < \varepsilon_2 < \varepsilon_3$), equivalent plastic strain, elastic strain energy, and plastic strain energy. The stress, strain and energy responses in Table 5-11 indicate that the critical region undergoes mostly elastic deformation; this is as expected because the specimens were tested at relatively low stress ranges.

The direction of major principal stress in the specimen is shown in Figure 5-18. It is apparent from the figure that, except in the immediate region of the weld where deviation of the major principal stress from the loading direction amounts to a few degrees, the principal direction is almost exclusively the same as that of the remote stress field. The stress normal to section A-A is used to calculate stress intensity factors in mode I and only ΔK_I will be used for the crack propagation life calculation. The normal stress distribution along section A-A was obtained by extrapolating the stresses in two adjacent elements on either side of the section and the constants in the fourth order polynomial representing the normalized stress distribution (with respect to the nominal stress range) are shown in Table 5-12. The constants are almost identical for the four stress ranges, indicating that little plastic deformation took place at all stress range levels.

5.5.3. Fatigue Life Prediction

5.5.3.1. Fatigue crack initiation life

Since fatigue material properties for A588 steel are not available, the cyclic stress versus strain properties and the fatigue properties of HPS(LT) steel obtained from the test program presented in Chapter 4 were used in the finite element analysis and in the fatigue crack initiation life calculation of the cruciform specimens. The approximation of

154

material properties is justified because A588 steel and HPS(LT) steel have similar yield strengths, and therefore can be assumed as having similar cyclic stress versus strain curves and fatigue properties.

In order to account for the triaxial state of stress that exists in the plane strain model, the energy-based criterion for multiaxial stress state described in Section 3.2.2.3, which accounts for mean stress effect, is used for the fatigue crack initiation life prediction. For each tested stress range level, the elastic strain energy density at maximum load, ΔW^{e+}, and the plastic strain energy density at load range, ΔW^p, are both obtained directly from ABAQUS. Using the principal strains at the stress ranges listed in Table 5-11, the effective Poisson's ratio, ν, is calculated to be 0.3 from Equation (3-17). The multiaxial constraint factor, ρ, defined in Equation (3-16), is approximately 0.988 for the test specimens. The predicted fatigue crack initiation life for the cruciform specimens was calculated using Equation (3-15) where the material constants, obtained from the uniaxial energy versus life curve of HPS(LT) steel, are $F_i = 1463$ MJ/m^3, $\alpha_i = -0.721$, and $\Delta W_0' = 0.20$ MJ/m^3. According to Equation (3-15), fatigue crack initiation lives varying from 5.6×10^4 to 1.0×10^7 cycles are calculated for the tested cruciform specimens, while infinite fatigue life is predicted for the specimens tested at the 90 MPa stress range.

5.5.3.2. Fatigue crack propagation life

Linear elastic fracture mechanics was used to calculate the fatigue crack propagation life of the welded cruciform detail. For A588 steel, the mean plane strain mode I fracture toughness K_{IC} is reported as 50 $MPa\sqrt{m}$, the crack growth rate properties are reported as $C = 1.54 \times 10^{-9}$ and $m = 3.34$ for crack length a in mm and ΔK in $MPa\sqrt{m}$ (Yazdani et al. 1990). A constant crack aspect ratio of 0.5 was assumed for cruciform details, which is consistent with the assumption made by Yazdani et al. (1990) for crack growth rate prediction of a welded cruciform detail. The stress intensity factor at the end of the minor axis of the semi-elliptical crack was used for the crack growth calculations. The initial crack size was taken as 1 mm or that calculated from an initial value of $\Delta K =$

155

$6.2\ MPa\sqrt{m}$. The stress intensity factor range was calculated using Equation (3-22), where β_{E}, obtained from Equation (3-23), is 0.8 for a crack aspect ratio of 0.5, and β_{S} is taken as 1.12 for one free surface. The finite thickness correction factor, β_{W}, was obtained from Equation (3-24b) with W taken as twice the main plate thickness, that is, 20 mm. The stress gradient correction factor β_{G} is calculated using Equation (3-25) and the normalized stress distribution is described in Table 5-12. Although four stress ranges were used in the test program, crack propagation life was predicted only for the three highest stress ranges since the calculations indicate that no crack will initiate at the lowest test stress range. The predicted fatigue crack propagation lives for the three specimens with finite life varied from 6.1×10^4 to 7.5×10^5 cycles.

5.5.3.3. Comparison with test results

The fatigue life predictions for the welded cruciform specimens tested at four levels of stress range are presented in Table 5-10 and illustrated in Figure 5-19. The test results, mean regression line, and the upper and lower confidence limit lines, set at two standard deviations from the mean, are also presented in Figure 5-19. The predictions are found to fall generally within the scatter band of the test results delimited by the confidence limit lines. The difference between the total predicted fatigue life and the mean regression line of the test results seems to be larger at lower stress ranges, especially when the test fatigue life is greater than 2 million cycles. Since the energy ($\Delta W'$) versus life curve has a smooth transition near the fatigue limit (as illustrated in Figure 2-2 and Figure 4-29), predictions are unavoidably more sensitive to the calculated damage parameters near the transition, which could explain some discrepancy between test results and predictions. However, fatigue tests have a lot more variations at lower stress range levels, especially near the fatigue limit. Other important factors, such as weld imperfection, that would have a more significant effect at lower stress ranges, were not considered in the model.

The fatigue Category C' curve from CSA (2000), which was derived largely based on the test results on transverse stiffeners welded to the web and tension flange of beams (Fisher

156

et al. 1974), is shown in Figure 5-19 for comparison. The test results on the cruciform specimens were found to correlate well with the previous fatigue data for stiffeners. This confirmed the ability of the tensile cruciform specimens to simulate accurately the stress condition at transverse stiffeners of beam specimens.

5.6. Welded Cover Plate Detail (Friedland *et al.* 1982)

5.6.1. Test Description

Friedland, Albrecht, and Irwin (1982) also reported fatigue test results from tensile cover plate specimens. A typical test specimen, shown in Figure 5-20, consisted of a 330 x 64 x 10 mm main plate with two 102 x 45 x 7 mm cover plates welded to the main plate with 5 mm fillet welds. The cover plate length-to-width ratio is 2.3.

The specimens were made from the same heat of A588 steel plates as the cruciform specimens described in Section 5.5. The cover plates were welded using shielded metal arc welding and the stop and start points were located in the longitudinal welds 12.7 mm away from the corners of the cover plates, as indicated in Figure 5-20.

Twenty non-weathered control specimens were tested at stress ranges of 103, 145, 207, and 290 MPa. Five replicate tests were conducted at each stress range. Cyclic axial load was applied at the ends of the main plate. The minimum stress was kept at 3 MPa and the run-out level was defined as 10^7 cycles in all tests. The observed fatigue life varies from 4.1×10^4 to over 10^7 cycles, as shown in Table 5-13. The mean regression line for the test results was reported as $\log N = 13.4 - 3 \log \Delta\sigma$, with a standard deviation of 0.094.

Crack initiation and the crack propagation pattern in the cover plate specimens were found to be similar to that of the cruciform specimens described in Section 5.5. The crack initiated at multiple points along the weld toe lines. As they grew deeper and longer, they coalesced to form a long shallow part-through crack over the full length of the end weld. Failure eventually occurred when the deepest point of the crack front approached the back face of the plate, causing the net ligament to rupture in a ductile

157

mode at a mean net section stress nearly equal to the tensile strength (Friedland *et al.* 1982).

5.6.2. Finite Element Model

One eighth of the triply symmetric geometry was modelled with two layers of three-dimensional elements, one layer for the cover plate and one for the main plate, as shown in Figure 5-21. Three dimensional linear continuum elements C3D8R, C3D6, and C3D4 were used to model the plates, the weld line, and weld corner, respectively. All the nodes located on planes of symmetry were fixed in the direction perpendicular to the plane and free in the tangential directions. As for the cruciform specimens, the cyclic material properties obtained for HPS(LT) steel were used for the finite element model. Loads were applied to end elements of the main plate as uniform pressure.

In order to obtain the stress distribution normal to the potential crack plane (at the weld toe), a refined mesh was necessary. A refined 3D solid finite element submodel was set up for the specimen region within the dotted line shown in Figure 5-21. The displacement response from the global model was used to load the submodel shown in Figure 5-22. The nodes whose displacement response obtained from the analysis of global model were used as boundary conditions for the refined submodel are identified as black dots in Figure 5-22. Lines 1 to 8 represent the various positions along the y-axis corresponding to the centroid of solid elements.

Typically, the normal longitudinal stress, σ_x, along the y-axis for all the top main plate elements on either side of the potential crack plane under various loadings follows the distribution shown in Figure 5-23. The stress distribution is relatively uniform except at the submodel boundaries, where the accuracy might have been affected by submodelling. Therefore, several crack initiation sites are possible as observed experimentally. The middle position element, designated as the critical element in Figure 5-22, was arbitrarily selected as the critical element. The inelastic finite element analysis results are presented in Table 5-14 for stress, strain and energy responses in the critical element. Table 5-15

158

presents the fourth order polynomial coefficients for the stress distribution along the potential crack path, normalized in terms of the nominal stress in the main plate.

5.6.3. Fatigue Life Prediction

5.6.3.1. Fatigue crack initiation life

The energy-based criterion for multiaxial stress state described in Section 3.2.2.3 was used to calculate the fatigue crack initiation life of the cover plate specimens. The material properties used to predict the fatigue life of the cover plate specimens were the same as those used for modelling the cruciform specimens described in the previous section. Using the finite element analysis results presented in Table 5-14, the predicted initiation life of this cover plate detail is obtained and shown in Table 5-13. The calculated fatigue life varies from 5.6×10^4 to more than 1.0×10^7 cycles for the four stress ranges used in the experimental program. The analysis predicts a test run-out for the specimen subjected to a stress range of 103 MPa.

5.6.3.2. Fatigue crack propagation life

No attempt was made to incorporate the effect of interaction between multiple small cracks along the weld toe line because of the complexity and uncertainty of this type of analysis. Instead, only the shallow part-through crack formed after the crack coalescence at the early stage of crack propagation was considered. Similar parameters used in calculating the fatigue crack propagation life of the cruciform specimens described in Section 5.5.3.2 were used to calculate the crack propagation life of the cover plate details. An average crack aspect ratio of 0.25, as reported by Yazdani and Albrecht (1990) for cover plate details, was used for the current analysis. Using the normalized stress distribution shown in Table 5-15, the stress gradient correction factor β_G was calculated using the method outlined earlier. The fatigue crack propagation life of the cover plate specimens was found to vary from 4.1×10^4 to 4.2×10^5 cycles, depending on the applied stress range levels. Because the crack initiation life calculation for the specimen tested at

159

a stress range of 103 MPa indicated an infinitely long crack initiation life, no crack propagation life was calculated for these specimens.

5.6.3.3. Comparison with test results

The predicted fatigue lives for the cover plate specimens are listed in Table 5-13 and plotted in Figure 5-24, along with the test results, the mean regression line, and the upper and lower confidence limit lines. The predicted fatigue crack initiation life, shown as open triangles in Figure 5-24, are close to the lower confidence limit line of the test results and the total predicted fatigue life, shown as solid triangles, are close to the mean regression line of the test results. A comparison of the analysis results with the test results indicates that the analysis predicts the test results very well.

Fatigue Category C and D curves from CSA (2000) are shown in Figure 5-24 for comparison. Cover plate attachments on beams with a similar attachment length and thickness to those under consideration (Friedland et al. 1982) are classified as Category D details. As shown in Figure 5-24, however, all data points from the cover plate specimens fall above the Category C curve. The reason for the apparently long life from Friedland's test specimens is the low degree of restraint provided by the main plate in comparison to the more rigid beam flanges (Friedland et al. 1982). The fatigue life predictions are able to capture the characteristics of this particular cover plate detail. The fatigue resistance of this detail falls one category above that of previous data from girder tests (Fisher et al. 1974).

5.7. Large Scale Welded Plate Girders (Wright 2003)

5.7.1. Test Description

Experimental research was conducted by Wright (2003) to study the fracture resistance of fatigue cracked, full scale, I-girders fabricated from two grades of high performance steel: HPS 485W and HPS 690W. Two welded plate girders, designated as HPS-485W-C1 and HPS-690W-C1, were designed with transverse stiffener attachments on the web to initiate fatigue cracks. As implied by the specimen designations, specimen HPS-

160

485W-C1 was made of A709 HPS 485W steel and specimen HPS-690W-C1 was made of A709 HPS 690W steel. Although the girders were designed as doubly symmetric to allow two replicate tests by inverting the girder, only one valid test result was obtained in each girder due to unsuccessful repairs.

The geometry of the two girders is shown in Figure 5-25. The reported flange width, flange thickness and web thickness are measured values. All other dimensions are nominal dimensions. The stiffeners and web were cut from the same steel plate for each girder. The simply supported girders were tested under four point bending; the length of the constant moment region was 2743 mm for both tests. Lateral bracing was provided at the load and reaction points. The location of the lateral supports is indicated in Figure 5-25.

The test specimens were loaded cyclically at a stress range of 110 MPa and stress ratio $R = 0.5$ measured at the extreme fibre. Both tests were conducted at room temperature at a cyclic frequency of 1 Hz. Once cracks developed, the temperature of the test specimens was lowered to $-34°C$ and subjected to an overload cycle to attempt to initiate a brittle fracture from the fatigue crack. If no fracture occurred, the room temperature fatigue cycling was resumed to grow a larger fatigue crack and the overload test was repeated. Because of the periodic overload applied on the test specimens at regular intervals, fatigue life prediction for constant amplitude loading was performed only for the fraction of the fatigue life up to the application of first overload.

The girders were visually inspected every day and dye penetrant and eddy current methods were used to help define the cracks that were identified visually. A 13 mm and a 14 mm semi-elliptical surface crack was first detected at the toe of a stiffener-to-web weld in specimens HPS-485W-C1 and HPS-690W-C1, respectively. The dimensions of the fatigue cracks prior to the overload test were more accurately determined from a digital photograph of the fracture surface.

A cross section from specimen HPS-485W-C1 showing the shape of the fatigue crack at the time of crack detection and at the first overload test is shown in Figure 5-26. The

161

fatigue crack initiated at the toe of the stiffener-to-web fillet weld after 1.77 million load cycles and eventually became a through-thickness web crack. The first overload test was conducted at 2.80 million load cycles.

Figure 5-27 shows the fatigue crack propagation history for girder HPS-690W-C1. The crack initiated as a semi-elliptical surface crack along the toe of the stiffener fillet weld after 996,700 load cycles. The crack propagated into a through thickness crack and propagated in the web, eventually entering the tension flange when overload test 1 was performed at 1.89 million cycles.

5.7.2. Finite Element Model

Both girders HPS-485W-C1 and HPS-690W-C1 were modelled numerically to obtain stress, strain or energy response in order to predict their fatigue life. The cyclic material properties obtained from HPS(LT) steel of this test program were used for both girders. The reported extreme fibre stress ranges were used for loading the finite element models. The reported stress range and stress ratio were 114.5 MPa and 0.51, respectively, for girder HPS-485W-C1 and the corresponding values for HPS-690W-C1 were 119.5 MPa and 0.57, respectively. A coarse mesh model of the full test girder, including all stiffeners, was used to predict the global response of the girder. The results from the coarse mesh model were used as boundary conditions for a fine mesh submodel that focused on the local behaviour in the proximity of the critical stiffener.

The deformed shape of the coarse mesh model of girder HPS-485W-C1 is shown in Figure 5-28. The coarse mesh model consisted of over 2000 quadrilateral shell elements (S4R). The typical element size is 50 mm in the flanges, the web and the stiffeners. The mesh was found to be sufficiently fine to produce accurate global displacement predictions.

The refined mesh submodel for HPS-485W-C1 is shown in Figure 5-29. The height of the web portion of the submodel is 152.4 mm, which was determined by the approximate position of the upper crack tip prior to overload test 1, and the length of the model is

162

182.85 mm. Because of the symmetry of the girder about the x-z plane, only half of the region was modelled in the refined mesh model. The black dots shown in Figure 5-29 represent the nodes from the coarse mesh model that were used to control the submodel behaviour.

The submodel was discretized using 3D linear solid elements for the flange, the web, the stiffener and welds (including web-to-flange weld and stiffener-to-web weld). Element C3D6, a six-node linear triangular prism element, was used for the welds and C3D8R, an eight-node linear brick element with reduced integration, was used for the rest of the model. Over 30,000 solid elements were used in the submodel. The thickness of the web was divided into 10 layers of elements in order to capture details of the stress distribution through the web thickness. The BIAS parameter from ABAQUS was used to create a finer mesh closer to web surface. Similarly, a biased mesh was used in x and z directions so that element size was much smaller in the region of high stress concentration.

The stiffener-to-web welds in the test girders were stopped short of the bottom of the transverse stiffeners. This detail is common practice so that no end returns are used around transverse stiffeners as specified by AASHTO (1998). However, neither the position nor the shape of the weld stop was reported by Wright (2003). The weld stop was therefore modelled as an abrupt stop for meshing simplicity. The distance from the bottom of the stiffener to the effective weld stop location (accounting for the abrupt stop in the model weld and the gradual transition in the actual weld) was estimated at 12.5 mm for girder HPS-485W-C1 from Figure 5-26 and 11 mm for girder HPS-690W-C1 from Figure 5-27. Because the actual dimensions were not reported, a sensitivity analysis of the weld stop position and weld size was conducted, the results of which are discussed in Section 5.7.3.4.

5.7.3. Fatigue Life Prediction

5.7.3.1. Fatigue crack initiation life

Figure 5-30 shows a stress contour plot of the normal longitudinal stress, σ_x, in the x-z plane as obtained from the submodel of girder HPS-485W-C1. The critical zone at the weld toe is located about 8 mm from the end of the stiffener-to-web weld as indicated in Figure 5-30. Stress, strain and energy responses in the critical element from the submodel analyses are presented in Table 5-16. As for the welded cruciform and cover plate specimens, the energy-based method for multiaxial stress state as outlined in Section 3.2.2.3 was used to predict the fatigue crack initiation life of the two girders. The effective Poisson's ratio υ is equal to 0.3 for both girders, and the multiaxial constraint factor ρ is calculated to be around 1.009 for girder HPS-485W-C1 and 1.006 for girder HPS-690W-C1. The predicted fatigue crack initiation life is 7.6×10^5 cycles for girder HPS-485W-C1 and 2.7×10^5 cycles for girder HPS-690W-C1.

5.7.3.2. Fatigue crack propagation life

Prior to the application of the first overload, the crack propagation stage can be divided into two parts: 1) propagation of a surface thumbnail web crack and 2) propagation of a two-tip through-thickness web crack. In girder HPS-690W-C1, however, the crack had propagated into the bottom flange about 7.5 mm at the time of the first overload test, as shown in Figure 5-27. Nevertheless, because the stress intensity factor expression for this type of crack is not available in the literature and the life spent in propagating this small distance into the flange is believed to represent only a small portion of the total fatigue life, this stage is neglected in the analysis of girder HPS-690W-C1. The fatigue crack growth rate constant $C = 7.17 \times 10^{-9}$ and coefficient $m = 3.02$ (for the crack length a expressed in mm and ΔK in $MPa\sqrt{m}$) that are reported by Wright (2003) for HPS 485W and HPS 690W at a high R ratio are used for the following fracture mechanics calculations.

164

The stress intensity factor formula proposed by Newman and Raju (1984), as outlined in Section 3.2.3.5, was used for the thumbnail web crack. For convenience, the stress component σ_1 at the centre of the crack, i.e., the web surface stress at the height of the integration point of the critical element, was used for the stress σ in Equation (3-26a). The distribution of the normal longitudinal stress, σ_x, in the crack plane through the web thickness, calculated at the height of the critical element, is shown in Figure 5-31 for girder HPS-485W-C1. The coefficients of a fourth order polynomial expression fitted through this stress distribution, normalized by dividing by the stress at the centre of the crack, are presented in Table 5-17. As shown in Figure 5-31, the stress distribution through the web thickness (i.e., crack depth) is not the uniform tension stress for which the stress intensity factor expression proposed by Newman and Raju (1984) was derived. A modification is therefore made to the stress intensity factor proposed by Newman and Raju by multiplying their stress intensity factor by the stress gradient factor β_G. The stress gradient factor is obtained from Equation (3-25) using the fourth order polynomial coefficients presented in Table 5-17. The plate thickness t shown in Figure 3-6 represents the web thickness for the crack considered, that is, 9.4 mm for girder HPS-485W-C1 and 9.27 mm for girder HPS-690W-C1. The distance from the crack centre to the top surface of the bottom flange was used as the plate width W shown in Figure 3-6. The value is 44.43 mm for girder HPS-485W-C1 and 42.27 mm for girder HPS-690W-C1, respectively. By considering $\phi = \pi / 2$ and $\phi = 0$ (see Figure 3-6) for functions f_ϕ (Equation (3-26g)) and g (Equation (3-26i)), the stress intensity factors at the minor and the major axis tips of the semi-elliptical crack were considered.

As the thumbnail web crack has two crack tips that can propagate independently, the following procedure was used to follow the evolution of the crack tip during cyclic loading:

165

1. Assume an increment of the minor crack tip, Δa, say 1% of crack size a from the previous step.

2. Assume some arbitrary value for the increment of the major crack tip, Δc.

3. Using the current crack dimensions a and c, calculate the stress intensity factor range for the minor crack tip, ΔK_a.

4. Using the Paris crack growth model (Equation (3-19)), calculate da/dN. The number of cycles required to extend the crack by Δa, ΔN_a, is calculated as $\Delta a/(da/dN)$.

5. Similarly, calculate the number of cycles ΔN_c required to extend the major crack tip by Δc. The requirement that ΔN_c has to be the same as ΔN_a in any single step is used to solve for Δc. A new crack aspect ratio is thus obtained for the next step.

6. Repeat the procedure for the next crack growth increment.

The dimensions of the fatigue crack at first detection (see Figure 5-26 and 5-27) were used as the starting point of the numerical integration for the fatigue crack propagation life calculation. By backward integration, the initial thumbnail web crack size was calculated as $a = 1.87$ mm and $c = 2.50$ mm for girder HPS-485W-C1 and $a = 1.00$ mm and $c = 5.94$ mm for girder HPS-690W-C1, determined from the initial value of ΔK_a of 6.2 $MPa\sqrt{m}$, beyond which the calculation of fatigue crack propagation life by LEFM is carried out. The calculated number of load cycles from this initial crack size to the time of crack detection is 1.1×10^6 cycles for girder HPS-485W-C1 and 6.8×10^5 cycles for girder HPS-690W-C1. For both test specimens, forward integration indicated that an additional 2.3×10^5 cycles were required for the crack front to reach the back surface of the web plate and emerge as a through-thickness crack.

166

Two-tip through thickness web crack

Figure 5-32 shows the stress distribution along the web height, on the surface where the crack emerged, and along the path of the fatigue crack for test specimen HPS-485W-C1. It is apparent from Figure 5-32 that the presence of the transverse stiffener increases the stresses in the web. The expressions proposed by Feng (1996) for the stress intensity factor for a two-tip web crack in an I-girder (see Section 3.2.3.6) were used to calculate the crack propagation life of the through-thickness two-tip web crack. When the crack is contained within the high stress region (above the end of the fillet weld), σ_2 is used to calculate stress intensity factor for both crack tips from Equation (3-27a). However, once the lower crack tip grows outside that region, σ_1 is used to calculate the stress intensity factor for the lower crack tip and σ_2 is used for the upper crack tip. Since the stress immediately above the end of the fillet weld is higher than that below it, the upper crack tip is therefore expected to grow faster than the lower crack tip. This was confirmed by the experimental observations summarized in Figure 5-26 and Figure 5-27. The stresses obtained from the finite element analysis of girder HPS-485W-C1 are $\sigma_1 = 108.7$ MPa and $\sigma_2 = 152.5$ MPa, while $\sigma_1 = 115.0$ MPa and $\sigma_2 = 161.3$ MPa were calculated for girder HPS-690W-C1.

The size of the initial through-thickness web crack was calculated from the size of the final thumbnail web crack based on equivalent cross-sectional area of the crack, while the centre of the crack was assumed to remain at the same location. The final thumbnail web crack was very close to being semi-circular. For simplicity, the initial through thickness web crack length, $2 a_w$, is calculated to be around 14.6 mm for both girders from

$$a_{w,i} = \frac{\pi}{4} \times t_w,$$ where t_w is the web thickness.

Since the through-thickness web crack has two independent crack tips, the fatigue crack propagation life calculation was carried out in a step-by-step manner similar to the one used for the thumbnail web crack. The increment of the upper crack tip Δa_U was taken

167

as an independent variable from which the increment in the lower crack tip Δa_L was deduced. The girder geometry parameter β in Equation (3-27e) was calculated to be 2.03 and 1.78 for girders HPS-485W-C1 and HPS-690W-C1, respectively. For any crack with current upper crack tip position of Z_U and lower crack tip position of Z_L, the web crack has a size of $a_w = (Z_U - Z_L)/2$ and eccentricity $e = d_w/2 - (Z_U + Z_L)/2$. The parameters ε and λ_w can be obtained from Equations (3-27c) and (3-27d) and the stress intensity factor range for the upper and the lower crack tips follow from equations (3-27a) and (3-27b). Numerical integration was repeated until the lower crack tip reached the final position indicated in Figure 5-26 and Figure 5-27. The fatigue life spent in propagating the initial through thickness web crack until the application of the first overload was calculated to be 2.2×10^5 cycles and 2.0×10^5 cycles for girders HPS-485W-C1 and HPS-690W-C1, respectively.

5.7.3.3. Comparison with test results

Comparisons between the predicted fatigue life and the fatigue test results for girder HPS-485W-C1 and girder HPS-690W-C1 are shown in Figure 5-33 and Figure 5-34, respectively. The stress ranges plotted in the figures are the measured stress ranges at the transverse stiffener detail level, that is, 97.1 MPa and 104.5 MPa for girders HPS-485W-C1 and HPS-690W-C1, respectively. The mean and lower confidence limit for fatigue Category C' were derived from similar details fabricated from conventional steels (Keating and Fisher 1986). The open circle shows the point of first crack detection and the grey circle corresponds to when the first overload was applied. Both girder test results were found to fall above the fatigue Category C' fatigue curve. Because of the increased crack size tolerance provided by the higher toughness flange steel, the flange crack propagation phase in both girders was found to occupy a larger portion of fatigue life than for similar details made of conventional steels (Wright 2003).

The predicted fatigue life is shown as diamonds in the figures, where the open diamond represents predicted fatigue life at crack detection, and the grey diamond represents the

168

life at the first overload test. For both girders HPS-485W-C1 and HPS-690W-C1, the predicted fatigue life up to crack detection is very close to that observed in the tests. However, there is noticeable difference between the predicted and observed fatigue life at the first overload. The predicted fatigue crack propagation life spent from crack detection to the first overload is only about half of that observed in the tests (44% for girder HPS-485W-C1 and 48% for girder HPS-690W-C1).

5.7.3.4. Sensitivity of end weld position and weld size on predicted fatigue life

Since the stiffener-to-web weld stop position was only estimated from Figure 5-26 and Figure 5-27 and the nominal weld size was used in the previous analysis, it is necessary to check the sensitivity of the fatigue life prediction to these two factors. A sensitivity analysis was therefore carried out on girder HPS-485W-C1. The stiffener-to-web weld stop position of girder HPS-485W-C1 was fore set at 10, 12.5, and 15 mm from the bottom of the stiffener. Also, the size of the stiffener-to-web fillet weld was fore set at 5, 6, and 7 mm. Analysis was performed in the same manner as the base case for girder HPS-485W-C1, which was first analyzed with a stiffener-to-web weld stop position of 12.5 mm and stiffener-to-web weld size of 6 mm. Results of the finite element analysis and fatigue life prediction are presented in Table 5-16, Table 5-17 and Table 5-18. The analysis results are also plotted in Figure 5-35, which illustrates the effect of weld stop position, and Figure 5-36, which shows the effect of weld size. Generally, as the gap between the weld stop and the top surface of bottom flange increases, the predicted fatigue life tends to increase. In contrast, as the stiffener-to-web weld size increases, the fatigue life decreases. However, from Figure 5-35 and Figure 5-36, both effects are seen to be very small over the range of values investigated. Thus, the comparisons between fatigue life predictions and experimental observations made in Section 5.7.3.3 are considered valid.

169

It was observed that the discrepancy between the test results and the predicted fatigue life at first overload could be attributed mainly to the crack propagation stage of the through-thickness crack, which was predicted using stress intensity factors proposed by Feng (1996). Stress intensity factor expressions for two-tip through thickness web cracks at the transverse stiffener detail have therefore been derived specifically for girder HPS-485W-C1 from the finite element analysis described in Section 3.4. The stress intensity factor correction function f was given in Equation (3-28) where coefficients a_0 to a_7 are presented in Table 3-4. The reference stress range is the nominal stress range at mid-thickness of the bottom flange, namely, 108.7 MPa. Using the modified stress intensity factor expressions, the fatigue crack propagation life for the two-tip through-thickness web crack in girder HPS-485W-C1 was recalculated using a similar procedure to the one described above. By the time the lower crack tip reaches 10.3 mm above the top surface of the bottom flange (time of first overload test), the elapsed life was calculated to be 9.2×10^5 cycles.

The updated prediction from the modified stress intensity factor expressions for girder HPS-485W-C1 is shown in Figure 5-33 (grey triangle). The total predicted fatigue life up to the first overload test was found to match the test result very well. The use of the stress intensity factor equation proposed by Feng (1996) seems to be one uncertainty in the fatigue crack propagation predictions. The formula is a generic fitted equation for I-girders of different geometries. Moreover, it was obtained from finite element analysis of I-girders without stiffeners. The presence of the transverse stiffener is believed to restrain the crack opening of the through-thickness web crack, which has the effect of reducing the stress intensity factor.

Despite the excellent correlation between the test results and predicted fatigue life, it must be recognized that limitations exist with the analytical methods. Welding residual stresses were not considered in the analysis. Initial imperfections in the web of the girder

170

and in the weld geometry were not incorporated in the finite element model. The upper crack tip that is located in the weld region would be more affected by the residual stress effects. Furthermore, only the stress intensity factor for mode I (crack opening) was used for the lower crack tip although the effect of mixed mode loading might be significant near the web gap region. Despite the above-mentioned limitations, the analytical methods used in the project seem to be able to predict the fatigue life of the large-scale welded plate girders very well.

5.8. Summary

Stress-based, strain-based, and energy-based methods were used, along with the linear elastic fracture mechanics approach, to predict the fatigue life of six details, namely, a plate with a circular hole, bearing-type bolted shear splices, large scale beam with unfilled holes, welded tensile cruciform detail, welded tensile cover plate detail, and the transverse stiffener location of large scale welded plate girders. The first three details involve riveted and bolted connections and the last three details include welded details. The following summarizes the findings of the analytical investigations.

1. The fatigue life prediction methods investigated in this research were found to predict fatigue test results very well for all the details investigated.

3. The numerical methods implemented in this investigation are useful tools for classifying the severity of different structural details.

4. The numerical methods were found to provide a useful tool to derive fatigue curves for common details made of high performance steel.

5. The fatigue performance of non-welded details made of high performance steel was found to be slightly better than those made of conventional structural steels.

6. The current fatigue design provisions do not provide adequate design curves for riveted and bolted connections. The fatigue life for these details is significantly

171

overestimated by the current design fatigue curves. A review of the fatigue design standard for bearing-type bolted shear splices is required.

7. The fatigue life predictions of welded details were found to be relatively insensitive to the material cyclic and fatigue properties.

8. Both the strain-based approach and the energy-based approach can predict fatigue crack initiation life accurately.

9. The stress-based method, used in conjunction with an inelastic stress analysis, provides an accurate prediction of crack initiation life.

10. It is necessary to account for the mean stress effect in fatigue crack initiation calculations of non-welded details when a tensile mean stress is present.

11. The stress intensity factor expression taking the existence of stiffeners into account provides a better characterization of the stress field near a two-tip through thickness web crack in plate girders with transverse stiffeners.

12. Small variations in the position of the weld stop and weld size of a plate girder stiffener-to-web weld do not affect the fatigue life of the detail significantly.

172

Table 5-1 Cyclic Stress versus Strain Curves Definition

ASTM A36		ASTM A7		HPS(LT)		HPS(HT)	
$E = 200000$ MPa		$E = 201400$ MPa		$E = 197100$ MPa		$E = 197000$ MPa	
$\upsilon = 0.3$		$\upsilon = 0.3$		$\upsilon = 0.3$		$\upsilon = 0.3$	
Stress	Plastic Strain	Stress	Plastic Strain	Stress	Plastic Strain	Stress	Plastic Strain
200	0	100	0	350	0	325	0
225	0.000377472	125	0.00013508	375	0.000253107	350	0.00021067
250	0.000601661	150	0.000281753	400	0.00044807	375	0.000522223
275	0.000917287	175	0.000524585	425	0.000766206	400	0.001220829
300	0.001348067	200	0.000898782	450	0.001270642	425	0.002710742
325	0.001920994	225	0.001445155	475	0.002050315	450	0.005750615
350	0.002666467	250	0.002210144	500	0.003228173	475	0.011713213
375	0.003618402	275	0.003245835	525	0.004971331	500	0.023003108
400	0.004814351	300	0.004609987	550	0.007503497	525	0.043711236
425	0.006295605	325	0.006366042	575	0.011120025		
450	0.008107302	350	0.008583145	600	0.016205996		
475	0.010298525	375	0.011336158	625	0.023257738		
500	0.012922398			650	0.032908266		
525	0.016036186						
540	0.018165019						

Table 5-2 FEA and Fatigue Life Prediction Results for Plates Tested by Schitoglu (1983)

Nominal Stress Amplitude (MPa)	Test Fatigue Life (Cycle)	Inelastic FEA Result		Predicted Crack Initiation Life (Cycle)			Predicted Crack Propagation Life (Cycle)		Predicted Total* Fatigue Life (Cycle)
		σ_{max} (MPa)	ε_{max} (%)	Stress-based Method		Strain-based Method	General	Empirical	
				Inelastic	Elastic				
118	1.2×10^6	233.2	0.161	7.7×10^5	3.3×10^5	5.9×10^5	1.4×10^4	1.4×10^4	6.1×10^5
126	5.9×10^5	243.9	0.176	5.1×10^5	1.8×10^5	3.9×10^5	1.2×10^4	1.2×10^4	4.0×10^5
136	4.2×10^5	255.2	0.193	3.4×10^5	9.3×10^4	2.5×10^5	1.0×10^4	9.9×10^3	2.6×10^5
144	2.3×10^5	265.0	0.210	2.4×10^5	5.2×10^4	1.8×10^5	8.6×10^3	8.5×10^3	1.9×10^5
163	1.3×10^5	284.2	0.248	1.3×10^5	1.8×10^4	9.1×10^4	6.3×10^3	6.4×10^3	9.7×10^4
180	5.2×10^4	302.3	0.289	7.3×10^4	6.9×10^3	5.2×10^4	4.9×10^3	5.0×10^3	5.7×10^4
225	1.3×10^4	357.5	0.471	1.6×10^4	9.2×10^2	1.1×10^4	2.7×10^3	2.5×10^3	1.3×10^4
271	2.8×10^3	414.3	0.768	4.2×10^3	1.7×10^2	2.7×10^3	1.4×10^3	1.2×10^3	4.0×10^3
271	3.6×10^3								

* Summation of value presented in seventh column and eighth column.

173

Table 5-3 Fatigue Life Prediction for Plates Tested by Sehitoglu (1983)

(Using A7 Steel Properties)

| Nominal Stress Amplitude (MPa) | Inelastic FEA Result | | Predicted Crack Initiation Life (Cycle) | | | | Predicted Crack Propagation Life (Cycle) | Predicted Total* Fatigue Life (Cycle) |
| | σ_{max} (MPa) | ε_{max} (%) | Strain-based Method | Energy-based Method | | | | |
				ΔW^p	ΔW	ΔW^e		
118	207.3	0.208	4.7×10^4	4.5×10^4	4.6×10^4	4.5×10^4	1.7×10^4	6.4×10^4
126	219.4	0.240	3.0×10^4	2.9×10^4	2.9×10^4	2.9×10^4	1.4×10^4	4.4×10^4
136	231.0	0.276	1.9×10^4	1.9×10^4	1.9×10^4	1.9×10^4	1.2×10^4	3.1×10^4
144	241.1	0.312	1.4×10^4	1.3×10^4	1.4×10^4	1.3×10^4	9.7×10^3	2.3×10^4
163	261.2	0.395	7.0×10^3	7.1×10^3	7.2×10^3	7.1×10^3	7.2×10^3	1.4×10^4
180	281.9	0.499	3.8×10^3	3.9×10^3	3.8×10^3	3.9×10^3	5.4×10^3	9.2×10^3
225	332.6	0.863	9.5×10^2	1.0×10^3	9.5×10^2	1.0×10^3	2.9×10^3	3.8×10^3
271	375.5	1.454	2.8×10^2	3.3×10^2	2.8×10^2	3.2×10^2	1.7×10^3	1.9×10^3

* Summation of value presented in fourth column and eighth column.

Table 5-4 Fatigue Life Prediction for Plates with a Circular Hole Detail made with

HPS 485W Steel

| Nominal Stress Amplitude (MPa) | Inelastic FEA Result | | Predicted Crack Initiation Life (Cycle) | Predicted Crack Propagation Life (Cycle) | Predicted Total Fatigue Life (Cycle) |
	σ_{max} (MPa)	ε_{max} (%)			
118	288.8	0.146	7.4×10^6	1.5×10^5	7.5×10^6
126	309.0	0.156	3.0×10^6	1.2×10^5	3.2×10^6
136	332.1	0.168	1.2×10^6	9.5×10^4	1.3×10^6
144	351.8	0.179	6.1×10^5	7.7×10^4	6.8×10^5
163	370.0	0.207	1.6×10^5	5.3×10^4	2.1×10^5
180	391.2	0.235	6.2×10^4	3.9×10^4	1.0×10^5
225	435.5	0.317	1.5×10^4	2.1×10^4	3.5×10^4
271	468.0	0.417	5.7×10^3	1.3×10^4	1.8×10^4

174

Table 5-5 Example of Numerical Integration

C	6.90x10⁻⁹	(for K in $MPa\sqrt{m}$ and da in mm)
m	3	
W	21.2 mm	(the distance from hole edge to plate edge)
σ	118 MPa	

Increment No.	a (mm)	da (mm)	average a (mm)	β_E	β_S	β_W	β_G	ΔK $MPa\sqrt{m}$	da/dN mm/cycle	dN cycle	N cycle
1	1.00	0.01	1.01	1.00	1.12	1.01	2.10	26.53	1.29×10^{-4}	78	7.8×10^{1}
2	1.01	0.01	1.02	1.00	1.12	1.01	2.09	26.64	1.30×10^{-4}	77	1.6×10^{2}
3	1.02	0.01	1.03	1.00	1.12	1.01	2.09	26.74	1.32×10^{-4}	77	2.3×10^{2}
4	1.03	0.01	1.04	1.00	1.12	1.01	2.09	26.85	1.34×10^{-4}	77	3.1×10^{2}
5	1.04	0.01	1.05	1.00	1.12	1.01	2.09	26.95	1.35×10^{-4}	77	3.9×10^{2}
6	1.05	0.01	1.06	1.00	1.12	1.01	2.08	27.06	1.37×10^{-4}	77	4.6×10^{2}
7	1.06	0.01	1.07	1.00	1.12	1.01	2.08	27.16	1.38×10^{-4}	77	5.4×10^{2}
8	1.07	0.01	1.08	1.00	1.12	1.01	2.08	27.27	1.40×10^{-4}	77	6.2×10^{2}
9	1.08	0.01	1.09	1.00	1.12	1.01	2.08	27.37	1.42×10^{-4}	77	6.9×10^{2}
10	1.09	0.01	1.10	1.00	1.12	1.01	2.07	27.48	1.43×10^{-4}	76	7.7×10^{2}
11	1.10	0.01	1.11	1.00	1.12	1.01	2.07	27.59	1.45×10^{-4}	76	8.5×10^{2}
12	1.12	0.01	1.12	1.00	1.12	1.01	2.07	27.69	1.47×10^{-4}	76	9.2×10^{2}
13	1.13	0.01	1.13	1.00	1.12	1.01	2.07	27.80	1.48×10^{-4}	76	1.0×10^{3}
14	1.14	0.01	1.14	1.00	1.12	1.01	2.06	27.90	1.50×10^{-4}	76	1.1×10^{3}
15	1.15	0.01	1.16	1.00	1.12	1.01	2.06	28.01	1.52×10^{-4}	76	1.1×10^{3}
16	1.16	0.01	1.17	1.00	1.12	1.01	2.06	28.12	1.53×10^{-4}	76	1.2×10^{3}
17	1.17	0.01	1.18	1.00	1.12	1.01	2.06	28.23	1.55×10^{-4}	76	1.3×10^{3}
18	1.18	0.01	1.19	1.00	1.12	1.01	2.05	28.33	1.57×10^{-4}	75	1.4×10^{3}
19	1.20	0.01	1.20	1.00	1.12	1.01	2.05	28.44	1.59×10^{-4}	75	1.5×10^{3}
20	1.21	0.01	1.21	1.00	1.12	1.01	2.05	28.55	1.61×10^{-4}	75	1.5×10^{3}
21	1.22	0.01	1.23	1.00	1.12	1.01	2.04	28.66	1.62×10^{-4}	75	1.6×10^{3}
22	1.23	0.01	1.24	1.00	1.12	1.01	2.04	28.76	1.64×10^{-4}	75	1.7×10^{3}
23	1.24	0.01	1.25	1.00	1.12	1.01	2.04	28.87	1.66×10^{-4}	75	1.8×10^{3}
24	1.26	0.01	1.26	1.00	1.12	1.01	2.04	28.98	1.68×10^{-4}	75	1.8×10^{3}
25	1.27	0.01	1.28	1.00	1.12	1.01	2.03	29.09	1.70×10^{-4}	75	1.9×10^{3}
"	"	"	"	"	"	"	"	"	"	"	"
"	"	"	"	"	"	"	"	"	"	"	"
217	8.58	0.09	8.62	1.00	1.12	1.86	1.28	87.55	4.63×10^{-3}	19	1.4×10^{4}
218	8.66	0.09	8.71	1.00	1.12	1.90	1.27	89.76	4.99×10^{-3}	17	1.4×10^{4}
219	8.75	0.09	8.79	1.00	1.12	1.95	1.27	92.14	5.40×10^{-3}	16	1.4×10^{4}
220	8.84	0.09	8.88	1.00	1.12	1.99	1.27	94.72	5.86×10^{-3}	15	1.4×10^{4}
221	8.93	0.09	8.97	1.00	1.12	2.05	1.27	97.54	6.40×10^{-3}	14	1.4×10^{4}
222	9.02	0.09	9.06	1.00	1.12	2.10	1.27	100.62	7.03×10^{-3}	13	1.4×10^{4}

175

Table 5-6 Geometry and Test Results for Bearing-Type Shear Splices (Josi et al. 1999)

Test Series	Hole Staggers (mm)	Gauge Width g (mm)	Load Range (kN)	Gross Section Stress Range (MPa)	Corrected Stress Range $\Delta\sigma_{sc}$ (MPa)	Tested Fatigue Life for Replicate Specimen 1 (Cycles)	2 (Cycles)	3 (Cycles)
P	0	60.3	240	113	109	5.7×10^5	—	—
S0	0	60.3	190	90	90	7.7×10^5	2.2×10^6	5.8×10^6
	0	60.3	240	113	113	3.6×10^5	5.8×10^5	6.2×10^5
S1	25.4	44.5	160	88	92	2.8×10^6	2.9×10^6	8.5×10^6
	25.4	44.5	200	110	115	2.6×10^5	3.0×10^5	1.6×10^6
S2	50.8	44.5	160	88	93	1.5×10^6	2.7×10^6	3.8×10^6
	50.8	44.5	200	110	116	1.1×10^6 [a]	3.1×10^5	6.5×10^5
S3	76.2	44.5	130	72	76	3.6×10^6	1.6×10^7 [*]	1.4×10^7 [b]
	76.2	44.5	200	110	116	5.2×10^5	6.9×10^5	7.0×10^5
G	25.4	60.3	190	90	93	1.0×10^6	1.9×10^6	2.9×10^6
	25.4	60.3	240	113	117	3.0×10^5	3.2×10^5	5.2×10^5

[a] Specimen failed at gross section.
[*] Run-out.
[b] Specimen failed in main plate.

Table 5-7 Inelastic FEA Results for Bearing-Type Shear Splices (Josi et al. 1999)

Test Series	Load Range (kN)	$\Delta\sigma/2$ (MPa)	$\Delta\varepsilon/2$ (%)	σ_{max} (MPa)	ε_{max} (%)	A_0	A_1	A_2	A_3	A_4
P	240	209.6	0.113	390.1	0.594	3.804164	-0.812403	0.107859	-0.006770	0.000150
S0	190	184.6	0.091	336.8	0.376	4.120566	-1.011651	0.151234	-0.010558	0.000260
	240	213.4	0.120	395.9	0.623	3.881882	-0.767843	0.089474	-0.004927	0.000091
S1	160	188.0	0.093	346.5	0.409	4.261944	-1.043203	0.157147	-0.011004	0.000272
	200	214.1	0.121	411.2	0.702	3.999602	-0.777182	0.089899	-0.004880	0.000089
S2	160	191.3	0.095	345.2	0.405	4.343139	-1.063410	0.160145	-0.011208	0.000277
	200	215.4	0.124	405.8	0.673	4.032576	-0.750001	0.081091	-0.004017	0.000062
S3	130	155.0	0.077	305.7	0.287	4.337112	-1.059791	0.159941	-0.011201	0.000277
	200	215.1	0.123	402.6	0.658	4.031630	-0.750886	0.081961	-0.004105	0.000065
G	190	189.6	0.094	342.5	0.395	4.226584	-1.037658	0.155255	-0.010836	0.000267
	240	215.5	0.124	405.1	0.669	3.921798	-0.729971	0.077632	-0.003776	0.000056

176

Table 5-8 Predicted Fatigue Life for Bearing-Type Shear Splices
Tested by Josi *et al.* (1999)

Test Series	Load Range (kN)	Predicted Crack Initiation Life (Cycles)				Predicted Crack Propagation Life (Cycles)	Predicted Total Fatigue Life* (Cycles)
		Stress-based Method		Strain-based Method			
		no σ_m	σ_m	no σ_m	SWT		
P	240	2.0×10^6	4.1×10^5	4.2×10^6	4.0×10^5	9.9×10^3	4.0×10^5
S0	190	6.5×10^6	1.7×10^6	1.7×10^7	1.2×10^6	2.4×10^4	1.3×10^6
	240	1.7×10^6	3.4×10^5	2.9×10^6	3.1×10^5	8.2×10^3	3.2×10^5
S1	160	5.5×10^6	1.4×10^6	1.5×10^7	1.1×10^6	2.2×10^4	1.1×10^6
	200	1.7×10^6	2.9×10^5	2.7×10^6	2.7×10^5	7.9×10^3	2.8×10^5
S2	160	4.7×10^6	1.2×10^6	1.3×10^7	1.0×10^6	2.0×10^4	1.0×10^6
	200	1.6×10^6	2.9×10^5	2.4×10^6	2.6×10^5	7.2×10^3	2.7×10^5
S3	130	3.2×10^7	8.5×10^6	5.9×10^7	3.2×10^6	4.4×10^4	3.3×10^6
	200	1.6×10^6	3.0×10^5	2.5×10^6	2.7×10^5	7.2×10^3	2.8×10^5
G	190	5.1×10^6	1.3×10^6	1.4×10^7	1.1×10^6	2.1×10^4	1.1×10^6
	240	1.6×10^6	2.9×10^5	2.4×10^6	2.7×10^5	7.2×10^3	2.7×10^5

* The initiation life is from the strain-based method with the SWT mean stress effect correction.

Table 5-9 Inelastic FEA and Fatigue Life Prediction Results for Bearing-Type Shear Splices Using HPS(LT) Steel Properties

Test Series	Load Range (kN)	$\Delta\sigma/2$ (MPa)	$\Delta\varepsilon/2$ (%)	σ_{max} (MPa)	ε_{max} (%)	Predicted Crack Initiation Life (Cycles)	Predicted Crack Propagation Life (Cycles)	Predicted Total Fatigue Life (Cycles)
P	240	222.7	0.112	467.2	0.390	1.6×10^6	2.1×10^4	1.6×10^6
S0	190	184.5	0.093	433.0	0.295	9.7×10^6	4.1×10^4	9.7×10^6
	240	233.1	0.117	475.1	0.416	1.1×10^6	1.9×10^4	1.1×10^6
S1	160	188.2	0.095	436.5	0.302	8.0×10^6	3.9×10^4	8.0×10^6
	200	235.2	0.118	477.3	0.423	9.7×10^5	1.8×10^4	9.9×10^5
S2	160	191.4	0.096	439.2	0.310	6.8×10^6	3.7×10^4	6.8×10^6
	200	239.2	0.120	479.6	0.432	8.4×10^5	1.7×10^4	8.6×10^5
S3	130	155.0	0.078	395.2	0.234	6.4×10^7	7.2×10^4	6.4×10^7
	200	238.5	0.120	479.0	0.431	8.7×10^5	1.7×10^4	8.9×10^5
G	190	189.8	0.095	437.5	0.305	7.4×10^6	3.8×10^4	7.5×10^6
	240	239.7	0.121	479.7	0.432	8.3×10^5	1.7×10^4	8.5×10^5

177

Table 5-10 Fatigue Life Prediction for Non-Load-Carrying Cruciform Specimens

Stress Range (MPa)	Tested Fatigue Life (Cycles) for Replicate Specimen					Predicted Fatigue Life (Cycles)		
	1	2	3	4	5	Initiation	Propagation	Total
90	1.0×10^7 *	1.0×10^7 *	5.3×10^6	2.8×10^6	1.0×10^7 *	1.0×10^7 *	—	1.0×10^7 *
138	6.3×10^5	9.9×10^5	1.5×10^6	1.4×10^6	5.7×10^5	2.4×10^6	7.5×10^5	3.1×10^6
207	2.6×10^5	3.2×10^5	3.0×10^5	3.1×10^5	2.0×10^5	1.3×10^5	1.9×10^5	3.3×10^5
290	1.3×10^5	1.1×10^5	1.4×10^5	8.5×10^4	1.1×10^5	5.6×10^4	6.1×10^4	1.2×10^5

* Run-out.

Table 5-11 Inelastic FEA Results in the Critical Region of Non-Load-Carrying Cruciform

Stress Range (MPa)	Response	Principal Stress (MPa) σ_1 σ_2 σ_3	Von Mises Equivalent Stress (MPa)	Principal Strain (%) ε_1 ε_2 ε_3	Principal Plastic Strain (%) ε_1^p ε_2^p ε_3^p	Equivalent Plastic Strain (%)	Elastic Strain Energy (MJ/m³)	Plastic Strain Energy (MJ/m³)
90	Amplitude	13.9	83.5	-0.015	0.000	0.000	0.02	0.00
		36.1		0.000	0.000			
		106.3		0.046	0.000			
	Maximum	28.9	173.4	-0.030	0.000	0.000	0.10	0.00
		74.9		0.000	0.000			
		220.7		0.096	0.000			
138	Amplitude	21.4	128.5	-0.022	0.000	0.000	0.06	0.00
		55.5		0.000	0.000			
		163.5		0.071	0.000			
	Maximum	43.9	263.4	-0.046	0.000	0.000	0.23	0.00
		113.7		0.000	0.000			
		335.1		0.146	0.000			
207	Amplitude	32.1	192.7	-0.034	0.000	0.000	0.13	0.00
		83.2		0.000	0.000			
		245.2		0.107	0.000			
	Maximum	76.0	371.4	-0.078	-0.015	0.022	0.49	0.08
		181.1		0.000	-0.006			
		488.6		0.230	0.021			
290	Amplitude	45.0	269.8	-0.047	0.000	0.000	0.25	0.00
		116.5		0.000	0.000			
		343.3		0.150	0.000			
	Maximum	98.4	446.2	-0.169	-0.087	0.119	0.75	0.48
		264.6		0.000	-0.027			
		603.9		0.365	0.114			

178

Table 5-12 Stress Distribution Coefficients for Crack in Welded Cruciform

Stress Range (MPa)	A_0	A_1	A_2	A_3	A_4
90	1.910516	-1.681338	1.003032	-0.250550	0.021953
138	1.910303	-1.680983	1.002830	-0.250502	0.021949
207	1.910686	-1.681500	1.003100	-0.250564	0.021954
290	1.910534	-1.681529	1.003252	-0.250623	0.021961

Table 5-13 Fatigue Life Prediction Results for Welded Cover Plate Specimens

Stress Range (MPa)	Test Fatigue Life (Cycles) for Replicate Specimen					Predicted Fatigue Life (Cycles)		
	1	2	3	4	5	Initiation	Propagation	Total
103	3.5×10^6	2.1×10^6	1.0×10^7 *	2.0×10^6	2.2×10^6	1.0×10^7 *	—	1.0×10^7 *
145	1.2×10^6	7.1×10^5	1.1×10^6	1.5×10^6	9.7×10^5	6.1×10^5	4.2×10^5	1.0×10^6
207	4.1×10^5	2.9×10^5	2.6×10^5	2.9×10^5	2.6×10^5	1.2×10^5	1.3×10^5	2.5×10^5
290	8.6×10^4	1.0×10^5	7.9×10^4	1.2×10^5	1.1×10^5	5.6×10^4	4.1×10^4	9.7×10^4

* Run-out.

179

Table 5-14 Inelastic FEA Results in the Critical Element for the Cover Plate Specimens Tested by Friedland *et al.* (1982)

Stress Range (MPa)	Response	Principal Stress (MPa) σ_1 σ_2 σ_3	Von Mises Equivalent Stress (MPa)	Principal Strain (%) ε_1 ε_2 ε_3	Principal Plastic Strain (%) ε_1^p ε_2^p ε_3^p	Equivalent Plastic Strain (%)	Elastic Strain Energy (MJ/m³)	Plastic Strain Energy (MJ/m³)
103	Amplitude	14.2	107.1	-0.018	0.000	0.000	0.04	0.00
		35.0		-0.004	0.000			
		130.1		0.059	0.000			
	Maximum	29.3	221.3	-0.037	0.000	0.000	0.15	0.00
		72.4		-0.009	0.000			
		269.0		0.121	0.000			
145	Amplitude	19.8	149.9	-0.025	0.000	0.000	0.07	0.00
		49.0		-0.006	0.000			
		182.2		0.082	0.000			
	Maximum	40.6	307.0	-0.051	0.000	0.000	0.30	0.00
		100.4		-0.012	0.000			
		373.1		0.168	0.000			
207	Amplitude	28.3	214.2	-0.036	0.000	0.000	0.14	0.00
		70.0		-0.008	0.000			
		260.3		0.117	0.000			
	Maximum	65.1	392.4	-0.092	-0.026	0.039	0.51	0.14
		158.7		-0.017	-0.012			
		495.9		0.256	0.038			
290	Amplitude	39.6	299.9	-0.050	0.000	0.000	0.28	0.00
		98.0		-0.012	0.000			
		364.4		0.164	0.000			
	Maximum	89.7	456.4	-0.184	-0.102	0.147	0.75	0.61
		238.0		-0.025	-0.041			
		601.9		0.398	0.143			

Table 5-15 Stress Distribution along Potential Crack Path in Welded Cover Plate

Stress Range (MPa)	A_0	A_1	A_2	A_3	A_4
90	1.997836	-1.273516	0.604012	-0.143859	0.012493
138	1.998535	-1.276628	0.606858	-0.144743	0.012580
207	1.998616	-1.276306	0.606377	-0.144569	0.012562
290	1.998284	-1.274500	0.604819	-0.144096	0.012515

180

Table 5-16 Critical Element Responses from Inelastic FEA for HPS Plate Girders

Girder	Weld Stop Location* (mm)	Weld Size (mm)	Response	Principal Stress (MPa) σ_1 σ_2 σ_3	Von Mises Equivalent Stress (MPa)	Principal Strain (%) ε_1 ε_2 ε_3	Equivalent Plastic Strain (%)	Elastic Strain Energy (MJ/m³)	Plastic Strain Energy (MJ/m³)
HPS-485W-C1	10	6	Amplitude	5.0	79.7	-0.012	0.000	0.02	0.00
				8.6		-0.010			
				86.5		0.042			
			Maximum	20.3	325.3	-0.049	0.000	0.29	0.00
				35.1		-0.039			
				352.8		0.171			
	12.5	5	Amplitude	4.6	76.8	-0.012	0.000	0.02	0.00
				8.4		-0.009			
				83.2		0.040			
			Maximum	18.8	313.4	-0.047	0.000	0.27	0.00
				34.1		-0.037			
				339.6		0.164			
	12.5	6	Amplitude	4.9	78.6	-0.012	0.000	0.02	0.00
				9.1		-0.009			
				85.5		0.041			
			Maximum	20.0	320.7	-0.049	0.000	0.28	0.00
				37.2		-0.037			
				349.0		0.168			
	12.5	7	Amplitude	5.2	80.3	-0.012	0.000	0.02	0.00
				9.8		-0.009			
				87.8		0.042			
			Maximum	21.2	327.8	-0.050	0.000	0.30	0.00
				40.1		-0.037			
				358.1		0.172			
	15	6	Amplitude	4.8	77.5	-0.012	0.000	0.02	0.00
				9.5		-0.009			
				84.5		0.041			
			Maximum	19.7	316.0	-0.048	0.000	0.27	0.00
				38.8		-0.036			
				344.8		0.166			
HPS-690W-C1	11	6	Amplitude	5.3	84.5	-0.013	0.000	0.02	0.00
				10.6		-0.009			
				92.3		0.044			
			Maximum	26.0	365.8	-0.066	0.016	0.37	0.05
				56.1		-0.044			
				406.0		0.209			

* The distance is measured from the bottom of the stiffener.

181

Table 5-17 Web Stress Distribution in HPS Plate Girders

Girder	Weld Stop Location* (mm)	Weld Size (mm)	Stress Field in Through-Thickness Direction (for Thumbnail Web Crack)					along Web Height (for 2-tip Web Crack)	
			A_0	A_1	A_2	A_3	A_4	$\sigma_1{}^a$ (MPa)	$\sigma_2{}^a$ (MPa)
HPS-	10	6	1.011125	-0.371085	0.158945	-0.031776	0.002405	108.7	153.6
485W-	12.5	5	1.012365	-0.380922	0.164328	-0.032731	0.002457	108.7	152.2
C1	12.5	6	1.011142	-0.369723	0.157121	-0.031241	0.002356	108.7	152.5
	12.5	7	1.009774	-0.366003	0.156141	-0.031474	0.002411	108.7	153.2
	15	6	1.011091	-0.368436	0.155873	-0.030915	0.002328	108.7	151.5
HPS- 690W- C1	11	6	1.011180	-0.370188	0.158535	-0.031788	0.002420	115.0	161.3

* The distance is measured from the bottom of the stiffener.

a Refer to Figure 5-32 for a definition of σ_1 and σ_2.

Table 5-18 HPS Plate Girders Fatigue Life Prediction Results

Girder	Weld Stop* Location (mm)	Weld Size (mm)	Predicted Crack Initiation Life (Cycles)	Predicted Crack Propagation Life (Cycles)			Predicted Total Fatigue Life (Cycles)	
				Thumbnail Crack		Through Thickness Crack		up to OL1
				up to Detection	after Detection	Feng's SIF (Modified SIF)	up to Detection	Feng's SIF (Modified SIF)
HPS-	10	6	6.8×10^5	1.1×10^6	2.2×10^5	2.1×10^5	1.8×10^6	2.2×10^6
485W-	12.5	5	9.7×10^5	1.1×10^6	2.3×10^5	2.2×10^5	2.0×10^6	2.5×10^6
C1	12.5	6	7.6×10^5	1.1×10^6	2.3×10^5	2.2×10^5	1.8×10^6	2.3×10^6
						(9.2×10^5)		(3.0×10^6)
	12.5	7	6.2×10^5	1.1×10^6	2.3×10^5	2.1×10^5	1.7×10^6	2.2×10^6
	15	6	8.6×10^5	1.1×10^6	2.4×10^5	2.2×10^5	1.9×10^6	2.4×10^6
HPS- 690W- C1	11	6	2.7×10^5	6.8×10^5	2.3×10^5	2.0×10^5	9.5×10^5	1.4×10^6

* The distance is measured from the bottom of the stiffener.

182

Figure 5-1 Test specimens from Sehitoglu (1983)

(a) full mesh

(b) mesh around the centre hole
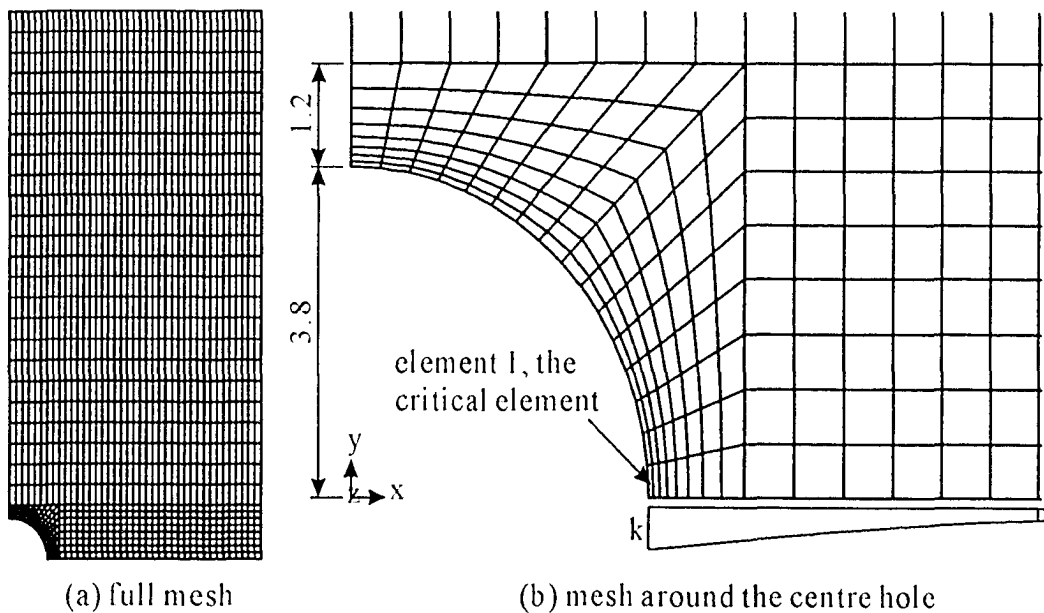
Figure 5-2 Typical Mesh for Plate with a Circular Hole

183

The first figure shows a stress-strain curve with equations:

$$\Delta\varepsilon / 2 = \frac{\Delta\sigma / 2}{200000} + \left(\frac{\Delta\sigma / 2}{1336}\right)^{1.0226}$$

$$\Delta\varepsilon / 2 = \frac{}{200000} + \left(\frac{}{1336}\right)^{1.0226}$$

stress vs. strain curve
used in ABAQUS

ABAQUS input
*MATERIAL, NAME=A36
*ELASTIC
00000,.3
*PLASTIC
*MATE 00.0
*ELAS 25.0.000377472
200000 50.0.000601661
*PLAS 75.0.000917287
200.0 00.0.001348067
225.0.0 25.0.001920994
250.0.0 50.0.002666467
275.0.0 75.0.003618402
300.0.0 00.0.004814351
325.0.0 25.0.006295605
350.0.0 50.0.008107302
375.0.0 75.0.010298525
400.0.0 00.0.012922398
425.0.0 25.0.016036186
450.0.0 40.0.018165019
475.0.0
500.0.0
525.0.0
540.0.0

Figure 5-3 Elastic Isotropic Hardening Material Model in ABAQUS (A36)

Nominal Stress Amplitude (MPa)	A_0	A_1	A_2	A_3	A_4
118	2.007727	-0.398004	0.051108	-0.002753	0.000053
126	1.952015	-0.364752	0.045640	-0.002414	0.000045
136	1.893370	-0.332026	0.040450	-0.002100	0.000039
144	1.842829	-0.303387	0.035926	-0.001827	0.000033
163	1.750687	-0.251168	0.027789	-0.001342	0.000024
180	1.671735	-0.211272	0.022213	-0.001037	0.000018
225	1.604682	-0.208304	0.023990	-0.001200	0.000021
271	1.546548	-0.155382	0.014876	-0.000651	0.000010

$$k = 1.546548 - 0.155382x + 0.014876x^2 - 0.000651x^3 + 0.000010x^4$$

Figure 5-4 Normalized Stress Distribution for the Use of Stress Gradient Correction

Factor, β_G, Calculation

184
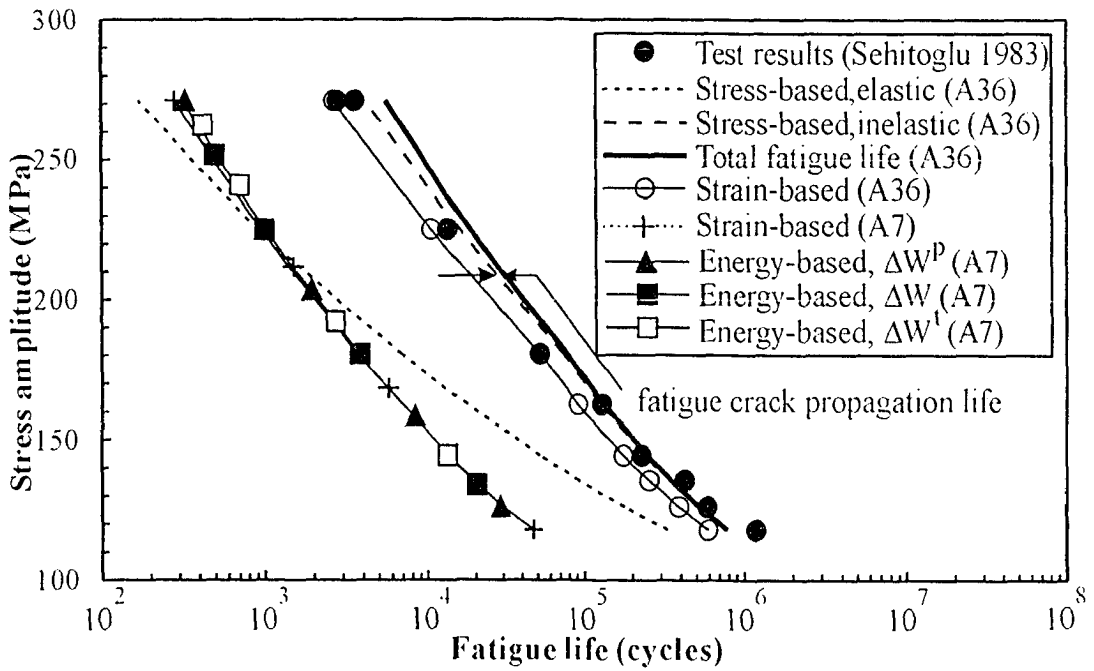
Figure 5-5 Comparison of Predicted Fatigue Life with Test Results for Plates with a Circular Hole (Sehitoglu 1983)
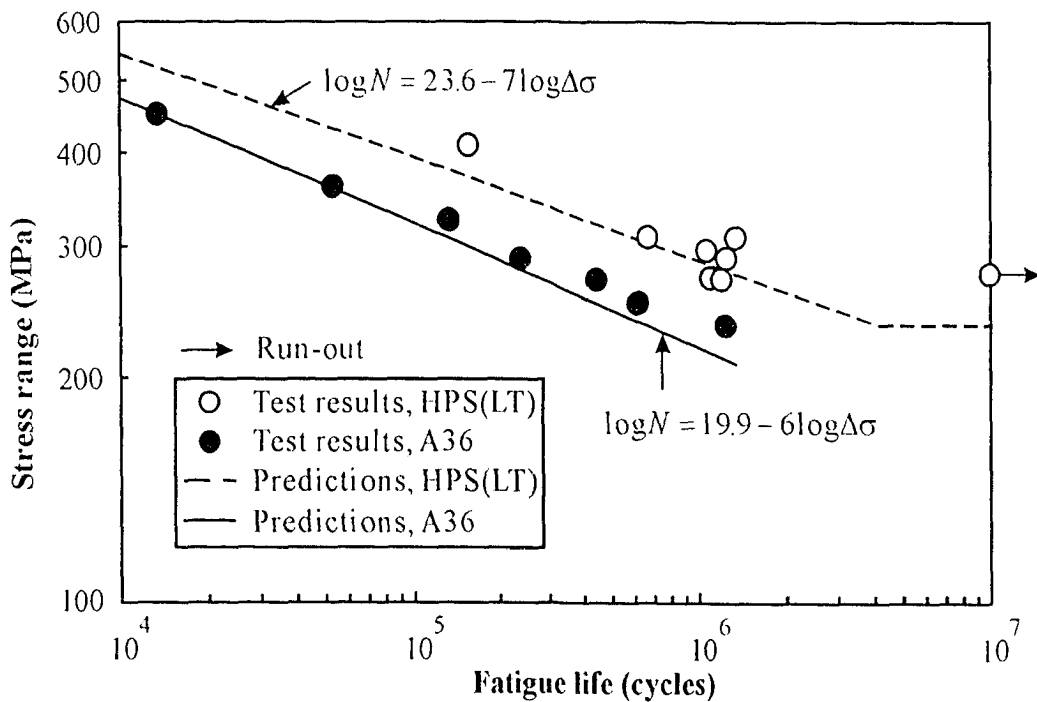
Figure 5-6 Fatigue Test Results and Predictions of Plate with a Circular Hole Detail Made with A36 and HPS(LT) Steels

185
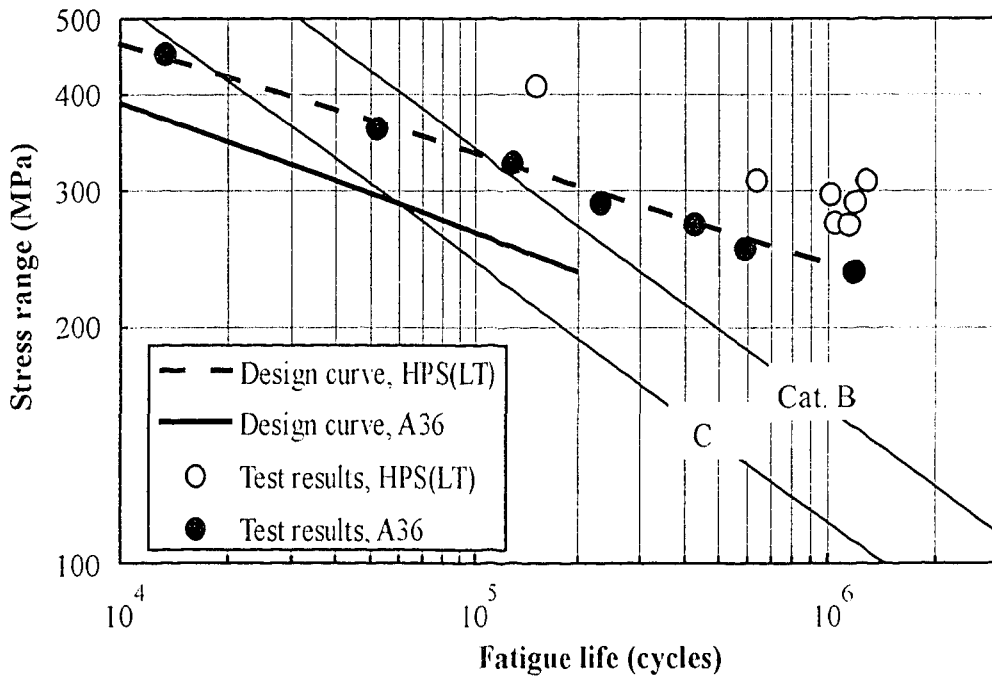
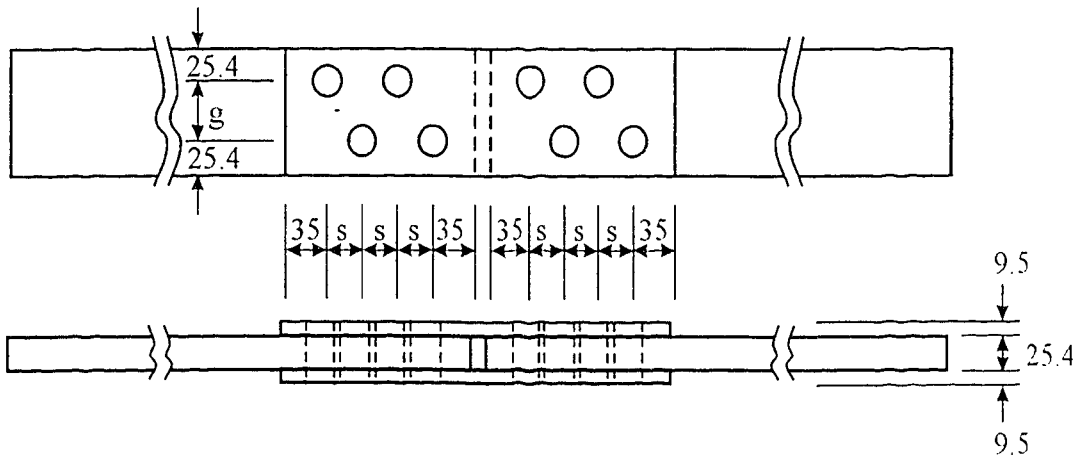Figure 5-7 *S-N* Curves for Plate with a Circular Hole Detail

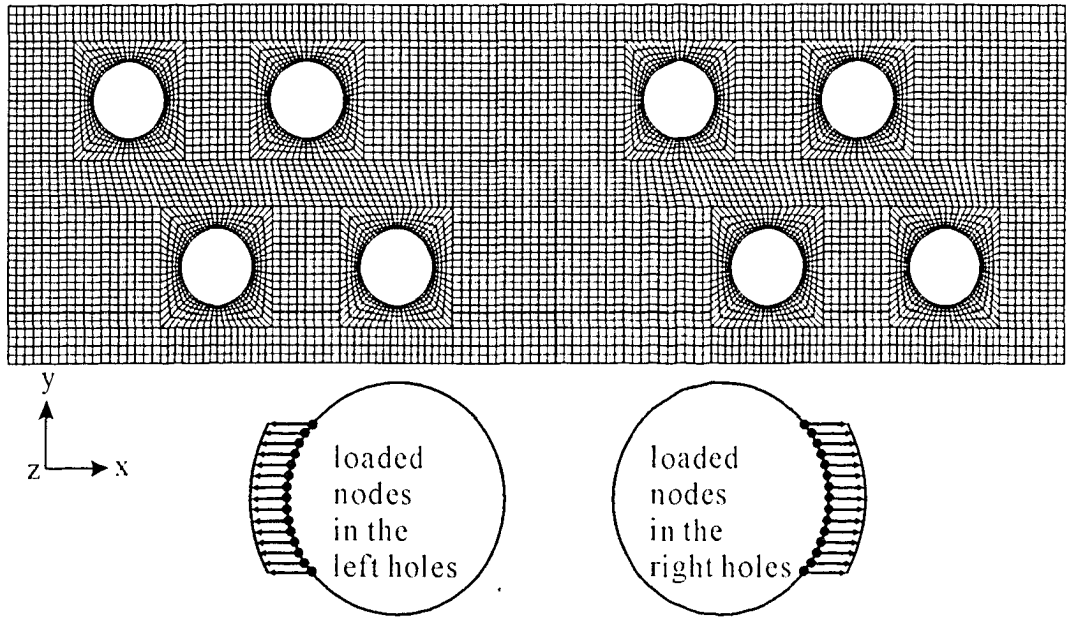Figure 5-8 Typical Bearing-Type Shear Splice Tested by Josi *et al.* (1999)

186

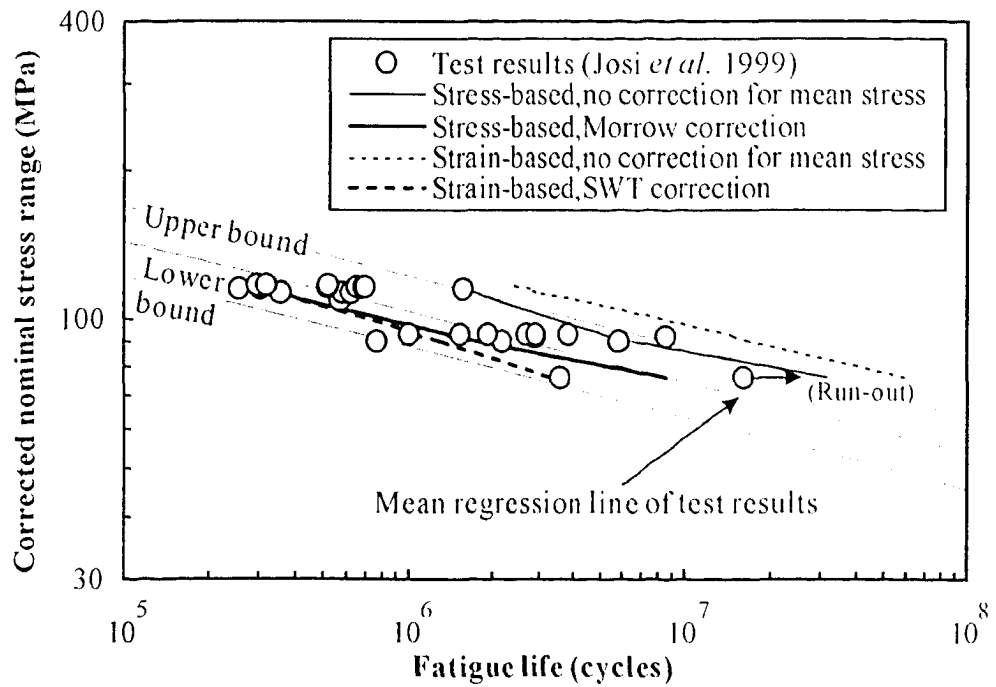Figure 5-9 Typical Mesh Refinement for Bearing-Type Shear Splice

Figure 5-10 Comparison of Predicted Fatigue Life with Test Results for Bearing-Type
Shear Splices

187
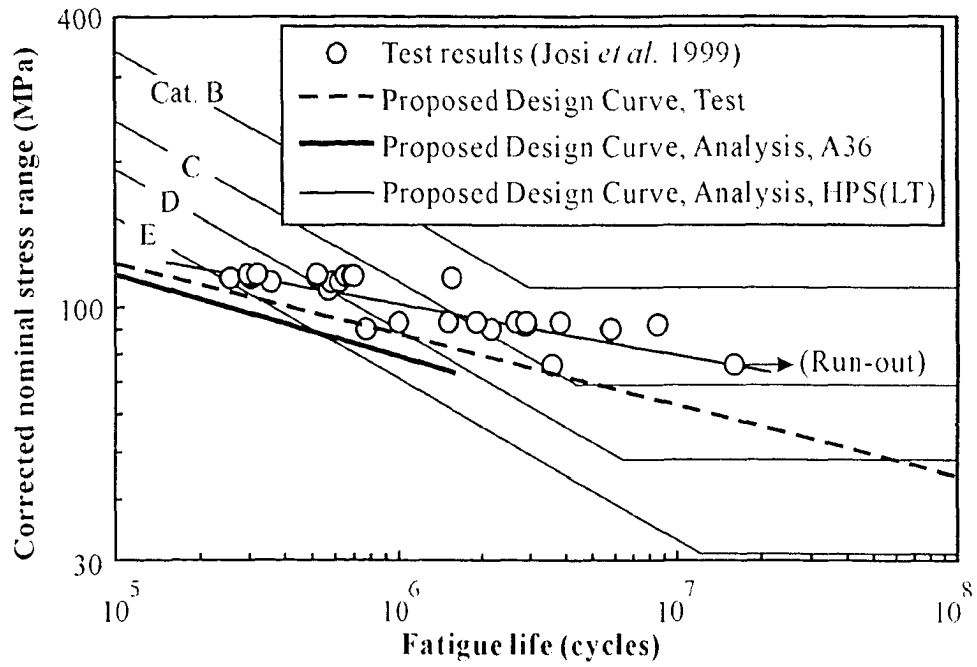
Figure 5-11 Design Curve for Bolted Shear Splices
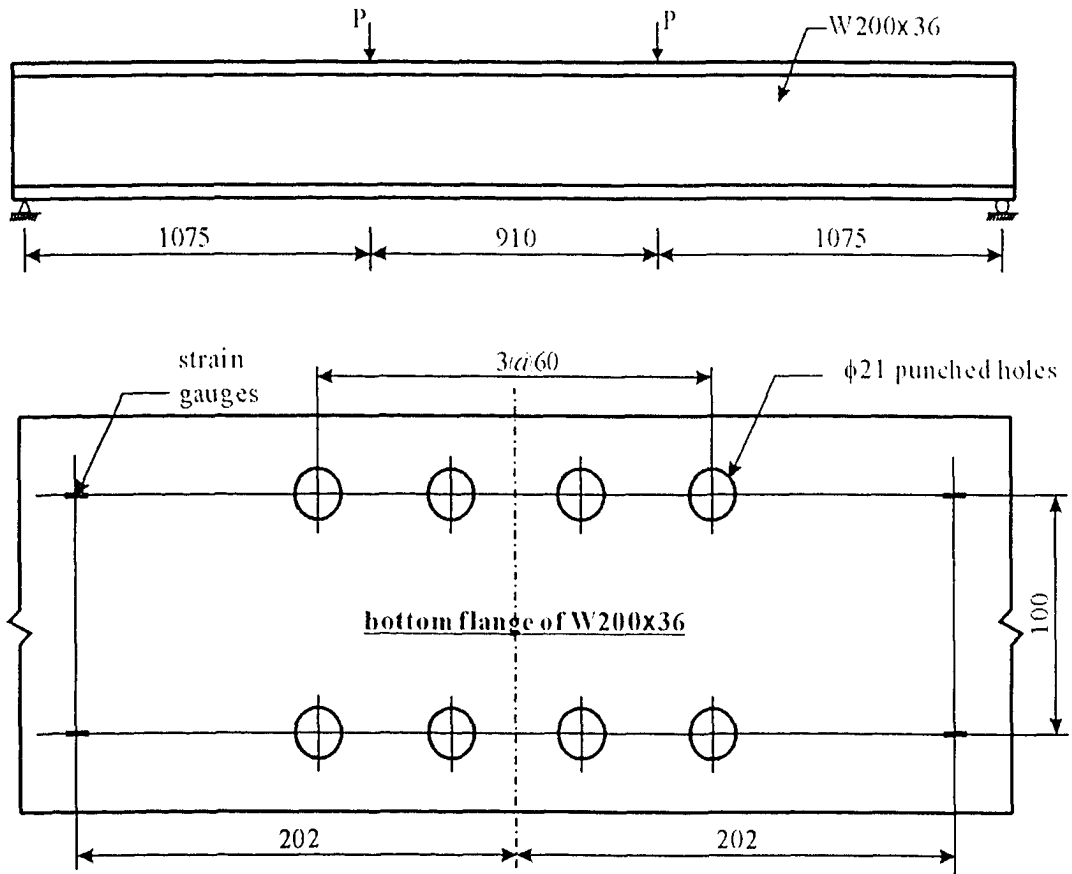
Figure 5-12 Large Scale Beam with Unfilled Holes (Baker and Kulak 1985)

188
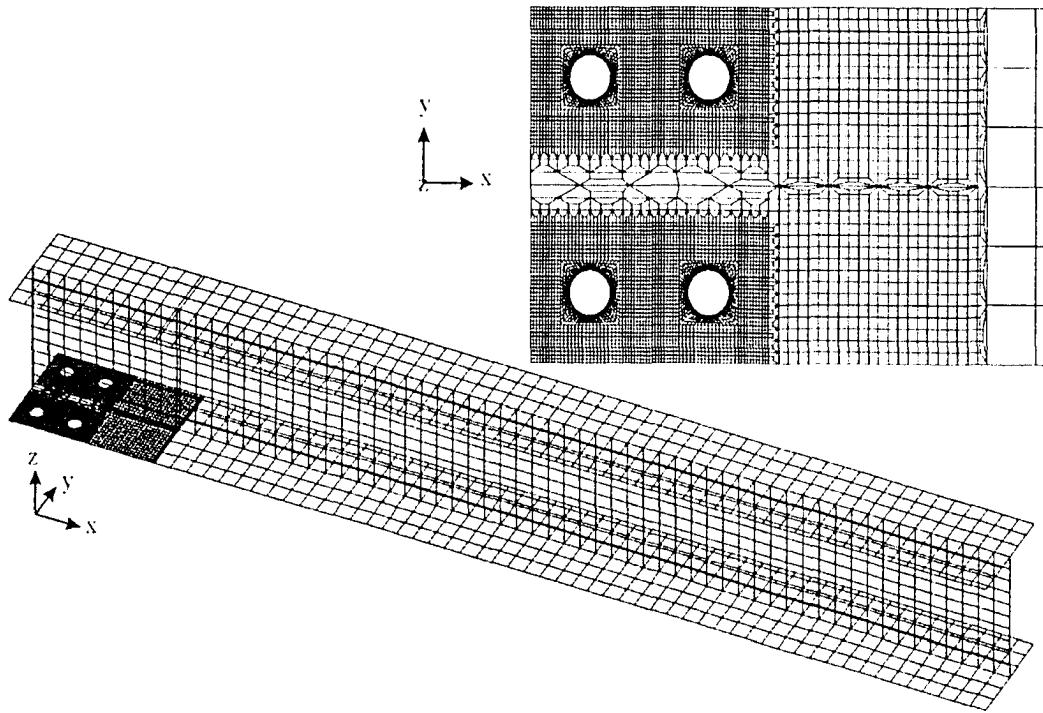
Figure 5-13 Finite Element Model for Large Scale Beam with Open Holes
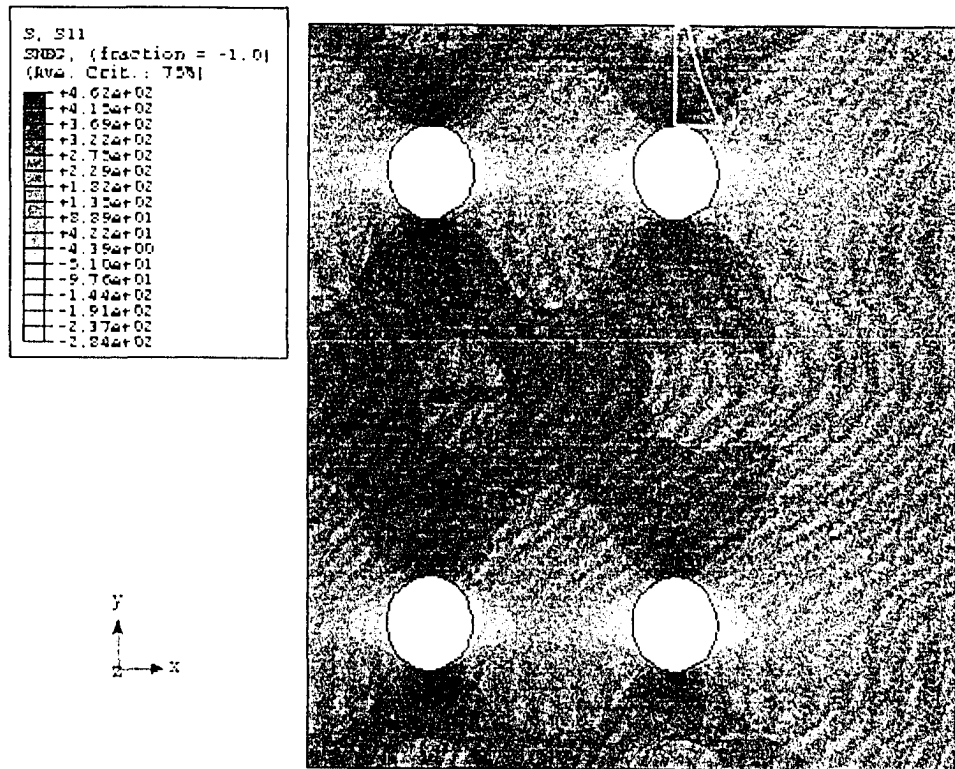
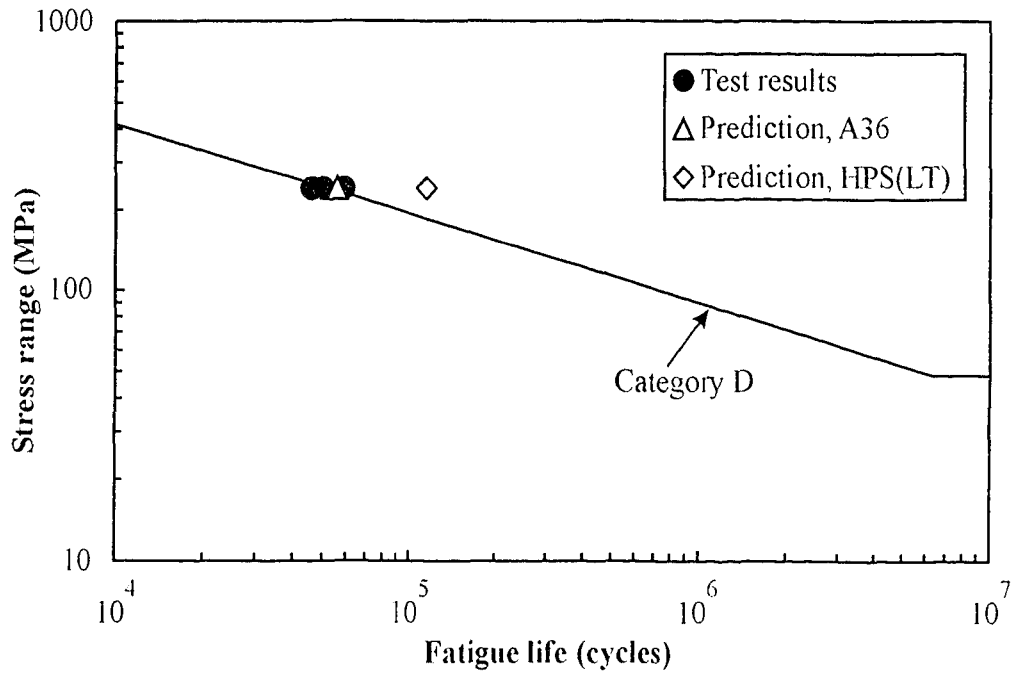Figure 5-14 Stress Contour near Midspan Section of Beam and Stress Distribution along

Crack Path

189

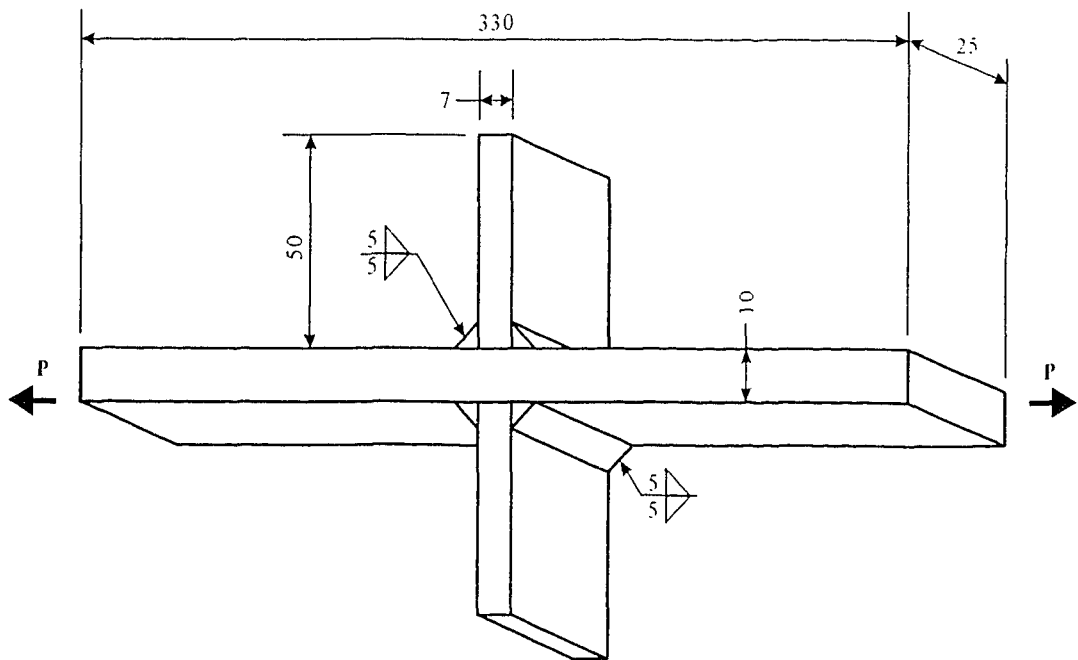Figure 5-15 Comparison between Predicted Fatigue Life and Test Results for Large Scale Beam with Unfilled Holes

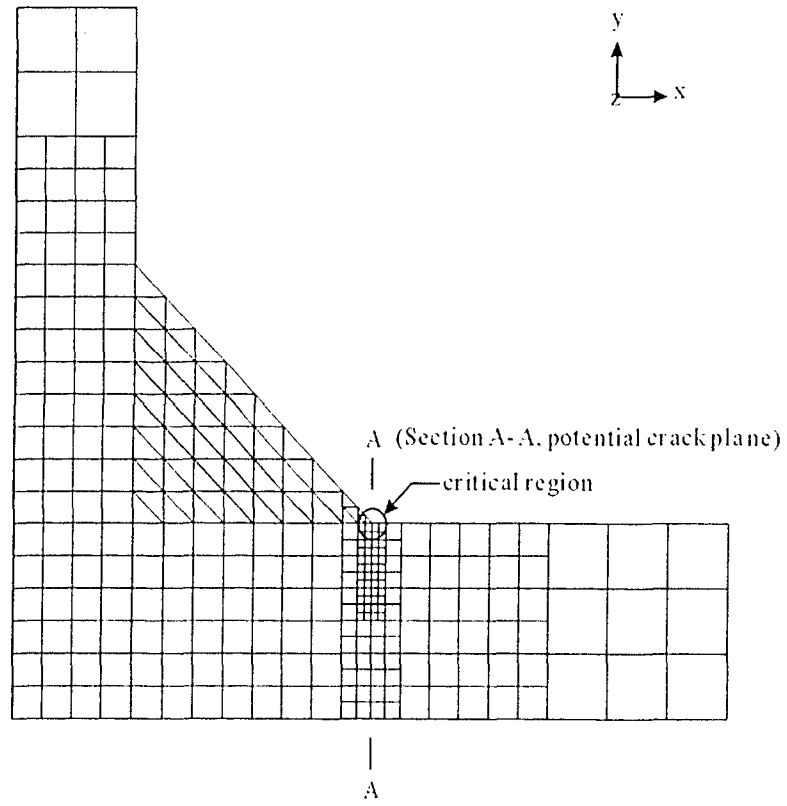Figure 5-16 Non-Load-Carrying Cruciform Specimen (Friedland *et al.* 1982)

190

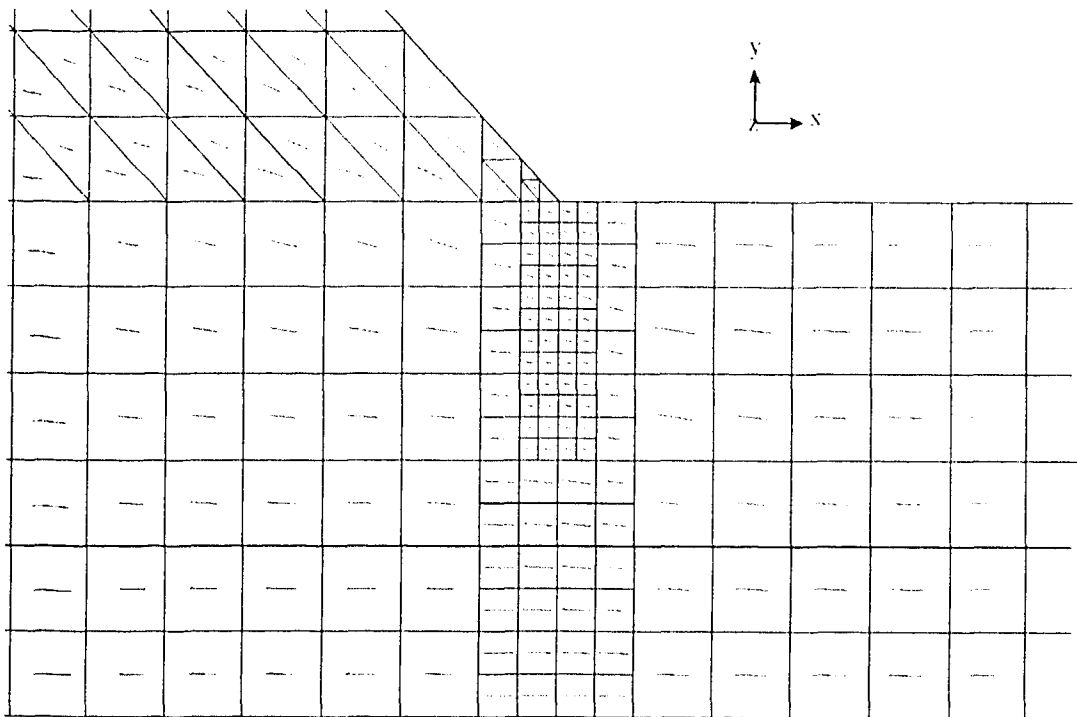Figure 5-17 Finite Element Model for Cruciform Specimen

Figure 5-18 Major Principal Tensile Stress Direction near Weld Region in Cruciform
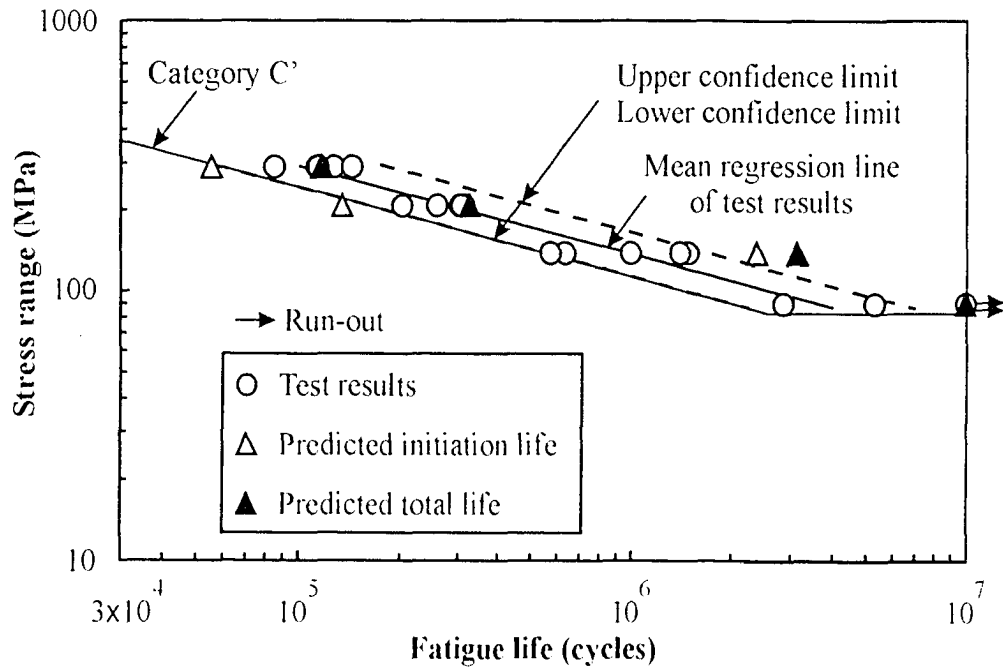
191

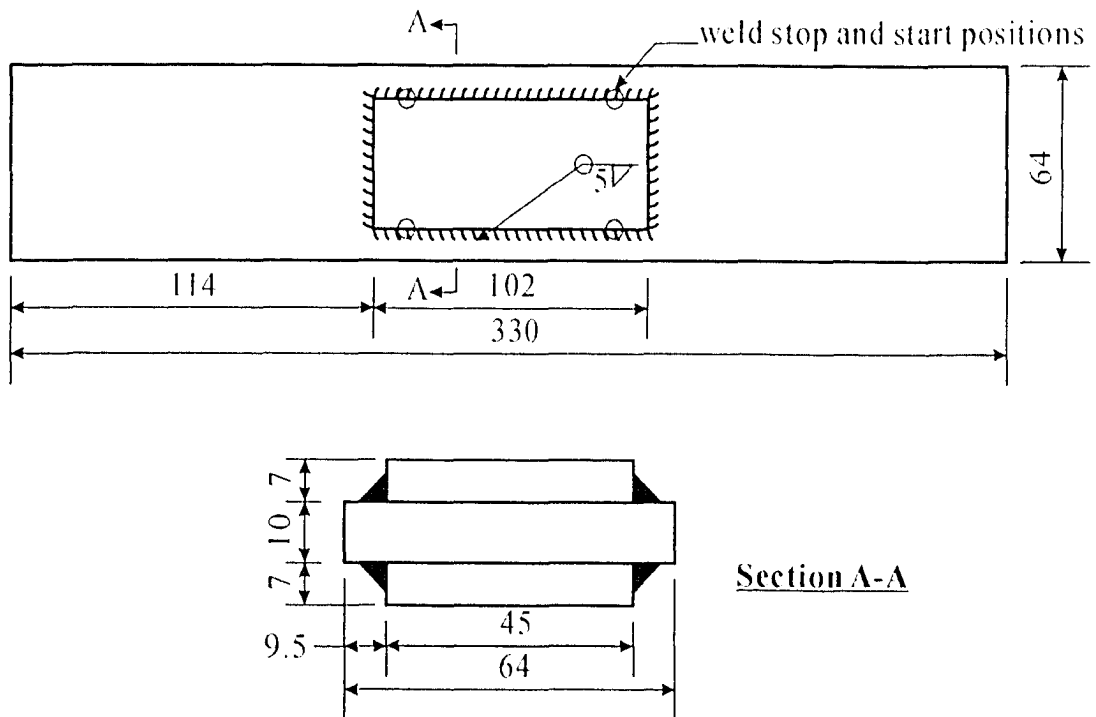Figure 5-19 Comparison between Fatigue Life Predictions and Test Results for Cruciform Detail

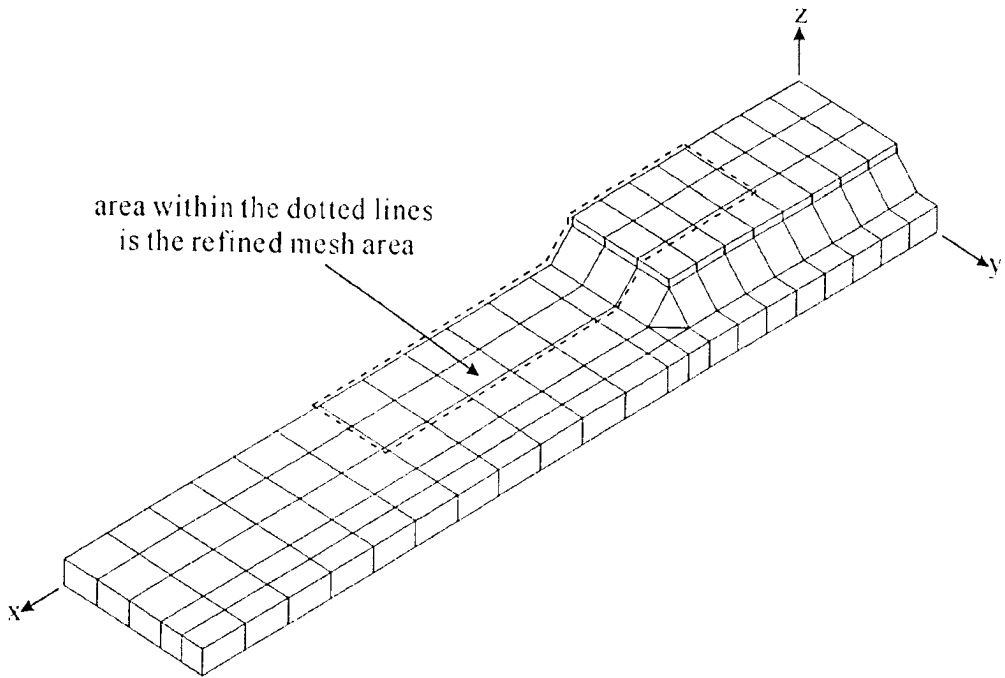Figure 5-20 Cover Plate Specimen (Friedland *et al.* 1982)

192

Figure 5-21 Global Model of the Cover Plate Detail

Note:

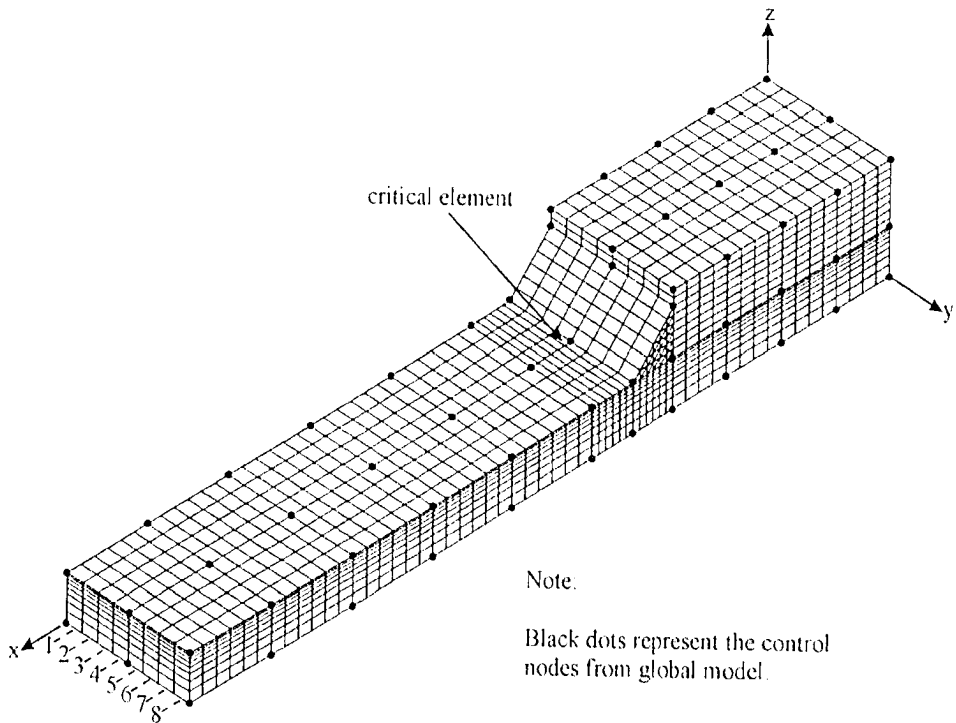Black dots represent the control nodes from global model.

Figure 5-22 Submodel of the Cover Plate Detail

193
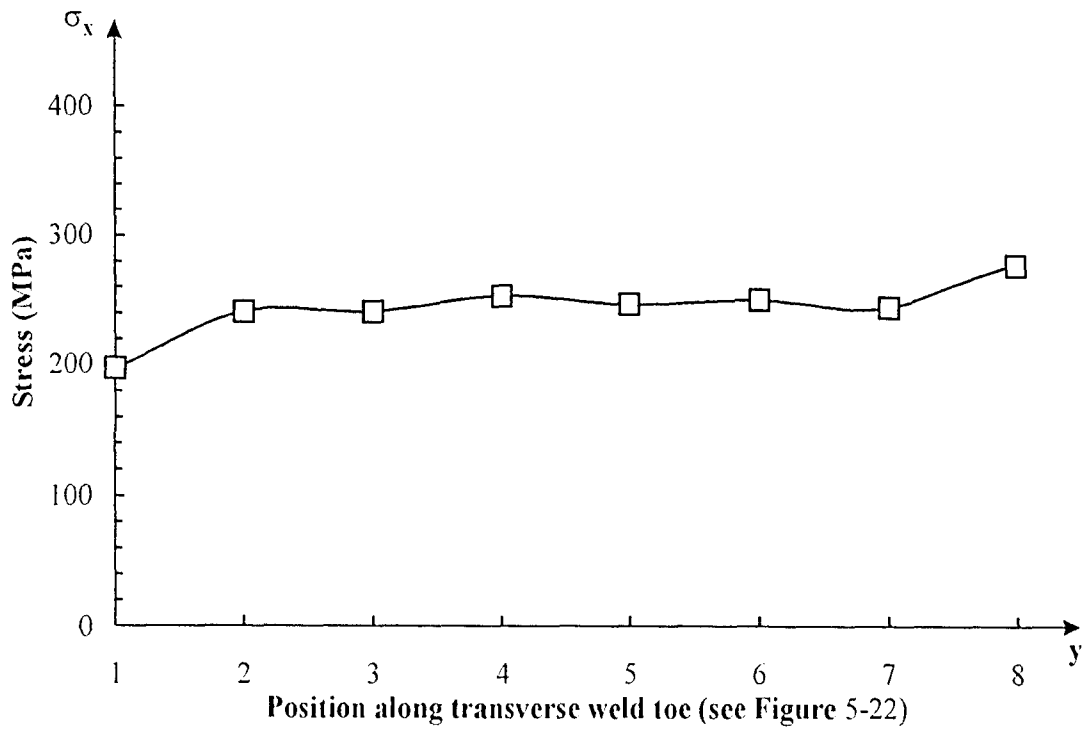
Figure 5-23 Stress Distribution along Transverse Weld Toe of Cover Plate
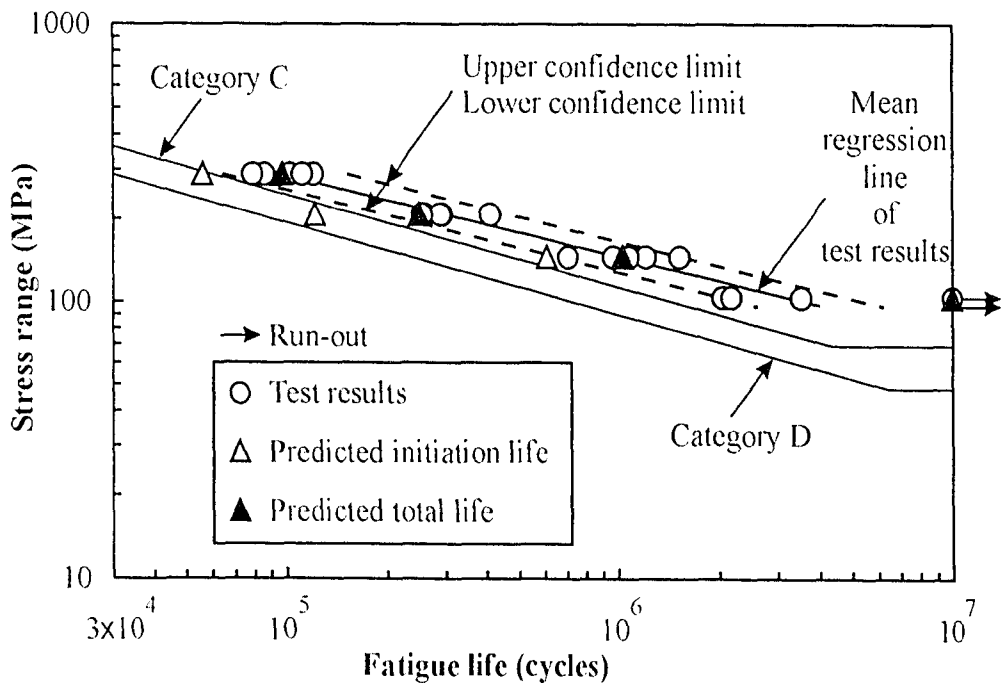
Figure 5-24 Comparison of Predicted Fatigue Life with Test Results for Cover Plate Specimens

194

195

Figure 5-25 Geometry and Test Layout for Girders HPS-485W-C1 and HPS-690W-C1 (Wright 2003)
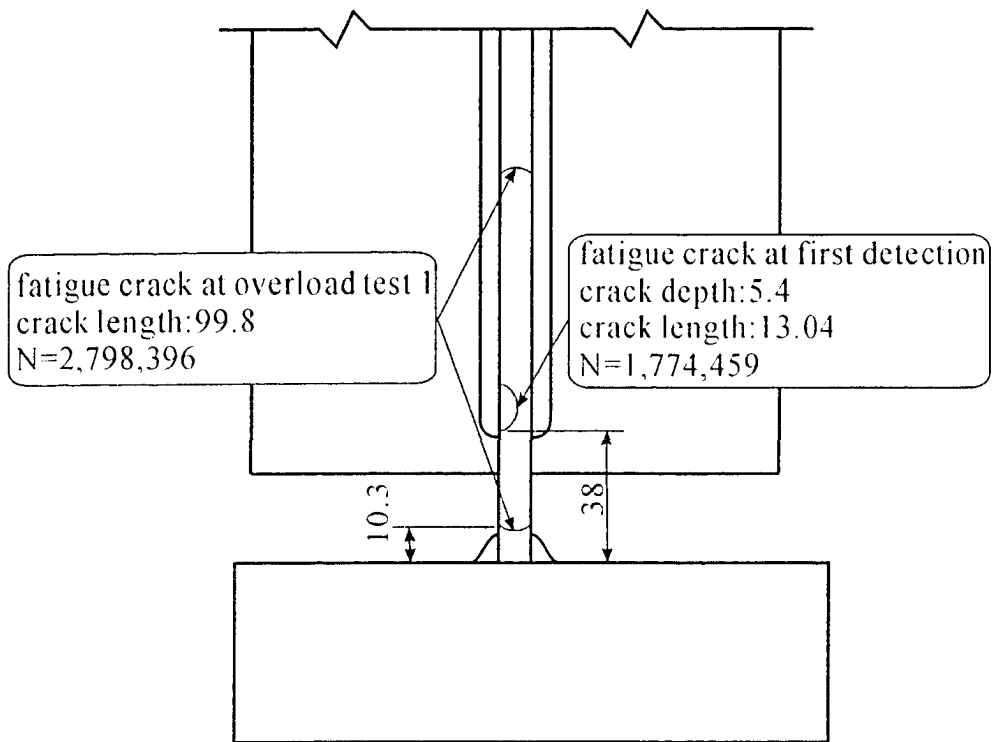
Figure 5-26 Crack History for Girder HPS-485W-C1 (Wright 2003)
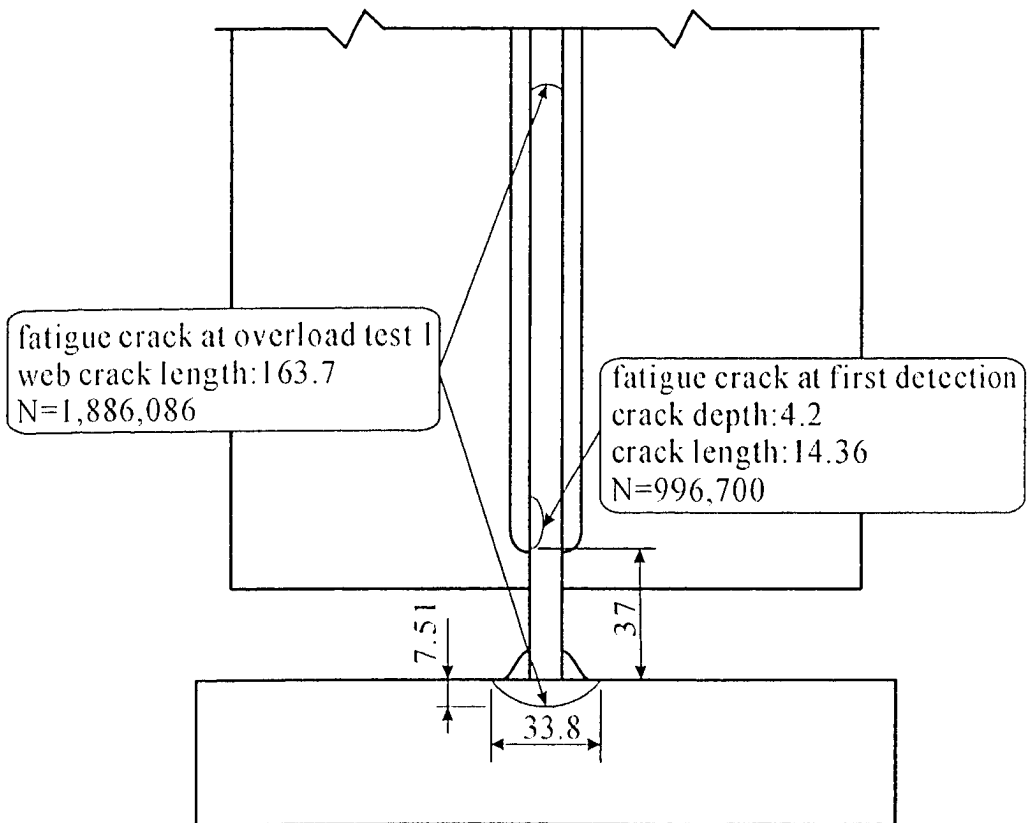
Figure 5-27 Crack History for Girder HPS-690W-C1 (Wright 2003)

196
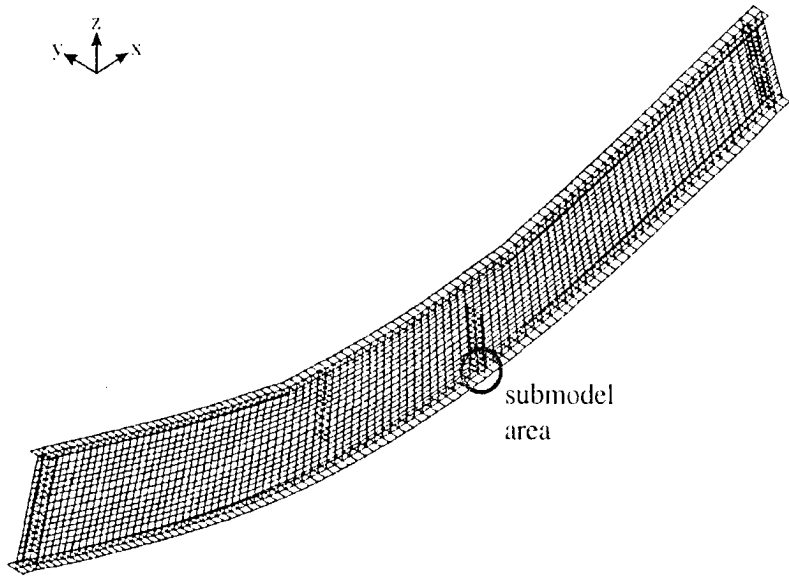
Figure 5-28 Global Model of Girder HPS-485W-C1, Deformed Shape
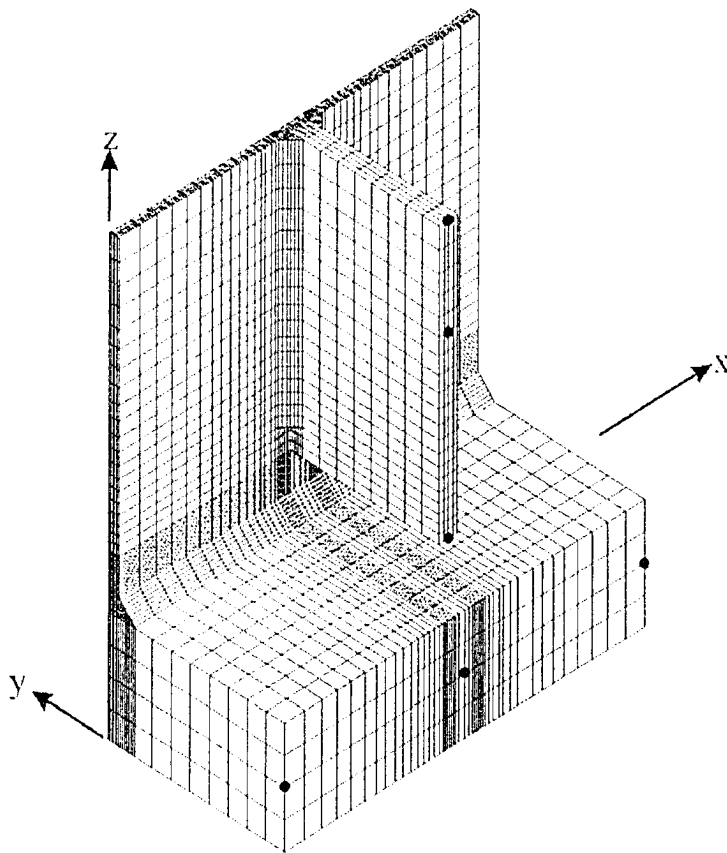
Figure 5-29 Submodel of Girder HPS-485W-C1

197
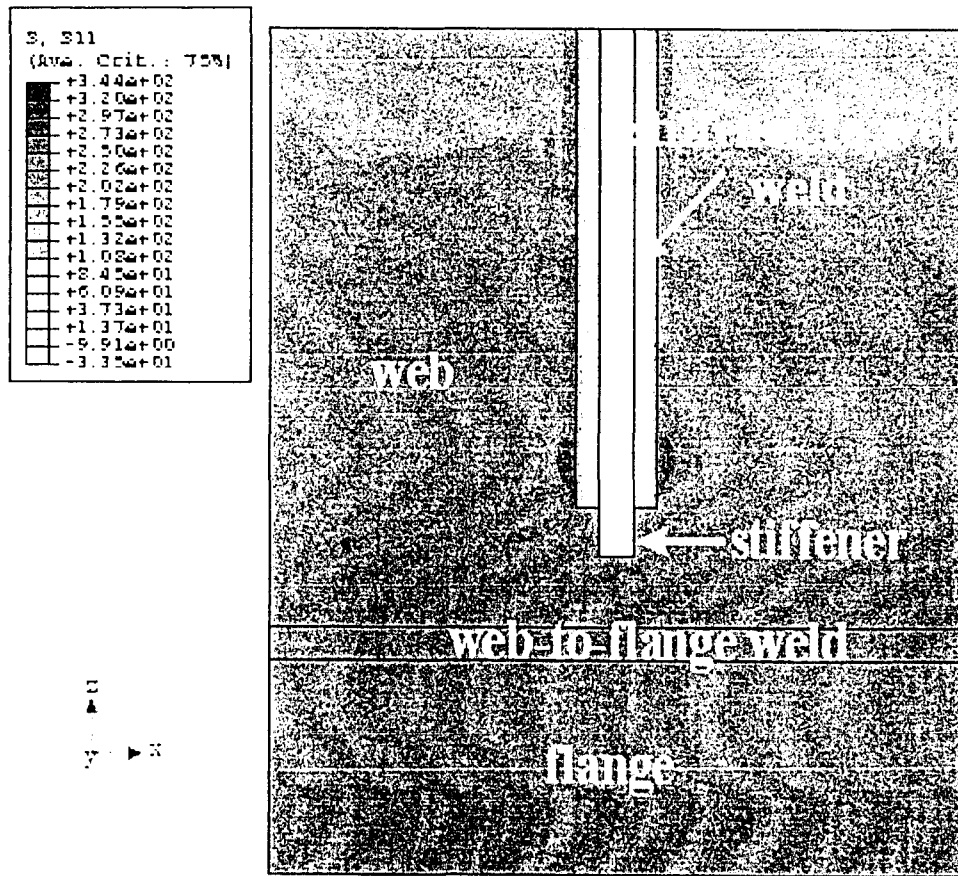
Figure 5-30 Normal Longitudinal Stress (σ_x) Distribution near a Stiffener in Girder HPS-485W-C1
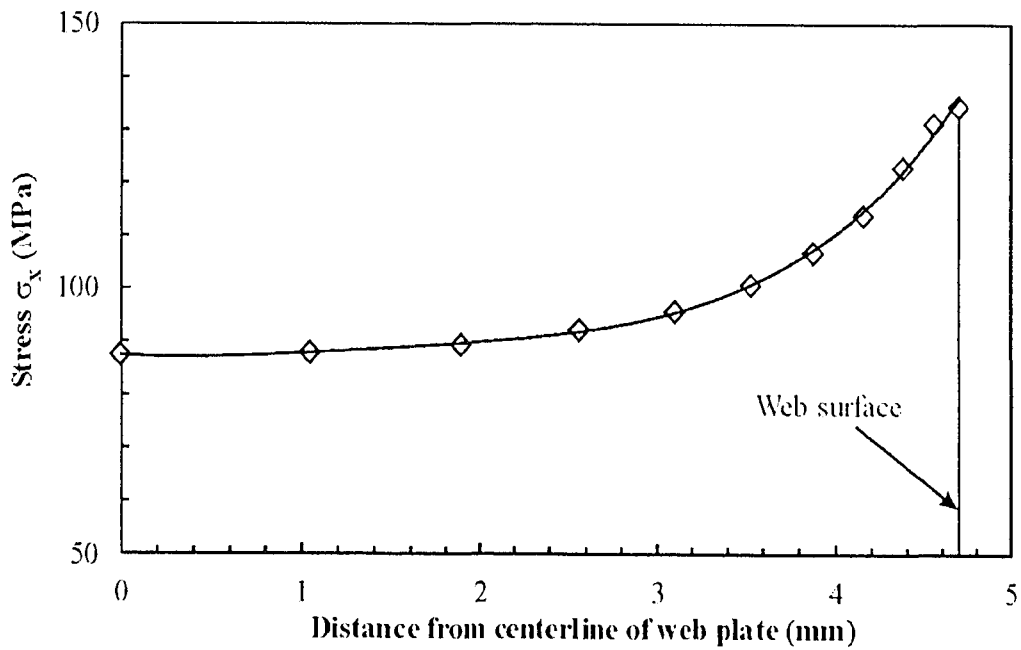
Figure 5-31 Stress Distribution through the Web Thickness in Girder HPS-485W-C1

198
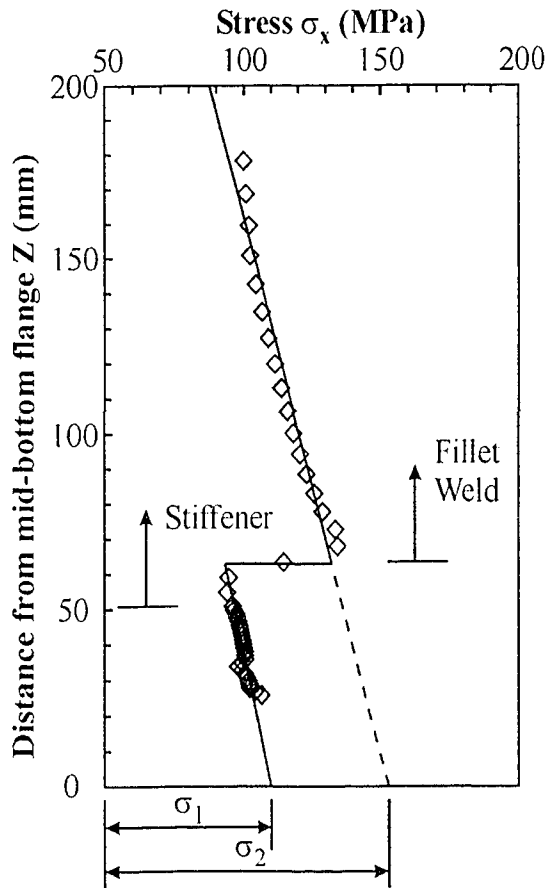
Figure 5-32 Stress Distribution along the Web Height in Girder HPS-485W-C1
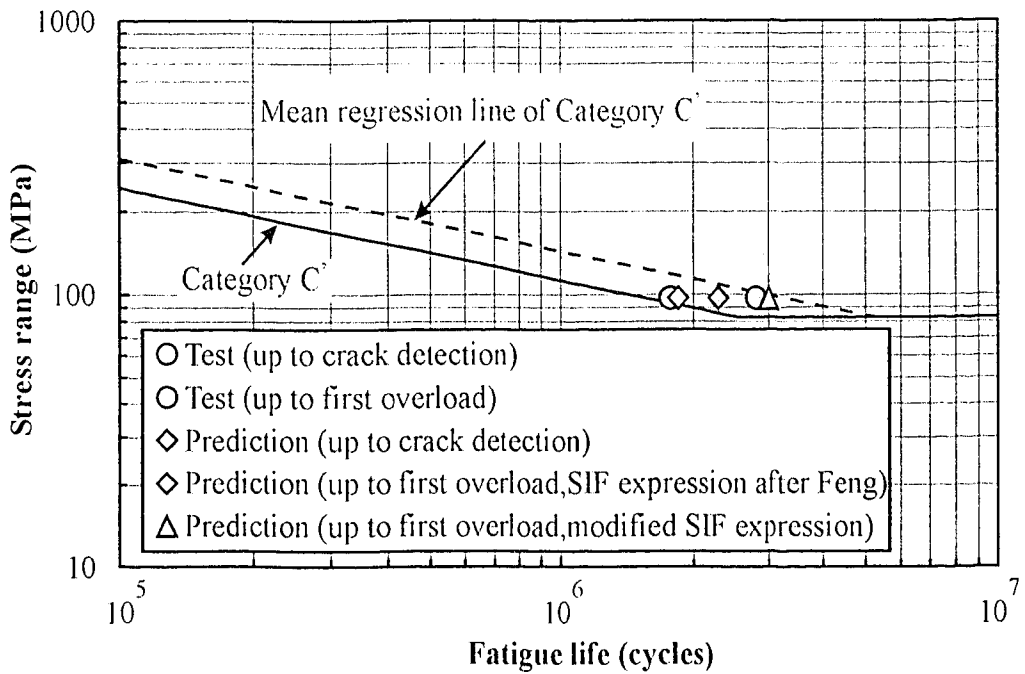
Figure 5-33 Fatigue Crack Initiation and Propagation in Girder HPS-485W-C1

199
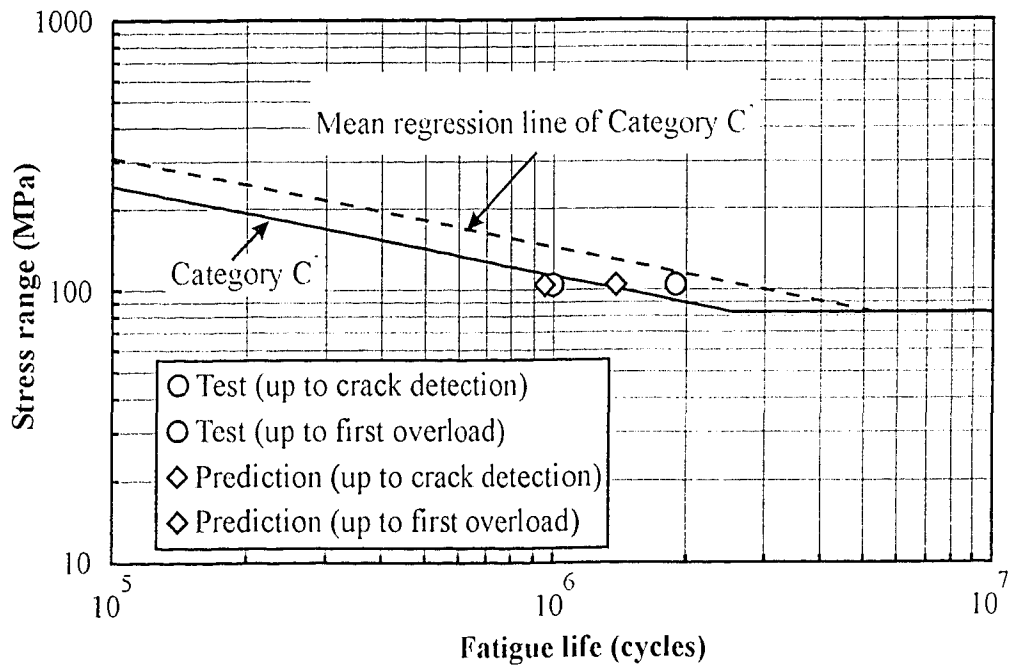
Figure 5-34 Fatigue Crack Initiation and Propagation in Girder HPS-690W-C1
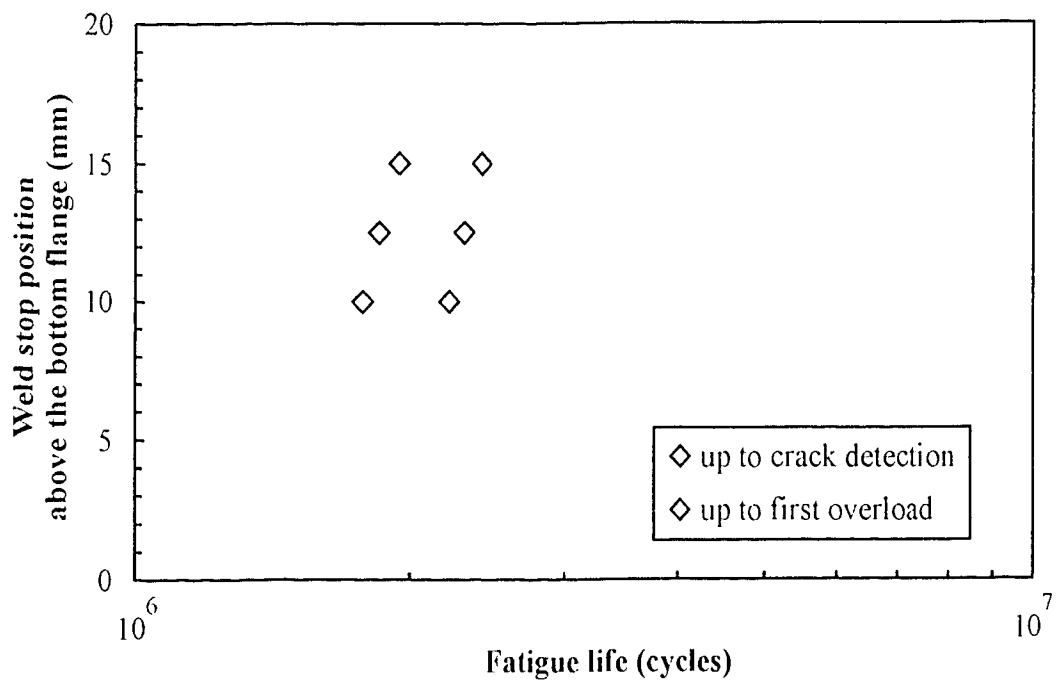
Figure 5-35 Effect of Stiffener-to-Web Weld Stop Position on Predicted Fatigue Life

(Girder HPS-485W-C1)

200
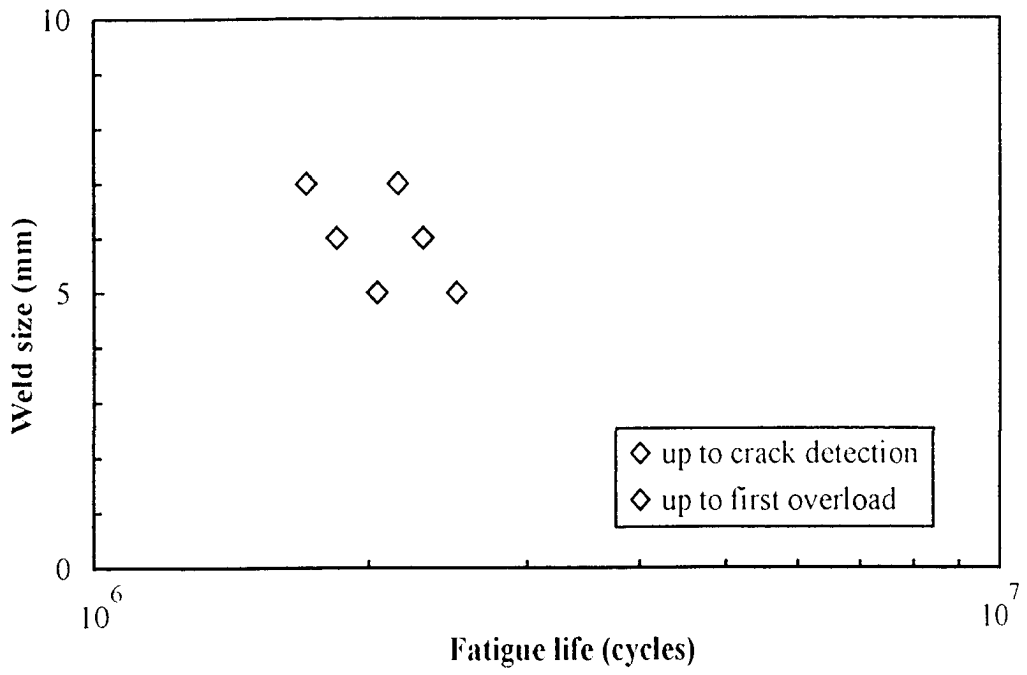
Figure 5-36 Effect of Stiffener-to-Web Weld Size on Predicted Fatigue Life
(Girder HPS-485W-C1)

201

CHAPTER 6.

SUMMARY, CONCLUSIONS, AND RECOMMENDATIONS

6.1. Summary

High performance steel (HPS) provides improved strength, ductility, weldability and fracture toughness. Its increasing popularity in applications such as highway bridges over the past few years has encouraged research in many areas of their behaviour. Although the strength and stability of members made of HPS have received a lot of attention, the fatigue resistance of HPS has not been well characterized. Fatigue performance of details made of HPS is commonly assumed to be the same as for conventional structural steels. Based on this assumption, cost savings associated with the use of HPS with higher yield strength may not be possible under current design standards because the fatigue limit state is likely to control the design. A research program was therefore initiated to determine whether or not the superior toughness of HPS can be used to relax the fatigue design provisions. Since fatigue testing is time consuming and expensive, an analytical method that can predict both fatigue crack initiation and fatigue crack propagation is desirable to study the fatigue behaviour of HPS.

An experimental and analytical investigation of the fatigue resistance of conventional structural details made of high performance steel was carried out to assess the effect of the high toughness of HPS on fatigue resistance. Stress-based, strain-based and energy-based methods for crack initiation life prediction and a linear elastic fracture mechanics approach for crack propagation life prediction were selected as the analysis tools based on a literature review. Material fatigue testing was conducted on HPS to obtain the material properties required for fatigue life prediction methods and to compare with those of conventional structural grade steels. A total of 57 smooth specimen fatigue tests, 17 crack growth rate tests and seven fracture toughness tests were carried out to characterise the cyclic and fatigue properties of HPS. Based on the analytical techniques and the results from the experimental program, fatigue life prediction was conducted on six common structural details made of HPS and traditional structural steel. Half of the

202

structural details investigated were welded details and the other half had stress raisers such as circular holes with or without bolts bearing against the holes. Analysis results were compared to the test results available for these details and the fatigue resistance of details made of HPS were predicted using the validated analytical techniques.

6.2. Conclusions

The following conclusions can be drawn from the results of the work described above:

1. High performance steel shows slightly higher fracture toughness at low temperature than the conventional notch tough 350WT steel and has a significantly lower transition temperature than A7 steel. HPS from two different heats produced at different times showed significantly different toughness properties.

2. Crack initiation properties of HPS are similar to conventional structural steels in terms of strain and energy, but, because of their superior strength, they are very different in terms of stress. The fatigue crack initiation properties of the higher toughness HPS 485W steel, HPS(HT), do not seem to be better than those of the lower toughness HPS(LT) steel. The smooth HPS specimens tested showed a significantly higher fatigue limit than conventional structural steels.

3. A comparison of crack propagation properties of HPS and 350WT steel indicates that HPS behaves similarly to conventional grades of structural steel.

4. Experimental results on plates with a circular hole detail made from HPS(LT) steel show HPS performs slightly better than conventional A36 steel.

5. The fatigue life prediction methods investigated in this research can predict fatigue test results accurately both for welded and non-welded details. The analytical methods provide a useful tool for classifying the severity of different structural details and can be used to derive fatigue curves for common details made of HPS.

6. The stress-based method, combined with inelastic stress analysis, the strain-based approach and the energy-based approach can all predict fatigue crack initiation life

203

accurately. Morrow's model and the SWT model provide a good prediction of the mean stress effect on crack initiation life of non-welded details. Linear elastic fracture mechanics provides accurate prediction of the crack propagation stage.

7. The stress intensity factor for a crack at a welded transverse stiffener can be evaluated accurately from an elastic finite element analysis. The stress intensity factor expression taking the existence of stiffeners into account provides a better characterization of the stress field near a two-tip through thickness web crack in plate girders with transverse stiffeners. Small variations in the location of the weld stop and size of the stiffener-to-web weld in plate girders do not affect the fatigue life of such details significantly.

8. The fatigue resistance of the non-welded HPS details analysed in this research is about one fatigue category higher than those made of conventional structural steels.

9. The current fatigue design provisions do not provide adequate design curves for bearing-type shear connections. The current design fatigue curves significantly overestimate the fatigue life of bearing-type shear connections.

10. Analytical and experimental data on welded details confirm that the current fatigue design curves for unloaded fillet transverse welds in cruciform specimens, cover plate specimens, and transverse stiffeners of plate girders (Category C', D, and C', respectively) are appropriate for HPS.

6.3. Recommendations

The analytical methods used in this study predicted fatigue life of three common welded structural details very well despite the fact that the effect of varying material properties through the base metal, weld metal, and heat affected zone, and the high tensile residual stresses in the vicinity of welds were not accounted for in the analysis. Since these factors are often thought to be important, their effects should be investigated systematically.

204

The stress intensity factor expression for a two-tip through thickness web crack at the transverse stiffener detail in a plate girder was obtained only for one particular geometry through finite element analysis. In order to investigate the fatigue resistance of transverse stiffener details made of HPS, a wider range of transverse stiffener details should be investigated. The variables may include I-girder geometry parameters, stiffener geometry parameters and weld geometry parameters.

Material tests such as Charpy V-Notch tests, crack growth rate tests and fracture toughness tests have been conducted on 350WT steel, however, results from smooth specimen fatigue test are not yet available. Such information is required for completeness so that a direct comparison between modern structural steel and high performance steel can be made.

The welded details investigated involved details where welds were not loaded. The fatigue behaviour of loaded weld details can be quite different. Such details are more sensitive to the effect of weld flaws. Details such as full penetration groove welds loaded in tension should be investigated. Further validations of the analytical methods are required for such details.

205

REFERENCES

AASHTO, (1998). AASHTO LRFD Bridge Design Specifications: SI Units, Second Edition. American Association of State Highway and Transportation Officials, Washington, D.C.

AASHTO, and AWS, (1995). ANSI/AASHTO/AWS D1.5-95 – Bridge Welding Code. American Welding Society, Miami, FL., American Association of State Highway and Transportation Officials, Washington D.C.

ABAQUS/Standard, (2003). Hibbitt, Karlsson & Sorensen, Inc., Pawtucket, Pl.

Albrecht, P., and Yamada, K., (1977). Rapid Calculation of Stress Intensity Factors. Journal of the Structural Division, ASCE, Vol. 103, No. ST2, pp. 377-389.

Anderson, T.L. (1995). Fracture Mechanics – Fundamentals and Applications, Second Edition. CRC Press, New York.

ASTM, (1965). ASTM Designation: A 7-61T – Tentative Specification for Steel for Bridges and Buildings. American Society for Testing and Materials, West Conshohocken, PA.

ASTM, (2000a). ASTM Designation: A 370-97a – Standard Test Methods and Definitions for Mechanical Testing of Steel Products. American Society for Testing and Materials, Philadelphia, PA.

ASTM, (2000b). ASTM Designation: E 606-92 (Reapproved 1998) – Standard Practice for Strain-Controlled Fatigue Testing. American Society for Testing and Materials, Philadelphia, PA.

ASTM, (2000c). ASTM Designation: E 647-99 – Standard Test Method for Measurement of Fatigue Crack Growth Rates. American Society for Testing and Materials, Philadelphia, PA.

ASTM, (2000d). ASTM Designation: E 1820-99 – Standard Test Method for Measurement of Fracture Toughness. American Society for Testing and Materials, Philadelphia, PA.

ASTM, (2002a). ASTM Designation: A 709/A 709M-01a – Standard Specification for Carbon and High-Strength Low-Alloy Structural Steel Shapes, Plates, and Bars and Quenched-and-Tempered Alloy Structural Steel Plates for Bridges. American Society for Testing and Materials, Philadelphia, PA.

ASTM, (2002b). ASTM Designation: G 101 – Guide for Estimating the Atmospheric Corrosion Resistance of Low-Alloy Steels. American Society for Testing and Materials, Philadelphia, PA.

AWS, (2002). AWS D1.1/D1.1M: 2002 – Structural Welding Code – Steel, 18th Edition. American Welding Society, Miami, FL.

Azizinamini, A., Barth, K., Dexter, R., and Rubeiz, C., (2004). High Performance Steel: Research Front – Historical Account of Research Activities. Journal of Bridge Engineering, ASCE, Vol. 9, No. 3, pp. 212-217.

Baker, K.A., and Kulak, G.L., (1985). Fatigue of Riveted Connections. Canadian Journal of Civil Engineering, Vol. 12, No. 1, pp. 184-191.

Barsom, J.M., and Rolfe, S.T, (1999). Fracture and Fatigue Control in Structures – Applications of Fracture Mechanics. ASTM, West Conshohocken, PA.

Barth, K.E., Roeder, C.W., Christopher, R.A., and Wu, H., (2003). Evaluation of Live Load Deflection Criteria for I-Shaped Steel Bridge Girders. High Performance Materials in Bridges: Proceedings of the International Conference, Kona, HI, Azizinamini, A. et al. (Editors), ASCE, Reston, VA, pp. 193-208.

Barth, K.E., White, D.W., and Bobb, B.M., (2000). Negative Bending Resistance of HPS70W Girders. Journal of Constructional Steel Research, Vol. 53, No. 1, pp. 1–31.

Blatt, D., John, R., and Coker, D., (1994). Stress Intensity Factor and Compliance Solutions for a Single Edge Notched Specimen with Clamped Ends. Engineering Fracture Mechanics, Vol. 47, No. 4, pp. 521-532.

Boyer, H.E. (Editor), (1986). Atlas of Fatigue Curves, American Society for Metals: Metals Park, OH.

Breen, D.H., and Wene, E.M., (1979). Fatigue in Machines and Structures-Ground Vehicles. Fatigue and Microstructure, American Society for Metals, Metals Park, OH, pp. 77.

Broek, D., (1989). The Practical Use of Fracture Mechanics. Kluwer Academic Publishers, Boston.

BSI, (1999). BS 7910:1999/BSI 10-2000 – Guide on Methods for Assessing the Acceptability of Flaws in Metallic Structures. British Standard Institution, London.

Canadian Standards Association, (1998). CAN/CSA G40.21-98 – General Requirements for Structural Quality Steels. Canadian Standards Association, Toronto, Ontario.

Canadian Standards Association, (2000). CAN/CSA-S6-00 – Canadian Highway Bridge Design Code. Canadian Standards Association, Toronto, Ontario.

207

Chan, K.S., and Miller, A.K., (1982). Prediction of Fatigue Failure in Structural Alloys: Initiation and Crack Propagation. International Symposium for Testing and Failure Analysis, ASM International, Metals Park, OH, pp. 272-279.

Dexter, R.J., Alttstadt, S.A., and Gardner, C.A., (2002). Strength and Ductility of HPS70W Tension Members and Tension Flanges with Holes. University of Minnesota, Minneapolis, MN.

Dexter, R.J., Fisher, J.W., and Beach, J.E., (1993). Fatigue Behavior of Welded HSLA-80 Members. OMAE 1993: Proceedings of the 12th International Conference on Offshore Mechanics and Arctic Engineering, Chakrabarti, S.K. et al. (Editors), ASME, Vol. 3, Pt. B, pp. 493-501.

Dexter, R.J., Kaczinski, M.R., and Kaufmann, E.J., (1995). Fatigue Resistance of Various Longitudinal Weld Joints. Restructuring – America and beyond: Proceedings of Structures Congress XIII, Boston, MA, Sanayei, M. (Editor), ASCE, New York, pp. 1293-1296.

Dowling, N.E., (1982). A Discussion of Methods for Estimating Fatigue Life. Proceedings of the SAE Fatigue Conference, Dearborn, Mich., Society of Automotive Engineers, Warrendale, PA, pp. 161-174.

Dowling, N.E., (1999). Mechanical Behavior of Materials: Engineering Methods for Deformation, Fracture, and Fatigue, Second Edition. Prentice Hall, Inc., Upper Saddle River, NJ.

Dusicka, P., Itani, A.M., and Buckle, I.G., (2003). The Use of High Performance Steel in Seismic Applications. Presentation at NSBA World Steel Bridge Symposium, Baltimore, MD.

Ellyin, F., (1997). Fatigue Damage, Crack Growth and Life Prediction. Chapman & Hall, London; New York.

Everett, R.A., (1992). Comparison of Fatigue Life Prediction Methodologies for Rotorcraft. Journal of the American Helicopter Society, Vol. 37, No. 2, pp. 54-60.

Feng, D., (1996). Stress Intensity Factors for Structural Steel I-Beams. Ph.D. Dissertation, University of Maryland, College Park, MD.

Fisher, J.W., and Wright, W.J., (2001). High Performance Steel Enhances the Fatigue and Fracture Resistance of Steel Bridge Structures. International Journal of Steel Structures, Vol. 1, No. 1, Korean Society of Steel Construction.

Fisher, J.W., Albrecht, P.A., Yen, B.T., Klingerman, D.J., and McNamee, B.M., (1974). Fatigue Strength of Steel Beams with Welded Stiffeners and Attachments,

208

NCHRP Report 147. Transportation Research Board, National Research Council, Washington, D.C.

Fisher, J.W., Frank, K.H., Hirt, M.A., and McNamee, B.M., (1970). Effect of Weldments on the Fatigue Strength of Steel Beams, NCHRP Report 102. Highway Research Board, National Research Council, Washington, D.C.

Fisher, J.W., Kulak, G.L., and Smith, I.F.C., (1998). A Fatigue Primer for Structural Engineers. National Steel Bridge Alliance, American Institute of Steel Construction, Chicago, IL.

Focht, E.M., and Manganello, S.J., (1996). Stress-Strain Behavior of High-Performance 70W Bridge Steel. Materials for the New Millennium: Proceedings of the Fourth Materials Engineering, Washington, D.C., Chong, K.P. (Editor), ASCE, New York, pp. 1540-1550.

Friedland, I.M., Albrecht, P., and Irwin, G.R., (1982). Fatigue of Two-Year Weathered A588 Stiffeners and Attachments. Journal of the Structural Division, Proceedings of the ASCE, Vol. 108, No. ST1, pp. 125-144.

Frocht, M.M, (1936). Photoelastic Studies in Stress Concentration. Mechanical Engineering, pp. 485-489.

Gurney, T.R., (1968). Fatigue of Welded Structures. Cambridge University Press, New York.

Hash, J.B., and Azizinamini, A., (2001). Shear Capacity of Hybrid Steel Plate Girders. Final Report to FHWA, University of Nebraska-Lincoln, Lincoln, Neb.

Hatanaka, K., (1990). Cyclic Stress–Strain Response and Low Cycle Fatigue Life in Metallic Materials. JSME International Journal, Series I, Solid Mechanics, Strength of Materials, Vol. 33, No. 1, pp. 13-25.

Heuler, P., and Schuetz, W., (1986). Assessment of Concepts for Fatigue Crack Initiation and Propagation Life Prediction. Z. Werkstofftech, Vol. 17, No. 11, pp. 397-405.

Homma, K., and Sause, R., (1995). Potential for High Performance Steel in Plate-Girder Bridge. Restructuring – America and beyond: Proceedings of Structures Congress XIII, Boston, MA, Sanayei, M. (Editor), ASCE, New York, pp. 177-192.

Horton, R., Power, E., Van Ooyen, K., and Azizinamini, A., (2003). High Performance Steel Cost Comparison Study. High Performance Materials in Bridges: Proceedings of the International Conference, Kona, HI, Azizinamini, A. et al. (Editors), ASCE, Reston, VA, pp. 275-300.

Jaske, C.E., (1995). Life Prediction in High-Temperature Structural Materials. Journal of Pressure Vessel Technology, American Society of Mechanical Engineers. New York, Vol. 117, No. 1, pp. 1-6.

Josi, G., Grondin, G.Y., and Kulak, G.L., (1999). Fatigue of Bearing-Type Shear Splices, Structural Engineering Report No. 227. Department of Civil and Environmental Engineering, University of Alberta, Edmonton, Alberta.

Kaufmann, E.J., and Pense, A.W., (2000). Innovative HPS-70W Ford City Bridge Demonstration Project: Improved Weldability Using Optimized Weld Metal Strength. ATLSS Final Report to Pennsylvania Department of Transportation.

Keating, P.B., and Fisher, J.W., (1986). Evaluation of Fatigue Tests and Design Criteria on Welded Details. NCHRP Report 286. Transportation Research Board, National Research Council, Washington, D.C.

Klippstein, K.H., (1987). Variable Amplitude Load Fatigue. Task A – Literature Review, Volume III – Supplementary Information on Constant Amplitude Fatigue Behavior. U.S. Department of Transportation Report No. DTFH61-86-C-00036-III, Washington, D.C.

Krouse, D.C., (1999). High Performance Steel: Material Development. Materials and Construction: Exploring the Connection – Proceedings of the Fifth ASCE Materials Engineering Congress, Cincinnati, OH, Lawrence, C.B. (Editor), ASCE, Reston, VA, pp. 566-574.

Kujawski, D., and Ellyin, F., (1995). A Unified Approach to Mean Stress Effect on Fatigue Threshold Conditions. International Journal of Fatigue, Vol. 17, No. 2, pp. 101-106.

Kulicki, J.M., (2000). Steel Bridges for the 21st Century. Advanced Technology in Structural Engineering: Proceedings of the 2000 Structures Congress & Exposition, Philadelphia, PA, Elgaaly, M. (Editor), ASCE, Reston, VA.

Lee, H.K., Kim, K.S., and Kim, C.M., (2000). Fracture Resistance of a Steel Weld Joint under Fatigue Loading. Engineering Fracture Mechanics, Vol. 66, No. 4, pp. 403-419.

Leis, B.N., Gowda, C.V.B., and Topper, T.H., (1973). Cyclic Inelastic Deformation and the Fatigue Notch Factor. Symposium on Cyclic Stress–Strain Behavior – Analysis, Experimentation, and Failure Prediction, Bal Harbour, Fla., ASTM STP 519, Philadelphia, PA, pp. 133-150.

Lindstrom, R., Lidaar, P., and Rosborg, B., (2000). Fatigue Crack Growth Threshold Measurements in Structural Materials. Fatigue Crack Growth Thresholds,

Endurance Limits and Design, Newman, J.C., and Piascik, R.S. (Editors), ASTM STP1372, West Conshohocken, PA, pp. 400-410.

Little, R.E., and Jebe, E.H., (1975). Statistical Design of Fatigue Experiments. John Wiley & Sons, New York.

Maddox, S.J., (1974). Assessing the Significance of Flaws in Welds Subject to Fatigue. Welding Journal, Vol. 53, No. 9.

Mertz, D.R., (1999). High Performance Steel Bridge Design Issues. Structural Engineering in the 21st Century: Proceedings of the 1999 New Orleans Structures Congress, Avent, R.R., and Alawady, M. (Editors). ASCE. Reston, VA, pp. 749-752.

Morrow, J., and Socie, D.F., (1981). Evolution of Fatigue Crack Initiation Life Prediction Methods. Materials, Experimentation and Design in Fatigue: Proceedings of Fatigue '81, Warwick University, England, Sherratt, F., and Sturgeon, J.B. (Editors), Westbury House, Guildford, pp. 3-21.

Newman, J.C., and Raju, I.S., (1984). Stress Intensity Factor Equations for Cracks in Three Dimensional Finite Bodies Subjected to Tension and Bending Loads. NASA Technical Memorandum 85793. NASA Langley Research Centre, Hampton, VA.

Nowack, H., (1983). Macro and Micromechanics of Fatigue Crack Initiation and Propagation under Constant and Variable Amplitude Loading. Proceedings of the International Conference on Application of Fracture Mechanics to Materials and Structures, Freiburg im Breisgau, Germany. Sih, G.C. et al. (Editors), pp. 57-102.

Paris, P.C., (1998). Fracture Mechanics and Fatigue: a Historical Perspective. Fatigue and Fracture of Engineering Materials and Structures, Vol. 21, No. 5, pp. 535-540.

Radaj, D., and Sonsino, C.M., (1998). Fatigue Assessment of Welded Joints by Local Approaches. Abington Publishing, Cambridge, England.

Raj, B., Subramanian, C. V., and Jayakumar, T., (2000). Non-Destructive Testing of Welds. Narosa Publishing House, New Delhi, India, Distributed in North America by ASM International, Materials Park, OH.

Rice, R.C., Leis, B.N., and Nelson, D.V. (Editors), (1988). Fatigue Design Handbook, Second Edition. Society of Automotive Engineers, Warrendale, PA.

Sarihan, V., (1994). Energy Based Methodology for Damage and Life Prediction of Solder Joints under Thermal Cycling. IEEE Transactions on Components, Packaging, and Manufacturing Technology, Part B, Advanced Packaging, Vol. 17, No. 4, pp. 626-631.

211

Sause, R., (1996). Barriers to the Use of High Performance Steel in I-Girder Highway Bridges. Building an International Community of Structural Engineers: Proceedings of Structures Congress XIV, Chicago, IL, Ghosh, S. K. and Mohammadi, J. (Editors), ASCE, New York, pp. 108-115.

Sause, R., and Fahnestock, L.A., (2001). Strength and Ductility of HPS 100W I-Girders in Negative Flexure. Journal of Bridge Engineering, ASCE, Vol. 6, No. 5, pp. 316-323.

Sehitoglu, H., (1983). Fatigue Life Prediction of Notched Members Based on Local Strain and Elastic-Plastic Fracture Mechanics Concepts. Engineering Fracture Mechanics, Vol. 18, No. 3, pp. 609-621.

Smith, W.F., (1993). Structure and Properties of Engineering Alloys, Second Edition. McGraw-Hill, Inc., New York.

Stephens, R.I., Fatemi, A., Stephens, R.R., and Fuchs, H.O., (2000). Metal Fatigue in Engineering, Second Edition. John Wiley & Sons, New York.

Tada, H., Paris, P.C., Irwin, G.R., (2000). The Stress Analysis of Cracks Handbook, Third Edition. ASME Press, New York.

Takamori, H., and Fisher, J.W., (2000). Tests of Large Girders Treated to Enhance Fatigue Strength. Transportation Research Record 1696, Journal of Transportation Research Board, pp. 93-99.

Thomas, S.J., and Earls, C.J., (2003). Cross-Sectional Compactness and Bracing Requirements for HPS483W Girders. Journal of Structural Engineering, ASCE, Vol. 129, No. 12, pp. 1569-1583.

Thomas, V., (1996). Safety of Welded Modern High Strength Steel Constructions, in Particular Bridges. Welding in the World, Vol. 38, November, pp. 1-22.

Wilson, A.D., (2000). Production of High Performance Steels for U.S.A. Bridges. Steel Bridge Design and Construction for the New Millennium with Emphasis on High Performance Steel: Conference of High Performance Steel Bridge, Baltimore, MD.

Wilson, A.D., (2004). HPS Powerpoint Update. Presentation at HPS Meeting, American Iron and Steel Institute, February 13, 2004.

Wright, W., (2003). Fracture Initiation Resistance of I-Girders Fabricated from High Performance Steels. Ph.D. Dissertation, Lehigh University, Bethlehem, PA.

Wright, W., Tjiang, H., and Albrecht, P., (1995). Fracture Toughness and Ductility of High Performance Steel. Restructuring – America and beyond: Proceedings of

Structures Congress XIII, Boston, MA, Sanayei, M. (Editor), ASCE, New York, pp. 193-196.

Wright, W., Albrecht, P., and Tjiang, H., (2001). Development of HPS Toughness Specifications. Presentation at the AISI-AASHTO-T-14 Bridge Task Force Meeting, Jackson Hole, Wyo.

Yakel, A., Mans, P., and Azizinamini, A., (1999). Negative Bending Tests of High Performance Steel 485W Bridge Girders. Materials and Construction: Exploring the Connection – Proceedings of the Fifth ASCE Materials Engineering Congress, Cincinnati, OH, Lawrence, C.B. (Editor), ASCE, Reston, VA, pp. 558-565.

Yazdani, N., and Albrecht, P., (1990). Probabilistic Fracture Mechanics Application to Highway Bridges. Engineering Fracture Mechanics, Vol. 37, No. 5, pp. 969-985.

213

APPENDIX A.

PLASTIC STRAIN ENERGY DENSITY, ΔW^p

The plastic strain energy density per cycle, ΔW^p, corresponding to the area under a stable hysteresis loop, is essential in the energy-based approaches to fatigue life prediction. Three methods were used to obtain the value of ΔW^p from uniaxial loading, namely, spreadsheet numerical integration, finite element analysis output, and direct calculation from mathematical equations. The methods and their applications are described in this Appendix.

A.1. Spreadsheet Numerical Integration

Electronic spreadsheets can be used to calculate the area under a hysteresis loop by numerical integration using the trapezoidal rule. The numerical integration does not require a function formulation of the hysteresis loop but the accuracy depends on the number of data points in defining the hysteresis loop. The method is most suitable in obtaining the material fatigue properties such as energy-life curves from test results. In the test program, since as many as 250 data points were obtained to define one stable hysteresis loop, it is felt that the numerical integration method can give a sufficiently accurate result in the calculation of ΔW^p.

A.2. Finite Element Analysis Output

The plastic strain energy density ΔW^p can be directly obtained as output PENER from finite element program ABAQUS. The method is most useful for fatigue life prediction of different fatigue details, especially when the details are under multiaxial loadings.

A.3. Direct Calculation from Analytical Equations

A mathematical description of the branches of hysteresis loops is required in order to calculate the plastic strain energy density. However, once the parameters in material cyclic curve or master curve are known, the method can calculate ΔW^p conveniently. The equations are slightly different, depending on the types of material behaviour.

215

A.3.1. Masing-type Material

For this type of material, when stable hysteresis loops of various strain amplitudes are transferred to a common origin, the bottom tip of the hysteresis loops, the upper branch would form a unique curve. The behaviour is illustrated in Figure A-1. Thus, the ascending hysteresis loop branch can be described by the cyclic stress versus strain curve described by Equation (3-5), magnified by a factor of 2, as in the following:

$$\Delta\varepsilon = \frac{\Delta\sigma}{E} + 2(\frac{\Delta\sigma/2}{K'})^{1/n'} \tag{A-1}$$

Thus the area of a hysteresis loop with a stabilized stress range of $\Delta\sigma$ and plastic strain range of $\Delta\varepsilon^p$, is calculated as

$$\Delta W^p = 2\int_{0}^{\Delta\varepsilon^p} \Delta\sigma(d\Delta\varepsilon^p) - \Delta\sigma\Delta\varepsilon^p$$
$$= \frac{1-n'}{1+n'}\Delta\sigma\Delta\varepsilon^p \tag{A-2}$$

A.3.2. Non-Masing-type Material (Ellyin 1997)

Most carbon and low alloy steels display a non-Masing behaviour. The stable hysteresis loops of HPS-HT steel obtained from the test program are shown in Figure A-2 as an example. As illustrated in Figure A-3, by shifting the hysteresis loops along the linear portion, their upper branches for different strain amplitudes are matched to form a unique curve. This envelope of the loading branches of hysteresis loops is called master curve, with origin located at A, which corresponds to the bottom of the hysteresis loop with the minimum range. The equation of the master curve ABCD in Figure A-3 is:

$$\Delta\varepsilon^* = \frac{\Delta\sigma^*}{E} + 2(\frac{\Delta\sigma^*/2}{K^*})^{1/n^*} \tag{A-3}$$

The strength coefficient K^* and strain-hardening exponent n^* are obtained by fitting Equation (A-4) to the $\Delta\sigma - \delta\sigma_0$ versus $\Delta\varepsilon^p$ test data.

216

$$\Delta\sigma - \delta\sigma_0 = 2K^* (\Delta\varepsilon^p / 2)^{n^*} \tag{A-4}$$

where $\delta\sigma_0$ is the amount of shifting in order to get the matching upper branch of hysteresis loops and is an indication of the change in proportional stress. The constants K^* and n^* are presented in Table A-1 for the three steel sources and two orientations investigated in the test program.

The plastic strain energy of the hysteresis loop OABCDFO Figure A-3 consists of two parts, ABCDFA, and OAFO. The plastic strain energy of the loop ABCDFA corresponding to the Masing behaviour is

$$\Delta W_M^p = \frac{1 - n^*}{1 + n^*} \Delta\sigma^* \Delta\varepsilon^{p*} = \frac{1 - n^*}{1 + n^*} (\Delta\sigma - \delta\sigma_0) \tag{A-5}$$

The crosshatched area OAFO that represents the change in the plastic strain energy per cycle due to the non-Masing behaviour is equal to

$$\Delta W_N^p = OABF'D'DFO - ABF'D'DFA = \delta\sigma_0 \Delta\varepsilon^p \tag{A-6}$$

Thus, the plastic strain energy for a non-Masing-type material can be calculated as

$$\begin{aligned} \Delta W^p &= \Delta W_M^p + \Delta W_N^p \\ &= \frac{1 - n^*}{1 + n^*} \Delta\sigma\Delta\varepsilon^p + \frac{2n^*}{1 + n^*} \delta\sigma_0 \Delta\varepsilon^p \end{aligned} \tag{A-7}$$

where $\delta\sigma_0$ for any hysteresis loop can be evaluated easily from

$$\delta\sigma_0 = \Delta\sigma - 2K^* (\Delta\varepsilon^p / 2)^{n^*} \tag{A-8}$$

217

Table A-1 Master Curve Properties of HPS 485W and A7 Steels

Material	Orientation	K^* (MPa)	n^*
HPS(LT)	Longitudinal	1557	0.163
HPS(LT)	Transverse	1164	0.124
HPS(HT)	Longitudinal	1421	0.149
A7	Transverse	587	0.143

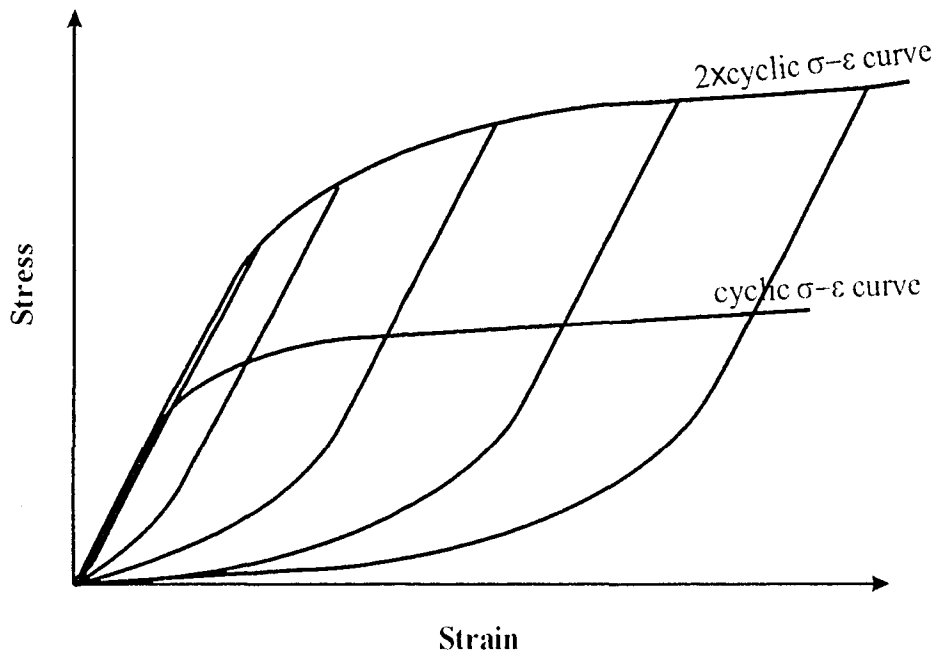218

Figure A-1 Illustration of Masing Behaviour

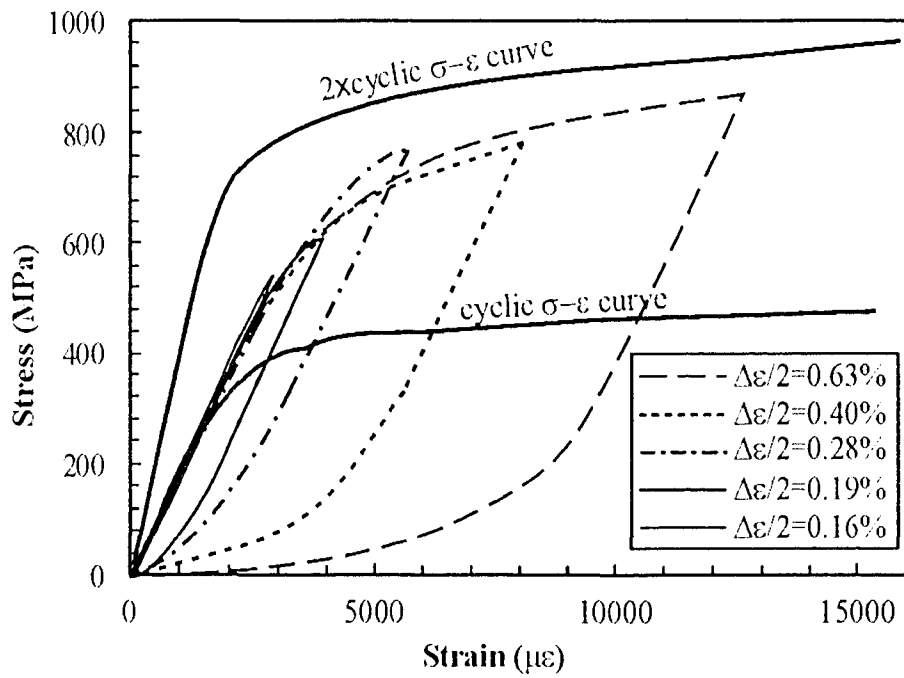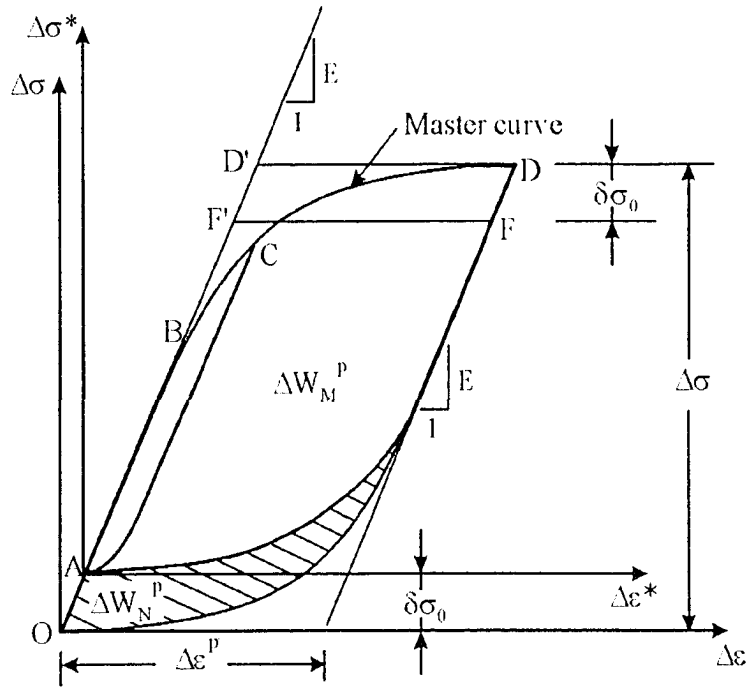Figure A-2 Non-Masing Behaviour of HPS(HT)

219

The two coordinate systems are related as:

$$\Delta\sigma^* = \Delta\sigma - \delta\sigma_0; \Delta\varepsilon^{p*} = \Delta\varepsilon^p; \Delta\varepsilon^{e*} = \Delta\varepsilon^e - \delta\sigma_0 / E$$

Figure A-3 Illustration of ΔW^p Calculation for a Non-Masing-type Material

220

APPENDIX B.

MATERIAL PROPERTIES IN ANALYTICAL INVESTIGATION

221

The material properties that were used in the analytical investigation presented in Chapter 5 are summarized in the following two tables: Table B-1 for the cyclic stress versus strain properties and fatigue crack propagation properties, and Table B-2 for the fatigue crack initiation properties. The blanks underneath energy-life curves in Table B-2 indicate energy-based methods were not used in the particular analysis. Energy-life properties are not available for A36 steel; however, such properties have been obtained from experimental program for HPS 485W steel and are presented in Table 4-11.

Table B-1 Cyclic Stress versus Strain Curve and Properties used for Fatigue Crack Propagation Life Prediction

Section	Detail Name	Specimen Material	Material used in Analysis	Cyclic Stress vs. Strain Curve			Material Properties for Crack Propagation Life Prediction		
				E (MPa)	K' (MPa)	n'	C	m	K_{IC} ($MPa\sqrt{m}$)
5.2	Plate with a Circular Hole	A36 HPS(LT)	A36	200000	1336	0.226	6.90×10^{-9}	3.00	50
			HPS(LT)	197100	956	0.113	2.27×10^{-10}	3.26	70
			A7	201400	1139	0.248	6.90×10^{-9}	3.00	50
			HPS(HT)	197000	666	0.076	2.27×10^{-10}	3.26	70
5.3	Shear Splice	300W	A36	200000	1336	0.226	6.90×10^{-9}	3.00	50
			HPS(LT)	197100	956	0.113	3.06×10^{-9}	3.12	70
5.4	Riveted Connection	300W	A36	200000	1336	0.226	6.90×10^{-9}	3.00	50
			HPS(LT)	197100	956	0.113	3.06×10^{-9}	3.12	70
5.5	Cruciform	A588	HPS(LT)	197100	956	0.113	1.54×10^{-9}	3.34	50
5.6	Coverplate	A588	HPS(LT)	197100	956	0.113	1.54×10^{-9}	3.34	50
5.7	Plate Girder	HPS485W HPS690W	HPS(LT)	197100	956	0.113	7.17×10^{-9}	3.02	
			HPS(LT)	197100	956	0.113	7.17E-09	3.02	

Table B-2 Material Properties used for Fatigue Crack Initiation Life Prediction

Section	Detail Name	Specimen Material	Material used in Analysis	σ_f' (MPa)	b	ε_f'	c	F_p (MJ/m³)	α_p	F (MJ/m³)	α	ΔW_0 (MJ/m³)	F_t (MJ/m³)	α_t	$\Delta W_0'$ (MJ/m³)
5.2	Plate with a Circular Hole	A36 HPS(LT)	A36	1036	-0.110	0.242	-0.480								
			HPS(LT)	851	-0.069	0.775	-0.701								
			A7	760	-0.121	0.196	-0.486	622	-0.642	431	-0.560	0.12	551	-0.621	0.03
			HPS(HT)	776	-0.073	6.207	-0.940								
5.3	Shear Splice	300W	A36	1036	-0.110	0.242	-0.480								
			HPS(LT)	851	-0.069	0.775	-0.701								
5.4	Riveted Connection	300W	A36	1036	-0.110	0.242	-0.480								
			HPS(LT)	851	-0.069	0.775	-0.701								
5.5	Cruciform	A588	HPS(LT)	851	-0.069	0.775	-0.701						1463	-0.721	0.20
5.6	Coverplate	A588	HPS(LT)	851	-0.069	0.775	-0.701						1463	-0.721	0.20
5.7	Plate Girder	HPS485W	HPS(LT)	851	-0.069	0.775	-0.701						1463	-0.721	0.20
		HPS690W	HPS(LT)	851	-0.069	0.775	-0.701						1463	-0.721	0.20